Polyethylene Glycol and Perfluoropolyether Graft Copolymer Electrolytes for Lithium-Ion Transport

Dissertation

zur Erlangung des akademischen Grades
eines Doktors der Naturwissenschaften (Dr. rer. nat.)
im Promotionsprogramm „Polymer Science“
der Bayreuther Graduiertenschule für Mathematik und Naturwissenschaften (BayNAT)

vorgelegt von

Hubertus Burchardt-Tofaute

geboren in Göttingen, Deutschland

Bayreuth, 2024

Die vorliegende Arbeit wurde in der Zeit von Dezember 2013 bis Mai 2018 in der Arbeitsgruppe Angewandte Funktionspolymere der Universität Bayreuth unter Betreuung von Herrn Professor Dr. Mukundan Thelakkat angefertigt. Ab Juni 2018 wurde der schriftliche Teil der Arbeit ohne der Anstellung als wissenschaftlicher Mitarbeiter der Universität Bayreuth fertiggestellt.

Vollständiger Abdruck der von der Bayreuther Graduiertenschule für Mathematik und Naturwissenschaften (BayNAT) der Universität Bayreuth genehmigten Dissertation zur Erlangung des akademischen Grades eines Doktors der Naturwissenschaften (Dr. rer. nat.).

Form der Dissertation:	Monographie
Dissertation eingereicht am:	02.11.2023
Zulassung durch das Leitungsgremium am:	07.12.2023
Wissenschaftliches Kolloquium am:	03.06.2024

Amtierender Direktor der Graduiertenschule: Prof. Dr. Jürgen Köhler

Prüfungsausschuss:

Prof. Dr. Mukundan Thelakkat (Gutachter)
Prof. Dr. Andreas Greiner (Gutachter)
Prof. Dr. Georg Papastavrou (Vorsitz)
Prof. Dr. Ralf Moos

Die vorliegende Arbeit ist als Monographie verfasst.

Teile der Arbeit (Kapitel 3.2) sind bereits in der folgenden Publikation erschienen:

The effect of fluorination on chain transfer reactions in the radical polymerization of oligo ethylene glycol ethenesulfonate monomers

H. Burchardt-Tofaute, M. Thelakkat, *Polym. Chem.* **2018**, *9*, 4172–4186.

DOI: 10.1039/c8py00623g

Diese Publikation ist in der vorliegenden Arbeit mit der Literaturstelle [152] zitiert.

‘A person with a new idea is a crank until the idea succeeds.’

Mark Twain

Content

Abbreviations

Abbreviation	Long text
(P4VP-*g*-EGSA)-*b*-PS	poly(4-vinylpyridine)-*grafted*-oligo(ethylene glycol)sulfonic acid-*block*-poly(styrene)
1,2-PBD	1,2-polybutadiene
^{19}F NMR	fluorine-19 nuclear magnetic resonance
^{1}H NMR	proton nuclear magnetic resonance
2FEG2ES	2,2-difluoro-2-(1,1,2,2-tetrafluoro-2-(trifluoromethoxy)ethoxy)ethyl 2-(2-,2-difluoro-2-(1,1,2,2-tetrafluoro-2-(trifluoromethoxy)ethoxy)ethoxy)ethanesulfonate
2FEG3ES	2,2-difluoro-2-(1,1,2,2-tetrafluoro-2-(1,1,2,2-tetrafluoro-2-(trifluoromethoxy)ethoxy)ethoxy)ethyl 1,1,1,3,3,4,4,6,6,7,7,9,9-tridecafluoro - 2,5,8,11-tetraoxatridecane-13–sulfonate
A^-	lithium salt anion
AC	alternating current
AIBN	2,2'-azobis(isobutyronitrile)
A_N	nucleophilic addition
ATR	attenuated total reflection
br	broadened (NMR spectroscopy)
C	hexagonally packed cylinders
CA	chronoamperometric
CEI	cathode electrolyte interface
ClO_4^-	perchlorate
CTA	chain transfer agent
CuAAC	copper(I)-catalyzed alkyne-azide cycloaddition
CV	cyclic voltammetry
d	doublet (NMR spectroscopy)
DC	direct current
DCTB	*trans*-2-[3-(4-*tert*-butylphenyl)-2-methyl-2-propenylidene]malononitrile
dd	doublet of doublets (NMR spectroscopy)
DEC	diethyl carbonate
DHB	2,5-dihydroxybenzoic acid
DMA	dynamic mechanical analysis
DMC	dimethyl carbonate

DSC	differential scanning calorimetry
EC	ethylene carbonate
EEC	equivalent electrical circuit
EES	ethyl ethenesulfonate
EG	ethylene glycol
EG1ES	2-methoxyethyl ethenesulfonate
EG3ES	2-(2-(2-methoxyethoxy)ethoxy)ethyl ethenesulfonate
EGA	methoxypolyethylene glycol acrylate
EGES	oligo ethylene glycol ethenesulfonate
EGMA	oligo(ethylene glycol) methyl ether methacrylate
EGS	thiol-functionalized monomethoxy ethylene glycol (dimers or trimers)
EIS	electrochemical impedance spectroscopy
EMC	ethyl methyl carbonate
engl.	englisch
EPETA	2-(ethoxycarbonothioylthio)propanoic (*O*-ethyl carbonothioic) thio-anhydride
Eq	equilibrium
ES	ethenesulfonate
ETT-3	tri(oxymethylene)
FEG	fluorinated ethylene glycol
FEG2ES	2,2-difluoro-2-(1,1,2,2-tetrafluoro-2-(trifluoromethoxy)ethoxy)ethyl ethenesulfonate
FEG3	2-difluoro-2-(1,1,2,2-tetrafluoro-2-(1,1,2,2-tetrafluoro-2-(trifluoromethoxy)ethoxy)ethoxy)ethanol
FEG3E	1,1,1,3,3,4,4,6,6,7,7,9,9-tridecafluoro-2,5,8,11-tetraoxatridecane
FEG3ES	2,2-difluoro-2-(1,1,2,2-tetrafluoro-2-(1,1,2,2-tetrafluoro-2-(trifluoromethoxy)ethoxy)ethoxy)ethyl ethenesulfonate
FEGES	fluorinated oligo ethylene glycol ethenesulfonate
FRP	free radical polymerization
FSI	bis(fluorosulfonyl)imide
FT	fourier transform
G	double gyroid
HFB	hexafluorobenzene
HFIP	hexafluoroisopropanol
I	initiator

IAA	*trans*-3-indoleacrylic acid
IR	infrared
KTFA	potassium trifluoroacetate
L	lamellae
L	ligand
Li_2O	lithium oxide
Li_2S	lithium sulfide
LiAPTFSI	lithium 3-azidoproanesulfonyltrifluoro-methanesulfonylimide
LIB	lithium-ion battery
$LiCoO_2$	lithium cobalt(III) oxide
LiFEG3	lithium 2,2-difluoro-2-(1,1,2,2-tetrafluoro-2-(1,1,2,2-tetrafluoro-2-(trifluoromethoxy)ethoxy)ethoxy)ethan-1-olate
$LiFePO_4$	lithium iron(II) phosphate
LiFSI	lithium bis(fluorosulfonyl)imide
LiMA	lithium methacrylate
$LiMn_2O_4$	lithium manganese(III, IV) oxide
LiOH	lithium hydroxide
Li-S-battery	lithium-sulfur-battery
LiTFSI	lithium bis(trifluoromethanesulfonyl)imide
Li_xMeO_y	lithium metal oxide
M	monomer
m	multiplet (NMR spectroscopy)
MADIX	macromolecular design via the interchange of xanthates
MALDI-ToF MS	matrix-assisted laser desorption/ionization time-of-flight mass spectrometry
Na_4EDTA	tetrasodium ethylenediaminetetraacetate hydrate
NCA	lithium nickel cobalt aluminum oxide ($LiNi_xCo_yAl_zO_2$)
NCM	lithium nickel manganese cobalt oxide ($LiNi_xCo_yMn_zO_2$, $x + y + z = 1$)
NMRP	nitroxide-mediated radical polymerization
OEMDTC	*O*-ethyl-*S*-(1-methoxycarbonyl) ethyldithiocarbonate
PAGE	poly(allyl glycidyl ether)
PAGE-*g*-EGS	poly(allyl glycidyl ether)-*grafted*-thiol-functionalized monomethoxy ethylene glycol (dimers or trimers)
PC	propylene carbonate
PC	poly(carbonate)

PCL	poly(ε-caprolactone)
PE	poly(ethylene)
PE-*b*-(PEG-*co*-PG)-*b*-PE	poly(ethylene)-*block*-(poly(ethylene glycol-*co*-propylene glycol)-*block*-poly(ethylene)
PEC	poly(ethylene carbonate)
PEES	poly(ethyl ethenesulfonate)
PEES-RAFT	poly(ethyl ethenesulfonate) synthesized by RAFT (reference polymer from the literature)
PEES-RAFT1	PEES synthesized by RAFT (polymer 1)
PEES-RAFT2	PEES synthesized by RAFT (polymer 2)
PEG	poly(ethylene glycol)
PEG1ES	poly(2-methoxyethyl ethenesulfonate)
PEG3ES	poly(2-(2-(2-methoxyethoxy)ethoxy)ethyl ethenesulfonate
PEGMA-*co*-LiMA	poly(oligo(ethylene glycol) methyl ether methacrylate-*co*-lithium methacrylate)
PEG-OH	poly(ethylene glycol) monomethyl ether
PEIS	potentiostatic electrochemical impedance spectroscopy
PEO-*co*-EC	poly(ethylene oxide-*co*-ethylene carbonate)
PES	poly(ethenesulfonate)
PES	poly(ether-sulfone)
PESO	poly(ether-sulfoxide)
PETE	poly(ether-thioether)
PF_6^-	hexafluorophosphate
PFA	perfluoroalkyl
PFAP	perfluoroalkylated pyrazolide anion without a modification
PFAPB	perfluoroalkylated pyrazolide anion with a trifluoroborate group
PFD	perfluorodecalin
PFEG2ES	poly(2,2-difluoro-2-(1,1,2,2-tetrafluoro-2-(trifluoromethoxy)ethoxy)ethyl ethenesulfonate
PFEG2ES-RAFT	PFEG2ES synthesized by RAFT
PFEG3ES	poly(2,2-difluoro-2-(1,1,2,2-tetrafluoro-2-(1,1,2,2-tetrafluoro-2-(trifluoro-methoxy)ethoxy)ethoxy)ethyl ethenesulfonate
PFEG3ES-FRP-UP	PFEG3ES synthesized by FRP (up-scaling)
PFEG3ES-RAFT	PFEG3ES synthesized by RAFT
PFEG3ES-RAFT-UP	PFEG3ES synthesized by RAFT (up-scaling)
PFEGES	poly(fluorinated oligo ethylene glycol ethenesulfonate)

PFPE	perfluoropolyether
PGPE	poly(glycidyl propargyl ether)
PGPE-*g*-(EG3-*co*-Bn-*co*-LiAPTFSI)	poly(glycidyl propargyl ether)-*grafted*-(azide-functionalized ethylene glycol-*co*-benzyl-*co*-lithium 3-azidoproanesulfonyltrifluoro-methanesulfonylimide)
PI	poly(isoprene)
PLiSsTFSI	poly(lithium (4-styrenesulfonyl)(trifluoromethyl(*S*-trifluoromethylsulfonylimino)sulfonyl)imide
PLiSTFSI	poly(lithium 4-styrenesulfonyl(trifluoromethylsulfonyl)imide)
PMA	poly(methacrylate)
PMDETA	*N*,*N*,*N*′,*N*″,*N*″-pentamethyldiethylenetriamine
PMMA	poly(methyl methacrylate)
POS	poly(4-(propargyloxy)styrene)
PPC	poly(propylene carbonate)
PPOS-*g*-PEG	poly(4-(propargyloxy)styrene)-*grafted*-poly(ethylene glycol)
PRES	poly(ethenesulfonate)s carrying different R substituents
PS	poly(styrene)
PS-*b*-(PMA-*g*-EG)-*b*-PS	poly(styrene)-*block*-(poly(methacrylate)-*grafted*-ethylene glycol)-*block*-poly(styrene)
PS-*b*-PEG	poly(styrene)-*block*-poly(ethylene glycol)
PS-*b*-PI	poly(styrene)-*block*-poly(isoprene)
PSS	Polymer Standards Service GmbH
PTMC	poly(trimethylene carbonate)
PTMC-*co*-CL	poly(trimethylene carbonate-*co*-*ε*-caprolactone)
PTMSPOS	poly(4-(3’-trimethylsilylpropargyloxy)styrene)
PVDF-*co*-HFP	poly(vinylidene fluoride-*co*-hexafluoropropylene)
q	quartet (NMR spectroscopy)
RAFT	reversible addition-fragmentation chain transfer
S	body centred cubic
s	singlet (NMR spectroscopy)
SAXS	small-angle X-ray scattering
SEC	size exclusion chromatography
SEI	solid electrolyte interface
SPE	solid polymer electrolyte
t	triplet (NMR spectroscopy)

TBAB	tetrabutylammonium bromide
TBAF	tetrabutylammonium fluoride
td	triplet of doublets (NMR spectroscopy)
TEM	transmission electron microscopy
TFS	trifluoromethanesulfonate
TFSI	bis(trifluoromethanesulfonyl)imide
TGA	thermal gravimetric analysis
TIPNO	2,2,5-trimethyl-4-phenyl-3-azahexane-3-nitroxide
TMC	trimethylene carbonate
TMSPOS	4-(3’-trimethylsilylpropargyloxy)styrene
TR	1,4-disubstituted 1,2,3-triazole
TSC	theoretical specific capacity
VTF	Vogel-Tammann-Fulcher
W	Watanabe
WAXS	wide-angle x-ray scattering

Symbols and Constants

Symbols and Constants	Name
$[CTA]_0$	initial molar concentration of the chain transfer agent
$[I]_0$	initial molar concentration of the initiator
$[M]_0$	initial molar concentration of the monomer
μ_-	ion mobility of anions
μ_+	ion mobility of cations
a	active cell area
A	pre-exponential factor (Arrhenius law)
A_{VTF}	pre-exponential factor (VTF relation)
b	intercept of the linear equation form (Arrhenius law or VTF relation)
B	material-dependent constant/pseudo-activation energy (VTF relation)
c_-	anion concentration
c_+	cation concentration
C_b	geometrical capacitance of the electrolyte/blocking electrode structure
C_{dl}	double layer capacitance
conv.	monomer conversion
CPE_b	constant phase element replacing the geometrical capacitance of the electrolyte/blocking electrode structure
CPE_{dl}	double layer constant phase element
$Đ$	dispersity
DP_n	degree of polymerization
E	mass of end group
E	potential
E'	storage modulus
E''	loss modulus
E_a	activation energy for the ion movement (Arrhenius law)
E_{pa}	anodic peak potential
f	regular frequency
$F_\pm$	attractive force between the charges + and -
f_A	volume fraction of the polymer block A
i	imaginary unit $(-1)^{1/2}$

I_-	current transported by anions
I_+	current transported by cations
I_0	initial current (CA measurement)
I_0	alternating current amplitude
I_a	integral of the NMR signal a
I_{AC}	alternating current
I_b	integral of the NMR signal b
I_c	integral of the NMR signal c
I_s	steady state current (CA measurement)
I_Ω	initial current according to Ohm's law (CA measurement)
J	coupling constant (NMR spectroscopy)
J	current density
M	molecular weight/molar mass
m	mass
m	slope of the linear equation form (Arrhenius law)
$M_{n,\,NMR}$	number-average molecular weight determined by NMR spectroscopy
$M_{n,\,SEC}$	number-average molecular weight determined by SEC
$M_{n,\,theor}$	theoretical number-average molecular weight
$M_{p,\,MALDI}$	peak molecular weight determined by MALDI-ToF MS
$M_{p,\,SEC}$	peak molecular weight determined by SEC
$m_{polymer}$	mass of polymer
$M_{polymer}$	molar mass of one monomer unit
m_{salt}	mass of lithium salt
n	molar amount
N	number of atoms
n	charge carrier concentration
N	degree of polymerization
n	degree of polymerization
n_{Li+}	molar amount of lithium ions in the salt
$N_{Li+,\,salt}$	number of lithium atoms in the lithium salt
n_O	molar amount of oxygen atoms
$N_{O,\,polymer}$	number of oxygen atoms in the polymer monomer unit
$N_{O,\,salt}$	number of oxygen atoms in the lithium salt
$n_{polymer}$	molar amount of the polymer monomer units

n_{salt}	molar amount of the lithium salt
O/Li	molar ratio of oxygen to lithium atoms
q	charge
R	molar gas constant, 8.314472 J mol^{-1} K^{-1}
r	LiTFSI concentration
$r_{\pm}$	distance between the charges + and -
R_{app}	apparatus resistance
R_b	electrolyte bulk resistance
R_{b0}	electrolyte bulk resistance before the DC polarization (CA measurement)
R_{bs}	electrolyte bulk resistance after the DC polarization (CA measurement)
R_c	charge transfer resistance
R_f	passivation film resistance
R_i	overall interface resistance
R_{i0}	interface resistance before the DC polarization (CA measurement)
R_{is}	interface resistance after the DC polarization (CA measurement)
t	electrolyte thickness
T	temperature
t	time
t^+	transference number
t^+_{BV}	transference number determined by the Bruce-Vincent method
t^+_W	transference number according to Watanabe *et al.*
T_0	thermodynamic Kauzmann temperature (VTF relation)
tanδ	loss factor
T_c	melt-crystallization temperature
T_{cc}	cold-crystallization temperature
$T_{d,\,1\%}$	temperature at which the sample lost 1 wt% (TGA)
$T_{d,\,5\%}$	temperature at which the sample lost 5 wt% (TGA)
T_g	glass transition temperature
T_m	melting temperature
tn^+	transport number
T_p	peak temperature
V_0	voltage amplitude
V_{AC}	alternating current voltage
$\underline{Z}$	complex impedance

Z'	real part of the complex impedance
Z''	imaginary part of the complex impedance
Z_0	impedance amplitude
Z_d	diffusion impedance
δ	chemical shift (NMR spectroscopy)
ΔA	error of the pre-exponential factor (Arrhenius law)
ΔA_{VTF}	error of the pre-exponential factor (VTF relation)
Δb	error of the intercept of the linear equation form (Arrhenius law or VTF relation)
ΔB	error of the material-dependent constant/pseudo-activation energy (VTF relation)
ΔE_a	error of the activation energy for the ion movement (Arrhenius law)
ΔH_c	normalized melt-crystallization enthalpy
ΔH_{cc}	normalized cold-crystallization enthalpy
ΔH_m	normalized melting enthalpy
$\Delta H_{m,\,total}$	normalized total melting enthalpy
Δm	error of the slope of the linear equation form (Arrhenius law)
ΔT_0	error of the thermodynamic Kauzmann temperature (VTF relation)
ΔV	direct current voltage
$\Delta\sigma$	standard deviation
ε_0	vacuum permittivity, 8.8542×10^{-12} CV^{-1} m^{-1}
ε_r	dielectric constant
η	nucleation overpotential
μ	charge carrier mobility
σ	ionic conductivity
φ	phase shift
χ	Flory-Huggins-parameter
ω	angular frequency

Abstract

Lithium-ion batteries (LIB) are conquering the market especially in the electric mobility and as stationary energy storage systems. Common solid polymer electrolytes (SPE) for LIBs base on linear poly(ethylene glycol) (PEG). To increase the ionic conductivity σ and thus the charge time of the battery, graft copolymers are promising materials due to their generally lower crystallinity and glass transition temperature T_g. In the first chapter of this thesis, the thermal, morphological and electrochemical properties of linear PEG SPEs with those of triazole-linked graft copolymer SPEs at different PEG side-chain lengths were compared. New graft copolymers, poly(4-(propargyloxy)styrene)-*grafted*-poly(ethylene glycol)s, featuring narrow molecular weight distributions and high grafting densities were synthesized. Below the melting temperature T_m, the graft copolymer SPEs showed a lower crystallinity than their linear counterparts. Nearly all graft copolymer SPEs were amorphous. Above T_m, or for the amorphous SPEs above T_g, the only material parameter influencing σ was T_g. Since it was higher for the graft copolymer SPEs and the shorter side-chain, these SPEs showed a lower σ. However, the triazole-linkage in the graft copolymers revealed a positive contribution to σ by supporting lithium salt dissociation. Their high thermal and electrochemical stability plus their ability for lithium plating/stripping at an electrode make the new SPEs to powerful materials for LIBs.

In the second chapter of this thesis, graft copolymers comprising a poly(ethenesulfonate) (PES) backbone with oligo ethylene glycol or oligo perfluoropolyether side-chains were synthesized for the first time. The effect of fluorination on the polymerization of oligo ethylene glycol ethenesulfonate (EGES) monomers, containing one (EG1ES) or three (EG3ES) ethylene glycol units, was studied. In a conventional free radical polymerization EGES monomers formed only oligomers. In contrast, the fluorinated oligo ethylene glycol ethenesulfonate (FEGES) monomers, containing two (FEG2ES) or three (FEG3ES) fluorinated ethylene glycol units, showed high conversions and high molecular weights. An end-group analysis by matrix-assisted laser desorption/ionization time-of-flight mass spectrometry (MALDI-ToF MS) revealed that the suppression of chain transfer reactions from methylene ether and methoxy groups was the reason for this drastic effect. This technique was not only used for a detailed end-group analysis, but also to determine the absolute molecular weight of PESs. Furthermore, the reversible addition-fragmentation chain transfer (RAFT) polymerization of the FEGES monomers was tested. Whereas the RAFT polymerization of FEG2ES was dominated by recombination processes, high end-group fidelity for PFEG3ES with an ethyldithiocarbonate chain

transfer agent was achieved. PFEG2ES synthesized by RAFT was semi-crystalline, while PFEG3ES was fully amorphous at room temperature. This was proven by differential scanning calorimetry (DSC), dynamic mechanical analysis (DMA) and wide-angle x-ray scattering (WAXS). Their low crystallinity, their adequate thermal stability and their reduced flammability due to the fluorination make PFEGES polymers potential materials as SPEs for battery applications.

LIBs still suffer from a too low specific energy, which limits the range of an electric car, for example. High values can be realized by high cell voltages. To maintain a high level of safety, the electrolyte as one main component of the battery must be dimensionally stable, nonflammable and electrochemically stable against high potentials. Perfluoropolyether (PFPE) SPEs provide high safety but only a low solubility for common perfluoroalkyl lithium salts such as lithium bis(trifluoromethanesulfonyl)imide (LiTFSI). This issue requires the synthesis of new PFPE lithium salts. The question here is whether the incorporation of PFPE tails in lithium salts can increase the solubility and thus σ in PFPE SPEs. For this purpose, the new salt, lithium 2,2-difluoro-2-(1,1,2,2-tetrafluoro-2-(1,1,2,2-tetrafluoro-2-(trifluoromethoxy)ethoxy)ethoxy)ethan-1-olate (LiFEG3) was synthesized in the third chapter of this thesis. The solubility and ionic conductivity of LiTFSI and LiFEG3 in PFEG3ES as a PFPE SPE host polymer were compared. In contrast to LiTFSI SPEs, LiFEG3 SPEs (SPE-O/Li ratio) could be prepared from solution. The maximum ion concentration A contributing to σ was observed for SPE-15. However, the maximum ionic conductivity was shifted to SPE-5 ($(1.22 \pm 0.24) \times 10^{-6}$ S cm^{-1} at 80 °C) since it showed the lowest activation energy for ion movement E_a. The SPEs are electrochemically stable up to at least 5 V vs. Li/Li$^+$ at 60 °C. So they are of great importance for the safe use in LIBs with high cell voltages.

Kurzfassung

Lithium-Ionen-Batterien erobern den Markt vor allem im Bereich der Elektromobilität und als stationäre Energiespeichersysteme. Gängige polymere Feststoffelektrolyte (engl. solid polymer electrolyte, SPE) für Lithium-Ionen-Batterien basieren auf linearem Poly(ethylenglykol) (PEG). Um die Ionenleitfähigkeit σ und damit die Ladezeit der Batterie zu erhöhen, sind Pfropfcopolymere aufgrund ihrer allgemein geringeren Kristallinität und Glasübergangstemperatur T_g vielversprechende Materialien. Im ersten Kapitel dieser Arbeit wurden die thermischen, morphologischen und elektrochemischen Eigenschaften von linearen PEG-SPEs mit denen von triazolverknüpften Pfropfcopolymer-SPEs bei unterschiedlichen PEG-Seitenkettenlängen verglichen. Es wurden neue Pfropfcopolymere, Poly(4-(propargyloxy)styrol)-*gepfropftes*-Poly(ethylenglykol)e, mit engen Molekulargewichtsverteilungen und hohen Pfropfdichten synthetisiert. Unterhalb der Schmelztemperatur T_m zeigten die Pfropfcopolymer-SPEs eine geringere Kristallinität als ihre linearen Gegenstücke. Nahezu alle Pfropfcopolymer-SPEs waren amorph. Oberhalb T_m und bei den amorphen SPEs oberhalb T_g war der einzige Materialparameter, der σ beeinflusste, T_g. Da sie für die Pfropfcopolymer-SPEs und die kürzere Seitenkette höher war, zeigten diese SPEs ein niedrigeres σ. Die Triazolverknüpfung in den Pfropfcopolymeren zeigte jedoch einen positiven Beitrag zu σ, indem sie die Dissoziation des Lithiumsalzes unterstützte. Ihre hohe thermische und elektrochemische Stabilität, sowie ihre Fähigkeit, Lithium an einer Elektrode abzuscheiden und wieder abzulösen, machen die neuen SPEs zu leistungsfähigen Materialien für Lithium-Ionen-Batterien.

Im zweiten Kapitel dieser Arbeit wurden erstmals Pfropfcopolymere bestehend aus einem Poly(ethensulfonat)-Rückgrat (PES) mit Oligoethylenglykol- oder Oligoperfluorpolyether-Seitenketten synthetisiert. Der Effekt der Fluorierung auf die Polymerisation von Oligoethylenglykol-Ethensulfonat (EGES)-Monomeren, die eine (EG1ES) oder drei (EG3ES) Ethylenglykoleinheiten enthalten, wurde untersucht. Bei einer konventionellen radikalischen Polymerisation bildeten die EGES-Monomere lediglich Oligomere. Im Gegensatz dazu zeigten die fluorierten Oligoethylenglykol-Ethensulfonat (FEGES)-Monomere, die zwei (FEG2ES) oder drei (FEG3ES) fluorierte Ethylenglykoleinheiten enthielten, hohe Umsätze und hohe Molekulargewichte. Eine Endgruppenanalyse mittels Matrix-unterstützter Laserdesorptions/-ionisations-Flugzeit Massenspektrometrie (engl. matrix-assisted laser desorption/ionization time-of-flight mass spectrometry, MALDI-ToF MS) ergab, dass die Verhinderung von Kettenübertragungsreaktionen von Methylenether- und Methoxygruppen der Grund für diesen gravierenden Effekt war. Diese Technik

wurde nicht nur für eine detaillierte Endgruppenanalyse verwendet, sondern auch zur Bestimmung des absoluten Molekulargewichts der Poly(ethensulfonat)e. Darüber hinaus wurde die reversible Additions-Fragmentierungs Kettenübertragungs (RAFT)-Polymerisation der FEGES-Monomere getestet. Während die RAFT-Polymerisation von FEG2ES von Rekombinationsprozessen dominiert wurde, konnte für PFEG3ES mit einem Ethyldithiocarbonat-Kettentransferreagenz eine hohe Endgruppenqualität erzielt werden. Das durch RAFT synthetisierte PFEG2ES war teilkristallin, während PFEG3ES bei Raumtemperatur vollständig amorph war. Dies wurde mittels dynamischer Differenzkalorimetrie (engl. differential scanning calorimetry, DSC), dynamisch-mechanischer Analyse (DMA) und Weitwinkelröntgenstreuung (engl. wide-angle x-ray scattering, WAXS) nachgewiesen. Ihre geringe Kristallinität, ihre ausreichende thermische Stabilität und ihre reduzierte Entflammbarkeit aufgrund der Fluorierung machen PFEGES-Polymere zu potenziellen Materialien als SPEs für Batterieanwendungen.

Lithium-Ionen-Batterien haben nach wie vor eine zu niedrige spezifische Energie, welche beispielsweise die Reichweite eines Elektroautos limitiert. Hohe Werte können durch hohe Zellspannungen realisiert werden. Um ein hohes Maß an Sicherheit zu gewährleisten, muss der Elektrolyt als ein Hauptbestandteil der Batterie formstabil, nicht brennbar und elektrochemisch stabil gegenüber hohen Potenzialen sein. Perfluorpolyether (PFPE)-SPEs bieten eine hohe Sicherheit, aber nur eine geringe Löslichkeit für gängige Perfluoralkyllithiumsalze wie Lithiumbis(trifluormethansulfon)imid (LiTFSI). Dieses Problem erfordert die Synthese neuer PFPE-Lithiumsalze. Die Frage besteht hier, ob der Einbau von PFPE-Schwänzen in Lithiumsalze die Löslichkeit und damit σ in PFPE-SPEs erhöhen kann. Zu diesem Zweck wurde im dritten Kapitel dieser Arbeit das neue Salz Lithium-2,2-difluor-2-(1,1,2,2- tetrafluor-2-(1,1,2,2- tetrafluor-2- (trifluormeth-oxy)ethoxy)ethoxy)ethan-1-olat (LiFEG3) synthetisiert. Die Löslichkeit und Ionenleitfähigkeit von LiTFSI und LiFEG3 in PFEG3ES als PFPE SPE-Hostpolymer wurden verglichen. Im Gegensatz zu LiTFSI-SPEs konnten LiFEG3-SPEs (SPE-O/Li-Verhältnis) aus Lösung hergestellt werden. Die maximale Ionenkonzentration A, die zu σ beiträgt, wurde für SPE-15 beobachtet. Das Maximum von σ war jedoch zu SPE-5 ($(1{,}22 \pm 0{,}24) \times 10^{-6}$ S cm^{-1} bei 80 °C) verschoben, da es die niedrigste Aktivierungsenergie für die Ionenbewegung E_a aufwies. Die SPEs sind bis zu mindestens 5 V vs. Li/Li$^+$ bei 60 °C elektrochemisch stabil. Sie sind daher von großer Bedeutung für den sicheren Einsatz in Lithium-Ionen-Batterien mit hohen Zellspannungen.

1 Introduction

1.1 Safety aspects of lithium-ion batteries

Lithium-ion batteries (LIBs) have conquered the market as the portable energy source for laptops, mobile phones, digital cameras and in the field of the electric mobility in the last three decades, since they show a high specific energy.[1–3] They are also gaining great attention in the field of stationary home and grid storage systems to buffer the fluctuation of photovoltaic energy, though the specific energy is not as important as in portable applications.[4] In all these applications, the safety of the battery must be absolutely guaranteed even in the case of mechanical, electrical or thermal abuse. Especially when cells are stacked together to large modules and packs, ignition by thermal runaway and the self-heating must be prevented.[5] In the last two decades, several LIB fires in all application fields have received great media attention.[6]

Since suitable materials for the interior of LIBs are still lacking to ensure both high safety and short charging times, external additional equipment is required. For instance, flame resistant compression pads made of polymer foam between the cells in the stack are actually used.[7,8] They compensate the dimensional change of the LIBs during cycling and reduce the heat transfer between the cells.[8] However, additional equipment means lower specific energy regarding the entire storage system. For this reason, and to ensure an intrinsic safety of the cell, the development and investigation of new materials is still required.

Besides the anode and cathode, the electrolyte is the most important component of the battery.[2] It determines the charge time, specific energy, lifetime and safety depending on its ionic conductivity, electrochemical stability and selective transport of lithium ions.[9,10] Currently, liquid and flammable electrolytes based on organic carbonates are still used commercially.[11] Particularly lithium polymer batteries with a solid polymer electrolyte (SPE) are distinguished for a high energy density and a safe application. In this context, especially fluorinated electrolytes might be nonflammable and also operate in a wide voltage and temperature window. Therefore, novel polymer electrolytes, also based on fluorinated polymers, will be synthesized and characterized within the scope of this thesis.

1.2 Set-up and materials of a lithium-ion battery

A typical lithium-ion battery (LIB) is composed of a graphite anode and a lithium metal oxide (Li_xMeO_y) cathode (Fig. 1).[2,12] The materials are coated on metal current collectors that are connected to the external circuit.[13] Inside the cell they are electrically isolated by a lithium ion conducting electrolyte. It determines the charge time, power, specific capacity, lifetime and safety. The electrolyte can be an inorganic crytalline, a glassy or lquid organic, a polymer gel, an ionic liquid or a solid polymer electrolyte (SPE).[14,15] A typical SPE consists of poly(ethylene glycol) (PEG) and a lithium salt.[16]

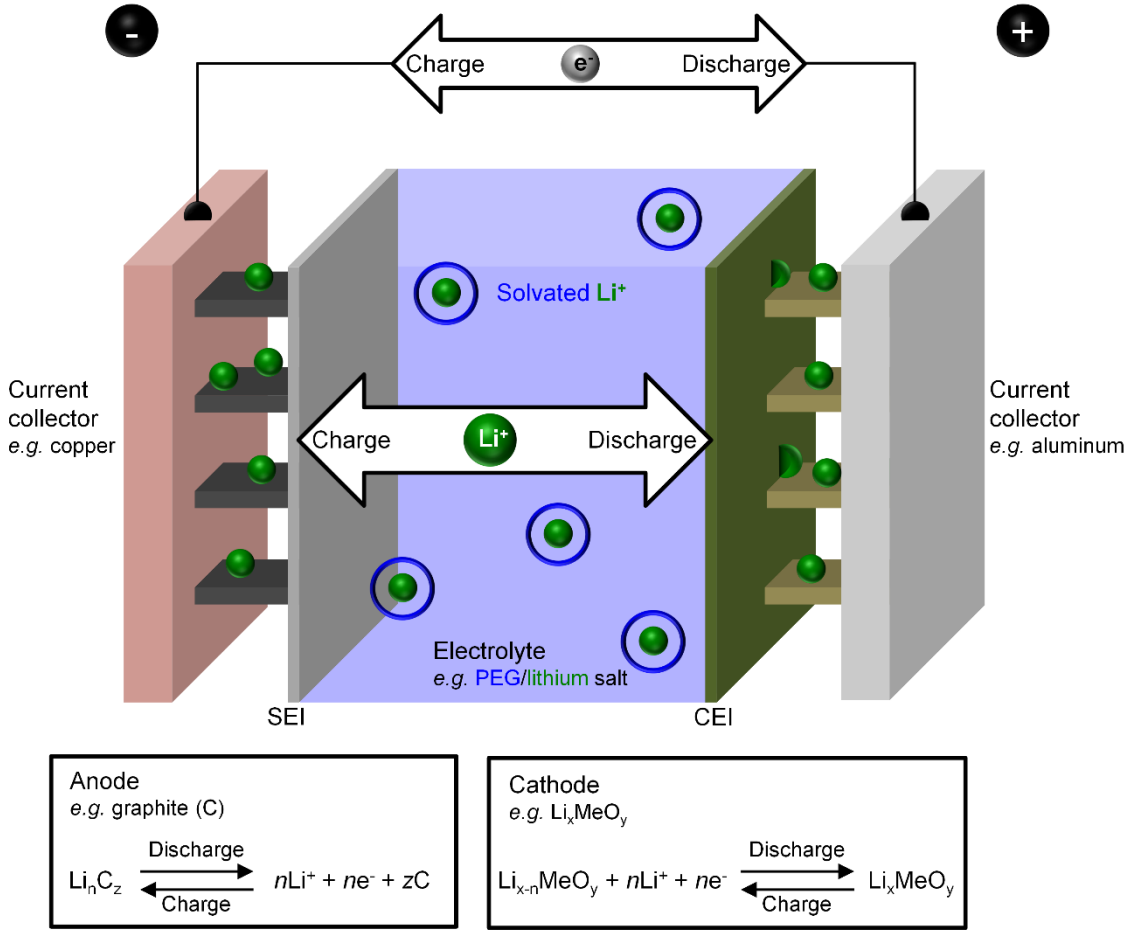

Fig. 1 Schematic set-up of a LIB. (SEI: Solid electrolyte interface; CEI: Cathode electrolyte interface; Li_xMeO_y: Lithium metal oxide with Me: *e.g.* Fe, Ni, Co, Mn and Al).[2,12]

When the battery is charged by applying an external voltage to the electrodes, the Li_xMeO_y is oxidized at the cathode. It releases lithium ions at the cathode electrolyte interface (CEI) into the electrolyte. The lithium ions are solvated by the electrolyte and move through it and the solid electrolyte interface (SEI) to the anode. Here, they are reduced and incorporated between the carbon layers of the graphite. During

battery discharge, the described process automatically proceeds in the reverse direction and provides electric power.[2,12]

Anode and cathode materials must maintain their dimensions while inserting and releasing lithium to prevent a failure of the battery. Intercalating electrode materials such as graphite and Li_xMeO_y meet this criterion to a certain extent since they offer space for the lithium in their layer structure.[17] To achieve a high energy density (product of voltage and capacity), the cathode material should have not only a high potential difference vs. Li/Li^+, but also a high weight fraction of cyclizable lithium, that is capacity.[18,19] The theoretical specific capacity (TSC) defines the maximum range of an electric car, for instance. An example of a Li_xMeO_y is lithium manganese(III, IV) oxide ($LiMn_2O_4$) with a TSC of 148 mAh g^{-1}.[20] Lithium cobalt(III) oxide ($LiCoO_2$) appears to have a significantly higher TSC of 278 mAh g^{-1}.[18] However, only half of the theoretical amount of lithium can be extracted, as further extraction would cause the structure to collapse. Therefore, its TSC should only be reported as 139 mAh g^{-1}.[18]

Furthermore, the use of cobalt is controversial due to increasing industrial demand and price, as well as questionable mining conditions. To replace cobalt, lithium iron(II) phosphate ($LiFePO_4$) cathodes with an acceptable TSC of 170 mAh g^{-1} are used.[21] Another approach to reduce the amount of cobalt and prevent the structural collapse at high lithium extraction is to add nickel and manganese.[22] This lithium nickel manganese cobalt oxide (NCM, $LiNi_xCo_yMn_zO_2$, $x + y + z = 1$) cathodes can achieve a relatively high TSC of 278 mAh g^{-1} and find actually application in the Volkswagen ID3.[18,23] A comparable TSC, but higher capacity in practice, is achieved by replacing manganese with aluminum in lithium nickel cobalt aluminum oxide (NCA, $LiNi_xCo_yAl_zO_2$) cathodes used in the Tesla Models S and X.[24,25] The TSC can only help as a value to compare different systems under ideal conditions and its calculation is controversial. In reality, other components of the battery also affect the specific capacity, such as the weight of the binders, additives, separators or current collectors.[18] However, the practical maximum specific capacity is changing very rapidly due to the great research efforts in this field.

Lithium uptake in non-intercalating cathodes is based on electrochemical reactions in which the lithium ions remain positively charged at the cathode during reduction. Due to the high weight fraction of lithium in lithium sulfide (Li_2S), a Li_2S cathode with the redox couple $S_8/8S^{2-}$ has a very high TSC of 1675 mAh g^{-1}.[26] An even higher TSC than for a lithium-sulfur-battery (Li-S-battery) can be achieved in a lithium-air/O_2-battery with aqueous or non-aqueous electrolytes.[1,27,28] Using an aqueous electrolyte, oxygen is reduced in the presence of lithium ions and water to lithium hydroxide (LiOH) at the cathode during discharge.[1] In the absence of water, the oxygen is reduced to lithium oxide (Li_2O)

obtaining a minimal TSC of 1790 mAh g^{-1}.[1] Nevertheless, lithium-air/O_2-batteries require a lot of additional heavy components. Therefore, the practical maximum specific capacity is much lower.
The capacity of a battery is always limited by the electrode material with the lower capacity. When a graphite anode is used, the maximum theoretical specific capacity of the battery is limited to 339 mAh g^{-1}.[18] Pure metallic lithium anodes provide the highest TSC of 3861 mAh g^{-1}. So the capacity of the LIB is limited only by the capacity of the cathode material.[18] However, lithium is not intercalated into the layers of the material, but deposited on the lithium metal surface, which can lead to lithium dendrite growth. This phenomenon can lead to battery failure and makes the choice of the appropriate electrolyte essential (chapter 1.4).

1.3 Quantification and detection of lithium ion transport processes

The charge time and electric power of a LIB are determined by the speed at which the lithium ions move through the electrolyte. This can be quantified by the ionic conductivity σ which depends on the charge carrier concentration n, charge q and mobility μ:[29]

$$\sigma = nq\mu \tag{1}$$

To increase n, a lithium salt is added to the electrolyte. The dissociation of the lithium salt by solvation of the electrolyte is the prerequisite for the ion conduction. The attractive force $F_{\pm}$ between the lithium cation and anion of the salt considered as point charges q^+ and q^- with a distance $r_{\pm}$ can be expressed by the Coulomb's law:[30]

$$F_{\pm} = \frac{q_+ q_-}{4\pi\varepsilon_0\varepsilon_r r_{\pm}^2} \tag{2}$$

where ε_0 is the vacuum permittivity (8.8542 x 10^{-12} CV^{-1} m^{-1}), and ε_r is the dielectric constant of the electrolyte. According to equation (2) the dissociation is facilitated in electrolytes with high ε_r.[31]
Delocalization of the negative charge in large anions with electron withdrawing groups can also contribute to easier dissociation of the lithium salt, since the charge is not concentrated at one point in space. Representatives of this group include perchlorate (ClO_4^-), hexafluorophosphate (PF_6^-), trifluoromethanesulfonate (TFS), bis(fluorosulfonyl)imide (FSI) and bis(trifluoromethanesulfonyl)imide (TFSI) anions (Fig. 2).[15,32,33]

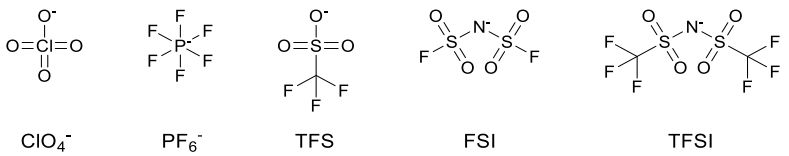

Fig. 2 Typical lithium salt anions for electrolytes in LIBs.[15,32,33]

Since the ion transport between the electrodes results in electron flow (Fig. 1), σ can be determined by measuring the electric current. However, if a direct current (DC) voltage is applied, the system changes chemically by out-of-equilibrium reactions, as in electrolysis. Therefore, a sinusoidal alternating current (AC) voltage V_{AC} with a small amplitude V_0 over time t is used:[34]

$$V_{AC}(t) = V_0 \sin(\omega t) \tag{3}$$

where ω is the angular frequency (regular frequency $f = \omega\,(2\pi)^{-1}$). The resulting current I_{AC} with the current amplitude I_0 is measured and its phase shift φ towards V_{AC} is determined (Fig. 3a):

$$I_{AC}(t) = I_0 \sin(\omega t - \varphi) \tag{4}$$

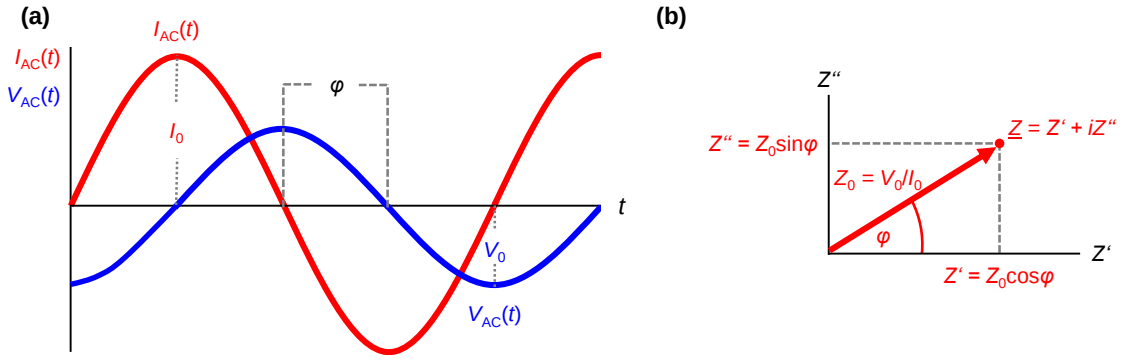

Fig. 3 (a) Plot of sinusoidal AC voltage V_{AC} with amplitude V_0 and its current response I_{AC} with amplitude I_0 as a function of time t. V_{AC} and I_{AC} are phase-shifted by φ. (b) Representation of the complex impedance $\underline{Z}$ for a given frequency f in the complex plane.[34]

The transformation of equations (3) and (4) into complex plane notation with $i = (-1)^{1/2}$ allows for a simpler consideration of the time-dependent variables:

$$\underline{V_{AC}}(t) = V_0 \exp(i\omega t) \tag{5}$$

$$\underline{I_{AC}}(t) = I_0 \exp(i\omega t - i\varphi) \tag{6}$$

The time-independent complex resistance of the system, the complex impedance $\underline{Z}$, is calculated in accordance with Ohm's Law:

$$\underline{Z} = \frac{\underline{V_{AC}}(t)}{\underline{I_{AC}}(t)} = \frac{V_0}{I_0}\frac{\exp(i\omega t)}{\exp(i\omega t - i\varphi)} = Z_0\exp(i\varphi) \quad (7)$$

where $Z_0 = V_0 / I_0$ is the impedance amplitude. Equation (7) can be split into real Z' and imaginary parts Z'' using Euler's formula $\exp(ix) = \cos x + i\sin x$:

$$\underline{Z} = Z_0\cos\varphi + iZ_0\sin\varphi = Z' + iZ'' \quad (8)$$

The representation of $\underline{Z}$ for a given regular frequency f ($f = \omega\,(2\pi)^{-1}$) in the complex plane is shown in Fig. 3b. As Z' and Z'' are frequency-dependent, an impedance spectrum is obtained when f is varied. The underlying method is called electrochemical impedance spectroscopy (EIS) or potentiostatic EIS (PEIS) if a voltage is applied and the resulting current is measured. The plot in the form of $-Z''$ against Z' is named Nyquist plot or Nyquist diagram. Different transport processes occur on different time scales. Therefore, they can be distinguished by changing the frequency f.[34]
The ionic conductivity σ of an electrolyte depends on its dimensions and is inversely proportional to its bulk resistance R_b:

$$\sigma \propto \frac{1}{R_b} \quad (9)$$

EIS of symmetric cells with blocking electrodes such as stainless steel, platinum or gold can be used to determine R_b. Blocking electrodes are assumed not to be penetrated by lithium ions from the electrolyte compared to non-blocking electrodes. There are no electrochemical reactions as in complete LIBs with active anode and cathode materials that simplifies interpretation.[35] Nevertheless, lithium ions and lithium salt anions (A^-) from the electrolyte can be adsorbed at the charged electrode surfaces and built up an ion monolayer as electrical double layer (Fig. 4a).

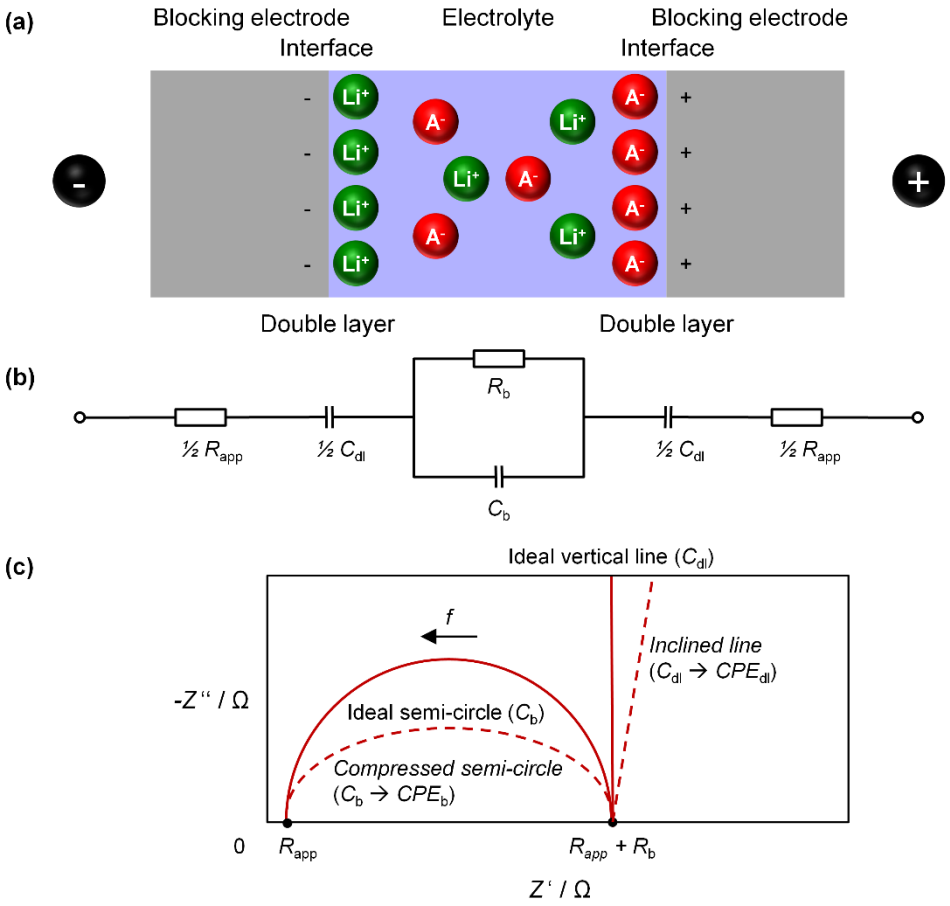

Fig. 4 (a) Schematic illustration of the electrical double layer at blocking electrodes (*e.g.* stainless steel, platinum or gold) which cannot be penetrated by the mobile lithium ions (A^-: lithium salt anion, solvation of electrolyte is not shown). (b) Equivalent electrical circuit (EEC). (c) Impedance spectrum of the EEC shown in Nyquist plot for ideal (solid line) and non-ideal (dashed line) behavior.[35]

EIS anaylsis uses equivalent electrical circuits (EEC) to approximate the real complex system in a simple approach. For a symmetric cell with blocking electrodes, the double layer may be represented by a capacitor with the capacitance C_{dl} under ideal conditions (Fig. 4b).[35] Next to the electrolyte bulk resistance R_b, the geometrical capacitance of the electrolyte/blocking electrode structure C_b is considered. The resistance of the apparatus, such as current collectors and metal wires, is assigned to the resistance R_{app} which is normally very small and might be neglected. In the Nyquist plot, this EEC results in an intact semi-circle in the high frequency region with intercepts on the Z' axis of R_{app} and $R_{app} + R_b$ (solid line in Fig. 4c). C_{dl} causes a subsequent vertical line. Under non-ideal conditions, a compressed semi-circle and an inclined line are often observed in practice (dashed line in Fig. 4c). To describe such a system, the capacitors C_b and C_{dl} are replaced by the constant phase elements CPE_b and

CPE_{dl}. They consider dipolar relaxations in the bulk of the electrolyte and inhomogeneous electrode surfaces, for instance.[35,36]

Non-blocking electrodes such as lithium metal electrodes can be penetrated by lithium ions from the electrolyte. Through reduction and oxidation, lithium can be deposited on and stripped from the electrode (Fig. 5a).[37] Therefore, the charge transfer resistance R_c of these processes at the electrolyte/electrode interface must be considered in the ECC for interpretation. The electrode material can react with the electrolyte forming a solid film on the electrode. The resistance of this passivation film R_f also contributes to the overall interface resistance R_i (Fig. 5b).[38,39] The mass transfer of lithium is limited by diffusion which increases the impedance. In case of high frequencies, the lithium ions do not have to move far. Therefore, the additional impedance of the diffusion process Z_d is negligible. However, at higher frequencies the ions have to move longer distances and Z_d increases. The frequency-dependent impedance might be approximated by a Warburg element W in the ECC.[38,40] The Warburg element results in a spur with 45° incline in the Nyquist plot at low frequencies. When it becomes zero at higher frequencies, the curve (solid line in Fig. 5c) ends up with an intercept on the Z' axis of $R_{app} + R_b + R_i$. With further increasing frequeny, the resistance of the capacitor C_{dl} connected in parallel with R_i tends towards zero. The semi-circle shows a second intercept at $R_{app} + R_b$. Under non-ideal conditions, the described curve characterisitics deviate accordingly as described above.[39]

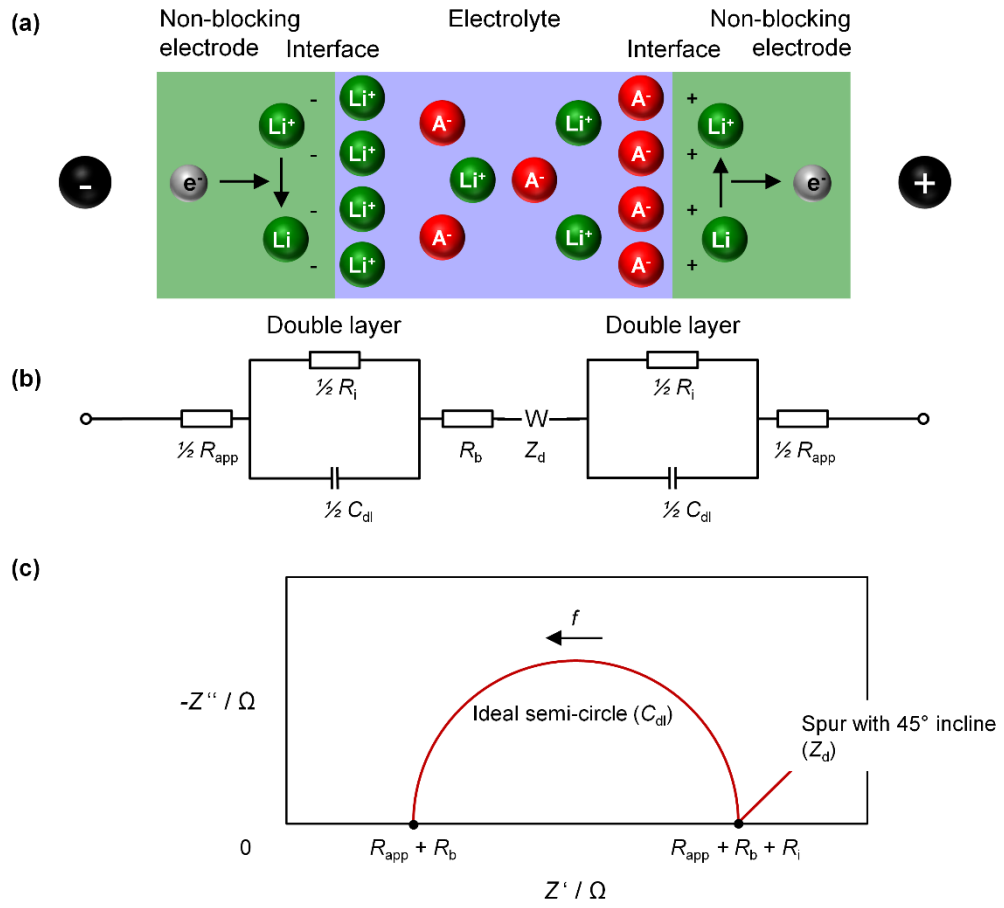

Fig. 5 (a) Schematic illustration of the electrical double layer and reduction-oxidation of lithium at non-blocking electrodes (*e.g.* lithium metal) which can be penetrated by the mobile lithium ions (A^-: lithium salt anion, solvation of electrolyte is not shown). (b) EEC. (c) Impedance spectrum of the EEC shown for ideal behavior in Nyquist plot.[38,40]

The ionic conductivity of an electrolyte determined by EIS considers the charge transport contributions from all charged mobile ions.[41] An incomplete lithium salt dissociation may lead to the formation of associated ion species.[42] Next to the lithium ions and the lithium salt anions, also ion-pairs, triplets and even larger ion clusters can support the charge transport. Even uncharged species can contribute to the total electrical current. They are moved along by the other mobile charged species.[43] If no external voltage is applied, the system is in equilibrium state with no concentration gradient of the ion species (Fig. 6a).[41,44] When an external voltage is applied, all ion types initially contribute to the charge transport resulting in a non-steady state. A concentration gradient of positively and negatively charged ions builds up in the electrolyte if the electrodes are blocking towards the anions (Fig. 6b). Under these conditions, the anions cannot discharge and remain immobile. The measured current decreases until it stays constant, since now only the cations contribute to the charge transport (steady state, Fig. 6c).

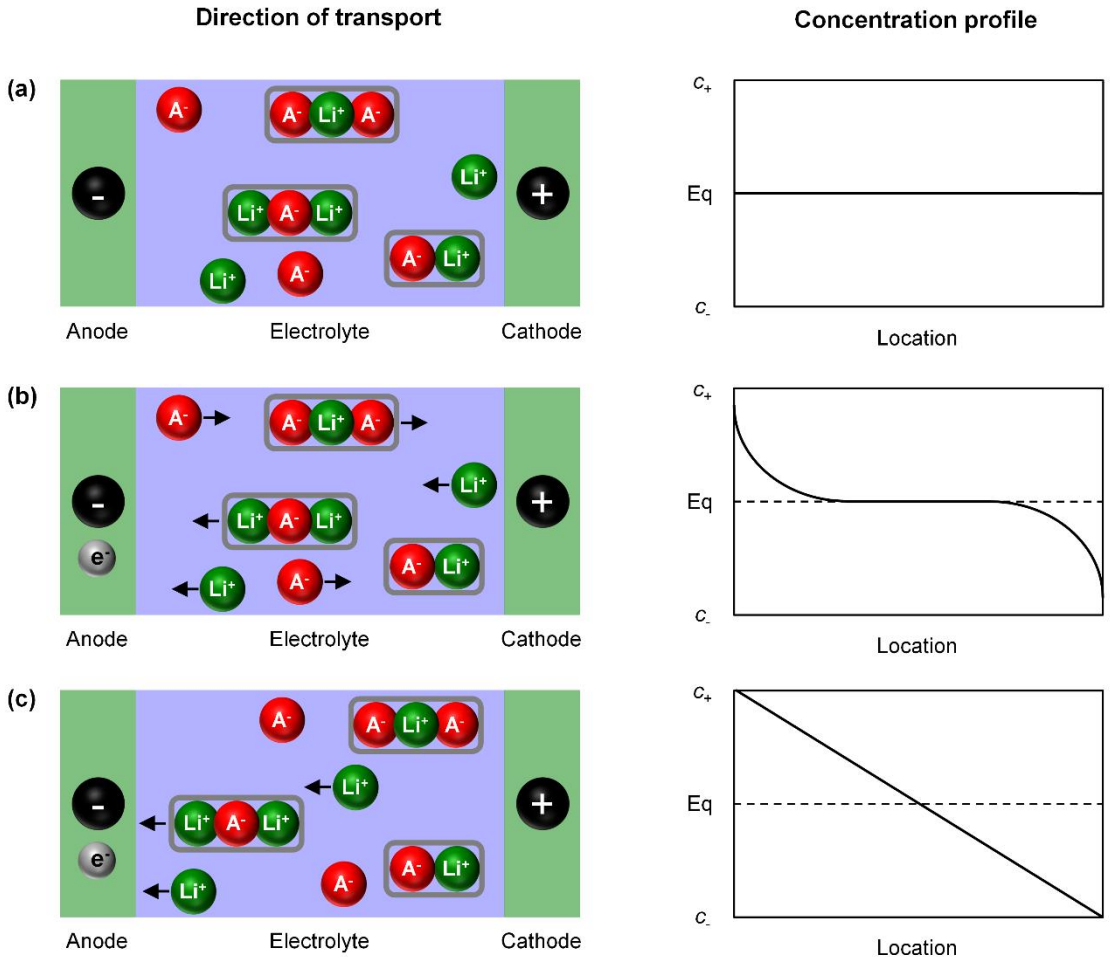

Fig. 6 Schematic representation of the transport of different ion species (here: lithium ions, lithium salt anions, ion-pairs and triplets). The corresponding concentration profile of the cation and anion concentrations, c_+ and c_-, at (a) equilibrium (Eq), (b) non-steady and (c) steady state is also shown. The electrodes are blocking towards the anion species.[41,44]

The relative amount of current transported by the cations can be expressed by the transport number tn^+ as follows:[15]

$$tn^+ = \frac{I_+}{I_t} = \frac{I_+}{I_+ + I_-} = \frac{\mu_+}{\mu_+ + \mu_-} \tag{10}$$

where I_+ and I_- are the currents transported by the cations and anions, respectively, and I_t is the total current. The ion mobilities of the cations and anions, μ_+ and μ_-, are linked with σ by equation (1).

To evaluate the performance of electrolytes in batteries, it is meaningful to consider all moving species, which can be quantified by the transference number t^+.[43] It can be determined by the Bruce-Vincent

method (t^+_{BV}).[44,45] For this purpose, the electrolyte is sandwiched between two non-blocking lithium electrodes. At first, PEIS is used to determine R_i according to the procedure described in Fig. 5. A subsequent chronoamperometric (CA) measurement is performed under applying a DC voltage ΔV until the current stays constant. The initial current I_0 and steady state current I_s of the CA measurement are taken from the *I*-*t*-curve. Finally, R_i is measured again by PEIS to account for the resistance of a possible passivation film on the electrode formed during the CA measurement. t^+_{BV} is calculated according to equation (11):

$$t^+_{BV} = \frac{I_s(\Delta V - I_0 R_{i0})}{I_0(\Delta V - I_s R_{is})} \tag{11}$$

where the subscripts 0 and s define the values before and after the DC polarization.
Another approach to determine t^+ is described by Watanabe *et al.* (t^+_W).[46-48] Here, only the resistances of the PEIS before the polarization are used:

$$t^+_W = \frac{R_{b0}}{\Delta V / I_s - R_{i0}} \tag{12}$$

The concentration gradient as described in Fig. 6 leads to a polarization of the electrolyte which counteracts the movement of the cations during charging and discharging of a battery. In addition, irreversible side-reactions of the anions with the electrode material at the electrode interface can occur. Negative consequences are higher charge times, a lower power performance and a capacity loss after several charging/discharging cycles of the battery.[45,46,49] Therefore, single-ion conducting electrolytes with high t^+ values near one ($\mu_- = 0$) are in demand. Some approaches will be presented in chapter 1.8.

1.4 Challenges for electrolytes in lithium-ion batteries

Common liquid/separator or polymer gel electrolytes use organic carbonate solvents. Typical are mixtures of dimethyl (DMC), ethyl methyl (EMC), diethyl (DEC), propylene (PC) and ethylene (EC) carbonate (Fig. 7).[50–52] High ionic conductivities in the order of 10^{-2} S cm^{-1} were obtained even at 20 °C, which is sufficient for commercialization where at least 10^{-3} S cm^{-1} at 20 °C are required.[53,54]

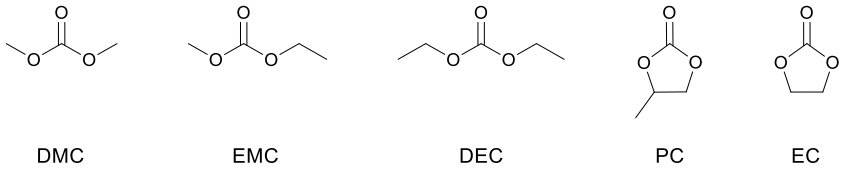

Fig. 7 Typical organic carbonates for liquid and gel electrolytes.[50–54]

However, especially DMC, EMC and DEC are volatile and flammable.[10,52,55] The battery suffers from a serious lack of safety in case of thermal runaways since it may become inflamed.[9,56] In addition, the organic carbonates are instable against high potentials above 4.5 V vs. Li/Li^+ making them unsuitable for high voltage batteries.[2]

PC and EC are less volatile and flammable than DMC, EMC and DEC. They also enable good lithium salt dissociation due to their high dielectric constants (PC: $\varepsilon_r = 64.4$ at 30 °C[50]; EC: $\varepsilon_r = 89.6$ at 40 °C[51]). However, the usage of liquid electrolytes can entail a leakage of the battery. A rigid and heavy metal case reducing the specific energy of the whole battery is necessary.[57]

The mechanical stability of the electrolyte is also essential to reduce lithium dendrite growth during battery cycling.[58–60] Especially when pure lithium metal anodes are used to achieve high specific energies. In contrast to graphite anodes in which the lithium atoms have defined intercalation positions, the dissolution and deposition of lithium proceeds irregularly in the case of metallic lithium anodes (Fig. 8a).[60,61]

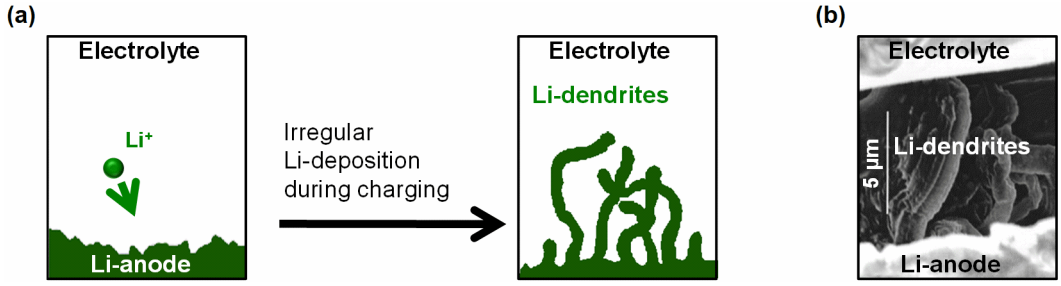

Fig. 8 (a) Schematic illustration of lithium dendrite growth on a lithium metal anode by irregular deposition of lithium during charging. Adapted with permission from reference[62]. Copyright 2004 American Chemical Society. (b) Scanning electron microscopy image of lithium dendrites after charging a battery using a PEG/lithium bis(trifluoromethanesulfonyl)imide electrolyte at a current density of 0.5 mA cm^{-2} for 1 h (V_2O_5 cathode). Used with permission of The Electrochemical Society/IOP Publishing, Ltd, from reference[61], Copyright 2002; permission conveyed through Copyright Clearance Center, Inc.

Lithium dendrite growth can lead to a capacity loss during cycling when lithium metal particles of the dendrites spread out in the electrolyte. At a sufficient length the lithium dendrites reach the counter

electrode and an internal circuit occurs. This reduces the cycle life and can lead to a thermal runaway of the battery.[60,61]

1.5 Linear poly(ethylene glycol) electrolytes

Solid polymer electrolytes (SPE) can reduce the lithium dendrite growth by providing sufficient mechanical stability. They are also non-volatile and less flammable than liquid and gel electrolytes, which are based on low molecular weight organic carbonates.[9,10,58,63–67] The most common lithium ion conducting polymer in SPEs is PEG.[16] The coordination of the lithium salt by PEG occurs via Lewis acid-base interactions between the lithium ions and the lone electron pairs of the ether oxygen atoms (Fig. 9).[68]

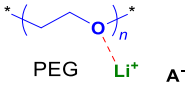

Fig. 9 Coordination of lithium ions by PEG via Lewis acid-base interactions (A^-: lithium salt anion).

The coordination sites can be considered as local energy minima between which the ions move by 'hopping'-processes.[69,70] The ionic conductivity increases with increasing temperature, since the energy barriers between these sites can be overcome easier. In addition, the ionic conductivity in PEG electrolytes is closely linked to the polymer chain mobility.[69–72] The ion conduction takes place predominantly in the amorphous phase of the PEG electrolyte above the glass transition temperature T_g. Here, the segmental motion of the polymer chains starts and provides a continous rearrangement around the ions. In contrast, the ion conduction in the amorphous phase below the T_g and in the crystalline phase is usually very low.[69–76] Above the melting temperature of the crystalline phase T_m of linear PEG, the self-diffusion of the polymer with the coordinated ions occurs.[69,70] This movement decreases with M^{-1} for short polymers and even with M^{-2} when the polymer chains are long enough to form entanglements.[77-79]

Although PEG electrolytes provide higher mechanical stability than liquid electrolytes, their mechanical stability is drastically reduced if their degree of crystallization is low and the ambient temperature is above their T_g. Then, even PEG electrolytes show lithium dendrite growth (Fig. 8b).[61] Linear PEG blended with the common lithium salt lithium bis(trifluoromethanesulfonyl)imide (LiTFSI) suffers from a lack of mechanical strength at high salt concentrations due to the plasticizing effect of the TFSI anion.[32,76,80] However, a high salt concentration is essential to provide sufficient charge carriers and achieve a maximum ionic conductivity.

A soft PEG phase with an elastic modulus below 1 MPa is required for ion conduction.[66] The simultaneous presence of a soft and hard phase in SPEs can be achieved by block copolymers. If the different blocks show a sufficient incompatibility towards each other (quantified by the interaction parameter or Flory-Huggins-parameter χ) and chain length (expressed by the degree of polymerization N), they can undergo microphase separation. Possible AB diblock copolymer morphologies depending on the volume fraction of the block A f_A are shown in Fig. 10.[81]

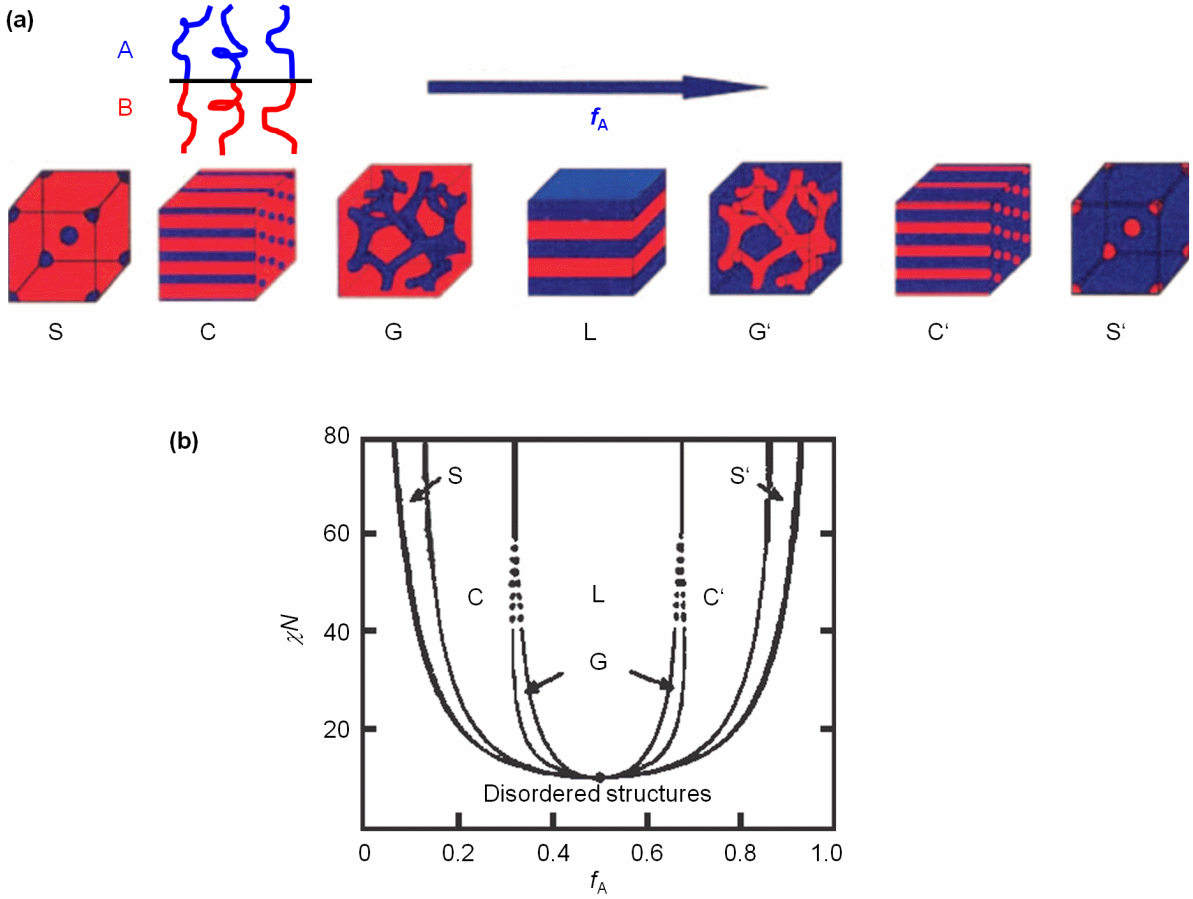

Fig. 10 (a) Example morphologies of microphase separating AB diblock copolymers depending on the volume fraction of the block A f_A: Spheres arranged in a body centred cubic (S), hexagonally packed cylinders (C), the double gyroid (G) and lamellae (L). (b) Phase diagram (χ: interaction parameter between blocks A and B; N: degree of polymerization). Used with permission of Springer, from reference[81], Copyright 2005; permission conveyed through Copyright Clearance Center, Inc.

The most studied AB diblock copolymer combined with LiTFSI for SPEs is poly(styrene)-*block*-PEG (PS-*b*-PEG, Fig. 11a).[82–84] The diblock copolymer undergoes microphase separation into a mechanically reinforcing PS phase and ion conducting PEG phase. Lamellar and hexagonally perforated lamellar morphologies were identified by small-angle X-ray scattering (SAXS) and transmission electron microscopy (TEM).

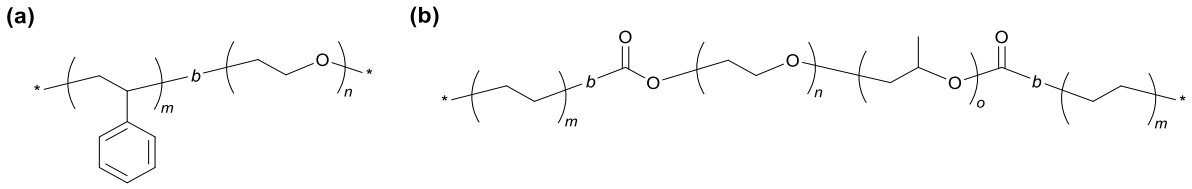

Fig. 11 Chemical structures of linear PEG containing polymers for SPEs: (a) PS-*b*-PEG[82,83] and (b) PE-*b*-(PEG-*co*-PG)-*b*-PE.[85]

In addition to PS, semi-crystalline poly(ethylene) (PE) phases with a melting temperature T_m above the SPE operating temperature were also used to enhance the mechanical stability of SPEs. Jannasch synthesized ABA triblock copolymers with a PEG-poly(propylene glycol) (PPG) copolymer as midblock (PE-*b*-(PEG-*co*-PG)-*b*-PE, Fig. 11b).[85] The ion conducting phase of PEG and PPG mixed with LiTFSI showed a T_m below 0 °C. The solid PE phase served for physical cross-linking below its T_m (about 100 °C).

1.6 Graft copolymer poly(ethylene glycol) electrolytes

Linear PEG blended with the common lithium salt LiTFSI suffers from a low ionic conductivity below T_m when crystalline domains are prevailing and the polymer chain mobility is low.[80] Many attempts have been made to reduce the crystallinity and the T_g of PEG electrolytes. Graft copolymer electrolytes with PEG side-chains can fulfill these requirements. They show a higher amount of end-groups and chain mobility compared to linear PEG electrolytes at an equivalent molecular weight.[86–92]

Ikeda *et al.* showed that an increase of tri(oxymethylene) (ETT-3) side chains along a PEG backbone can decrease the crystallinity of an SPE with $LiClO_4$ as lithium salt (PEG-*co*-ETT-3, Fig. 12).[87] At the same time, the ionic conductivity at 30 °C increased.

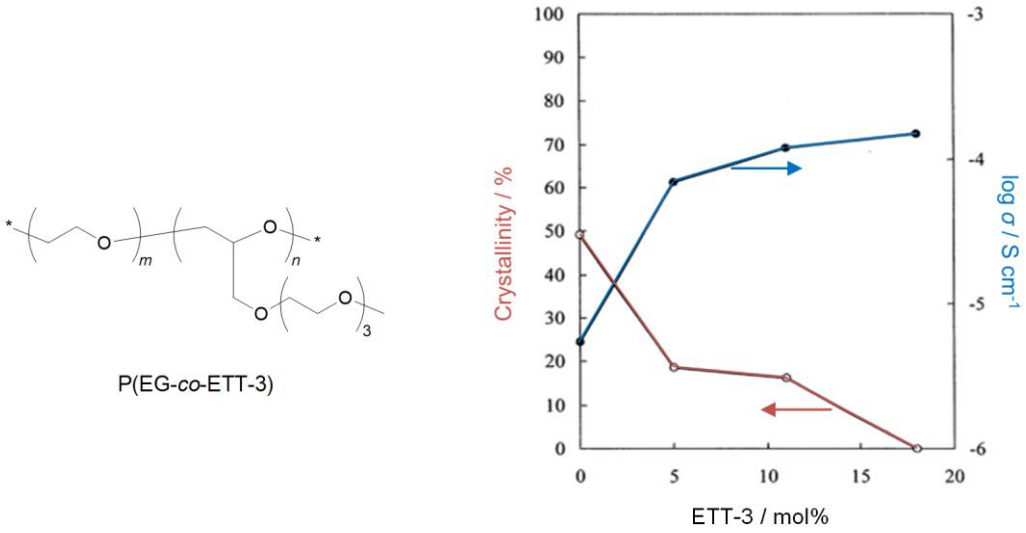

Fig. 12 Dependence of the crystallinity and the ionic conductivity σ on the amount of ETT-3 in the copolymer PEG-*co*-ETT-3 at 30 °C. The different copolymers show comparable molecular weights (around 10^5 g mol^{-1}) and are mixed wih $LiClO_4$ as lithium salt. Reprinted from reference[87], Copyright 2000, with permission from Elsevier.

Barteau *et al.* grafted thiol-functionalized monomethoxy dimers or trimers of ethylene glycol (EGS) onto poly(allyl glycidyl ether) (PAGE) via the thiol-ene reaction (PAGE-*g*-EGS, Fig. 13a).[80] The concept was triggered by the promising properties of PAGE: its low glass transition temperature around -80 °C and high oxygen content for lithium ion conduction. By preventing crystallization below 60 °C, they achieved an ionic conductivity two orders of magnitude higher than for PEG at equivalent LiTFSI concentrations. The maximum ionic conductivity was around 7 x 10^{-5} S cm^{-1} at 40 °C.

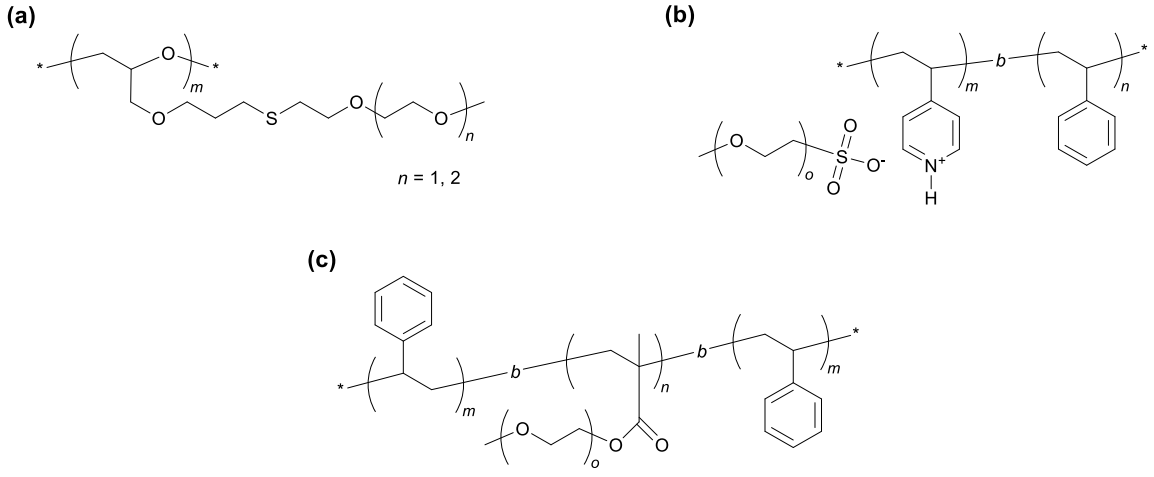

Fig. 13 Chemical structures of PEG-related graft copolymers for SPEs: (a PAGE-*g*-EGS,[80] (b) (P4VP-*g*-EGSA)-*b*-PS[93] and (c) PS-*b*-(PMA-*g*-EG)-*b*-PS.[91]

Kosonen *et al.* synthesized the semi-grafted diblock copolymer, poly(4-vinylpyridine)-*grafted*-oligo(ethylene glycol)sulfonic acid-*block*-poly(styrene) ((P4VP-*g*-EGSA)-*b*-PS, Fig. 13b).[93] In mixture with $LiClO_4$ it showed microphase separation with an ion-conducting P4VP-*g*-EGSA phase mechanically reinforced by a second PS phase. Analysis by small- and wide-angle X-ray scattering suggested an amorphous lamellar morphology. The maximum ionic conductivity at 40 °C was about 8×10^{-6} S cm^{-1}.

A further approach is the usage of triblock copolymers. Niitani *et al.* embedded an ion-conducting poly(methacrylate) (PMA) block grafted with PEG between two mechanically reinforcing PS blocks (PS-*b*-(PMA-*g*-EG)-*b*-PS, Fig. 13c).[91] The microphase separation was demonstrated by transmission electron microscopy (TEM). While the elastic modulus was higher than 3 MPa, the ionic conductivity using $LiClO_4$ as a salt still remained around 3×10^{-4} S cm^{-1} at 40 °C.

1.7 Click chemistry and triazoles as functional groups in electrolytes

The incorporation of disubstituted benzene or 1,4-disubstituted 1,2,3-triazole (TR) groups into linear PEG can also reduce the crystallinity and the T_g.[94–96] The break in the linear chain prevents the chains from arranging themselves evenly and increases the chain flexibility along the chain. In addition, the substituted benzene groups enhance the mechanical stability of polymer electrolytes. The TR groups have the advantage that they can coordinate lithium ions by their lone electron pairs. The high dielectric constant of the TR group facilitates lithium salt dissociation while the TR group is chemically inert against oxidation and reduction.[94–98] These features make it a versatile linking group with ion conductive properties.

The TR group results from the copper(I)-catalyzed alkyne-azide cycloaddition (CuAAC). That so-called click reaction forms new covalent connections between alkynes and azides based building blocks. It is quantitative, chemically inert to many reaction conditions and allows high yields.[97] By using Cu(I) as a catalyst it is possible to obtain regioselectively 1,4-disubstituted 1,2,3-triazoles.[99–101] Without catalyst, also the 1,5-triazole regioisomer would be formed. First, the alkyne binds to the catalyst as an acetylide while a coordination site of the ligand (L) and HA are released (Scheme 1, step **A**).

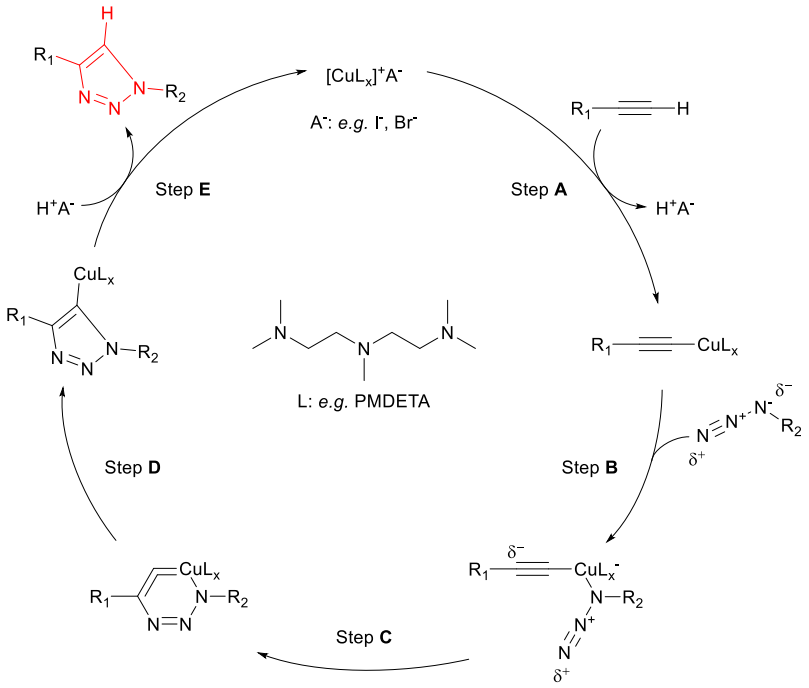

Scheme 1 Possible mechanism of the CuAAC to form a TR group (red marked).[99,100]

For example, *N*,*N*,*N*′,*N*″,*N*″-pentamethyldiethylenetriamine (PMDETA) can serve as the ligand and bromide or iodide as the anion (A^-).[102,103] In the next step, the azide replaces another ligand site by binding to the catalyst with its nucleophilic proximal nitrogen (step **B**). A new C-N bond is formed in a 5-triazolyl copper intermediate by an intramolecular nucleophilic attack of the Cu(I) acetylide segment to the electrophilic terminal nitrogen of the organic azide (step **C**). In the penultimate step, a copper-triazole derivative is formed by ring contraction (step **D**). Finally, the catalyst is recovered by splitting off the TR (step **E**).

1.8 Single-ion conducting solid polymer electrolytes

As described in chapter 1.3, the movement of locally not fixed lithium salt anions in polymer electrolytes leads to a polarization during charging and discharging of a battery and irreversible side-

reactions of the anions with the electrode material. Therefore, single-ion conducting solid polymer electrolytes are of great interest.

Kobayashi *et al.* achieved a single-ion conduction by incorporating the anion into the polymer backbone. They synthesized a graft copolymer of the monomers oligo(ethylene glycol) methyl ether methacrylate (EGMA) and lithium methacrylate (PEGMA-*co*-LiMA), Fig. 14a).[88] A self-standing, flexible and transparent polymer film was obtained. However, the nonconducting polymer backbone and poor dissociation between the lithium ions and the carboxylate groups limited the ionic conductivity to about 6×10^{-7} S cm^{-1} at 40 °C.

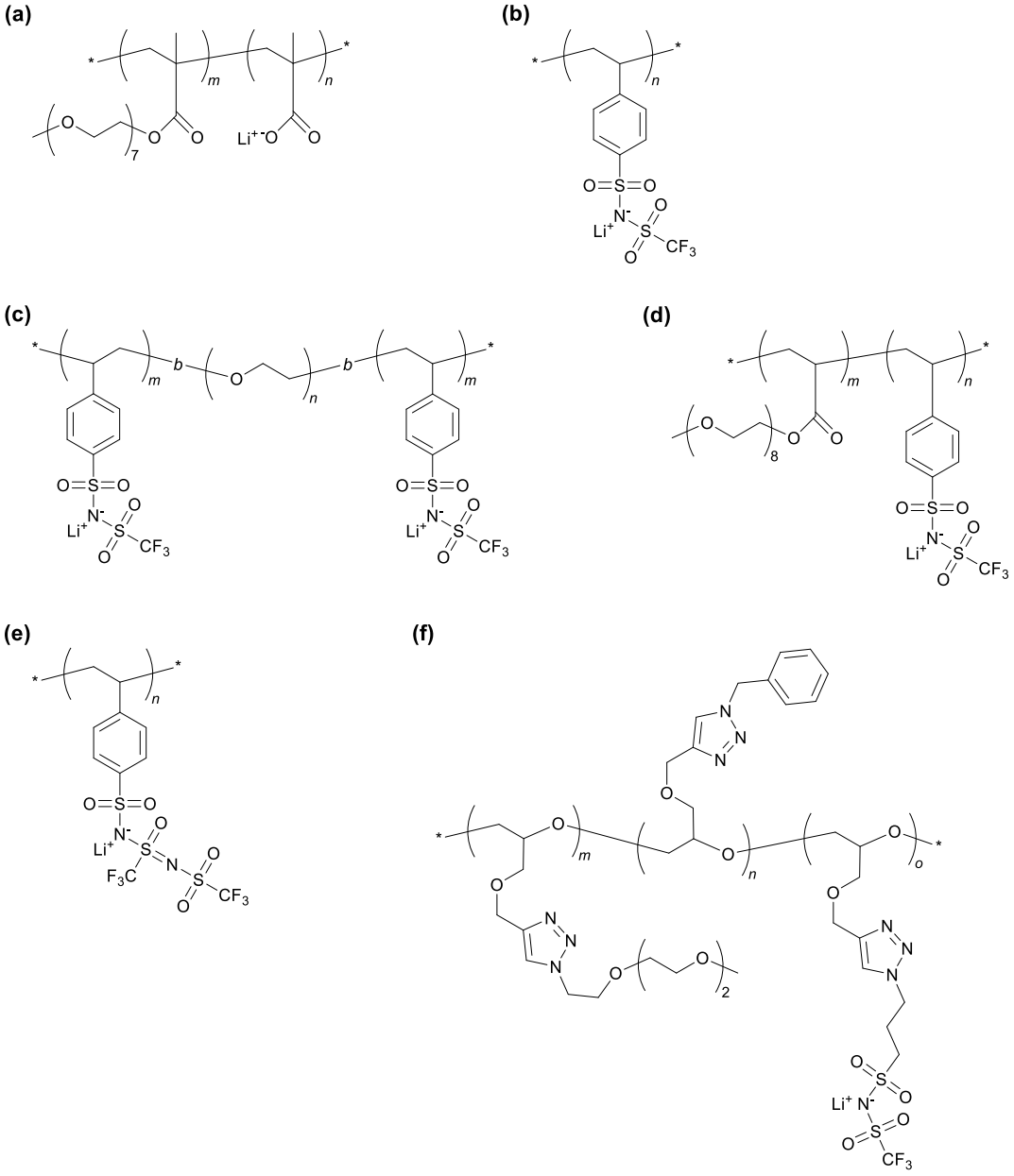

Fig. 14 Chemical structures of single-ion conducting polymers for SPEs: (a) P(EGMA-*co*-LiMA),[88] (b) PLiSTFSI,[104] (c) PLiSTFSI-*b*-PEG-*b*-PLiSTFSI,[63] (d) P(EGA-*co*-LiSTFSI),[86] (e) PLiSsTFSI,[105] and (f) PGPE-*g*-(EG3-*co*-Bn-*co*-LiAPTFSI).[89]

To facilitate the dissociation of the lithium salt, Meziane *et al.* increased the delocalization of the negative charge. Based on the structure of LiTFSI, they synthesized poly(lithium 4-styrenesulfonyl(trifluoromethylsulfonyl)imide) (PLiSTFSI, Fig. 14b).[104] The homopolymer PLiSTFSI was blended with linear PEG and achieved ionic conductivities of about 8 x 10^{-7} S cm^{-1} at 40 °C. Bouchet *et al.* embedded linear PEG into two side-blocks of PLiSTFSI (PLiSTFSI-*b*-PEG-*b*-PLiSTFSI, Fig. 14c).[63] They obtained a maximum ionic conductivity of about 10^{-6} S cm^{-1} at 45 °C and lithium ion transference numbers higher than 0.85 at 90 °C.

Feng *et al.* copolymerized methoxypolyethylene glycol acrylate (EGA) with LiSTFSI to obtain graft copolymer PEG (P(EGA-*co*-LiSTFSI), Fig. 14d).[86] The graft copolymer electrolyte showed a maximum ionic conductivity of about 2 x 10^{-5} S cm^{-1} at 40 °C. The higher ionic conductivity of the graft copolymer PEG electrolyte compared to the linear PEG electrolyte was attributed to its lower glass transition temperature (around -47 °C) and higher amorphous character. The lithium ion transference number was higher than 0.9 at 60 °C.

An even stronger negative charge delocalization was achieved by replacing a sulfonyl group in the STFSI structure with a strongly electron-withdrawing trifluoromethylsulfonylimino group.[105] The resulting poly(lithium (4-styrenesulfonyl)(trifluoromethyl(*S*-trifluoromethylsulfonylimino)sulfonyl)-imide) (PLiSsTFSI, Fig. 14e) blended with linear PEG showed a maximum ionic conductivity of about 2 x 10^{-7} S cm^{-1} at 40 °C and lithium ion transference number higher than 0.90 at 60 °C.

Li *et al.* replaced the 4-vinylphenyl group in LiSTFSI with a 3-azidopropyl group to allow incorporation of the TFSI-based anion into the polymer via CuAAC.[90] The resulting lithium 3-azidoproanesulfonyltrifluoro-methanesulfonylimide (LiAPTFSI) was clicked on poly(glycidyl propargyl ether) (PGPE) by Krimalowski and Thelakkat in our group.[89] This concept enables ion conduction in the polymer backbone. By the sequential grafting of azide-functionalized ethylene glycol (EG3), mechanically reinforcing benzyl groups (Bn) and LiAPTFSI for single-ion conduction onto PGPE, the desired properties could be adjusted in one single copolymer (PGPE-*g*-(EG3-*co*-Bn-*co*-LiAPTFSI), Fig. 14f). The maximum ionic conductivity was about 10^{-7} S cm^{-1} at 40 °C with a lithium ion transference number higher than 0.9. In all the presented concepts, the ionic and, if present, the styrene moieties also support mechanical stability.

1.9 Poly(ester) solid polymer electrolytes

The lithium ions in PEG electrolytes are subject to strong dipol attractions of the ether oxygen atoms. The resulting complex formation hinders the chain mobility and thus the ion movement. This situation is different for poly(ester)s such as poly(carbonate)s (PC) and poly(*ε*-caprolactone) (PCL).

PCs seem to be strong enough to ensure lithium salt dissociation due to their higher dielectric constant compared to PEG with nevertheless not so strong coordination.[29] In PEG electrolytes, the glass transition temperature increases with increasing salt concentration due to the decreasing mobility of the chains. In PC electrolytes, the mobility of the lithium ions seem to be decoupled from the chain mobility. Tominage and Yamazaki showed that an increase of the LiFSI concentration in poly(ethylene carbonate) (PEC, Fig. 15a), that is an increasing number of charge carriers, led to a steady increase of

the ionic conductivity. Therefore, high ionic conductivities generally require high salt concentrations. So PC SPEs can be classified as polymer-in-salt systems. The maximum lithium ion conductivity was almost an order of magnitude higher than that of a comparable PEG electrolyte (in the order of 10^{-4} S cm^{-1} at 60 °C).[106,107]

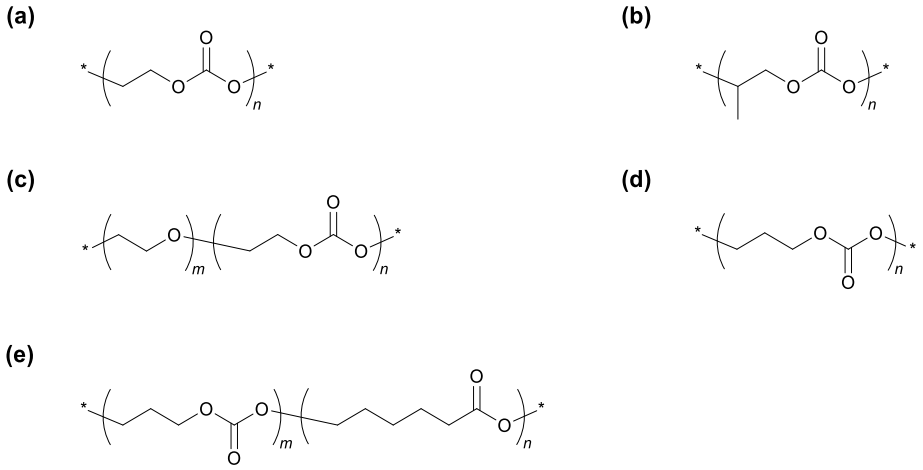

Fig. 15 Chemical structures of PCs for SPEs: (a) PEC,[106,107] (b) PPC,[108] (c) PEO-*co*-EC,[109,110] (d) PTMC[111–113] and (e) PTMC-*co*-CL.[114,115]

PEC SPEs show high lithium ion transference numbers (> 0.8) and good electrochemical stability (> 5.0 V vs. Li/Li^+ at 30 °C), especially in combination with titanium dioxide (around 1 wt%).[106,107] PEC and poly(propylene carbonate) (PPC, Fig. 15b) are both amorphous, but the glass transition temperature of PPC is generally slightly higher than that of PEC. This leads to a higher mechanical strength of PPC. By adding cellulose nonwoven, the mechanical strength of PPC SPEs could be even increased from about 4 MPa to 25 MPa.[108]

The ring-opening polymerization of ethylene carbonate can lead to a partial decarboxylation yielding the copolymer poly(ethylene oxide-*co*-ethylene carbonate) (PEO-*co*-EC), Fig. 15c). It has been investigated in SPEs. Compared to pure PEO, it was characterized by a higher dielectric constant and was amorphous resulting in a higher ionic conductivity.[109,110] To prevent the partial decarboxylation, more stable six-membered cyclic carbonates such as trimethylene carbonate (TMC) were polymerized successfully and used for SPEs in LIBs (PTMC, Fig. 15d).[111–113] Sun *et al.* achieved an electrochemical stability of up to 5.0 V vs. Li/Li^+ and good cycling behavior in $LiFePO_4$ half-cells using LiTFSI as lithium salt.[113]

Fonseca *et al.* tested PCL as a matrix polymer for SPEs due to its biodegradable nature. Complete biodegradation was observed after 110 days. The ionic conductivity was 1.2×10^{-6} S cm^{-1} at room temperature using the lithium salt $LiClO_4$.[116] The high electrochemical stability of 5 V vs. Li/Li^+ was

promising to build $LiNiCoO_2$/Li batteries. They showed a specific charge/discharge capacity loss from 182 mAh g^{-1} to 120 mAh g^{-1} after 50 cycles.[117]

PCLs possess a higher polymer chain flexibility and thus a lower glass transition temperature (around -60 °C) in comparison to PCs. Therefore, Mindemark *et al.* inserted CL repeating units into PTMC. The copolymer (PTMC-*co*-CL, TMC/CL ratio of 60/4, Fig. 15e) with LiTFSI showed a glass transition temperature of -26 °C and an ionic conductivity of 7.9 x 10^{-7} S cm^{-1} at 25 °C.[114] Li/$LiFePO_4$ cells showed coulombic efficiencies near 100% at room temperature even at high charge/discharge rates. This stable performance might result from the relatively high lithium ion transference numbers (> 0.6).[115]

1.10 Perfluoropolyether electrolytes

Conventional liquid alkyl carbonate electrolytes are flammable and instable against high potentials making them unsuitable for the safe use of high voltage batteries (compare chapter 1.4). These safety issues might be solved by the use of liquid perfluoropolyethers (PFPE) since they are intrinsically nonflammable and electrochemically stable against high potentials.[10]

Linear PFPEs are liquid even below -80 °C. The high flexibility of the PFPE chains prevents crystallization even at low temperatures, as the chains cannot align with each other.[118] In addition, due to the high conformal freedom, the glass transition temperature T_g of PFPEs is often well below -70 °C. In the case of PFPE oligomers and low molecular weight polymers the T_g is dependent on the chain length. It decreases with increasing molecular weight. For high molecular weight polymers and by the incorporation of branches, the T_g tends to increase.[119]

PFPEs show nearly single-ion conductor behavior quantified by a high lithium ion transference number > 0.8.[10,120] However, PFPEs in combination with perfluoroalkyl (PFA) lithium salts such as LiTFSI show poor ionic conductivity due to the limited solubility of LiTFSI[121] and the formation of ion clusters.[122] PFPEs show a higher conformal flexibility compared to PFAs as they require less energy to rotate along the chain due to the oxygen atoms. Perfluorohexane and perfluoro-3-oxahexane as representatives for PFAs and PFPEs can serve for computer-assisted calculations of the rotational energy barriers.[123] While these are higher than 15 kJ mol^{-1} for perfluorohexane, they are below 11 kJ mol^{-1} for perfluoro-3-oxahexane with the exception of the syn conformation. The energy barrier to be overcome regarding the syn conformation (around a torsion angle of 0°) is higher, but it is almost only half as large for perfluoro-3-oxahexane as for perfluorohexane (Fig. 16).

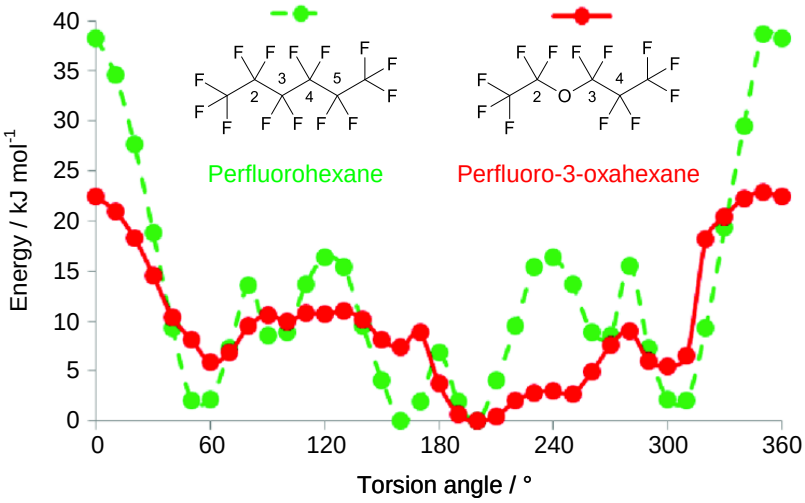

Fig. 16 Dependence of the energy on the perfluorohexane C2-C3-C4-C5 and on the perfluoro-3-oxahexane C2-O-C3-C4 torsion angle. Adapted with permission from reference[123]. Copyright 2012 American Chemical Society.

Density-functional theory calculations indicated that PFPEs can be more fluorophilic than their PFA analogues.[123] Due to the higher flexibility and energetically preferred curvature of the PFPE chain, the fluorine atoms can better shield other fluorophobic groups within the structure. These are no longer available for fluorophobic intermolecular interactions.[123] This might be the reason why the solubility of PFA lithium salts such as LiTFSI in PFPEs is low. As a consequence, the PFPEs were mixed with liquid organic carbonates[124] or PEG[121] (Fig. 17).

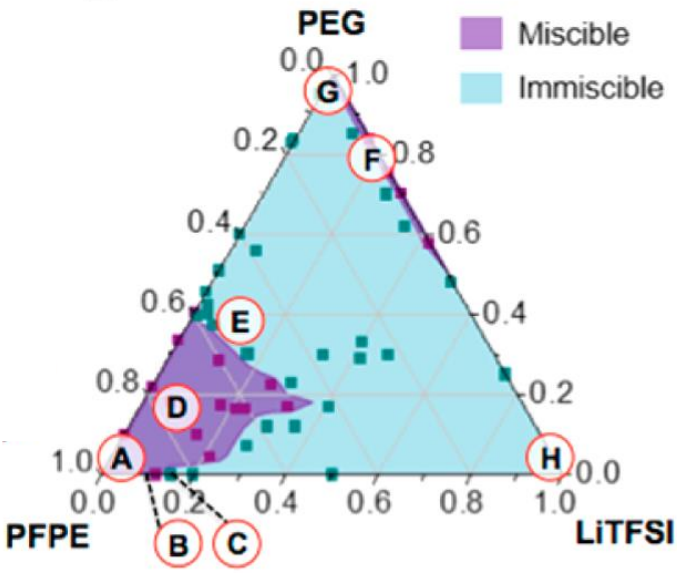

Fig. 17 Ternary phase diagram of PFPE (1000 g mol^{-1}, liquid at room temperature, two hydroxyl end-groups), PEG (400 g mol^{-1}, liquid at room temperature, two hydroxyl end-groups) and LiTFSI (solid at room temperature, scale in weight fractions) determined by FTIR spectroscopy. A: Pure PFPE, B: PFPE with 0.10 wt. fraction of LiTFSI (miscible), C: PFPE with 0.20 wt. fraction of LiTFSI (immiscible), D: PFPE with 0.18 wt. fraction of PEG and 0.10 wt. fraction of LiTFSI (miscible), E: PFPE with 0.35 wt. fraction of PEG and 0.12 wt. fraction of LiTFSI (immiscible), F: PEG with 0.20 wt. fraction of LiTFSI (miscible), G: pure PEG, H: pure LiTFSI. Reprinted with permission from reference[121]. Copyright 2015 American Chemical Society.

Another approach pursues the functionalization of the PFPEs with hydroxyl, PEG or methyl carbonate end-groups (Fig. 18).[121,125] However, the increased ionic conductivity was accompanied by a decrease in the lithium ion transference number.

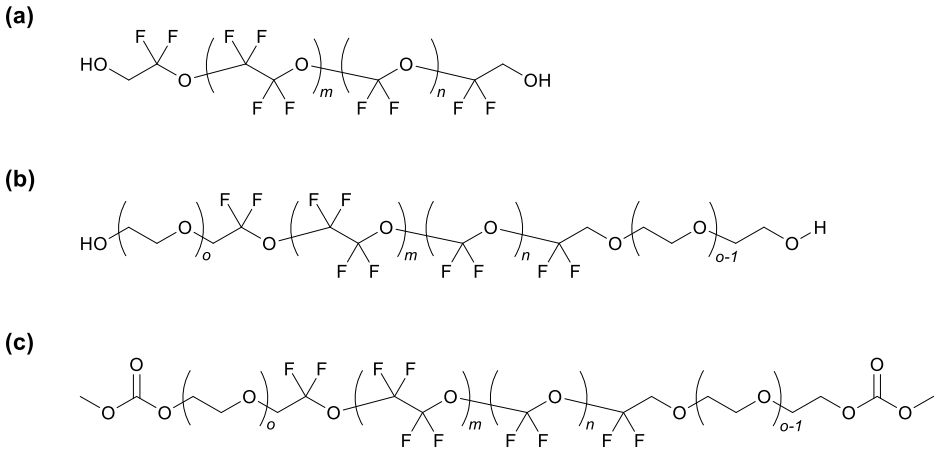

Fig. 18 Chemical structures of PFPEs for liquid electrolytes functionalized with (a) hydroxyl end-groups, (b) supplemented by PEG moieties and (c) methyl carbonate end-groups.[121,125]

Devaux *et al.* introduced the first PFPE SPEs crosslinked via urethane methacrylate end-groups or polyhedral oligomeric silsesquioxane in the presence of LiTFSI (Fig. 19a).[126,127] Despite the solid state character, their ionic conductivity was comparable with the liquid PFPEs at the solubility limit of LiTFSI.

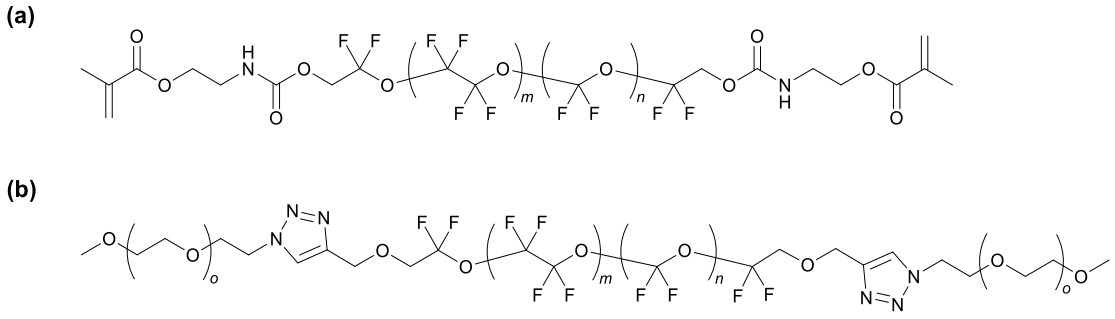

Fig. 19 Chemical structures of PFPEs for SPEs: (a) PFPE functionalized with urethane methacrylate end-groups for cross-linking and (b) PEG-*b*-PFPE-*b*-PEG triblock copolymer synthesized via CuAAC.[126–128]

Attractive forces between perfluorinated chains lead to the immiscibility in other non-fluorinated organic compounds especially at room temperature. So fluorinated compounds are often only soluble in each other. This is called the fluorous effect.[129] However, repulsive forces from the non-fluorinated organic compounds can also favor the segregation, which is called the fluorophobic effect. Then, the attractive forces between the non-fluorinated compounds are stronger than those to the fluorinated compounds.[129,130]

Due to the self-directed solubility of fluorinated compounds, phase separation often occurs in polymers with PFA or PFPE moieties. One of the basic requirements for microphase separation of block copolymers is a sufficiently high value of the product of N and χ (compare chapter 1.5). Chintapalli *et al.* studied the microphase separation in short chain PFPE-*block*-PEG copolymers. Despite a very low DP_n (~ 10), they detected high scattering intensities. This indicated a separation of PFPE- and PEO-rich domains caused by very high χ values (~ 2-2.5) and immiscibility between the segments.[131] PEG/PFPE triblock copolymers were synthesized by CuAAC and proposed as host polymers for electrolytes in LIBs by Lopez *et al.* (Fig. 19b).[128]

The block-selective incorporation of fluorine moieties into block copolymers can also be realized by polymer-analogous reactions. Ren *et al.* added difluoromethylene groups to the double bonds of poly(isoprene) (PI) in poly(styrene)-*block*-PI (PS-*b*-PI) copolymers.[132] In another approach they added perfluoroalkyl groups to the double bonds of 1,2-polybutadiene (1,2-PBD) in PS-*b*-1,2-PBD copolymers.[133] In both cases phase separation was enhanced by an increase of the χ value between the blocks when a high degree of fluorination was achieved.

1.11 Fluorophilicity of lithium salts

Highly-fluorous PFA host polymers such as poly(vinylidene fluoride-*co*-hexafluoropropylene) (PVDF-*co*-HFP, Fig. 20) for SPEs require the synthesis of novel lithium salt anions. The miscibility of the lithium salt anion with PVDF-*co*-HFP may be improved by increasing its fluorophilicity by inserting a higher amount of PFA moieties. PFA pyrazolide anions without a modification (PFAP) and with a trifluoroborate group (PFAPB) were investigated (Fig. 20). PFAPB showed a higher fluorophilicity than PFAP at the same PFA tail length (m = 0, 1, 2, 3). Both anions were more fluorophilic than the common TFS or TFSI anion independent on their PFA tail length. Regarding the pyrazolide anions, it was calculated that the longer the PFA tail of the anion, the higher its fluorophilicity.[134]

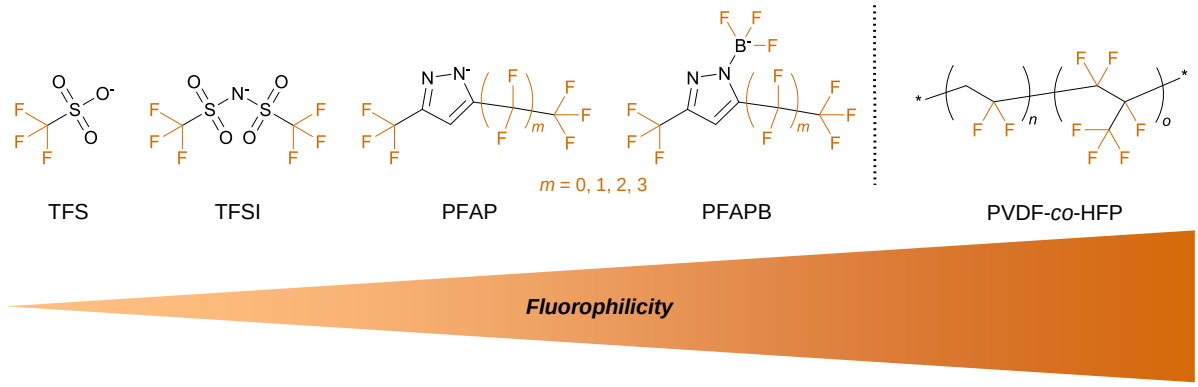

Fig. 20 Calculated relative fluorophilicity of TFS, TFSI, PFAP and PFAPB anions compared to PVDF-*co*-HFP.[134]

1.12 Sulfur in polymer electrolytes

The electrochemical stability of conventional PEG/LiTFSI SPEs is up to around 3.5 V vs. Li/Li^+ at 70 °C.[92] To further extend the electrochemical stability of SPEs, other chemical groups for the lithium salt dissociation are promising. Sulfur can not only be used as a cathode material in LIBs, but also serves as an important building block in polymer electrolytes. Thioether, sulfoxide and sulfon groups showed an extraordinary high electrochemical stability (> 5 V vs. Li/Li^+).[135–138] Their hydrophilic character makes them interesting for lithium salt dissolution.[137] Furthermore, their incorporation into PEG can reduce or even prevent the crystallization of SPEs (Fig. 21a-c).[137]

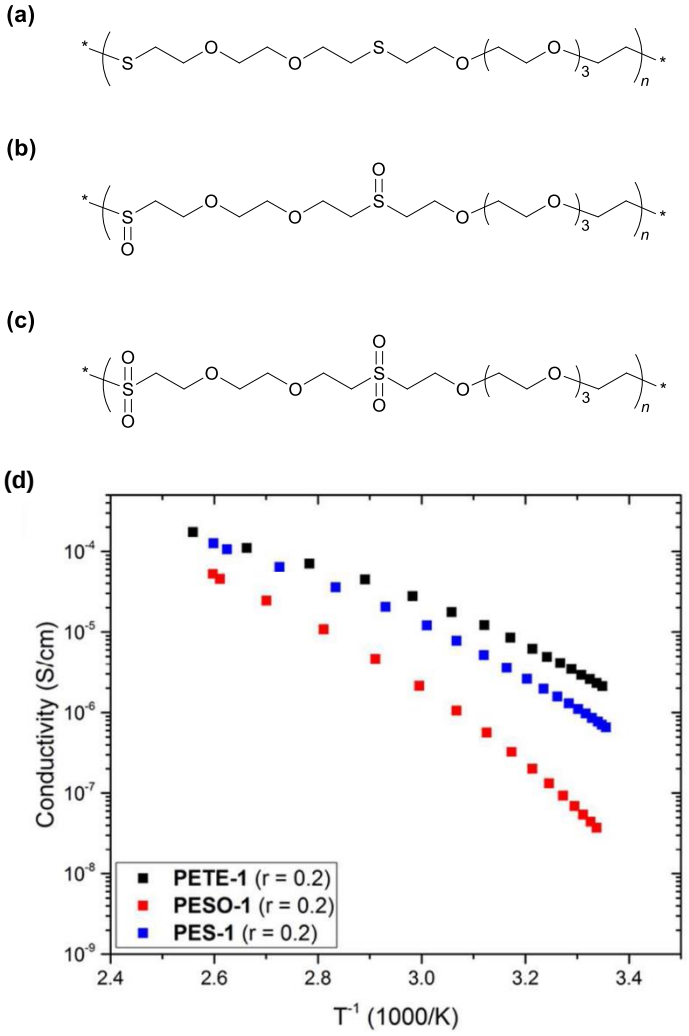

Fig. 21 Sulfur functionalized PEG host polymers for polymer electrolytes in LIBs: (a) poly(ether-thioether) (PETE), (b) poly(ether-sulfoxide) (PESO) and (c) poly(ether-sulfone) (PES). (d) Dependency of the ionic conductivity on the temperature T with a LiTFSI concentration r = Li/(total molar concentration of ether, thioether, sulfoxide, and sulfone functional groups) of 0.2. PETE-1, PESO-1 and PES-1 are amorphous with T_g values of -33.9, -21.1 and -20.8 °C. Reprinted with permission from reference[137]. Copyright 2016 American Chemical Society.

The oxidation state of sulfur in thioether, sulfoxide and sulfone groups is -2, 0 and +2, respectively. Interestingly, the ionic conductivity of a poly(ether-sulfone)/LiTFSI electrolyte is roughly three times higher than for a poly(ether-sulfoxide)/LiTFSI electrolyte at the same LiTFSI concentration and glass transition temperature (Fig. 21d). Thus a higher oxidation state which is coupled to a higher polymer backbone polarity can promote lithium ion mobility. Sulfur in sulfonate ester groups has an even higher oxidation state of +4 and has not been adequately studied in SPEs. One synthetic approach to combine sulfonate ester and PFPE moieties was presented by Marestin *et al.* using step-growth cyclopolymerization (Fig. 22).[139]

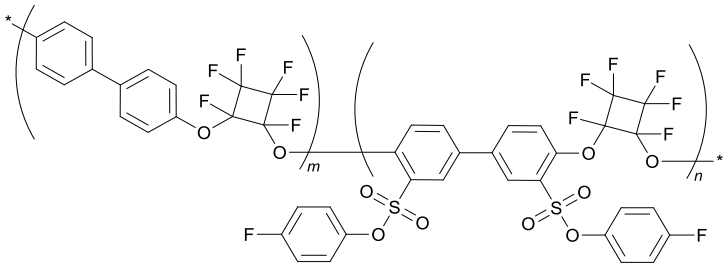

Fig. 22 Sulfonate ester- and PFPE-containing copolymer synthesized by step-growth cyclopolymerization.[139]

Another synthetic approach for incorporating sulfur into a polymer is based on coupling sulfonate esters with a vinyl group. So radical polymerization can be used to get poly(vinyl sulfonate) or also called poly(ethenesulfonate) (PES). Mori *et al.* reported the synthesis of PESs carrying different substituents by controlled radical polymerization using reversible addition-fragmentation chain transfer (RAFT) polymerization.[140–142] The RAFT mechanism is described in the next chapter.

1.13 Reversible addition-fragmentation chain transfer polymerization

The dispersity $Đ = M_w/M_n$ is a quantity for the width of the molecular weight distribution of a polymer. In conventional free radical polymerization (FRP) $Đ$ values are well above 1.5 according to the extent of chain transfer and chain termination by recombination or disproportionation.[143] In contrast, a $Đ$ near 1.1 is possible by means of controlled radical polymerization techniques such as RAFT[144] and nitroxide-mediated radical polymerization (NMRP).[145]

For RAFT, the same initiators (I) such as 2,2'-azobisisobutyronitrile (AIBN) as in the FRP can be used. Moreover, also a wide range of vinyl monomers (styrene, acrylonitrile, methacrylic esters, methacrylic acid and its salts, for instance) and solvents are applied.[144,146,147] In opposition to NMRP, a lower polymerization temperature is sufficient for the same monomer conversion. RAFT allows the synthesis of defined polymer structures such as homopolymers, copolymers, diblock, multiblock, star and graft copolymers.[148]

Chain start and propagation of the monomer (M) result in the polymer radical $P_m^{\bullet}$ (Scheme 2). The controlled property arises from the addition of a chain transfer agent (CTA) presented in the general form as dithioester-CTA **1**.[148] By replacing the general group Z by different functional groups, a large number of CTAs such as dithiobenzoates (Z = phenyl), trithiocarbonates (Z = S-R'), dithiocarbonates/xanthates (Z = O-R') and dithiocarbamates (Z = N-R'R'') is possible.

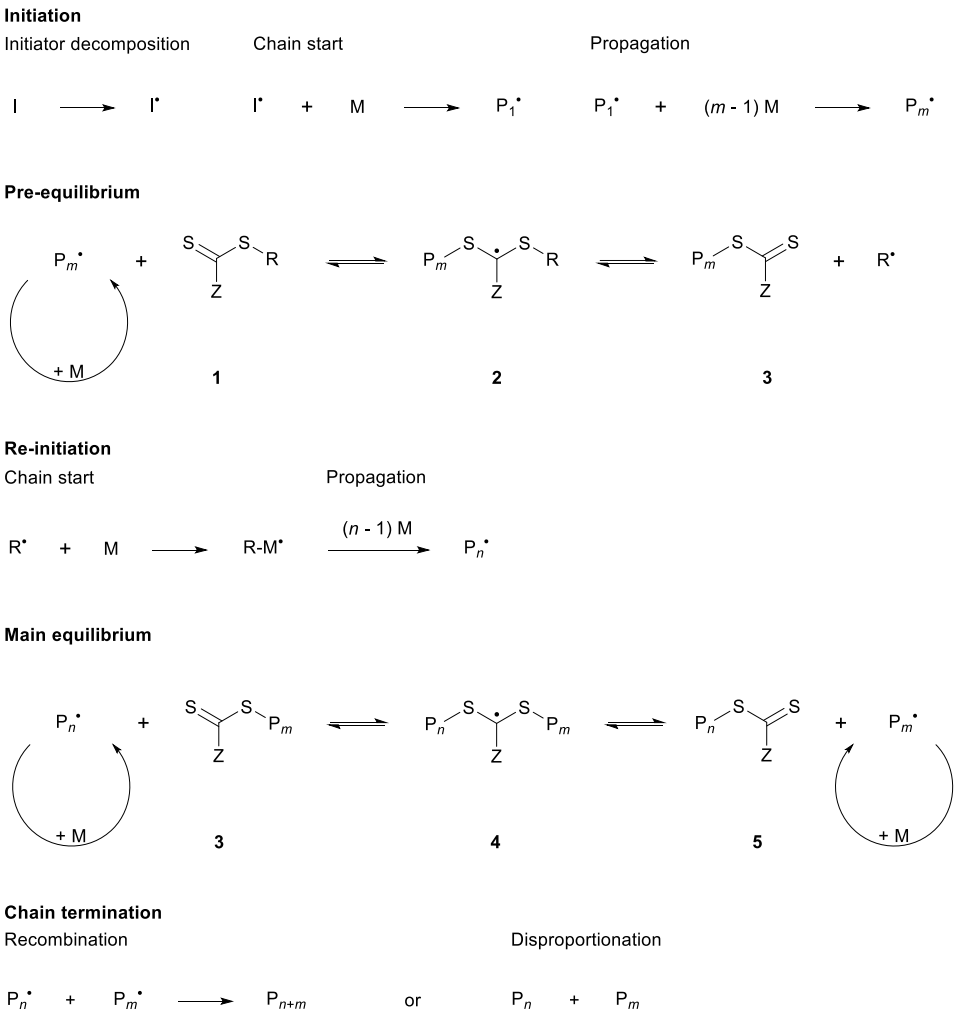

Scheme 2 General RAFT mechanism. Z = *e.g.* phenyl, S-R', O-R' or N-R'R".[148]

The polymer radical $P_m^{\bullet}$ is in a reversible chain transfer equilibrium with the intermediate radical **2** by the reaction with **1**. At the same time, the intermediate radical **2** can release a new reactive radical $R^{\bullet}$ during the pre-equilibrium and is converted into the dormant species **3** of $P_m^{\bullet}$. The radical $R^{\bullet}$ re-initiates and propagates with further monomers resulting in the polymer radical $P_n^{\bullet}$. The polymer radicals are transferred over the macro intermediate radical **4** between the dormant species **3** and **5** during the main equilibrium. A fast equilibrium between activated ($P_m^{\bullet}$ or $P_n^{\bullet}$) and dormant species (**3** or **5**) ensures a uniform chain growth.[147,148] The correct choice of the CTA and reaction conditions depending on the monomer is a key factor in achieving a low $Đ$ and high molecular weight. The Z group of the CTA is able to activate or deactivate the carbon-sulfur double bond C=S and determines the stability of the intermediate radical. A controlled polymerization with a fast equilibrium will be only possible, if the CTAs **1**, **3** and **5** carry C=S bonds, which are reactive enough towards the propagating radicals. The intermediate radical **4** will only decompose fast in both directions of the equilibrium, if the bonds P_m -S (in **3**) and P_n -S (in **5**) are weak enough. Additionally, the stability of the intermediate radical **4**

is appropriate according to the stability of the homolytically cleaved leaving groups $P_m^{\bullet}$ and $P_n^{\bullet}$. Furthermore, a high destabilization of the intermediate radical **2** is necessary to enable the release of all $R^{\bullet}$ radicals right at the beginning of the polymerization. This is only possible by a weak S-R bond in **2** and a high fragmentation tendency of **2**. Moreover, the $R^{\bullet}$ radicals have to re-initiate fast.[147,148]

By reducing the concentration of active propagating radicals [$P^{\bullet}$], chain terminations can be decreased. The termination reaction rates are proportional to [$P^{\bullet}$]^2 compared to the propagating rate which is only proportional to [$P^{\bullet}$]. So the termination reaction rates decrease faster than the propagating rate when [$P^{\bullet}$] is reduced. However, occasional chain terminations result in inactive polymers carrying I-, R-, hydrogen- or double bond-terminated end-groups, but no dithioester Z group. Nevertheless, the most polymers are supposed to carry the functionalization at the ω-chain end. For the synthesis of more complex polymer architectures such as AB-diblock copolymers these functionalized polymers can serve as macro-CTA (Scheme 3).[148]

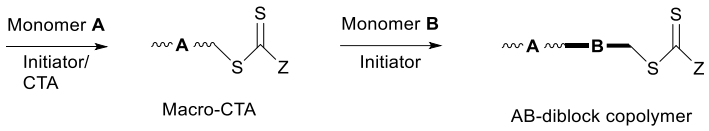

Scheme 3 Synthesis of an AB-diblock copolymer by RAFT.[148]

According to the general RAFT mechanism, the theoretical number-average molecular weight $M_{\mathrm{n,\,theor}}$ is calculated in dependence of the monomer conversion *conv.* as follows:[141]

$$M_{\mathrm{n,\,theor}} = \frac{[\mathrm{M}]_0}{[\mathrm{CTA}]_0} \cdot M_{\mathrm{M}} \cdot \frac{conv.(\text{in }\%)}{100\%} + M_{\mathrm{CTA}} \qquad (13)$$

where $[\mathrm{M}]_0$ and $[\mathrm{CTA}]_0$ are the initial molar concentrations of the monomer and the CTA, respectively. M_{M} and M_{CTA} are their molecular weights.

Mori *et al.* found out that especially dithiocarbonates/xanthates (Z = O-R') are suitable CTAs for the controlled radical polymerization of *O*-, *N*- and *S*-vinyl monomers.[140,141] In contrast, dithiobenzoates and dithiocarbamates as CTAs showed low conversions and broad molecular weight distributions. When xanthates are used as CTAs the additional term MADIX (macromolecular design via the interchange of xanthates) instead of RAFT is common in the literature.

There are some features in the main equilibrium of the RAFT mechanism which are demonstrated with ethenesulfonate (ES) monomers (also called vinyl sulfonate esters) as an example. This class of monomers will be investigated in this thesis. In general, the ES radicals are instable and reactive due to a non-conjugated structure. Therefore, it is advantageous that the intermediate radical is destabilized

by the electron pushing *O*-alkyl substituent. So the fragmentation into the poor leaving groups $P_m^{\bullet}$ or $P_n^{\bullet}$ can still occur fast. In addition, the released macro-CTA is supposed to be resonance-stabilized by the *O*-alkyl substituent. Consequently, the counterattack of the released polymer radicals $P_m^{\bullet}$ and $P_n^{\bullet}$, respectively, is disturbed (Scheme 4).[140,141]

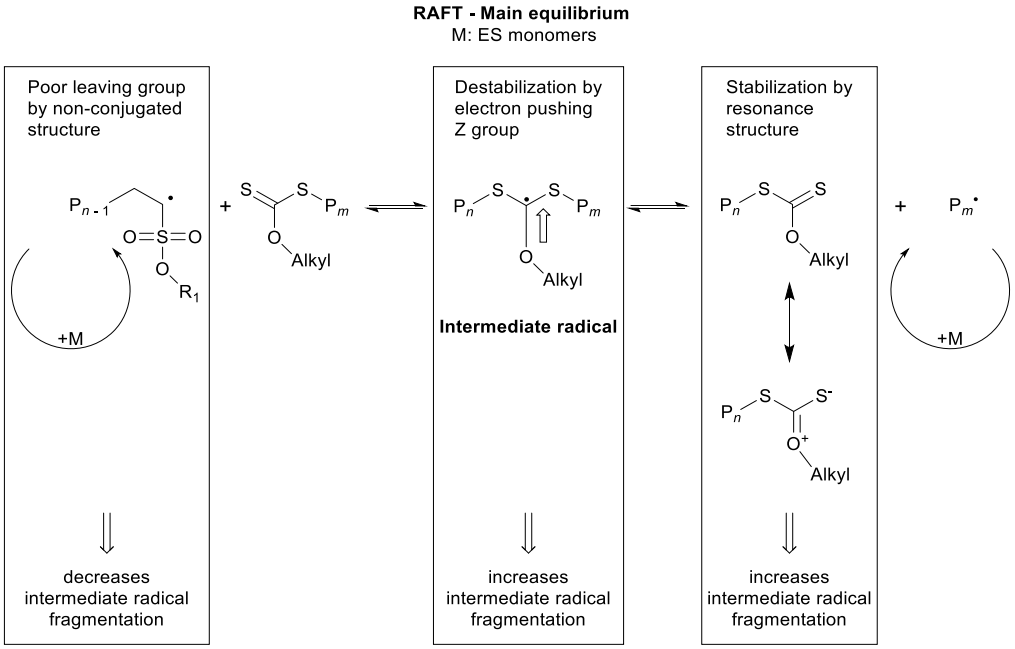

Scheme 4 Proposed mechanism of the RAFT polymerization of ES monomers using xanthate CTAs.[141]

1.14 Nitroxide-mediated radical polymerization

Whereas in RAFT the CTA is the important building block of the dormant species, in NMRP the concentration of active radicals is reduced by adding a persistent radical. It can deactivate the propagating radical by recombination. However, it cannot react with itself. In contrast to RAFT, no additional initiator is necessary. Alkoxyamines such as *N*-(*tert*-butyl)-*N*-(2-methyl-1-phenylpropyl)-*O*-(1-phenylethyl)hydroxylamine **1** can be used which thermally decompose into both the initiator radical $R^{\bullet}$ and the persistent radical **2** (Scheme 5).

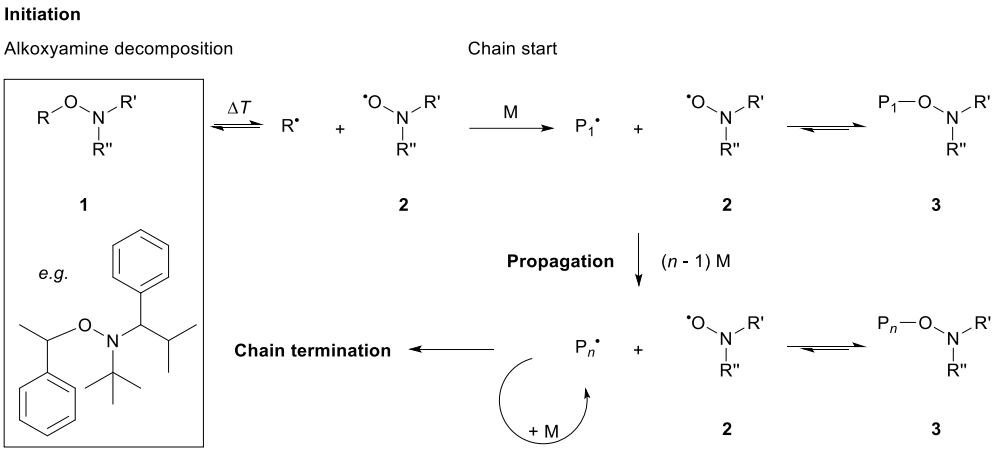

Scheme 5 General mechanism of NMRP.[149]

NMRP is suitable for numerous vinyl monomers (M) such as styrene, styrene derivatives, carbazoles, pyridines, acrylates and acrylamides.[149] R$^{\bullet}$ starts the chain growth by reacting with M to the radical $P_1^{\bullet}$ which propagates to the polymer radical $P_m^{\bullet}$. The active radicals $P_1^{\bullet}$ and $P_n^{\bullet}$ are in equilibrium with the dormant species **3**. Since the deactivation reaction proceeds much faster than the reaction of the active radicals with M, the equilibrium is on the side of **3**. To decrease chain termination, the equilibriums can be shifted further to the side of **3** by increasing the concentration of **2**. An example for a free nitroxide radical is 2,2,5-trimethyl-4-phenyl-3-azahexane-3-nitroxide (TIPNO, example structure **2** in Scheme 5).[150,151]

The theoretical number-average molecular weight $M_{\mathrm{n,\,theor}}$ under consideration of an ideal NMRP process can be calculated according to:

$$M_{\mathrm{n,\,theor}} = \frac{[\mathrm{M}]_0}{[\mathrm{I}]_0} \cdot M_{\mathrm{M}} \cdot \frac{conv.(\mathrm{in}\ \%)}{100\%} + M_{\mathrm{I}} \qquad (14)$$

where $[\mathrm{M}]_0$ and $[\mathrm{I}]_0$ are the initial molar concentrations of the monomer and the NMRP initiator, respectively. M_{M} and M_{I} are their molecular weights.[149]

2 Objective

Until now, graft copolymer poly(ethylene glycol) (PEG) solid polymer electrolytes (SPE) as lithium ion conductors in lithium polymer batteries have not been fully investigated. A systematic study on these SPEs with 1,4-disubstituted 1,2,3-triazole (TR)-linking groups and a poly(styrene) (PS) backbone to examine the effect of the PEG side-chain length on their thermal, morphological and electrochemical properties is missing. In the first chapter of this thesis the question is answered how linear and graft copolymer PEG SPEs differ in their properties. Linear poly(ethylene glycol) monomethyl ether (PEG-OH) SPEs with their graft copolymer counterparts, poly(4-(propargyloxy)styrene)-*grafted*-poly(ethylene glycol) (PPOS-*g*-PEG) SPEs, at different lithium bis(trifluoromethanesulfonyl)imide (LiTFSI) concentrations will be compared (Scheme 6). The graft copolymer backbone, PPOS, provides both a PS derivative for mechanical strength and a TR-linking group for grafting PEG side-chains. The lengths of the PEG chains were chosen relatively short to support sufficient chain mobility for ion conduction as reported in previous studies (degree of polymerization $DP_m = 17$ for PEG750 with 750 g mol^{-1} and $DP_m = 41$ for PEG2000 with 2000 g mol^{-1}).[79,91,94,96]

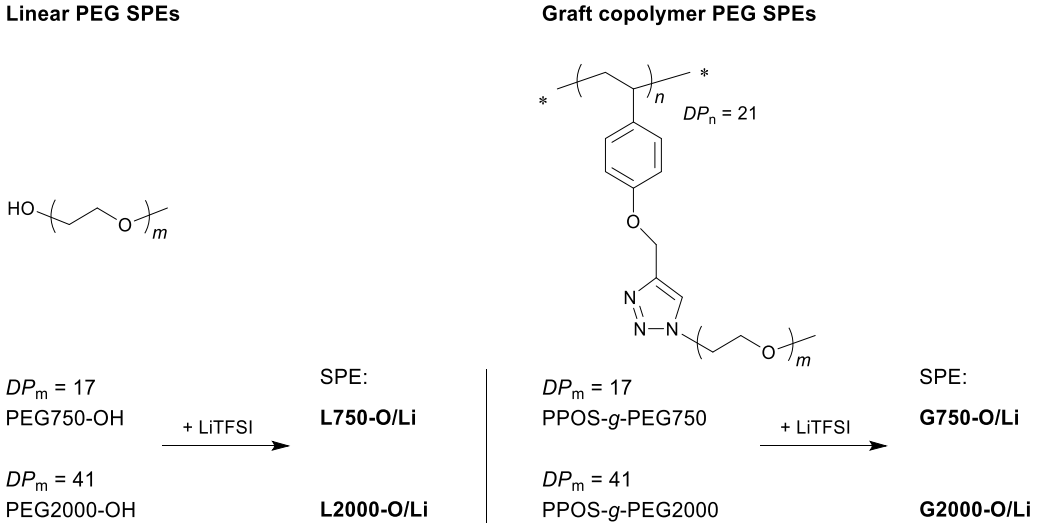

Scheme 6 Linear and graft copolymer poly(ethylene glycol) PEG solid polymer electrolytes (SPE) investigated in this study. DP_m is the degree of polymerization for PEG determined by MALDI-ToF MS. DP_n was calculated under consideration of an ideal NMRP process by equation (16). (O/Li: molar ratio of oxygen to lithium atoms; representing the LiTFSI concentration in the SPE)

The graft copolymers will be synthesized by copper(I)-catalyzed alkyne-azide cycloaddition (CuAAC) to attain a high grafting density. Nitroxide-mediated radical polymerization (NMRP) for the synthesis of PPOS will be used to attain a defined backbone length ($DP_n = 21$) and a narrow molecular weight

distribution. The chemical structures will be characterized by IR and ^{1}H NMR spectroscopy, size exclusion chromatography (SEC) and matrix-assisted laser desorption/ionization time-of-flight mass spectrometry (MALDI-ToF MS). The thermal and morphological properties will be examined by thermal gravimetric analysis (TGA) and differential scanning calorimetry (DSC). The ionic conductivity, the electrochemical stability and the lithium ion transference number will be evaluated by potentiostatic electrochemical impedance spectroscopy (PEIS) and cyclic voltammetry (CV). The results of this study will play a key role in the future design of polymers for PEG SPEs.

Another class of host polymers for SPEs besides PEG is based on perfluoropolyethers (PFPE). PFPEs are intrinsically nonflammable and show nearly single-ion conductor behavior.[10,120] However, PFPEs show poor ionic conductivity in combination with LiTFSI due to the limited solubility of LiTFSI.[121] Therefore, in previous studies, the PFPEs were functionalized with hydroxyl, PEG or methyl carbonate end-groups enhancing the lithium salt solubility.[125] These functional groups are only electrochemically stable up to around 3.5 V vs. Li/Li^{+} at 70 °C.[92] To further extend the electrochemical stability, other chemical groups for the lithium salt dissociation have to be tested. It was shown that thiols, sulfoxides and sulfones can interact with lithium salts and are highly electrochemically stable (> 5 V vs. Li/Li^{+}).[135–138] However, the synthesis and characterization of sulfonate ester-based graft copolymers carrying oligo ethylene glycol (EG) or fluorinated ethylene glycol (FEG) side-chains have not yet been reported in the literature.

A novel structural concept for graft copolymer SPEs will be designed in the second chapter of this thesis. It combines oligomeric FEG side-chains with a poly(ethenesulfonate) (PES) backbone to overcome the conventional usage of PEG and organic carbonates (Fig. 23).[152]

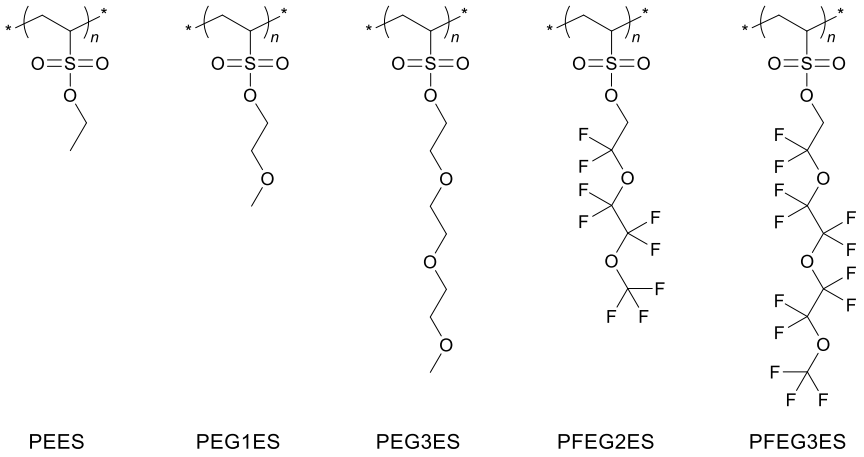

Fig. 23 Graft copolymers consisting of a poly(ethenesulfonate) (PES) backbone and ethylene glycol (EG) or fluorinated ethylene glycol (FEG) side-chains of different lengths synthesized in this study.[152] Poly(ethyl ethenesulfonate) (PEES) has been already synthesized in the literature and will serve as a reference compound to compare the polymerization behavior.[140–142]

The purpose of this study is to gain new insights into the conventional free radical polymerization (FRP) and reversible addition-fragmentation chain transfer (RAFT) polymerization of ethenesulfonate (ES) monomers having EG or FEG side-chains. The focus is on the fundamental understanding of the fluorination effect of oligo ethylene glycol ethenesulfonate (EGES) monomers on the kinetics of polymerization. Based on this, the monomer conversion and the polymer molecular weight will be optimized. Poly(ethyl ethenesulfonate) (PEES) has been already synthesized in the literature and will serve as a reference compound to compare the polymerization behavior.[140–142] For the first time, MALDI-ToF MS will be used to characterize PESs for a detailed end-group analysis revealing possible termination and chain transfer reactions. Furthermore, this technique allows the determination of absolute molecular weights. TGA, DSC, DMA and wide-angle x-ray scattering (WAXS) will be used to determine thermal properties. For the first time, the successful synthesis and characterization of poly(fluorinated oligo ethylene glycol ethenesulfonate)s (PFEGES) will be reported.

The third chapter of this thesis will determine the solubility of LiTFSI and of a new lithium salt in poly(2,2-difluoro-2-(1,1,2,2-tetrafluoro-2-(1,1,2,2-tetrafluoro-2-(trifluoromethoxy)ethoxy)ethoxy)-ethyl ethenesulfonate) (PFEG3ES) as a host polymer for SPEs. Density-functional theory calculations indicated that PFPEs are more fluorophilic than their perfluoroalkyl analogues.[123] Similar to the fluorous effect which applies to perfluoroalkyls, also PFPEs might be best soluble within each other. This hypothesis requires the synthesis and investigation of new PFPE lithium salts beyond perfluoroalkyl-based lithium salts. The question here is whether the incorporation of PFPE tails in lithium salts can increase the solubility and thus the ionic conductivity in PEG-free PFPE SPEs. For this purpose, the new PFPE lithium salt, lithium 2,2-difluoro-2-(1,1,2,2-tetrafluoro-2-(1,1,2,2-tetrafluoro-2-(trifluoromethoxy)ethoxy)ethoxy)ethan-1-olate (LiFEG3) will be synthesized. The solubility and ionic conductivity of LiTFSI with those of LiFEG3 in PFEG3ES will be compared (Fig. 24).

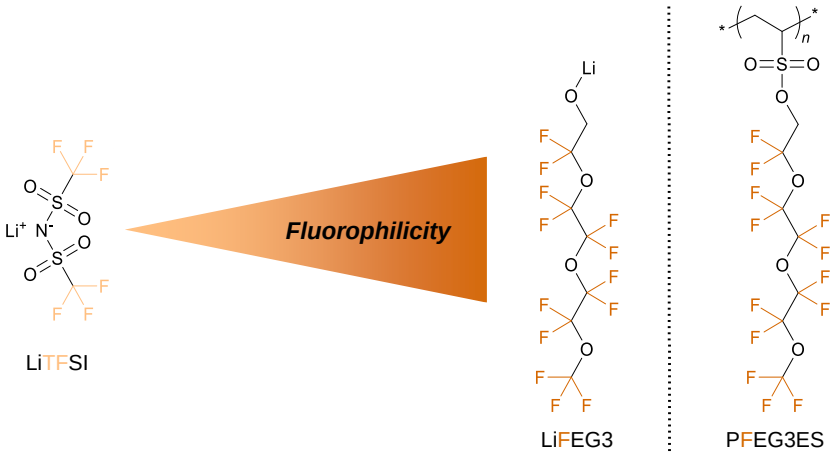

Fig. 24 Expected fluorophilicity of LiTFSI compared to LiFEG3 and PFEG3ES synthesized in this study.

LiFEG3 can be classified as a fluorosurfactant with a highly fluorophilic FEG3 tail and a hydrophilic lithium alkoxide head group.[153] The graft copolymer PFEG3ES also shows an amphiphilic character. It contains highly fluorophilic FEG3 side-chains and a hydrophilic PES backbone. Their structural similarity might promote the ion dissociation of LiFEG3.

The chemical structure of LiFEG3 will be characterized by ^{1}H and ^{19}F NMR spectroscopy. The thermal stability will be evaluated by TGA. To understand the effect of the thermal and morphological properties on the ionic conductivity DMA, DSC and polarization microscopy will be used. PEIS will be used to determine the ionic conductivity of LiFEG3 SPEs with O/Li ratios of 69, 15, 10 and 5 (SPE-O/Li). CV will serve to estimate the electrochemical stability. This study paves the way for the future design of new lithium salts for highly fluorophilic host polymers in SPEs for lithium-ion batteries.

3 Results and Discussion

3.1 Linear versus triazole-linked graft copolymer poly(ethylene glycol) solid polymer electrolytes

3.1.1 Polymer synthesis and characterization

The graft copolymers, PPOS-*g*-PEG750 and PPOS-*g*-PEG2000, were synthesized by grafting PEG750-N3 or PEG2000-N3 onto PPOS (Scheme 7). The graft copolymer backbone PPOS was synthesized by NMRP as already reported in the literature.[151,154] The polymerization was performed with TMSPOS in which the alkyne was protected by a trimethylsilyl group to prevent a cross-linking during polymerization.

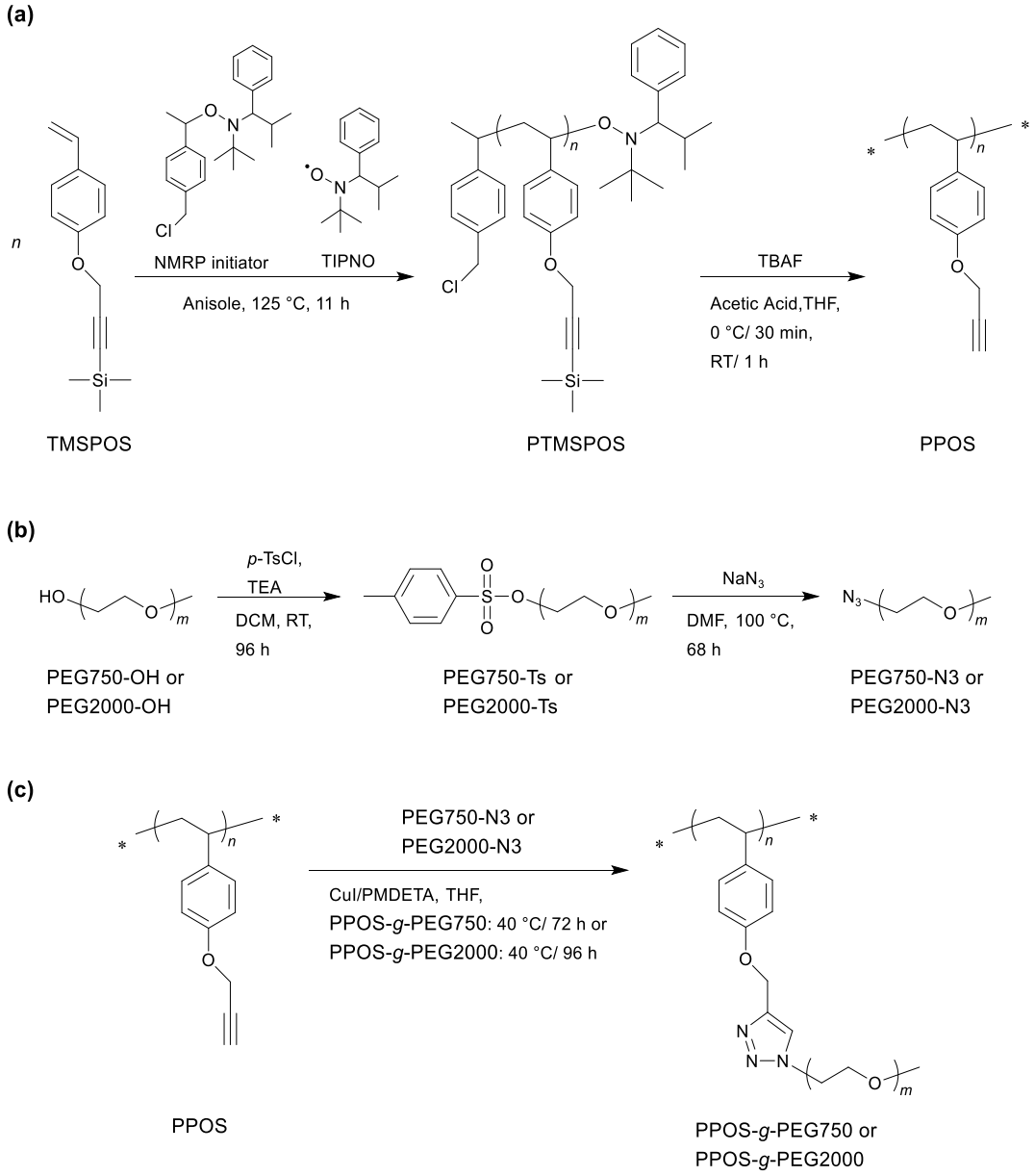

Scheme 7 Syntheses of (a) the graft copolymer backbone PPOS by nitroxide-mediated radical polymerization (NMRP), (b) of the graft copolymer side-chains PEG750-N3 and PEG2000-N3 and (c) of the graft copolymers PPOS-*g*-PEG750 and PPOS-*g*-PEG2000 via copper(I)-catalyzed alkyne-azide cycloaddition (CuAAC).

The selected NMRP initiator (*N*-*tert*-butyl-*O*-[1-[4-(chloromethyl)phenyl]ethyl]-*N*-(2-methyl-1-phenylpropyl)hydroxylamine) carries a chlorine atom for a future functionalization of the graft copolymers. For instance, the chlorine atom can be substituted by an azide or an alkyne group to enable the synthesis of diblock copolymers via a subsequent click reaction with alkyne- or azide-functionalized polymers. Additional free nitroxide radical, TIPNO, was added ($[M]_0/[I]_0/[TIPNO]_0$ = 35/1/0.1) to reduce chain terminations (compare chapter 1.14).[150,151]

Side-reactions such as chain termination and transfer reactions occur mainly at higher conversions since the monomer concentration decreases and the probability that two propagating high-molecular weight polymer radicals meet increases. The consequence would be a broadening of the molecular weight distribution with $Đ > 1.3$.[151] To still achieve a narrow molecular weight distribution, the ratio $[M]_0/[I]_0 = 35$ was set relatively high for the target DP_n of 20. In this manner, the polymerization could be stopped at a relatively low monomer conversion (60%, Fig. 79). A unimodal and narrow molecular weight distribution ($Đ = 1.16$) determined by SEC was achieved (Fig. 25).

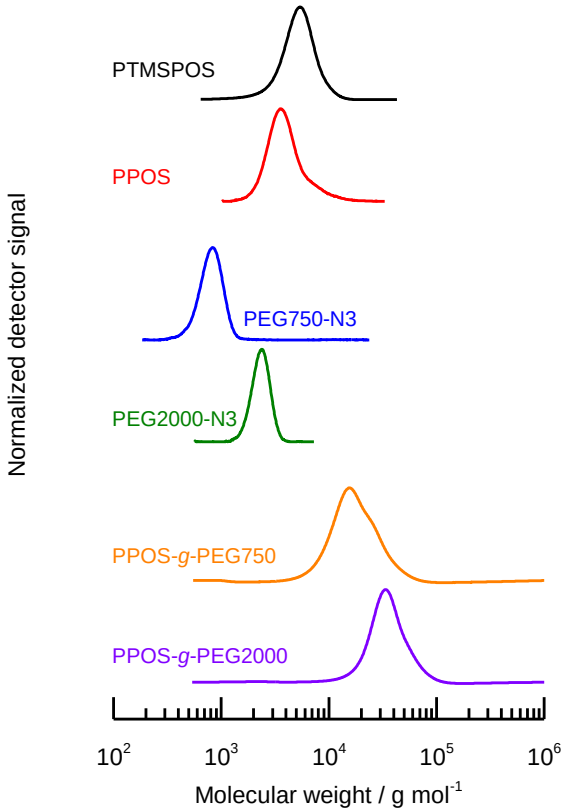

Fig. 25 SEC molecular weight distributions of PTMSPOS, PPOS, PEG750-N3, PEG2000-N3, PPOS-*g*-PEG750 and PPOS-*g*-PEG2000. For PTMSPOS, a UV detector and for the other polymers an RI detector was used. For PTMSPOS, PPOS, PEG750-N3 and PEG2000-N3 only THF and for PPOS-*g*-PEG750 and PPOS-*g*-PEG2000 THF with 0.25 wt% TBAB served as an eluent. PS standards were used for calibration.

A calculated DP_n of 21 with a theoretical number-average molecular weight $M_{n,\,theor}$ of 5,200 g mol^{-1} was achieved (equations (16) and (17), Table 1).

Table 1 Comparison of molecular weight values of PTMSPOS, PPOS, PEG750-N3, PEG2000-N3, PPOS-*g*-PEG750 and PPOS-*g*-PEG2000 determined by theoretical calculations, SEC and MALDI-ToF MS.

Polymer	DP_n[a]	DP_m	$M_{n,\,theor}$ (g mol^{-1})	$M_{n,\,SEC}$ (g mol^{-1})	$Đ$	$M_{p,\,SEC}$ (g mol^{-1})	$M_{p,\,MALDI}$ (g mol^{-1})
PTMSPOS	21	-	5,200[d]	4,700[i]	1.16[i]	5,500[i]	-
PPOS	21	-	3,700[e]	3,700[i]	1.18[i]	3,600[i]	-
PEG750-N3	-	17[b]	810[f]	770[i]	1.13[i]	820[i]	830[k]
PEG2000-N3	-	41[c]	1,860[g]	2,300[i]	1.04[i]	2,400[i]	1,830[k]
PPOS-*g*-PEG750	21	17[b]	20,600[h]	15,300[j]	1.27[j]	15,500[j]	15,500[l]
PPOS-*g*-PEG2000	21	41[c]	42,800[h]	32,100[j]	1.18[j]	33,600[j]	35,600[l]

[a]Calculated by equation (16). [b]Determined by MALDI-ToF MS (Fig. 85a). [c]Determined by MALDI-ToF MS (Fig. 85b). [d]Calculated by equation (17). [e]Calculated by equation (18). [f]Calculated by equation (19). [g]Calculated by equation (20). [h]Calculated according to equation (21). [i]Determined by SEC with THF as an eluent and calibrated with PS standards (Fig. 25). [j]Determined by SEC with THF containing 0.25 wt% TBAB as an eluent and calibrated with PS standards (Fig. 25). [k]Determined by MALDI-ToF MS in reflectron positive mode with IAA as a matrix. [l]Determined by MALDI-ToF MS in linear positive mode with IAA as a matrix.

Desilylation of PTMSPOS afforded complete conversion as shown by IR spectroscopy (Fig. 26). The characteristic signal of the alkyne carbon-hydrogen bond at 3287 cm^{-1} arose, whereas the signals of the methyl carbon-silicon bonds at 1249 cm^{-1}, 839 cm^{-1} and 759 cm^{-1} disappeared.

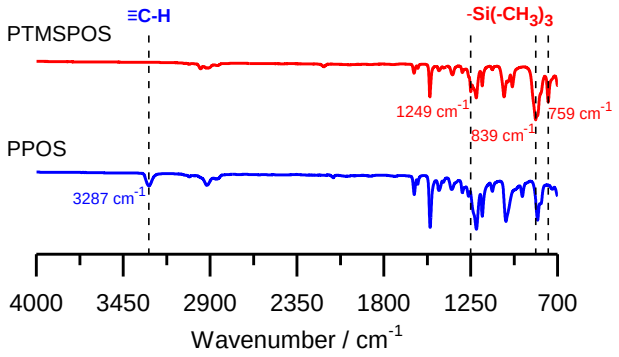

Fig. 26 Transmission IR spectra of PTMSPOS and PPOS.

^{1}H NMR spectroscopy also proved the complete desilylation. The signal of the methyl protons of the TMS group at 0.41-0.08 ppm was only present in the spectrum of PTMSPOS (Fig. 80), whereas the signal of the alkyne proton at 2.69-2.31 ppm was solely observed in the spectrum of PPOS (Fig. 27).

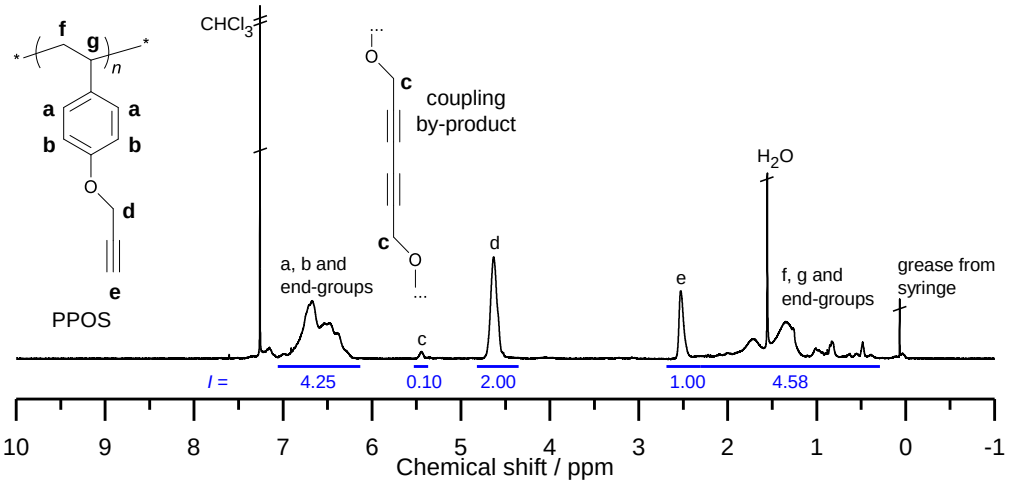

Fig. 27 ^{1}H NMR spectrum of PPOS in $CDCl_3$. The inset shows the structure of a possible coupling by-product between two polymer chains.

In the spectrum of PPOS an unexpected signal appeared at 5.53-5.37 ppm downfield shifted to the signal of the methylene protons which are adjacent to the alkyne group. This signal might be assigned to methylene protons which are neighbored to a diyne group arisen by a possible coupling of two polymer chains (inset of Fig. 27).[155] This observation might also explain the slight tailing of the SEC curve of PPOS (Fig. 25). The tailing had a negligible effect on the dispersity ($Đ$ = 1.18).

The graft copolymer side-chains PEG750-N3 and PEG2000-N3 were synthesized by a double nucleophilic substitution of PEG750-OH or PEG2000-OH via PEG750-Ts or PEG2000-Ts similar to the literature (Scheme 7b).[156] The complete tosylation of the isolated intermediates was proven by ^{1}H NMR spectroscopy. The integral of the signal of the methyl group protons in the tosyl group was equal to the integral of the signal of the methoxy group protons (Fig. 81 and Fig. 82). The activated tosyl ester was transformed into the azide by using sodium azide as the nucleophilic agent. The absence of the ^{1}H NMR signals of the tosyl group (Fig. 83 and Fig. 86) and the presence of the IR signal of the azide group around 2100 cm^{-1} (Fig. 84) proved the complete substitution of the end-group in the isolated products. Their molecular weight distribution was unimodal and narrow ($Đ$ < 1.2, Fig. 25) which allowed the analysis by MALDI-ToF MS. The intact azide end-group was visible in the spectrum of PEG750-N3 (Fig. 85a). In the spectrum of PEG2000-N3 (Fig. 85b), only a metastable nitrogen end-group N could be identified. This could be explained by the expulsion of N_2 during the MALDI-ToF MS measurement.[157] DP_m was calculated from the isotopic mean value averaged over all isotopic peaks for the series with the highest intensity (DP_m = 17 for PEG750-N3 and 41 for PEG2000-N3).

The graft copolymers, PPOS-*g*-PEG750 and PPOS-*g*-PEG2000, were synthesized by the CuAAC similar to the literature.[102,103,158] An excess of PEG-N3 was used to guarantee a complete conversion

of the alkyne groups in PPOS. Unreacted PEG750-N3 and PEG2000-N3 were removed successfully via dialysis. This was proven by IR spectroscopy where the vibrational band of the azide group around 2100 cm^{-1} was absent in the spectra of the graft copolymers (Fig. 88 and Fig. 90). SEC analysis of the graft copolymers revealed each a single peak which is shifted to higher molecular weights compared to the peak of PPOS (Fig. 25). The lack of peaks at low molecular weights proves again the successful removement of residual PEG-N3. Both graft copolymers were obtained in high purity. All the expected ^{1}H NMR signals could be well assigned (Fig. 87 and Fig. 89). The absence of the vibrational band of the alkyne group at 3287 cm^{-1} in the IR spectra and of the alkyne proton at around 2.5 ppm in the ^{1}H NMR spectra confirms a high grafting density.

$Đ$ was low for both graft copolymers (< 1.3) though there was a minor shoulder in the SEC curves at higher molecular weights (Fig. 25). This shoulder might result from coupled PPOS polymer chains as described above. However, ^{1}H NMR spectroscopy did not indicate a possible coupling product. The characteristic signal of the coupling by-product at around 5.5 ppm which was still visible in the ^{1}H NMR spectrum of PPOS (Fig. 27) disappeared. So the amount of coupling by-product was very low in the purified graft copolymers.

The theoretical molecular weights $M_{n,\,theor}$ of the graft copolymers were calculated under the consideration of a 100% grafting density (equation (21) and Table 1). As proven above by IR and ^{1}H NMR spectroscopy, the grafting density was very high (> 95%). Nevertheless, the number-average molecular weights determined by SEC $M_{n,\,SEC}$ of the graft copolymers were lower compared to $M_{n,\,theor}$. SEC is a relative technique only and yields no absolute molecular weights when the polymer used for calibration differs from the sample polymer. However, linear PS standards were used for calibration. In general, graft copolymers have smaller hydrodynamic volumes than linear polymers at the same molecular weight. Consequently, the SEC underestimated the absolute molecular weights.

A further analysis of the graft copolymer molecular weights was performed by MALDI-ToF MS which can serve absolute molecular weights (Fig. 28 and Table 1).

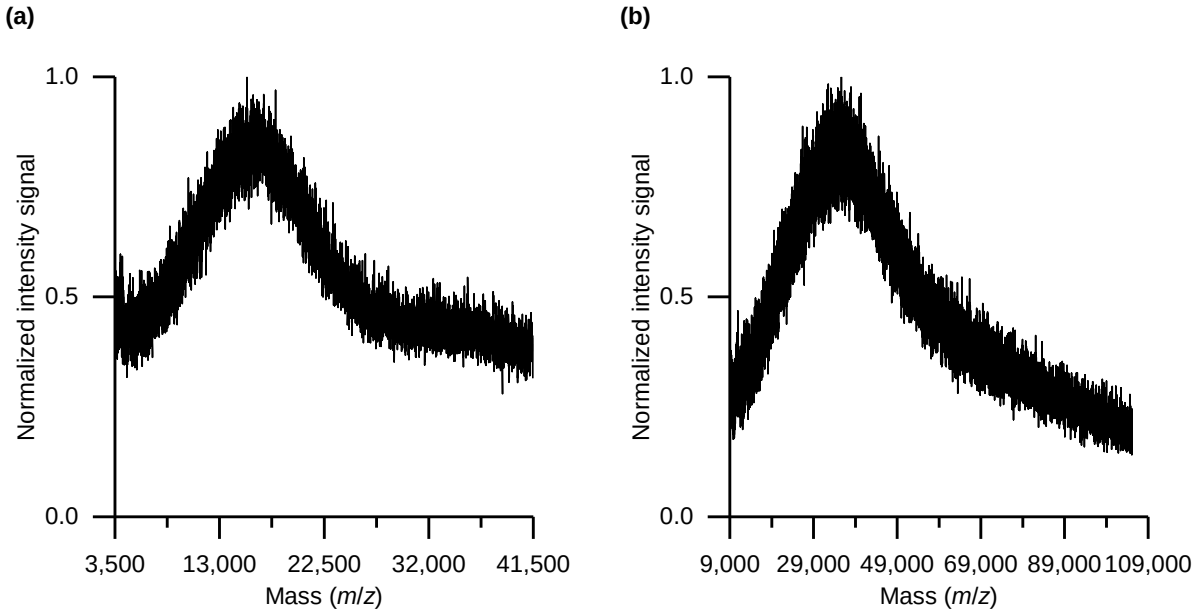

Fig. 28 MALDI-ToF MS spectra of (a) PPOS-*g*-PEG750 and (b) PPOS-*g*-PEG2000. Measurements were performed in linear positive mode.

For PPOS-*g*-PEG750 the peak molecular weight determined by MALDI-ToF MS $M_{p,\,MALDI}$ was equal to and for PPOS-*g*-PEG2000 it was slightly higher than the peak molecular weight determined by SEC $M_{p,\,SEC}$. The values of $M_{p,\,MALDI}$ were still slightly smaller than $M_{n,\,theor}$. This deviation results from the characteristics of the MALDI-ToF MS measurement. Mass discrimination of high molecular weight polymers can occur during the desorption/ionization process. Its extent is dependent on the sample preparation and instrumental settings as known in the literature.[159–161] Therefore, the absolute molecular weight of the graft copolymers must be quite close to $M_{n,\,theor}$.

All in all, the graft copolymers were synthesized in a controlled manner with a defined polymer architecture so that they could serve as standards for the comparative electrochemical characterization with their linear counterparts.

3.1.2 Solid polymer electrolyte preparation

The SPEs were prepared by dissolving different amounts of LiTFSI in the polymer melt at 60 °C. The linear PEG SPEs (L750 and L2000) and the graft copolymer PEG SPEs (G750 and G2000) are named according to their host polymers (PEG750-OH and PEG2000-OH; PPOS-*g*-PEG750 and PPOS-*g*-PEG2000) with the respective O/Li ratio appended (Scheme 6).

3.1.3 Thermal properties

3.1.3.1 Thermal stability

The thermal stability of the pure polymers and of the SPEs was determined by TGA. In the case of PTMSPOS and PPOS, more than 20 wt% solid residue was present after the thermal degradation (Fig. 29a).

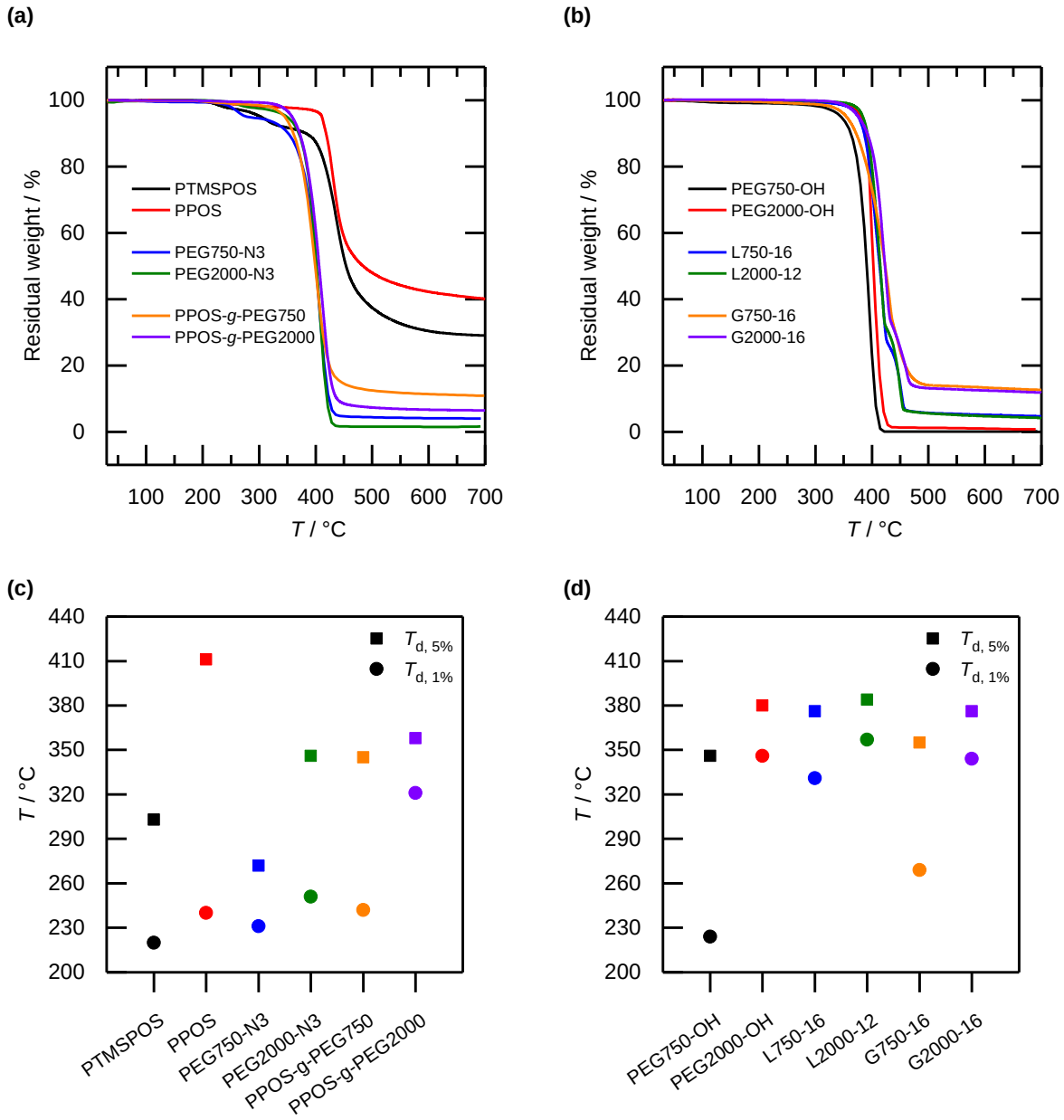

Fig. 29 (a, b) TGA thermograms (under nitrogen, 10 K min^{-1}) and (c, d) $T_{d,\,1\%}$ and $T_{d,\,5\%}$ values of (a, c) PTMSPOS, PPOS, PEG750-N3, PEG2000-N3, PPOS-*g*-PEG750 and PPOS-*g*-PEG2000 as well as of (b, d) PEG750-OH, PEG2000-OH, L750-16, L2000-12, G750-16 and G2000-16.

The amount of solid residue in the case of the graft copolymers was 2-11 wt% higher than for PEG-OH and PEG-N3 which decompose without nearly any residue. Furthermore, the amount of solid residue was higher for all SPEs in comparison to their pure polymers without LiTFSI (Fig. 29b). In general, the amount of solid residue increased with a higher amount of aromatic structures and LiTFSI. PPOS-*g*-PEG750 ($T_{d,\,1\%}$ = 242 °C) and PPOS-*g*-PEG2000 ($T_{d,\,1\%}$ = 321 °C) were thermally more stable than their corresponding linear PEG-N3 (Fig. 29c and Table 2).

Table 2 Comparison of the thermal properties of PTMSPOS, PPOS, PEG750-N3, PEG2000-N3, PPOS-*g*-PEG750 and PPOS-*g*-PEG2000.

Polymer	$T_{d,\,1\%}$[a] (°C)	$T_{d,\,5\%}$[a] (°C)	T_g[b] (°C)	T_{cc}[b] (°C)	$-\Delta H_{cc}$[b] (J g^{-1})	T_c[c] (°C)	$-\Delta H_c$[c] (J g^{-1})	T_m[b] (°C)	ΔH_m[b] (J g^{-1})
PTMSPOS	220	303	43.81	-	-	-	-	-	-
PPOS	240	411	60.67	-	-	-	-	-	-
PEG750-OH	224	346	-	-	-	15.67[d]	133.48[d]	30.17[d]	134.35[d]
PEG2000-OH	346	380	-	-	-	29.33[d]	173.23[d]	55.83	173.01
PEG750-N3	231	272	-7.41	-	-	5.67[d]	133.33[d]	29.00[d]	133.24[d]
PEG2000-N3	251	346	14.01	-	-	31.00[d]	161.90[d]	53.50	161.80
PPOS-*g*-PEG750	242	345	-52.65	-23.17	62.12	-	-	24.00	62.05
PPOS-*g*-PEG2000	321	358	-3.86	-	-	13.33	97.35	51.83	101.46

[a]Determined by TGA (under nitrogen, 10 K min^{-1}). [b]Obtained from the second heating DSC trace (under nitrogen, 10 K min^{-1}). [c]Obtained from the first cooling DSC trace (under nitrogen, 10 K min^{-1}). [d]Multiple peak.

The thermal stability of PPOS-*g*-PEG750 and PEG750-OH was almost comparable, whereas $T_{d,\,1\%}$ of PPOS-*g*-PEG2000 was around 25 °C lower than that of PEG2000-OH. The linear PEG SPEs, exemplarily stated L750-16 ($T_{d,\,1\%}$ = 331 °C) and L2000-12 ($T_{d,\,1\%}$ = 357 °C), showed a higher thermal stability than the pure polymers without LiTFSI (Fig. 29d and Table 3). The same relation applied to the graft copolymer SPEs, G750-16 ($T_{d,\,1\%}$ = 269 °C) and G2000-16 ($T_{d,\,1\%}$ = 344 °C). The graft copolymer SPEs were less stable than their linear counterparts.

Table 3 Comparison of the thermal properties of all PEG SPEs at different O/Li ratios.

SPE-O/Li	$T_{d,\ 1\%}$[a] (°C)	$T_{d,\ 5\%}$[a] (°C)	T_g[b] (°C)	T_{cc}[b] (°C)	$-\Delta H_{cc}$[b] (J g^{-1})	T_c[c] (°C)	$-\Delta H_c$[c] (J g^{-1})	T_m[b] (°C)	ΔH_m[b] (J g^{-1})
L750-25	-	-	-54.03	-	-	6.83	67.64[d]	22.95[d]	69.66[d]
L750-16	331	376	-59.01	-15.83	24.94	-13.81	8.44	14.64[d]	33.99[d]
L750-12	-	-	-53.13	-	-	-	-	-	-
L2000-16	-	-	-53.43	-1.52	38.07	0.17	10.76	39.24	37.46
L2000-12	357	384	-49.21	7.00	8.84	-	-	35.30	12.23
L2000-8	-	-	-38.91	-	-	-	-	-	-
G750-25	-	-	-42.30	-	-	-	-	-	-
G750-16	269	355	-37.66	-	-	-	-	-	-
G750-12	-	-	-32.68	-	-	-	-	-	-
G2000-25	-	-	-41.73	-	-	-2.33	48.39	41.20	56.59
G2000-16	344	376	-44.59	9.67	0.25	-	-	31.99	0.46
G2000-12	-	-	-38.65	-	-	-	-	-	-

[a]Determined by TGA (under nitrogen, 10 K min^{-1}). [b]Obtained from the second heating DSC trace (under nitrogen, 10 K min^{-1}). [c]Obtained from the first cooling DSC trace (under nitrogen, 10 K min^{-1}). [d]Multiple peak.

3.1.3.2 Thermal behavior and morphology

The thermal behavior of the pure polymers and of the SPEs was determined by DSC. PTMSPOS and PPOS were both amorphous with a T_g at 43.81 °C and 60.67 °C, respectively (Fig. 30 and Table 2).

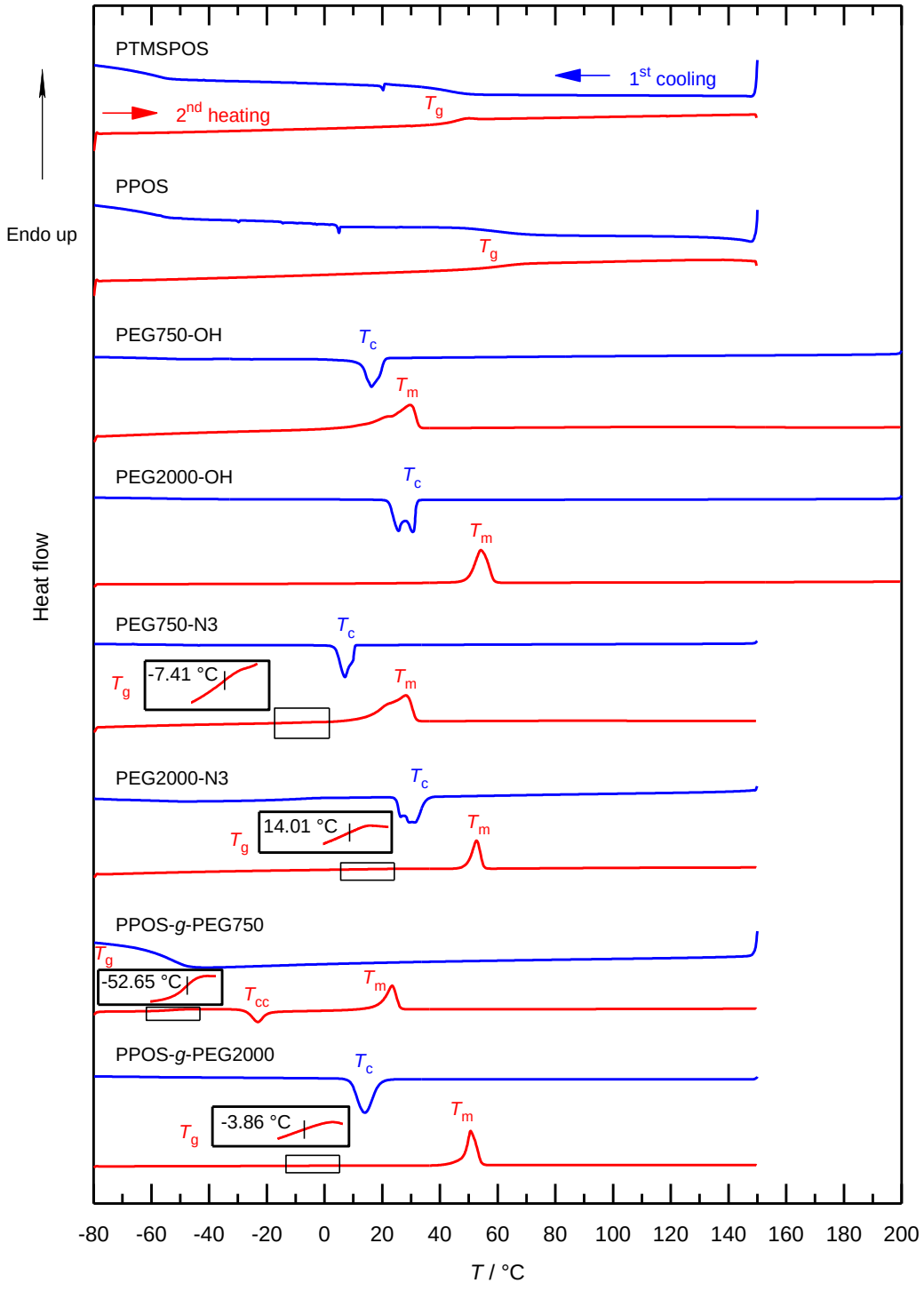

Fig. 30 First cooling (blue) and second heating (red) DSC traces of PTMSPOS, PPOS, PEG750-OH, PEG2000-OH, PEG750-N3, PEG2000-N3, PPOS-*g*-PEG750 and PPOS-*g*-PEG2000 (under nitrogen, 10 K min^{-1}).

By contrast, the PEGs with the hydroxyl and the azide end-groups were semi-crystalline. The substitution of the hydroxyl by the azide end-group had only a negligible influence on T_m. It was about

30 °C and 55 °C for the PEG750 and PEG2000 derivatives. A T_g was only visible for the PEGs with the azide end-group (at -7.41 °C for PEG750-N3 and at 14.01 °C for PEG2000-N3). The graft copolymers were semi-crystalline, too. The T_m of each copolymer was slightly lower in comparison to that of the linear PEG (T_m = 24.00 °C for PPOS-*g*-PEG750 and T_m = 51.83 °C for PPOS-*g*-PEG2000). The glass transition temperatures were significantly lower than those of the linear PEGs with the azide end-group (T_g = -52.65 °C for PPOS-*g*-PEG750 and T_g = -3.86 °C for PPOS-*g*-PEG2000). The melting enthalpies were also considerably lower than those of the linear PEGs with both the hydroxyl and the azide end-group. This indicates a lower crystallinity or a lower energy needed for the melting of the crystalline domains. The T_c for PPOS-*g*-PEG2000 was nearly 20 °C lower related to PEG2000-OH or PEG2000-N3. Obviously, crystallization was hampered in the graft copolymer structure.

The change from a linear polymer to a graft copolymer structure as well as the LiTFSI concentration within one polymer structure have a significant impact on the morphology, T_m and T_g. The latter is addressed in the following chapter about ionic conductivity. Regarding pure PEG750-OH and PEG2000-OH as well as their SPEs, T_m and ΔH_m decreased significantly by increasing salt concentration. L750-12 and L2000-8 have already been amorphous (Fig. 31 and Table 3).

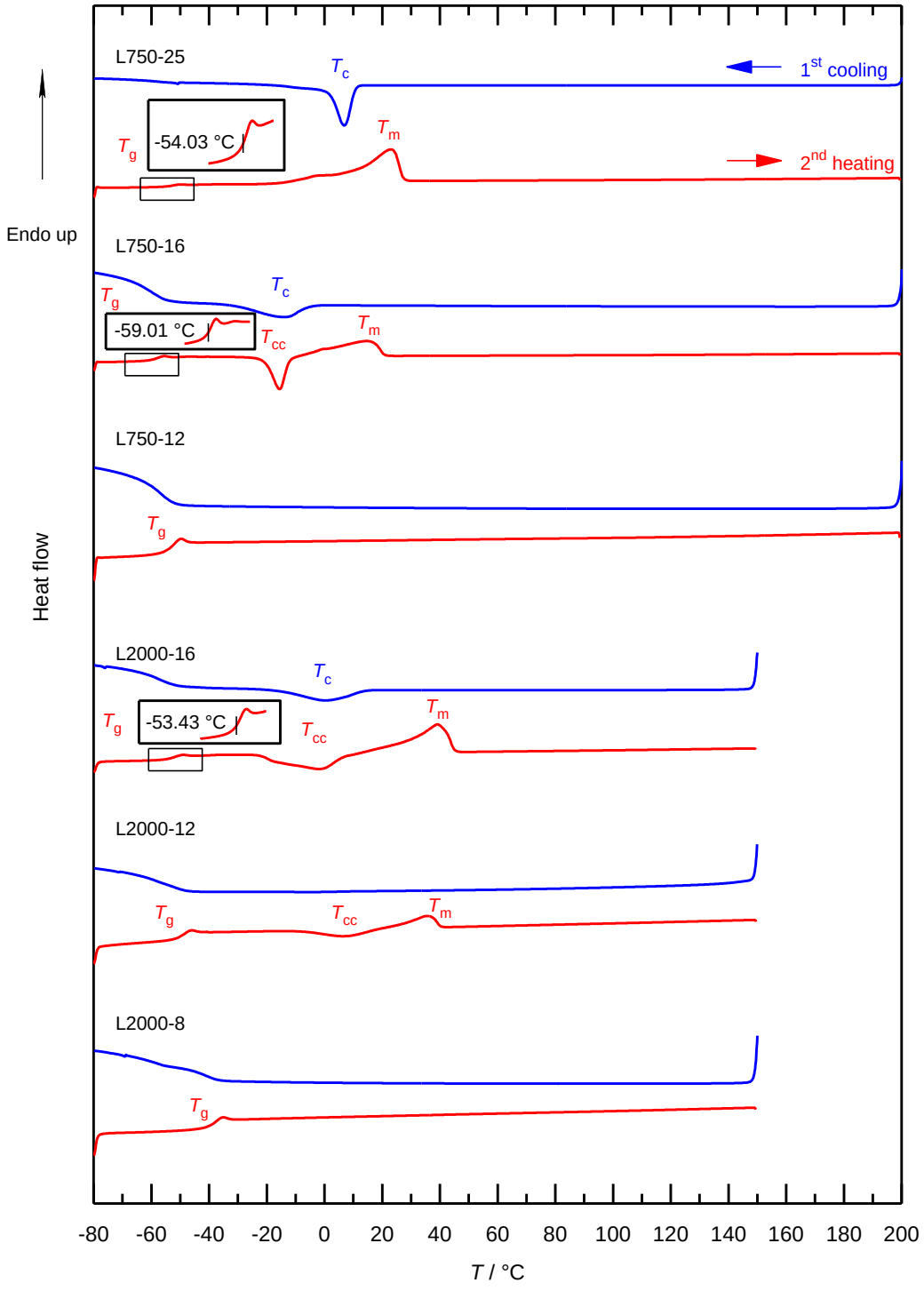

Fig. 31 First cooling (blue) and second heating (red) DSC traces of the SPEs, L750 and L2000, at different O/Li ratios (under nitrogen, 10 K min^{-1}).

While the pure PPOS-*g*-PEG750 was semi-crystalline, all its SPEs were amorphous. In the case of PPOS-*g*-PEG2000, only G2000-12 was amorphous (Fig. 32 and Table 3). T_m and ΔH_m decreased significantly by increasing salt concentration as for the linear PEG2000-OH.

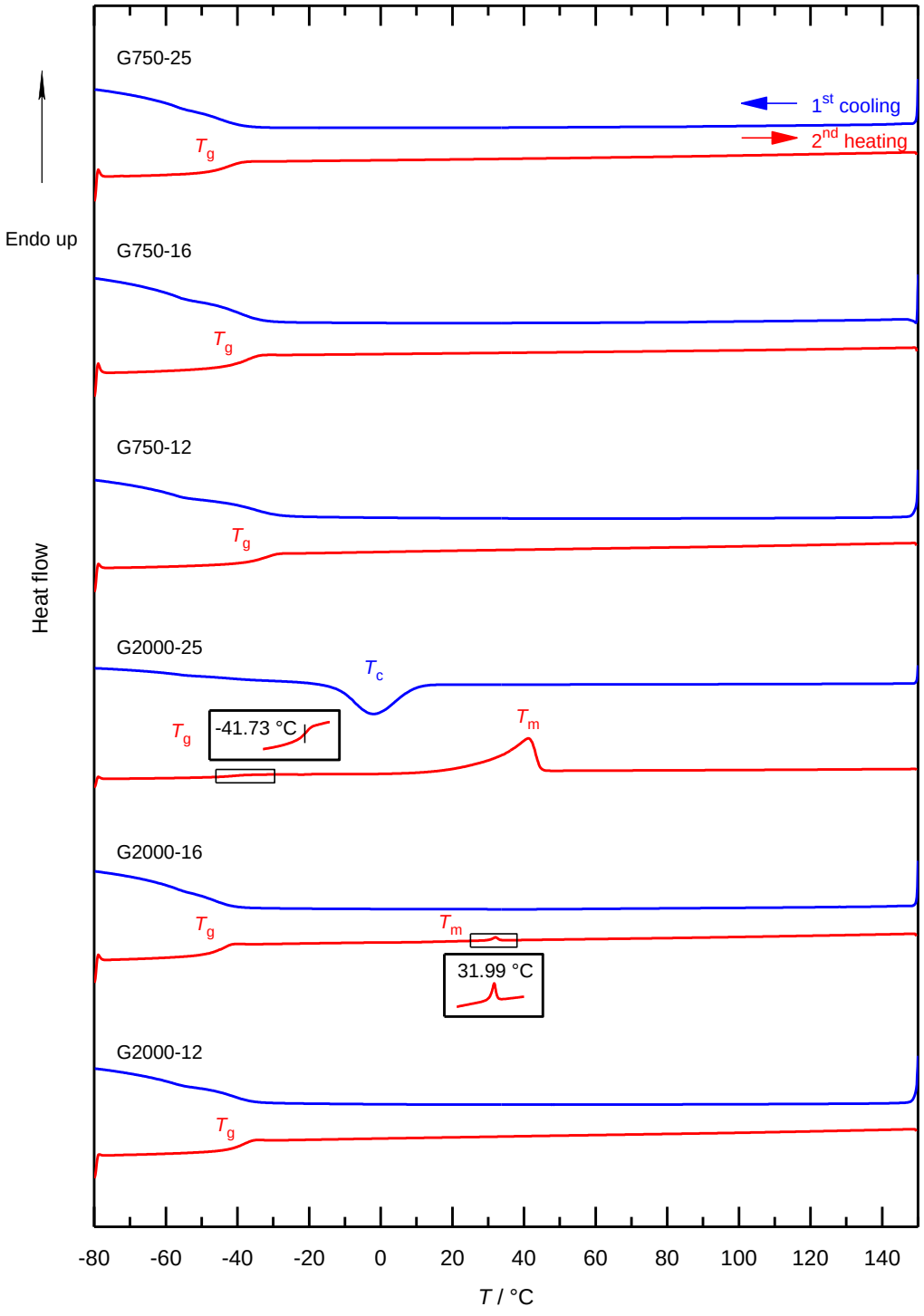

Fig. 32 First cooling (blue) and second heating (red) DSC traces of the SPEs, G750 and G2000, at different O/Li ratios (under nitrogen, 10 K min^{-1}).

In general, the T_m and the crystallinity, quantified by ΔH_m, decreased significantly by increasing salt concentration within one polymer structure. This can be attributed to the plasticizing effect of the TFSI

anion.[32,76] In each case the crystallinity, if present, and the T_m were lower for the graft copolymer SPEs in comparison to their linear counterparts at a given O/Li ratio.

3.1.4 Electrochemical properties

3.1.4.1 Ionic conductivity

According to equation (1), σ is directly proportional to n and μ. The amount of LiTFSI added to the SPE is known to have a strong effect on n and μ. Therefore, the O/Li ratio was varied to find the salt concentration with the maximum ionic conductivity. The Arrhenius plots in which typically the logarithm of σ is plotted against the inverse temperature T^{-1} are shown in Fig. 33. For each SPE, three salt concentrations were prepared so that the concentration of the SPE with the maximum ionic conductivity, ideally over the entire temperature range, was surrounded by one SPE with a higher and one SPE with a lower salt concentration.

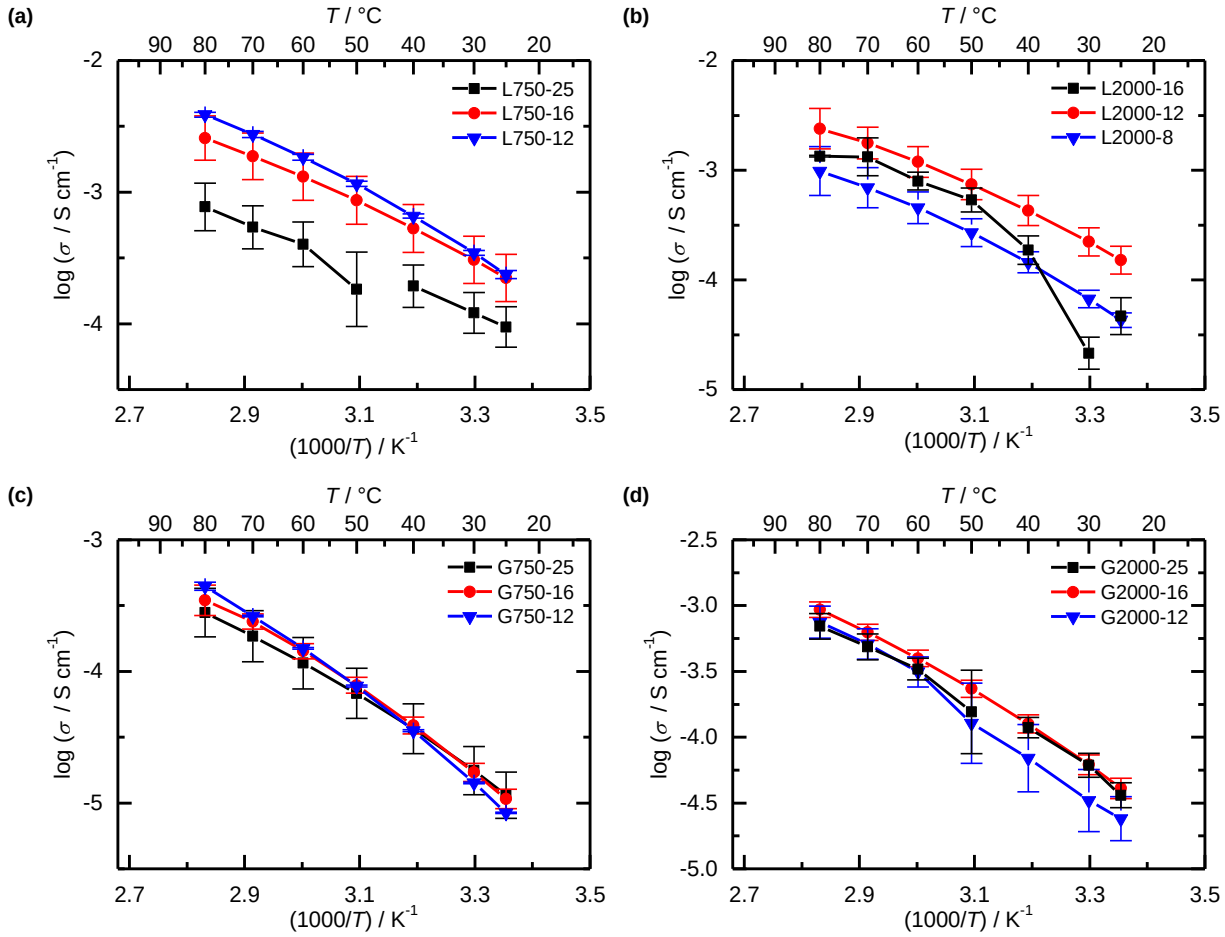

Fig. 33 Arrhenius plots for the ionic conductivity σ of the SPEs, (a) L750, (b) L2000, (c) G750 and (d) G2000 at different O/Li ratios. The error bar for log σ was calculated according to the error propagation law from the standard deviation of at least three independently measured coin cells (equation (29)). The solid lines are guides to the eye. The interruption of the solid line in the case of L750-25, L2000-16 and G2000-25 indicates the crystallization of the SPE.

The measurements were performed during cooling from 80 °C to 25 °C. The SPEs were in the amorphous melt state at 80 °C (Table 3). As can be seen by an interruption of the course of σ in the Arrhenius plot (Fig. 33), only L750-25 at 40-60 °C, L2000-16 at 25-40 °C and G2000-25 at 40-60 °C were subjected to crystallization. The crystallization temperatures determined by DSC show values below these temperature ranges (Table 3). However, the cooling rate during the ionic conductivity measurement was much lower compared to the one of the DSC measurement which caused an increase of T_c. The temperature dependency of the ionic conductivity above the crystallization temperature of the SPEs in the Arrhenius plot is exponential (Fig. 33). This indicates that the ion movement occurs not only by ion hopping processes but also via the segmental motion of the polymer chains. Arrhenius behavior is defined by a linear dependency of the ionic conductivity on the inverse temperature and by the assumption that the ion movement takes place only via ion hopping processes. This behavior might

be postulated in the case of L750-25 and G2000-25 below the crystallization temperature (below 50 °C).

The crucial parameter which affected μ in the amorphous melt state above T_c was T_g. The lower the T_g, the higher is the segmental motion of the polymer chains at a given temperature above T_g, and the higher is μ. Depending on the LiTFSI concentration, there are two known effects of the TFSI anion on T_g in the literature. On the one hand, there is the growing plasticizing effect of the TFSI anion with increasing salt concentration which lowers T_g.[32,76,162] On the other hand, the mobility of the PEG chains decreases with increasing salt concentration. The number of physical crosslinking points between the lithium ions and the oxygen atoms of the PEG chains grows which, in turn, raises T_g.[76,163] The correlation of σ with T_g at different LiTFSI concentrations is shown in Fig. 34. For the pure PEG750-OH, there was still no T_g detectable. With increasing LiTFSI concentration, the emerging T_g first decreased from L750-25 to L750-16 then increased for L750-12. The T_g of L750-12 was even higher than that of L750-25. σ increased in accordance with the plasticizing effect and the higher charge carrier concentration from L750-25 to L750-16, but then leveled off due to the growing number of physical crosslinking points. For PEG2000-OH, there was also no T_g visible. With increasing LiTFSI concentration, the appearing T_g increased from L2000-16 to L2000-8. Despite the increase of T_g caused by the higher number of physical crosslinking points, σ still increased from L2000-16 to L2000-12 due to the higher charge carrier concentration. Then, σ decreased since the growth of the number of physical crosslinking points was too distinct.

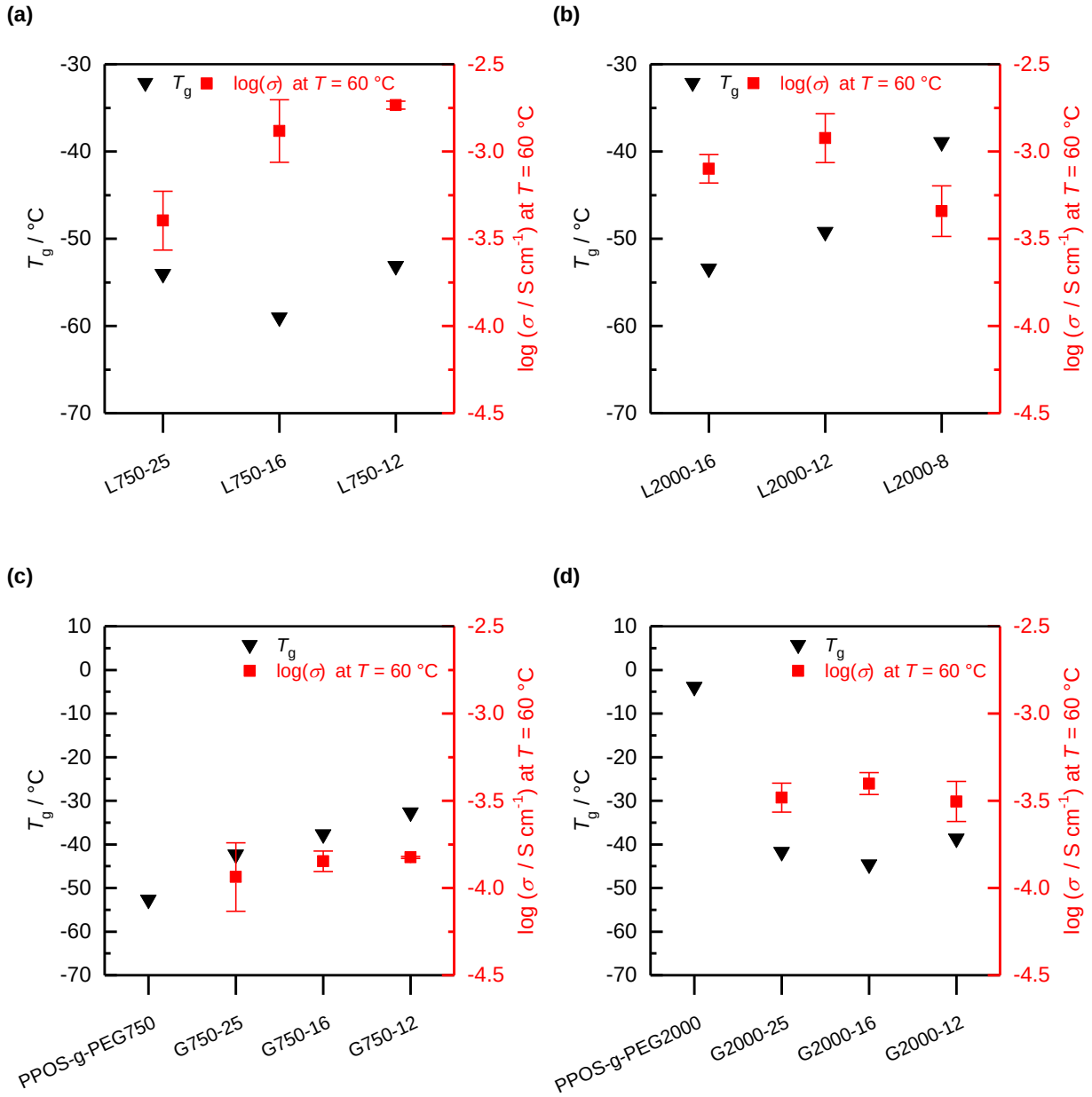

Fig. 34 Correlation of the logarithm of ionic conductivity log σ at 60 °C with the glass transition temperature T_g for the SPEs (a) L750, (b) L2000, (c) G750 and (d) G2000, arranged in the order of decreasing O/Li ratio (increasing LiTFSI concentration). For the host polymers PEG750-OH and PEG2000-OH of the SPEs, L750 and L2000, no T_g was detected. In (c) and (d), the T_g of the host polymers PPOS-*g*-PEG750 and PPOS-*g*-PEG2000 of the SPEs, G750 and G2000, is also shown. The error bar for log σ was calculated according to the error propagation law (equation (29)).

Regarding the pure PPOS-*g*-PEG750 and its SPEs, T_g increased steadily with increasing salt concentration, whereas σ remained nearly constant. The negative contribution of the increasing number of physical crosslinking points to σ was compensated by the growing number of charge carriers. Regarding the pure PPOS-*g*-PEG2000 and its SPEs, the T_g first decreased from the pure polymer to G2000-16 with increasing LiTFSI concentration and then increased for G2000-12. The T_g of

G2000-12 was even higher than that of G2000-25. Owing to the increasing charge carrier concentration and plasticizing effect from G2000-25 to G2000-16, σ increased slightly. Then, σ decreased since the physical crosslinking prevailed.

The optimum O/Li ratios with respect to a maximum ionic conductivity ideally over the entire measured temperature range were estimated as about 16 for L750, G750 and G2000 and 12 for L2000. Due to the exponential temperature dependency of the ionic conductivity in the Arrhenius plot, the usual Arrhenius equation cannot serve for a calculation of characteristic parameters (Fig. 35a).

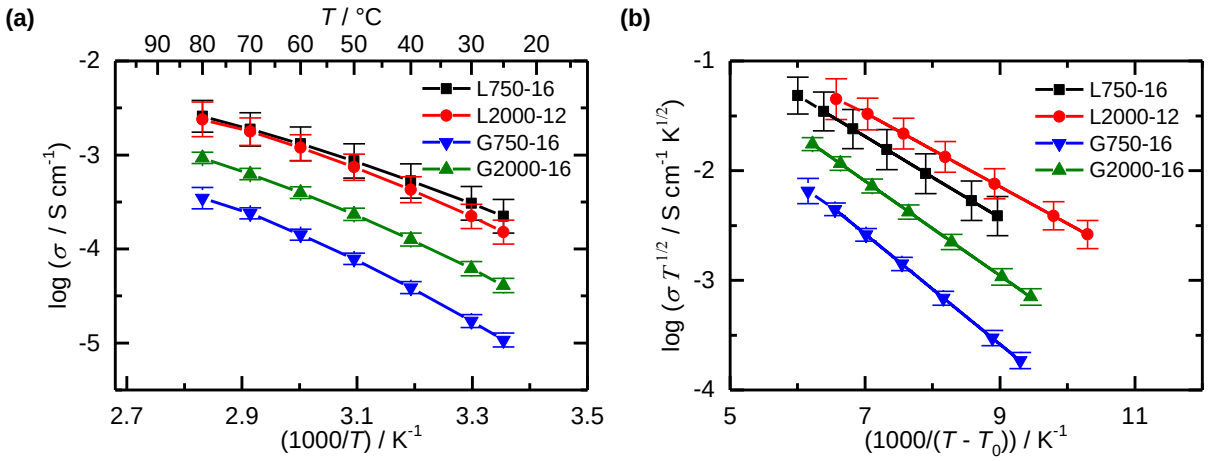

Fig. 35 (a) Arrhenius plot and (b) VTF plot for the ionic conductivity of L750-16, L2000-12, G750-16 and G2000-16 as the SPEs with the optimum O/Li ratios. The error bars for (a) log σ and for (b) log ($\sigma\ T^{1/2}$) were calculated according to the error propagation law from the standard deviation of at least three independently measured coin cells (equations (29) and (30)). The solid lines are (a) guides to the eye and (b) linear fitting curves (see Table 22 for T_0 values and Table 4 for linear fitting data).

In this case, the Vogel-Tammann-Fulcher (VTF) relation can describe the temperature dependency (equation (27)). Besides ion hopping processes the contribution of the segmental motion of the polymer chains to the ion movement is also considered.[94,164] As can be seen by the linear dependency of log ($\sigma\ T^{1/2}$) on $(T - T_0)^{-1}$ (equation (28), Fig. 35b and Table 4), the ionic conductivity followed VTF behavior.

Table 4 Linear fitting data of the VTF plot shown in Fig. 35b.

SPE-O/Li	Adjusted R^2	$m \pm \Delta m$ (10^{-2} K)	$b \pm \Delta b$ (x 10^{-2}, log of S cm^{-1} K$^{1/2}$)	$B \pm \Delta B^a$ (K)	$A_{VTF} \pm \Delta A_{VTF}{}^b$ (S cm^{-1} K$^{1/2}$)
L750-16	0.99996	-37.11 ± 0.13	90.93 ± 1.03	854.5 ± 3.1	8.12 ± 0.19
L2000-12	0.99999	-33.68 ± 0.06	88.56 ± 0.49	775.6 ± 1.3	7.68 ± 0.09
G2000-16	0.99997	-43.15 ± 0.09	92.58 ± 0.68	993.5 ± 2.1	8.43 ± 0.13
G750-16	0.99999	-50.31 ± 0.06	94.50 ± 0.43	1158.5 ± 1.3	8.81 ± 0.09

[a]Calculated by equations (31) and (33). [b]Calculated by equations (32) and (34).

The thermodynamic Kauzmann temperature T_0 represents a reference temperature which is usually associated with the disappearance of the free volume in the polymer matrix and thus at which the ionic mobility becomes zero.[165] Since polymer electrolytes do not behave as ideal glasses during typical cooling rates, their T_0 value is usually lower than T_g. Typical values for T_0 in the literature are 30 K,[94] 50 K or even further below T_g.[164] This behavior was also observed for the SPEs in this study. Whereas T_0 was slightly higher than T_g – 30 K for the linear PEG SPEs, the graft copolymer SPEs showed values lower than T_g – 30 K. For G750-16 it was even T_g – 50 K (Table 22 and Fig. 36a).

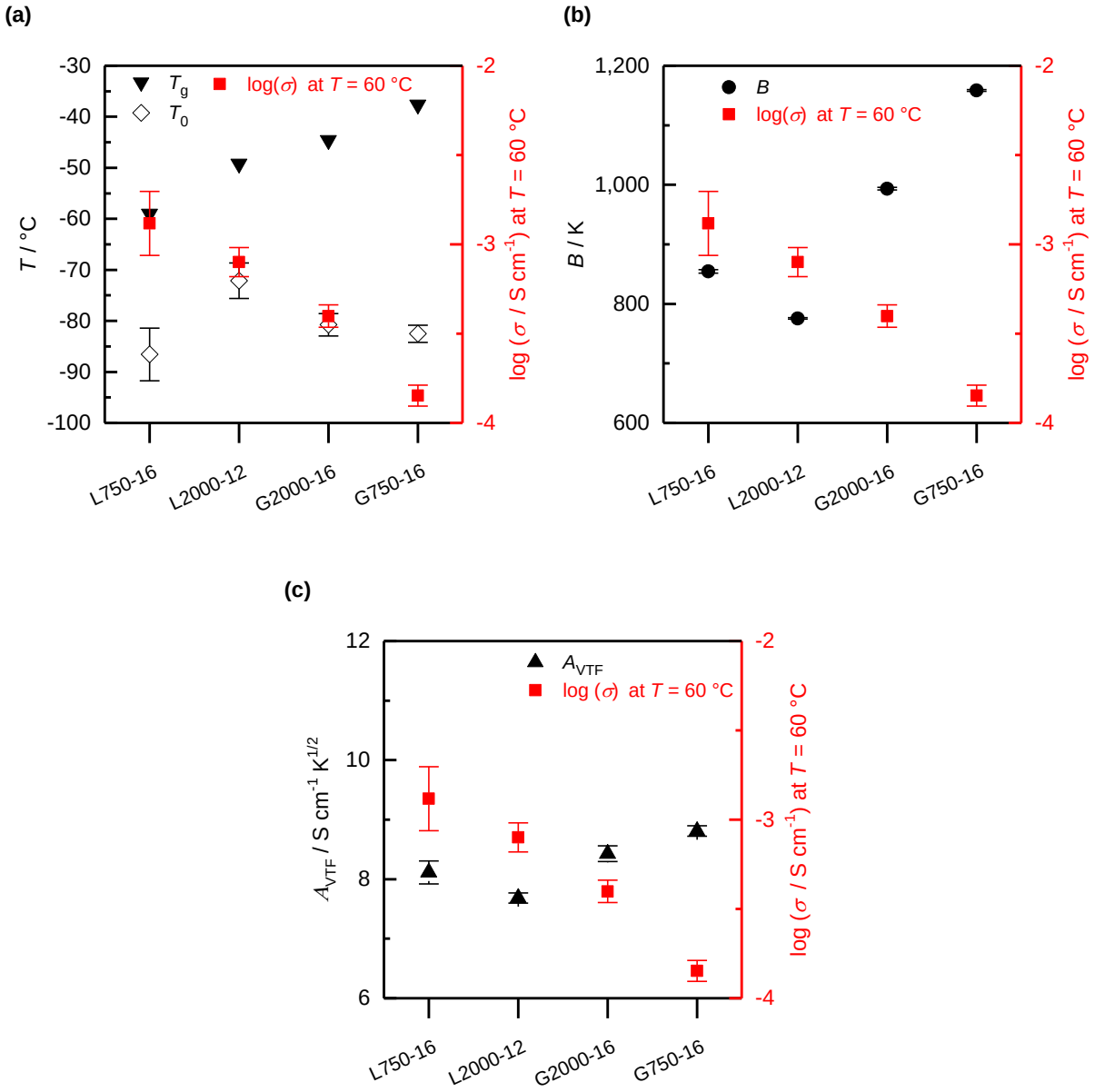

Fig. 36 Correlation of the logarithm of ionic conductivity log σ at 60 °C (a) with the glass transition temperature T_g and the thermodynamic Kauzmann temperature T_0, (b) with the material-dependent constant B and (c) with the pre-exponential factor A_{VTF} for L750-16, L2000-12, G750-16 and G2000-16 arranged in the order of decreasing ionic conductivity. The error bars for log σ, B and A_{VTF} were calculated according to the error propagation law (equations (29), (33) and (34)).

The material-dependent constant B and the pre-exponential factor A_{VTF} can be derived from the slope m and the intercept b of the linear form of the VTF equation (equations (31) to (34), Table 4). B equates a pseudo-activation energy needed for the ion movement between two energetic sites coupled with the chain dynamics. A_{VTF} is often related to the charge carrier concentration.[94,164,165] The dependencies of B and A on the SPEs and their correlation with the ionic conductivity are depicted in Fig. 36b and c.

The T_g increased according to the order L750-16, L2000-12, G2000-16 and G750-16 while the ionic conductivity decreased (Fig. 36a). Although the T_g of L2000-12 is higher than that of L750-16 and one might expect a higher energy needed for ion movement due to a lower chain dynamics, *B* is slightly lower for L2000-12. The reduced number of hydroxyl end-groups could facilitate the ion movement. From the literature it is known that the polar hydroxyl end-group has stronger interactions with the ions than the ethylene oxide repeating unit,[166,167] and thus might act as a kind of coordinating ion trap. Nevertheless, the ionic conductivity is slightly lower regarding L2000-12 due to the reduced number of charge carriers indicated by a decrease of A_{VTF}.

As expected from the course of the T_g, *B* is significantly higher for the graft copolymer than for the linear PEG SPEs. A shorter PEG side-chain increases the T_g and *B* at the same O/Li ratio (T_g and *B* are higher for G750-16 in relation to G2000-16). In addition, the higher amount of non-conductive polymer backbone might also hinder the ion movement and thus increases *B*. This applies for the graft copolymer compared to the linear PEG SPEs and for G750-16 compared to G2000-16.

The high *B* values of the graft copolymer SPEs were decisive for the decline of the ionic conductivity. Although their charge carrier concentrations expressed by A_{VTF} were slightly higher than those of the linear PEG SPEs. The higher value of A_{VTF} for the graft copolymer SPEs and for G750-16 compared to the linear PEG SPEs and G2000-16, respectively, can be explained by the higher content of TR groups. The latter support the dissociation of LiTFSI due to their high dielectric constant which is 40.5 at 24 °C for 1,2,3-triazole.[98]

3.1.4.2 Electrochemical stability

The electrolytes used in LIBs must be electrochemically stable within the operating potential range. This range is defined by the potential difference between the cathode and anode material. The electrochemical stability window of the SPEs was determined by cyclic voltammetry (CV) at 70 °C using a copper working and a lithium reference/counter electrode. A potential range between -0.2 V and 3.7 V vs. Li/Li^+ was scanned twice at a scan rate of 1 mV s^{-1}. A scan rate of 2 mV s^{-1} had to be applied for L750-16 since 1 mV s^{-1} resulted only in noisy data. The graft copolymer SPEs have a comparable electrochemical stability to the linear PEG SPEs and to similar PEG/LiTFSI electrolytes from the literature.[32,92] They were electrochemically stable against oxidation up to 3 V vs. Li/Li^+ (Fig. 37).

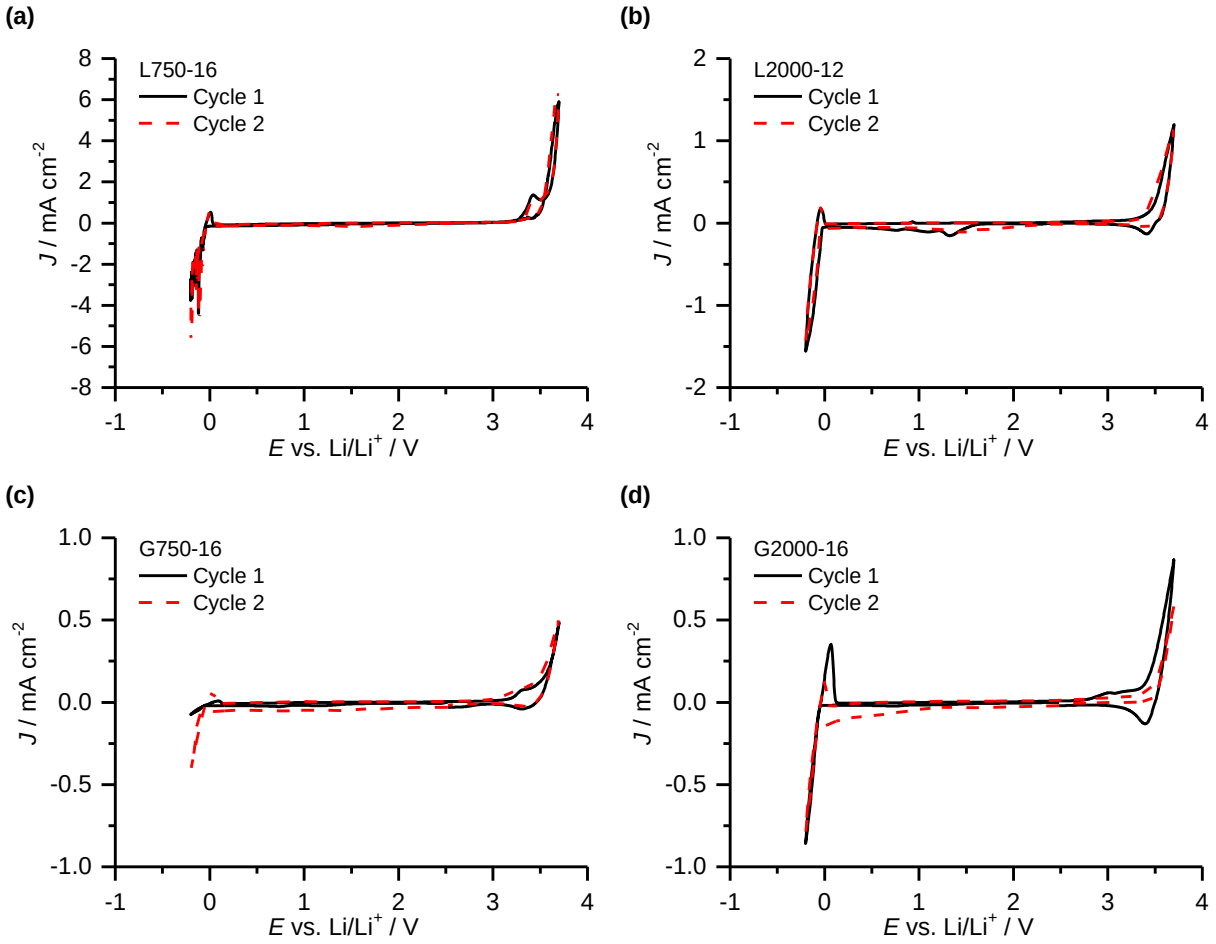

Fig. 37 Cyclic voltammograms vs. Li/Li$^+$ of (a) L750-16 (2 mV s^{-1}), (b) L2000-12 (1 mV s^{-1}), (c) G750-16 (1 mV s^{-1}) and of (d) G2000-16 (1 mV s^{-1}). The measurements were performed at 70 °C. All SPEs were electrochemically stable up to 3 V vs. Li/Li$^+$. Lithium plating and stripping at the copper electrode occurring around 0 V vs. Li/Li$^+$ was observed for all SPEs.

Furthermore, only negligible reduction peaks were observed for the graft copolymer SPEs in the first cycle during scanning in the negative potential direction. In the second cycle, a small reduction current was detected between 2 and 0 V vs. Li/Li$^+$. Since this cathodic current was not observed during the first cycle, these electrochemical reactions are attributed to the reduction of species which were oxidized previously in the first cycle above 3 V vs. Li/Li$^+$.

During scanning in the negative direction, an intense cathodic peak occurred below 0 V vs. Li/Li$^+$ for all SPEs. This peak could be attributed to lithium plating onto the copper electrode as it is typically observed for PEG electrolytes with LiTFSI as a salt.[61,168] On the reverse scan, a subsequent oxidation peak was observed at around 0 V vs. Li/Li$^+$ indicating that the reversible process happened, the lithium stripping from the working electrode. Both processes are of major importance for the application of the SPEs in LIBs. During charging and discharging the battery, lithium ions have to be deposited on the anode from the electrolyte, and extracted from the anode into the electrolyte, respectively.

Having a closer look at the lithium plating/stripping process, there was no effect of the polymer structure change on the nucleation overpotential η (Table 5).

Table 5 The nucleation overpotential η and the anodic peak potential E_{pa} deduced from the cyclic voltammograms in Fig. 37.

SPE-O/Li	Cycle	η (V vs. Li/Li$^+$)	E_{pa} (V vs. Li/Li$^+$)
L750-16	1	-0.03	0.01
	2	-0.03	0.00
L2000-12	1	-0.02	-0.04
	2	-0.03	-0.04
G750-16	1	-0.03	0.09
	2	-0.07	0.03
G2000-16	1	-0.03	0.07
	2	-0.05	0.00

For both SPE types, η was around -0.03 V vs. Li/Li$^+$ in the first cycle. The anodic peak potential E_{pa} of the first cycle was slightly higher for the graft copolymer SPEs but still comparable with those of the linear PEG SPEs. In the second cycle, η and E_{pa} of the graft copolymer SPEs were only slightly shifted to lower values. In general, the measured current densities were higher for the linear PEG SPEs compared to the graft copolymer SPEs which very likely resulted from the higher ionic conductivity of the linear PEG SPEs.

3.1.4.3 Lithium ion transference number

The lithium ion transference number of L750-16, L2000-12, G750-16 and G2000-16 was determined by the Bruce-Vincent (BV) method (t^+_{BV}) and according to Watanabe *et al.* (t^+_W) at 70 °C as presented in chapters 1.3 and 4.6.3 (Fig. 38 and Table 6).

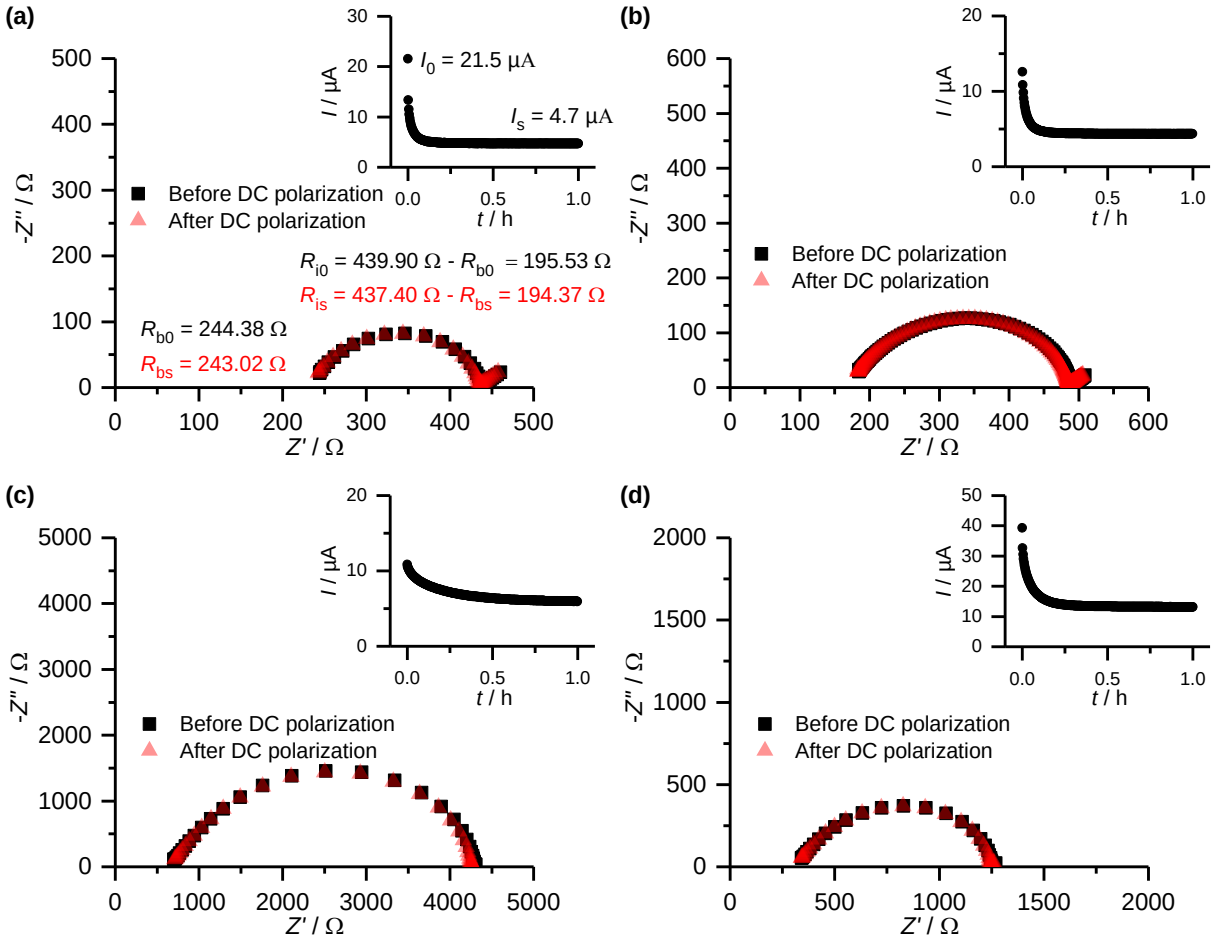

Fig. 38 Potentiostatic electrochemical impedance spectroscopy before and after the direct current (DC) polarization at 70 °C for (a) L750-16, (b) L2000-12, (c) G750-16 and (d) G2000-16 to determine the lithium ion transference number.

In the BV method, the initial current I_0 can be read off directly from the *I*-*t* curve (inset of Fig. 38a). However, these values differ from the calculation according to Ohm's law $I_\Omega = \Delta V/(R_{b0} + R_{i0})$,[42] especially for L2000-12 (compare I_0 and I_Ω in Table 6). Therefore, this method may contain errors, if I_0 is measured too late during the polarization. Then I_0 is shifted to lower values and thus t^+_{BV} to higher values. Therefore, I_0 for t^+_{BV} was calculated based on Ohm's law. Both methods are sensitive to ion-pairs and bigger aggregates deviating from free lithium ions.[42,49]

Table 6 Parameters extracted from Fig. 38 for the calculation of the lithium ion transference number t^+ according to the Bruce-Vincent (BV) and the Watanabe (W) method.

SPE-O/Li	R_{b0} (Ω)	R_{i0} (Ω)	ΔV (mV)	I_0 (µA)	I_Ω[a] (µA)	I_s (µA)	R_{bs} (Ω)	R_{is} (Ω)	t^+_{BV}[b]	t^+_W[c]
L750-16	244.38	195.53	10	21.5	22.7	4.7	243.02	194.37	0.13	0.13
L2000-12	184.88	305.94	10	12.6	20.4	4.3	183.80	304.04	0.09	0.09
G750-16	702.87	3607.37	50	10.8	11.6	6.0	712.75	3556.41	0.15	0.15
G2000-16	341.36	915.51	50	39.4	39.8	13.2	341.62	908.98	0.12	0.12

[a]Calculated according to $\Delta V/(R_{b0} + R_{i0})$. [b]Calculated by equation (11) and using I_Ω instead of I_0. [c]Calculated by equation (12).

The t^+_{BV} and t^+_W values showed excellent agreement and were all around 0.12 ± 0.03 (Table 6). The different polymer structures have no visible influence on t^+.

In general, the lithium ion transference number is dependent on the molecular weight of the polymer, the polymer end-groups, the measuring temperature, the determination method and the salt concentration. A comparison of the measured values with literature values is challenging.[42,49,169,170] In the following, some references for linear PEG/PEO electrolytes with LiTFSI are listed.

Timachova *et al.* determined the lithium ion transference number by pulsed field gradient-NMR at 90 °C.[170] It was 0.36 for PEG with a molecular weight of 600 g mol^{-1} and O/Li = 12.5. For PEG with a molecular weight of 2000 g mol^{-1}, a lithium ion transference number of 0.26 for O/Li = 12.5 was measured. Both values were higher than 0.13 for L750-16 and 0.09 for L2000-12, although their molecular weights were quite close. The differences might be attributed to the different end-groups, measuring temperature and method.

In a work of Pożyczka *et al.*, t^+_{BV} for PEO with a molecular weight of 5 x 10^6 g mol^{-1} was about 0.22 for O/Li = 16 and 0.12 for O/Li = 10 at 70 °C.[49] The t^+_W was about 0.28 for O/Li = 16 and 0.18 for O/Li = 10. For PEG with a lower molecular weight of 5000 g mol^{-1} and with hydroxyl end-groups on both sides, t^+_W was lower (0.11 for O/Li = 16 and 12 at 90 °C). This value is comparable to the ones determined in a previous study[42] and to this thesis.

3.2 The effect of fluorination on chain transfer reactions in the radical polymerization of oligo ethylene glycol ethenesulfonate monomers

3.2.1 Syntheses and characterization of ethenesulfonate monomers

The synthesis of different ethenesulfonate (ES) monomers with alkyl, halogenated alkyl, phenyl, cyclohexylmethyl and norbornenylmethyl groups, for example, has been described in the

literature.[140,141,171–174] Fujigaya *et al.* showed that the simultaneous dehalogenation and esterification of 2-chloroethanesulfonyl chloride with the corresponding alcohol in the presence of pyridine as a base is possible in a one-pot synthesis and in good yield.[171] Similar to this procedure the oligo ethylene glycol ES monomers EG1ES and EG3ES as well as the fluorinated ES monomers FEG2ES and FEG3ES with triethylamine were synthesized (Scheme 8a). EES was synthesized for a comparison of its polymerization behavior with these monomers and for a determination of the molecular weight and the end-groups of its polymer PEES by MALDI-ToF MS. It had been already polymerized successfully in the literature.[140–142]

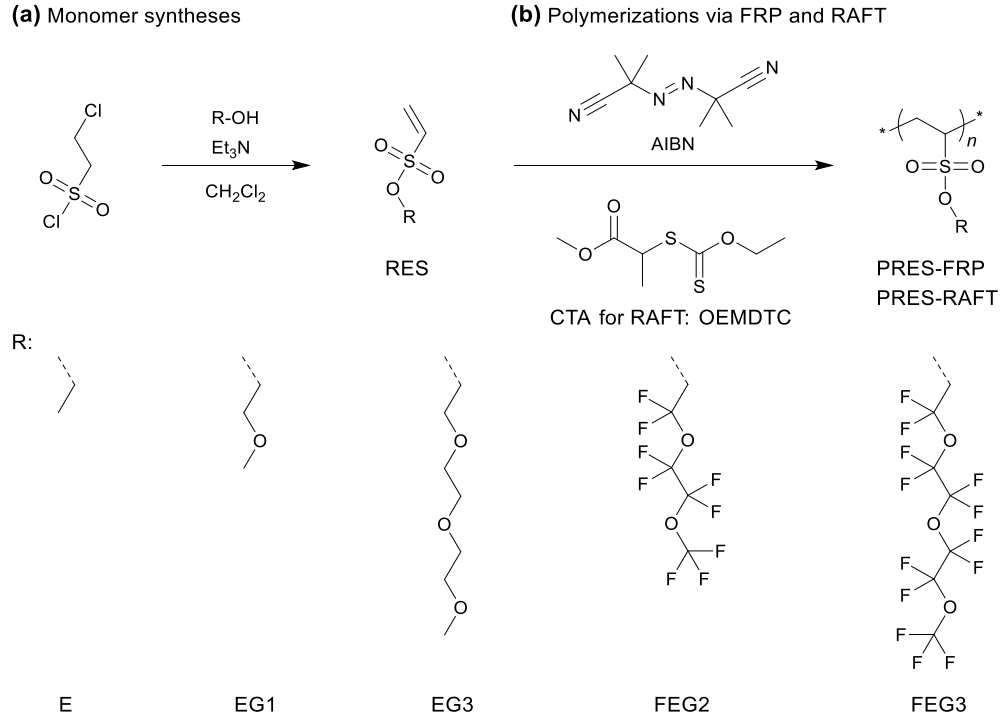

Scheme 8 (a) Syntheses of ethenesulfonate (ES) monomers and (b) their polymerizations via conventional free radical polymerization (FRP) and reversible addition-fragmentation chain transfer (RAFT) by using AIBN as a thermal initiator and *O*-ethyl-*S*-(1-methoxycarbonyl) ethyldithiocarbonate (OEMDTC) as a CTA.

Whereas EG3ES had to be purified by flash chromatography, EG1ES, FEG2ES and FEG3ES could be still isolated by vacuum distillation making an easy up-scaling up to more than 30 g with overall high yields of 60-80% possible. All products were obtained in high purity as proved by ^{1}H, ^{13}C and ^{19}F NMR spectroscopy. All the expected NMR signals could be well assigned (NMR spectra in chapter 4.4.1.2). The ^{1}H NMR signals of FEG3ES compared with the signals of EG3ES shift downfield due to the electron withdrawing effect of the fluorine substituents.

By ^{1}H NMR spectroscopy the formation of ethanesulfonate ethers (2FEG2ES and 2FEG3ES) as the main by-products during the synthesis of the fluorinated ES monomers was identified (Scheme 9,

Fig. 73 and Fig. 76). It follows that the fluorinated alcohols FEG2 and FEG3 seem to possess a higher acidity compared to their non-fluorinated analogs due to the electron withdrawing difluoromethyl groups. Therefore, they could react with already formed product (FEG2ES and FEG3ES) by a nucleophilic addition (A_N). The -M effect of the sulfonate group and the electron withdrawing effect of the fluorinated ether promoted the nucleophilic attack of the alcohol and stabilized the carbanion formed during the A_N.

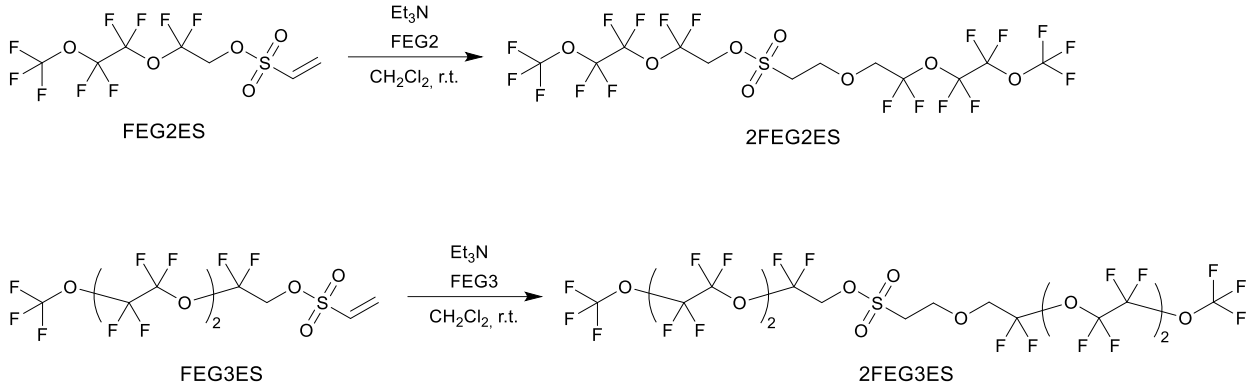

Scheme 9 Formation of the ethanesulfonate ethers 2FEG2ES and 2FEG3ES as the main by-products arising during the synthesis of FEG2ES and FEG3ES, respectively, via an A_N reaction.

3.2.2 Conventional free radical polymerization and characterization

First, the polymerization behavior of the five ethenesulfonate monomers (ES) under conventional free radical polymerization (FRP) conditions in bulk using AIBN as a thermal initiator (I) at 60 °C was studied (Scheme 8b). The ratio $[M]_0/[I]_0$ was adjusted to 500/1 for EES and 100/1 for the other monomers, EG1ES, EG3ES, FEG2ES and FEG3ES (Table 7). To compare the results from RAFT polymerization with the literature[141] in the following chapter and to use the same ratio $[M]_0/[I]_0$ for the conventional free radical polymerization as for RAFT, 500/1 was used for EES. A lower initiator concentration for EES could be used since it exhibits a higher polymerization rate in comparison to the other monomers.

Table 7 Conventional free radical polymerization (FRP) of the five ethenesulfonate (ES) monomers in bulk at 60 °C using AIBN as a thermal initiator (I).

Polymer	$[M]_0/[I]_0$	Time (h)	*conv.*[c] (%)	$M_{n,\,SEC}$ (g/mol)	$Đ$	$M_{p,\,SEC}$ (g/mol)
PEES-FRP[a]	500/1	24[b]	82	6,900[d]	2.10[d]	15,700[d]
PEG1ES-FRP[a]	100/1	24	31	1,400[d]	1.62[d]	2,200[d]
		48	38	1,400[d]	1.62[d]	2,300[d]
PEG3ES-FRP[a]	100/1	24	19	1,200[d]	1.30[d]	1,400[d]
		48	24	1,100[d]	1.28[d]	1,300[d]
PFEG2ES-FRP[a]	100/1	19[b]	71	12,100[e+f]	2.72[e+f]	11,200[e+f]
PFEG3ES-FRP[a]	100/1	21[b]	79	5,900[e+f]	3.38[e+f]	10,900[e+f]
PFEG3ES-FRP-UP[g]	100/1	29	50	8,500[e]	1.87[e]	11,700[e]

[a]Data measured from the crude reaction mixture. [b]Already highly viscous reaction mixture. [c]Determined by ^{1}H NMR spectroscopy and calculated according to equation (22). [d]Determined by SEC using THF as an eluent and calibrated with linear PS standards. [e]Determined by SEC using HFIP containing 0.5 wt% KTFA as an eluent and calibrated with PMMA standards. [f]Multimodal molecular weight distribution. [g]Up-scaling of PFEG3ES-FRP using a long tube reactor with a magnetic stirring bar extension paddle; data measured from purified product.

In accordance with the literature[141] EES showed a monomer conversion > 80% after 24 h. The number average molecular weight estimated by size-exclusion chromatography (SEC), $M_{n,\,SEC}$, was nearly 7,000 g/mol with a dispersity of $Đ$ = 2.10 (Fig. 39a). SEC served only as a relative technique here and yielded no absolute molecular weights due to the different hydrodynamic volumes for the same molecular weight of PS used for the calibration and PEES. A universal calibration for the SEC would be helpful at this point to obtain the absolute molecular weights and should be used in further studies. The focus in this study was on the determination of the absolute molecular weight by MALDI-ToF MS. From a comparison of the molecular weights determined by SEC and MALDI-ToF MS in the following chapter for the RAFT polymerization of EES, it is obvious that an $M_{n,\,SEC}$ of nearly 7,000 g/mol pointed out, that not only oligomers, but also longer chains were formed.

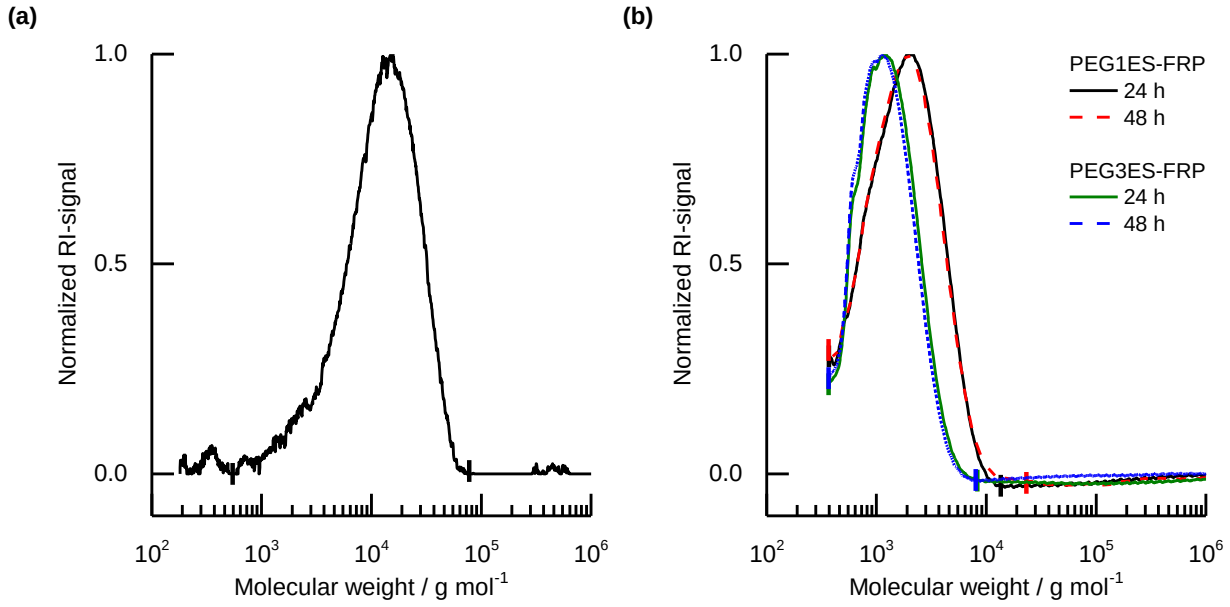

Fig. 39 SEC molecular weight distributions of (a) crude PEES-FRP after a reaction time of 24 h and of (b) crude PEG1ES- and PEG3ES-FRP each after a reaction time of 24 h and 48 h. The syntheses were performed by FRP in bulk at 60 °C using AIBN as a thermal initiator. The measurements were performed with THF as an eluent and PS standards for calibration. (b) The traces were limited by the PS calibration to 366 g/mol in the low molecular weight region.

In contrast to EES, the monomer conversion was smaller for the oligo ethylene glycol monomers (< 40% for EG1ES and < 25% for EG3ES after a reaction time of 48 h). There was no significant increase in viscosity as being typical for the formation of high molecular weight polymers. The $M_{n,\,SEC}$ values were lower than 1,500 g/mol for the polymerizations of EG1ES and EG3ES revealing that only oligomers were formed (Fig. 39b). Again, SEC is a relative technique here, because PS was used for the calibration. Therefore, MALDI-ToF MS was used to determine the absolute molecular weight of PEG1ES-FRP (Fig. 40a) and of PEG3ES-FRP (Fig. 40b). As can be seen from the MALDI-ToF MS spectra, only oligomers were formed.

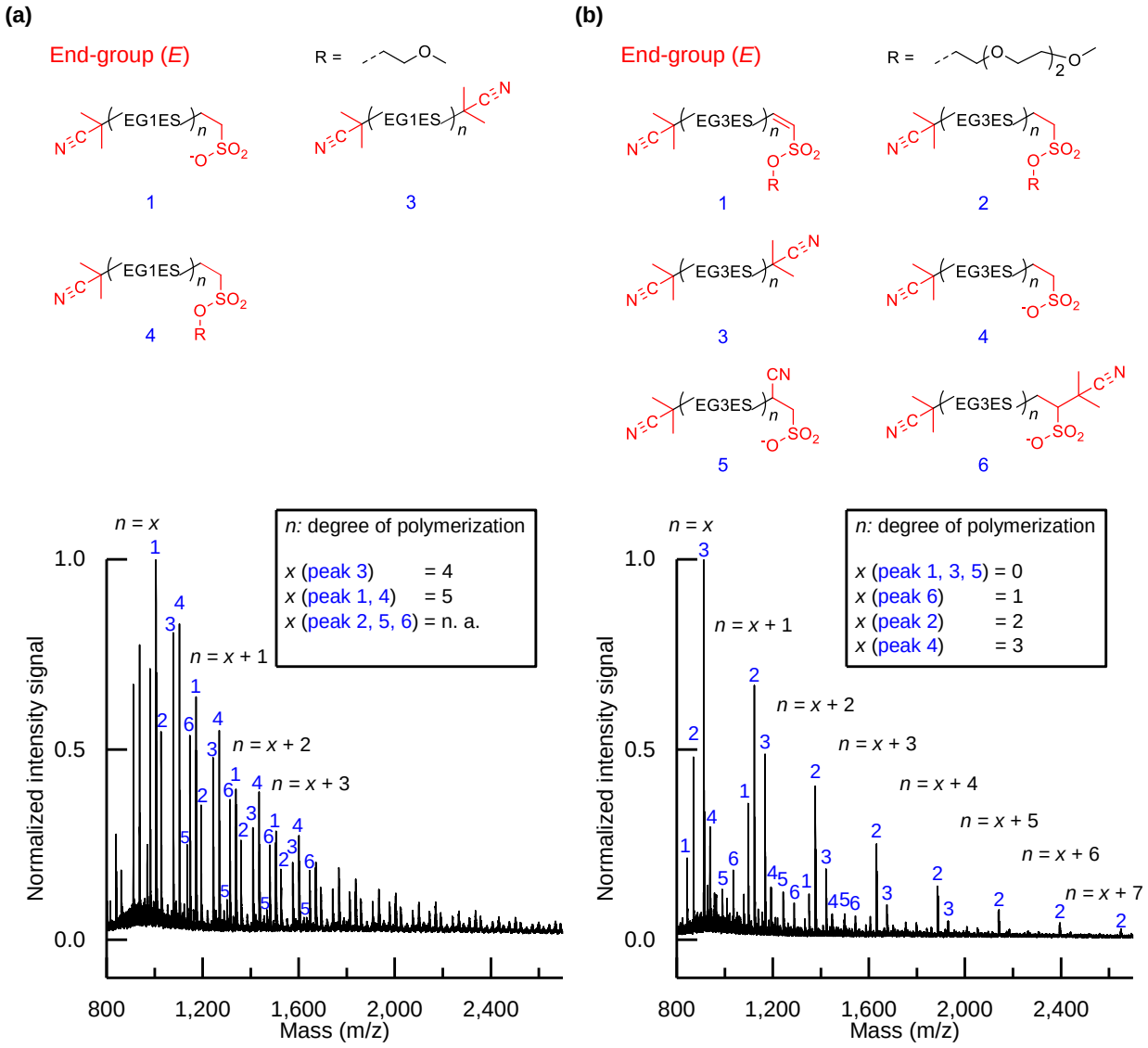

Fig. 40 MALDI-ToF MS spectrum of crude (a) PEG1ES-FRP and (b) PEG3ES-FRP synthesized by FRP in bulk at 60 °C using AIBN as a thermal initiator after a reaction time of 24 h. The measurements were performed in reflectron negative mode with DCTB as a matrix.

A detailed end-group analysis by MALDI-ToF MS of PEG1ES-FRP (Table 8) and of PEG3ES-FRP (Table 9) revealed reasons for possible termination and chain transfer reactions. The best resolution for the MALDI-ToF MS spectra was received when they were measured in reflectron negative mode using DCTB as a matrix. A high amount of adduct ions with the matrix was detected. Especially hydrogen terminated end-groups were found (peak numbers 1 and 4 for PEG1ES-FRP and peak numbers 2 and 4 for PEG3ES-FRP). Furthermore, end-groups derived from recombination could be assigned (peak number 3 for PEG1ES-FRP and peak numbers 3 and 6 for PEG3ES-FRP). The main peak 3 of the first peak series (degree of polymerization $n = 0$) for PEG3ES-FRP arose from a recombination of two isobutyronitrile radicals.

Table 8 End-group analysis of crude PEG1ES-FRP synthesized by FRP in bulk at 60 °C using AIBN as a thermal initiator after a reaction time of 24 h. The measurement was performed in reflectron negative mode with DCTB as a matrix.

Peak number	Observed mass[a] (m/z)	Mass of end-group E^b (m/z)	Calculated mass[c] (m/z)
1	176.0	176.23	$[E^-]^-$ = 176.2
2	n.a.	n.a.	n.a.
3	413.0	136.22	$[E + CN^- + DCTB]^-$ = 412.6
4	272.9	235.31	$[E + K^+ - 2 \times H^+]^-$ = 272.4
5	n.a.	n.a.	n.a.
6	n.a.	n.a.	n.a.

[a]See Table 17 for raw data. Isotopic mean values of the end-groups averaged for each peak series shown in Fig. 40a. [b]M_{EG1ES} = 166.20 g/mol. [c]M_{DCTB} = 250.34 g/mol. n.a. = not assigned.

Table 9 End-group analysis of crude PEG3ES-FRP synthesized by FRP in bulk at 60 °C using AIBN as a thermal initiator after a reaction time of 24 h. The measurement was performed by MALDI-ToF MS in reflectron negative mode with DCTB as a matrix.

Peak number	Observed mass[a] (m/z)	Mass of end group E^b (m/z)	Calculated mass[c] (m/z)
1	843.6	321.41	$[E + Na^+ + 2 \times DCTB - 2 \times H^+]^-$ = 843.1
2	361.2	323.41	$[E + K^+ - 2 \times H^+]^-$ = 360.5
3	913.9	136.22	$[E + CN^- + 3 \times DCTB]^-$ = 913.3
4	176.2	176.23	$[E^-]^-$ = 176.2
5	990.1	201.24	$[E^- + K^+ + 3 \times DCTB\text{-}H^+]^-$ = 990.4
6	781.6	243.34	$[E^- + K^+ + 2 \times DCTB\text{-}H^+]^-$ = 782.1

[a]See Table 18 for raw data. Isotopic mean values of the end-groups averaged for each peak series shown in Fig. 40b. [b]M_{EG3ES} = 254.30 g/mol. [c]M_{DCTB} = 250.34 g/mol.

Hydrogen terminated end-groups (**III** in Scheme 10) can either arise from disproportionation or chain transfer reactions from the propagating sulfonate ester radical (**I** or **V**). The amount of disproportionation derived end-groups containing a double bond (the remaining peak numbers 2, 5 and 6 at the most for PEG1ES-FRP and peak number 1 for PEG3ES-FRP) could not explain the high amount of hydrogen terminated end-groups. From this observation the conclusion follows that chain transfer reactions were the main reason for the low monomer conversions and for the formation of only low molecular weight oligomers.

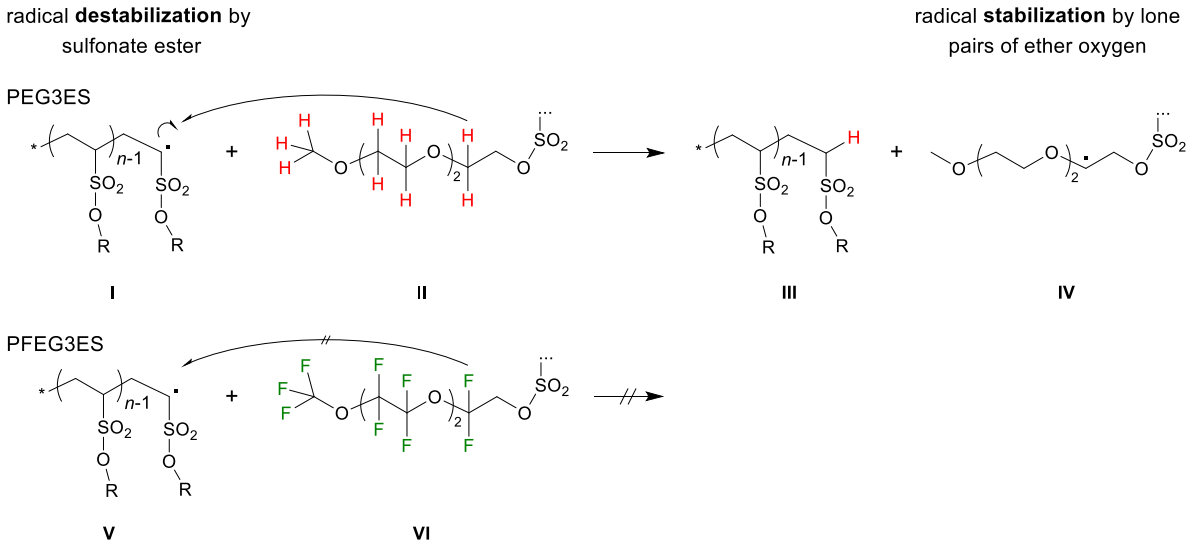

Scheme 10 Proposed mechanism of possible chain transfer reactions from a destabilized propagating sulfonate ester radical (**I**) to a monomer, another polymer or the same propagating polymer (**II**) exemplarily shown for PEG3ES. The chain transfer resulted in hydrogen terminated polymer chains (**III**) and radicals stabilized by adjacent lone pairs of ether oxygens (**IV**). By the replacement of the methylene ether and methoxy hydrogens (in red) by fluorine atoms (in green) as is the case for PFEG3ES (**V** and **VI**), the chain transfer reactions were suppressed from this sites due to the more stable carbon-fluorine bond. The radicals being located adjacent to the oxygen atoms (**IV**) probably recombine (*e.g.* with an isobutyronitrile radical) before they were able to re-initiate a monomer. The latter would result again in a relatively unstable sulfonate ester radical.

Chain transfer reactions could result from hydrogen abstraction from methylene ether and methoxy groups in the monomers EG1ES and EG3ES or their respective polymers (**II**). Therefore, the two fluorinated oligo ethylene glycol ethenesulfonate monomers, FEG2ES and FEG3ES, were synthesized and polymerized. The hydrogens were replaced by fluorine atoms to suppress possible chain transfer reactions due to the more stable carbon-fluorine bond (**VI**). And in fact, these monomers showed significantly higher monomer conversions and molecular weights. The monomer conversions have already been higher than 70% after 19 h for FEG2ES and after 21 h for FEG3ES accompanied by a significant increase in viscosity of the reaction mixture. For the estimation of the molecular weight, unlike for all non-fluorinated polymers, SEC with HFIP (with 0.5 wt% KTFA) as an eluent and PMMA standards for the calibration was used since the fluorinated polymers were only soluble in fluorinated solvents. Molecular weight distributions were multimodal and broad (Fig. 41a). $M_{p,\,SEC}$ values were higher than 10,000 g/mol. As shown in the next chapter for the RAFT polymerization of FEG2ES and FEG3ES, absolute molecular weights determined by MALDI-ToF MS were higher than those estimated by HFIP-SEC.

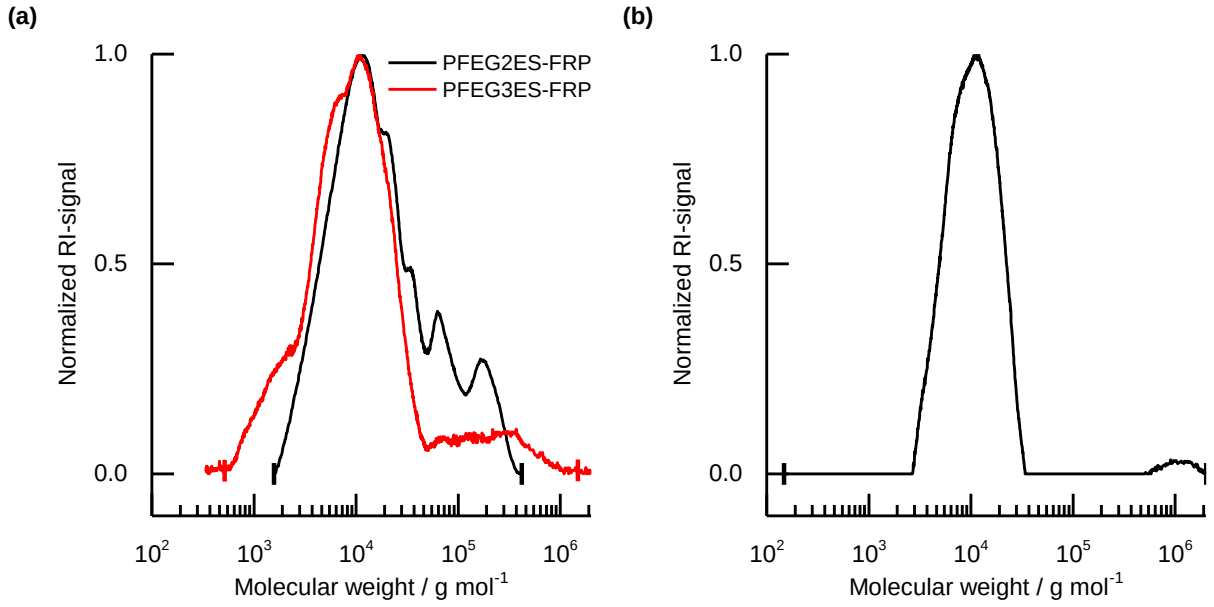

Fig. 41 SEC molecular weight distributions of (a) crude PFEG2ES-FRP and PFEG3ES-FRP and of (b) purified PFEG3ES-FRP-UP synthesized by FRP in bulk at 60 °C using AIBN as a thermal initiator. The measurements were performed with HFIP (with 0.5 wt% KTFA) as an eluent and linear PMMA standards for calibration.

The low monomer conversion of EG1ES and EG3ES and the low molecular weight of the obtained polymer chains showed that a degradative chain transfer was dominant. A degradative chain transfer is characterized by a low propagation rate constant in comparison to a high transfer rate constant and a low re-initiation rate constant related to the propagation rate constant. It is known from the literature that adjacent lone pairs from heteroatoms such as oxygen atoms can stabilize electron-deficient alkyl radicals by donating electron density to the half-empty orbital of the radical (**IV**).[175] The effect of stabilization is not as high as for carbocations,[175] but the propagating sulfonate ester radical of the ethenesulfonate monomers (**I** and **V**) is relatively unstable due to the electron-withdrawing sulfonate ester group.[140,141,176] This stabilization and destabilization effects could promote the radical transfer to the more stable positions next to the ether oxygen atoms (**IV**) and prevent a re-initiation with further monomers. The radicals being located adjacent to the oxygen atoms rather recombined before they were able to re-initiate. The most probable recombination of the transferred radical might occur by an isobutyronitrile radical. The polymerization of EES as described above showed a high monomer conversion and a relatively high molecular weight. This is also a good example for the reduction of chain transfer reactions due to the absence of stabilizing ether oxygen atoms in the ethyl group. The observation that EES and the fluorinated monomers polymerized under the same conditions point out to the fact that the methylene group adjacent to the sulfonate ester group was not involved in the chain transfer reactions.

An up-scaling of the FRP of the monomer FEG3ES at 60 °C using AIBN as a thermal initiator was achieved by using a special experimental setup. This consisted of a long tube reactor with a magnetic stirring bar extension paddle to enable a homogeneous mixing and a better heat transfer to the reaction mixture. So up to 30 mL of monomer could be polymerized in a batch process with a monomer conversion of 50% after 29 h. An overall yield of 75% with a total product mass of 17.50 g was achieved after purification (PFEG3ES-FRP-UP). ^{1}H NMR spectroscopy proved a high purity (Fig. 93). The peak molecular weight $M_{p,\,SEC}$ determined by HFIP-SEC was 11,700 g mol^{-1} with a broad molecular weight distribution as expected for FRP ($Đ$ = 1.87, Fig. 41b).

3.2.3 Reversible addition-fragmentation chain transfer and characterization

Due to the positive results from the FRP of FEG2ES and FEG3ES, they were also polymerized by RAFT. The aim was to receive defined end-groups and narrow molecular weight distributions for a better molecular weight analysis by MALDI-ToF MS (Scheme 8b). Mori *et al.* have already shown that *O*-ethyl-*S*-(1-methoxycarbonyl) ethyldithiocarbonate (OEMDTC) is a suitable CTA for the RAFT polymerization of EES.[141] To establish an appropriate method for the molecular weight determination, first, EES was polymerized analog their reaction conditions. The polymerization was performed in bulk using AIBN as a thermal initiator and OEMDTC as a CTA at 60 °C and at a ratio $[M]_0/[CTA]_0/[I]_0$ of 500/5/1 (Table 10). But the reaction was scaled up considerably.

Table 10 RAFT polymerization of EES in bulk at 60 °C using AIBN as a thermal initiator (I) and OEMDTC as a CTA[a].

Polymer	Initial monomer weight (g)	Time (h)	*conv.*[e] (%)	$M_{n,\,theor}$[g] (g/mol)	$M_{n,\,SEC}$ (g/mol)	$Đ$	$M_{p,\,SEC}$[i] (g/mol)	$M_{p,\,MALDI}$[k] (g/mol)	$M_{n,\,NMR}$[l] (g/mol)
PEES-RAFT1[b]	10.7	20.5[d]	60	8,400	3,600[i]	1.31[i]	4,900	-	-
PEES-RAFT1[c]					4,000[i]	1.30[i]	5,400	4,700	5,400[m]
PEES-RAFT,[c] Mori *et al.*[141]	0.3	20.5	75[f]	10,400[h]	25,000[h+j]	1.30[h+j]	-	-	11,800[h]
PEES-RAFT2[c]	1.2	17.5[d]	69	9,600	4,200[i]	1.29[i]	6,100	5,000	7,400[m]
PEES-RAFT,[c] Mori *et al.*[141]	0.3	17.5	70[f]	9,700[h]	23,600[h+j]	1.25[h+j]	-	-	9,700[h]

[a] $[M]_0/[CTA]_0/[I]_0 = 500/5/1$. [b]Data measured from the crude reaction mixture. [c]Measured from the purified polymer. [d]Already highly viscous reaction mixture. [e]Determined by ^{1}H NMR spectroscopy and calculated according to equation (22). [f]Taken from figure 3a in Mori *et al.*[141] [g]Calculated according to equation (13). [h]Taken from figure 3b in Mori *et al.*[141] [i]Determined by SEC using THF as an eluent and calibrated with PS standards. [j]Determined by SEC using DMF containing 10 mM lithium bromide as an eluent and calibrated with PS standards.[141] [k]Determined by MALDI-ToF MS in reflectron positive mode with IAA as a matrix. [l]Determined by ^{1}H NMR spectroscopy comparing the integral of the methylene protons of the ethyl group in the CTA derived end-group with the integral of the methylene protons in the repeating unit. [m]CTA derived ^{1}H NMR end-group signals hardly to identify.

In a first batch with a total mass of about 10.7 g of monomer (PEES-RAFT1), the molecular weight alters only slightly after purification from $M_{n,\,SEC}$ = 3,600 g/mol to 4,000 g/mol while keeping a constant dispersity $Đ$ of about 1.3 (Fig. 42a). The monomer conversion (60% after 20.5 h) was lower in comparison to the literature (75% after 20.5 h) obtained for small scale synthesis.[141] This deviation could result from a lower heat transfer to the reaction mixture, since the mass of monomer was more than thirtyfold in the present case. Using a less amount of monomer, only 1.2 g (PEES-RAFT2), the same conversion was received like in the literature (~ 70% after 17.5 h) with a comparable dispersity of the molecular weight distribution ($Đ$ ~ 1.3).[141]

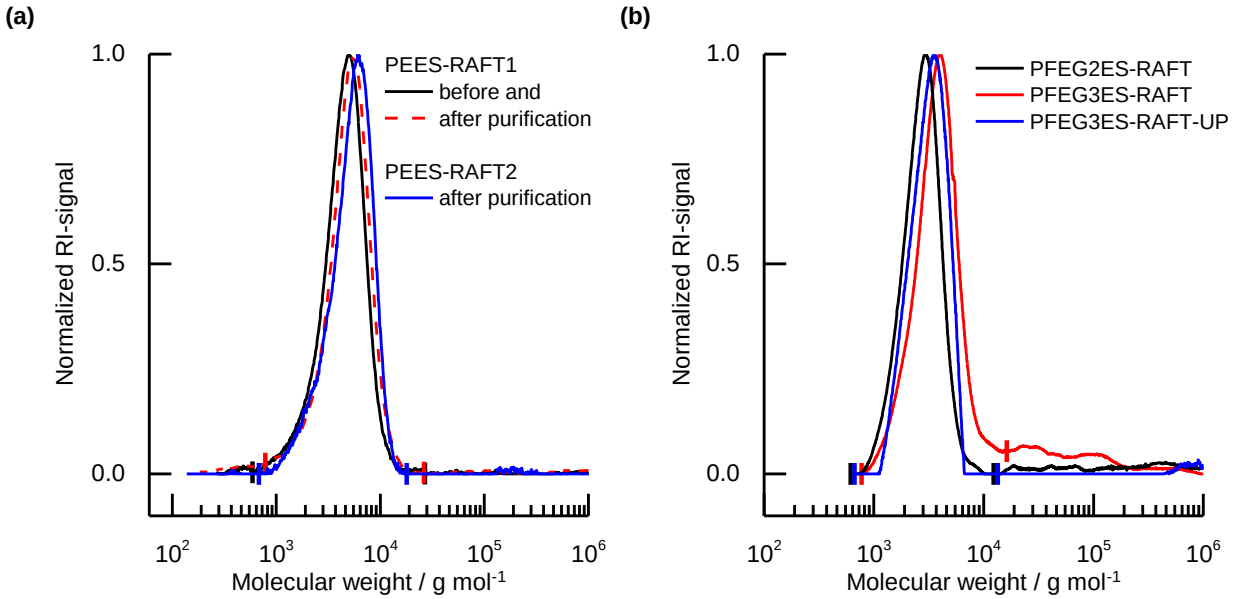

Fig. 42 SEC molecular weight distributions of (a) PEES-RAFT1 before and after purification, purified PEES-RAFT2 and of (b) purified PFEG2ES-RAFT, PFEG3ES-RAFT and PFEG3ES-RAFT-UP. The syntheses were performed by RAFT polymerization in bulk at 60 °C using AIBN as a thermal initiator and OEMDTC as a CTA. The measurements were performed (a) with THF as an eluent and PS standards for calibration and (b) with HFIP (with 0.5 wt% KTFA) as an eluent and PMMA standards for calibration.

To estimate the absolute molecular weight, first, NMR spectroscopy ($M_{n,\,NMR}$) was used comparing the integral of the methylene protons of the ethyl group in the CTA derived end-group with the integral of the methylene protons in the repeating unit. However, $M_{n,\,NMR}$ values were significantly lower in comparison to the theoretical ones, because the end-group signal was hardly to identify (Table 10). The error in estimation by NMR spectroscopy depends on the uncertainty of the integration values and end-group alteration. Therefore, the absolute molecular weight was determined by MALDI-ToF MS with IAA as a matrix. The molecular weights in MALDI-ToF MS (Fig. 43) were lower compared to the theoretical molecular weights ($M_{n,\,theor}$ = 8,400 g/mol for PEES-RAFT1 and $M_{n,\,theor}$ = 9,600 g/mol for PEES-RAFT2).

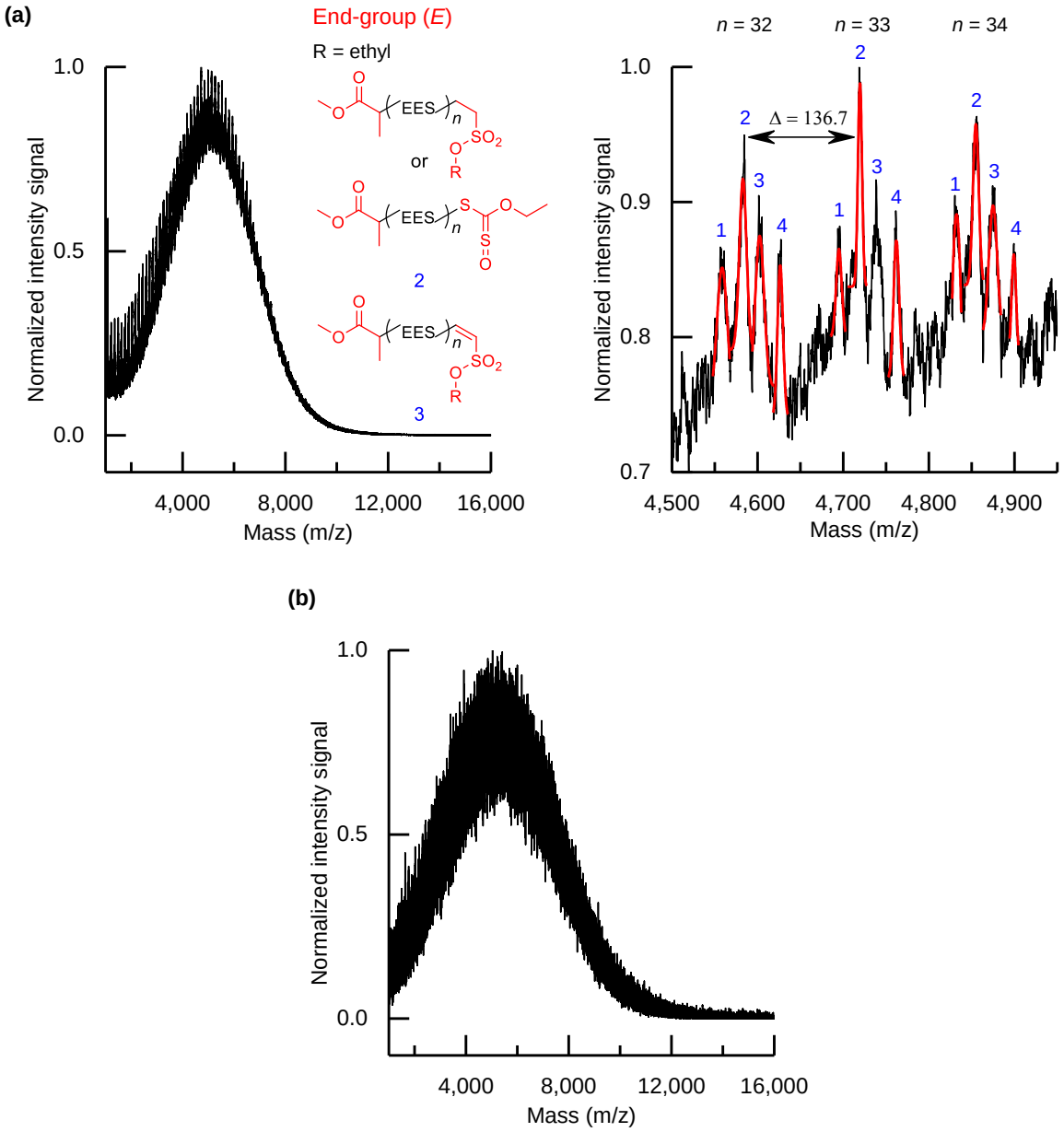

Fig. 43 MALDI-ToF MS spectrum of purified (a) PEES-RAFT1 and (b) PEES-RAFT2 synthesized by RAFT in bulk at 60 °C using AIBN as a thermal initiator and OEMDTC as a CTA. The measurements were performed in reflectron positive mode with IAA as a matrix. The red marked lines in (a) are Gaussian fitting traces to determine the isotopic mean values.

The main part of the polymer chains carries the initiating group of the CTA (peak numbers 2 and 3, Table 11). However, a significant amount of disproportionation derived-end groups was found being an explanation for the lower molecular weight determined by MALDI-ToF MS in comparison to the theoretical one. The main peak (peak number 2) could be attributed to both hydrogen and CTA derived-end groups.

Table 11 End-group analysis of purified PEES-RAFT1 synthesized by RAFT in bulk at 60 °C using AIBN as a thermal initiator and OEMDTC as a CTA. The measurement was performed by MALDI-ToF MS in reflectron positive mode with IAA as a matrix.

Peak number	Observed mass[a] (m/z)	Mass of end group *E*[b] (m/z)	Calculated mass (m/z)
1	n.a.	n.a.	n.a.
2	225.5	224.30 or 224.31	$[E + H^+]^+ = 225.3$
3	245.1	222.28	$[E + Na^+]^+ = 245.3$
4	n.a.	n.a.	n.a.

[a]See Table 19 for raw data. Isotopic mean values of the end-groups averaged for each peak series shown in Fig. 43a. [b]M_{EES} = 136.17 g/mol. n.a. = not assigned.

Nevertheless, the polymerization of EES by RAFT showed a lower dispersity ($Đ$ = 1.3) in comparison to its polymerization by FRP ($Đ$ = 2.10) indicating a reduction of chain termination and transfer reactions. Thus, OEMDTC was used as a CTA for the RAFT polymerization of FEG2ES and FEG3ES as well. The same conditions for the RAFT polymerization of FEG2ES and FEG3ES as for EES were used with the exception of the ratio $[M]_0/[CTA]_0/[I]_0$. It was changed to 100/2/1 because of the lower polymerization rate of the fluorinated monomers. As expected, the RAFT polymerization proceeded slower in comparison to the FRP of FEG2ES and FEG3ES. Monomer conversions were above 50% only at least after 48 h (Table 12). The RAFT polymerization of FEG3ES was up-scaled from 3.1 g to 48.4 g (PFEG3ES-RAFT-UP) using a long tube reactor with a magnetic stirring bar extension paddle as already described for PFEG3ES-FRP-UP. The up-scaled polymerization proceeded slower.

Table 12 RAFT polymerization of FEG2ES and FEG3ES in bulk at 60 °C using AIBN as a thermal initiator (I) and OEMDTC as a CTA[a].

Polymer	Time (h)	*conv.*[b] (%)	$M_{n,\,theor}$[c] (g/mol)	$M_{n,\,SEC}$[d] (g/mol)	$Đ$[d]	$M_{p,\,SEC}$[d] (g/mol)	$M_{p,\,MALDI}$[e] (g/mol)
PFEG2ES-RAFT	48	59	11,200	2,600	1.16	3,000	7,600
PFEG3ES-RAFT	48	69	17,100	3,400	1.24	3,900	11,100
PFEG3ES-RAFT-UP[f]	72	56	13,900	3,100	1.16	3,600	7,600

[a]$[M]_0/[CTA]_0/[I]_0$ = 100/2/1. Data were measured from the purified polymer. [b]Determined by ^{1}H NMR spectroscopy and calculated according to equation (22). [c]Calculated according to equation (13). [d]Determined by SEC using HFIP containing 0.5 wt% KTFA as an eluent and calibrated with PMMA standards. [e]Determined by MALDI-ToF MS in linear negative mode with DHB as a matrix. [f]Up-scaling of PFEG3ES-RAFT-UP using a long tube reactor with a magnetic stirring bar extension paddle.

PFEGES polymers could be purified by precipitation from DCM or chloroform, since these polymers are only soluble in fluorinated solvents, whereas their monomers are still soluble in DCM or chloroform. The polymers were obtained in sufficient yield (> 70%) and high purity as proved by ^{1}H NMR spectroscopy (Fig. 96-98). The molecular weights were estimated by HFIP-SEC (Fig. 42b)

and by MALDI-ToF MS. Molecular weights estimated by HFIP-SEC with a PMMA calibration were low in comparison to the theoretical ones (Table 12). In contrast, MALDI-ToF MS revealed, that the absolute molecular weights were significantly higher (Fig. 44).

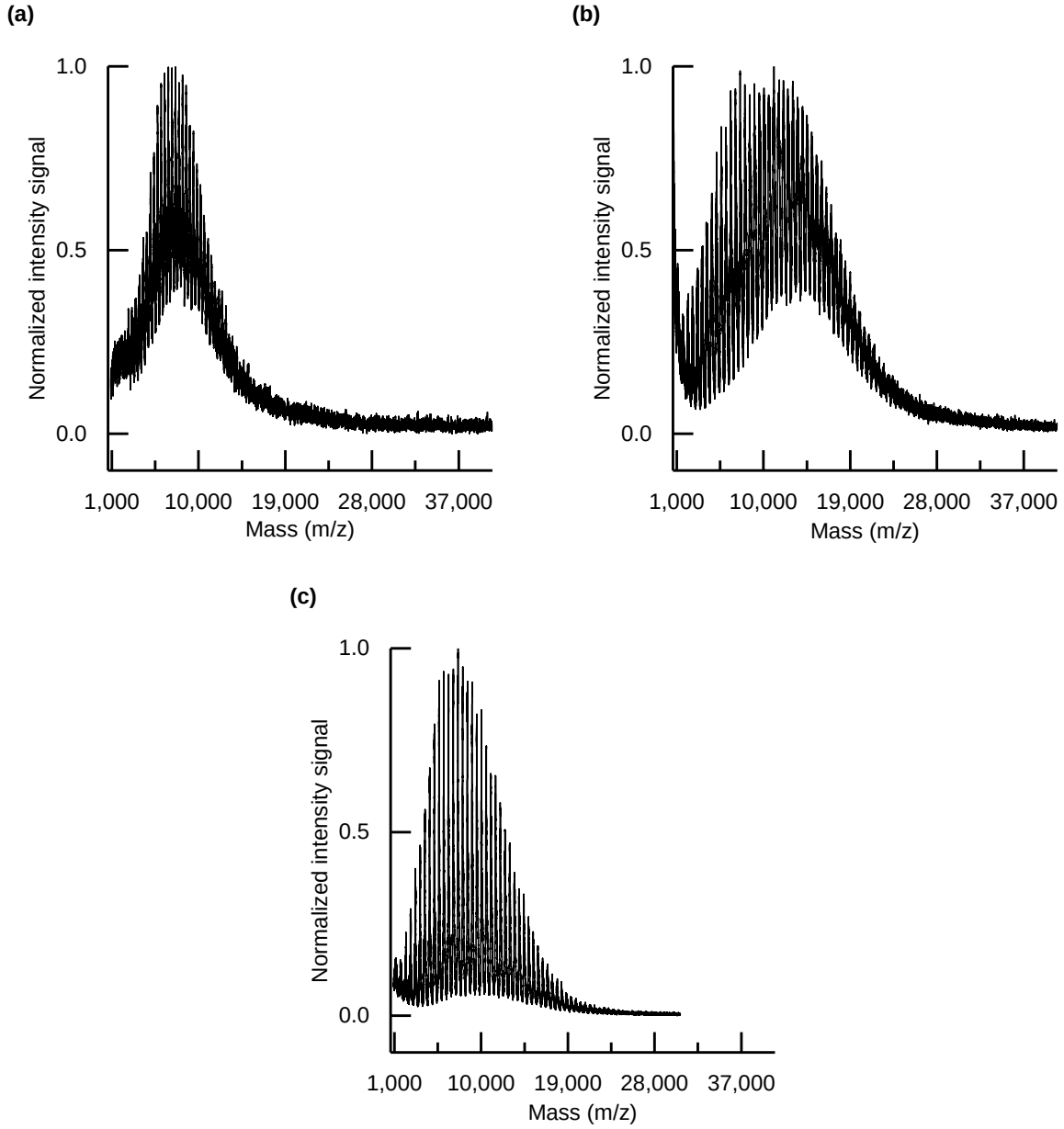

Fig. 44 MALDI-ToF MS spectrum of purified (a) PFEG2ES-RAFT, (b) PFEG3ES-RAFT and (c) PFEG3ES-RAFT-UP synthesized by RAFT polymerization in bulk at 60 °C using AIBN as a thermal initiator and OEMDTC as a CTA. The measurements were performed in linear negative mode with DHB as a matrix.

The best resolution for the MALDI-ToF MS spectra of the PFEGES polymers in linear negative mode was received using DHB as a matrix. Perfluoropolyethers seem to have strong interactions with anions. In addition, as already concluded from the MALDI-ToF MS analysis of the non-fluorinated polymers

above, partial cleavage of the sulfonate ester during the laser impact could form negatively charged sulfonate groups along the polymer backbone. The appropriate method to measure in reflectron negative mode calibrated at higher molecular weights was not available. So the measurement was performed in reflectron positive mode taking a loss of resolution, but it was still sufficient for a detailed-end group analysis (Fig. 45 and Fig. 46).

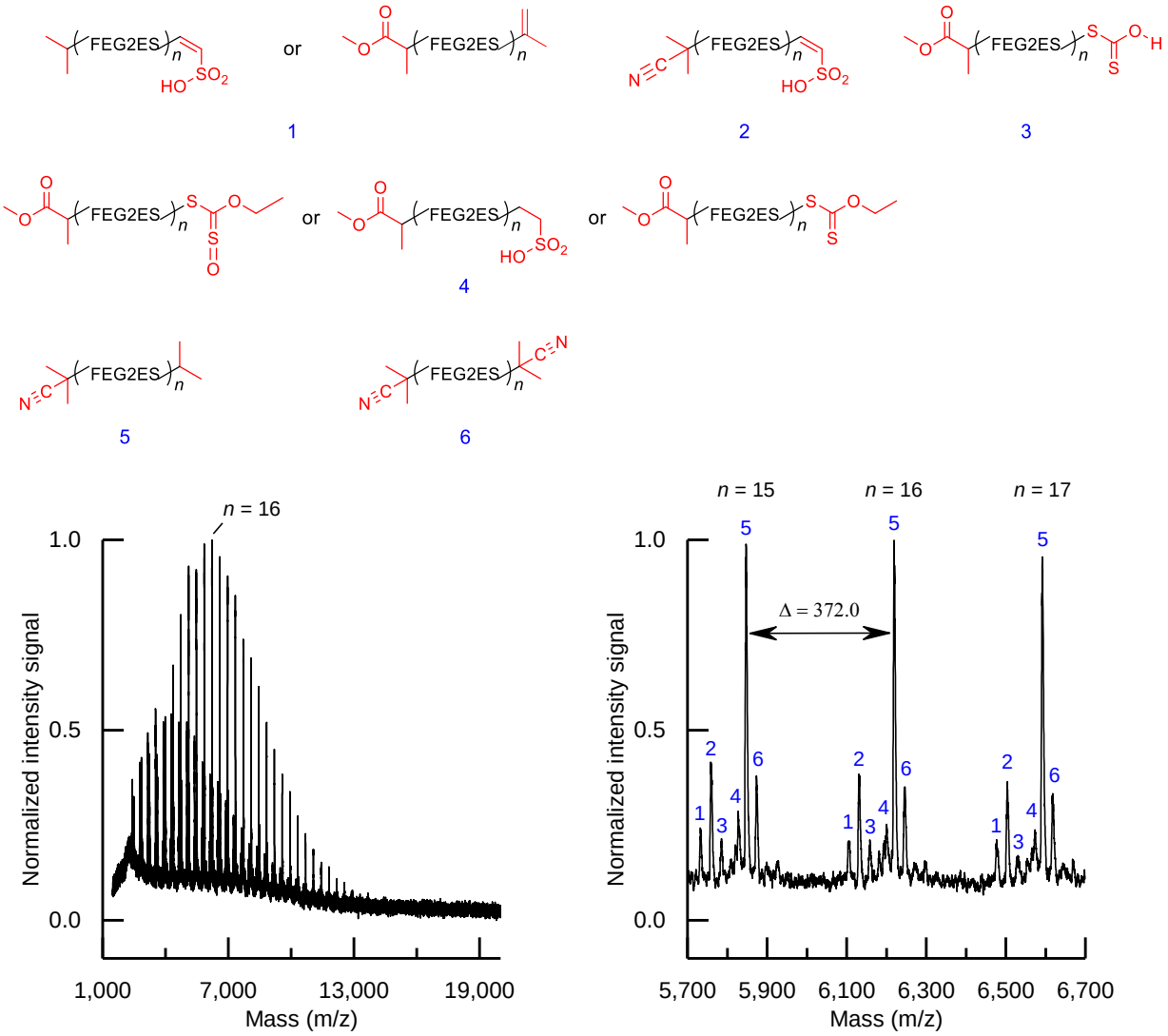

Fig. 45 MALDI-ToF MS spectrum of purified PFEG2ES-RAFT synthesized by RAFT polymerization in bulk at 60 °C using AIBN as a thermal initiator and OEMDTC as a CTA. The measurement was performed in reflectron positive mode with DHB as a matrix.

The isotopic mean values of the end-groups of PFEG2ES-RAFT could be mainly attributed to the disproportionation or recombination of polymer radicals carrying AIBN-derived end-groups (peak numbers 1, 2, 5 and 6 in Fig. 45 and Table 13). This observation revealed that the most growing polymer radicals disproportionated or recombined before the CTA was involved in the polymerization.

However, end-groups derived from chain transfer reactions were nearly completely absent. Only a small amount of polymers carried CTA-derived end-groups (peak numbers 3 and 4).

Table 13 End-group analysis of purified PFEG2ES-RAFT synthesized by RAFT polymerization in bulk at 60 °C using AIBN as a thermal initiator and OEMDTC as a CTA. The measurement was performed in reflectron positive mode with DHB as a matrix.

Peak number	Observed mass[a] (m/z)	Mass of end-group *E*[b] (m/z)	Calculated mass[c] (m/z)
1	151.2	150.23 or 128.19	$[E + H^+]^+ = 151.2$ or $[E + Na^+]^+ = 151.2$
2	177.0	175.24	$[E + H^+]^+ = 176.3$
3	203.5	180.26	$[E + Na^+]^+ = 203.3$
4	246.4	224.31 or 196.23 or 208.31	$[E + Na^+]^+ = 247.3$ or $[E + 2CN - 2H + H^+]^+ = 247.3$ or $[E + K^+]^+ = 247.4$
5	265.3	111.20	$[E + H^+ + DHB]^+ = 266.3$
6	291.4	136.22	$[E + H^+ + DHB]^+ = 291.4$

[a]See Table 20 for raw data. Isotopic mean values of the end-groups averaged for each peak series shown in Fig. 45 (for n = 12-24). [b]M_{FEG2ES} = 372.16 g/mol. [c]M_{DHB} = 154.12 g/mol.

In the case of PFEG3ES-RAFT isotopic mean values of the end-groups could be mainly attributed to the CTA (peak numbers 3, 4, 6 and 7 in Fig. 46 and Table 14). Next to potassium and sodium ions, adduct ions with hydrogen cyanide and sulfonic acid moieties formed possible structures. Pure hydrogen cyanide or structure elements incorporating the same could be formed from AIBN-derived end-groups during the laser impact. Disproportionation and especially recombination were significantly reduced in comparison to the polymerization of FEG2ES explaining also the higher monomer conversion. The longer FEG3 side-chain in FEG3ES in comparison to the shorter FEG2 side-chain in FEG2ES might sterically hinder the recombination of two polymer radicals.

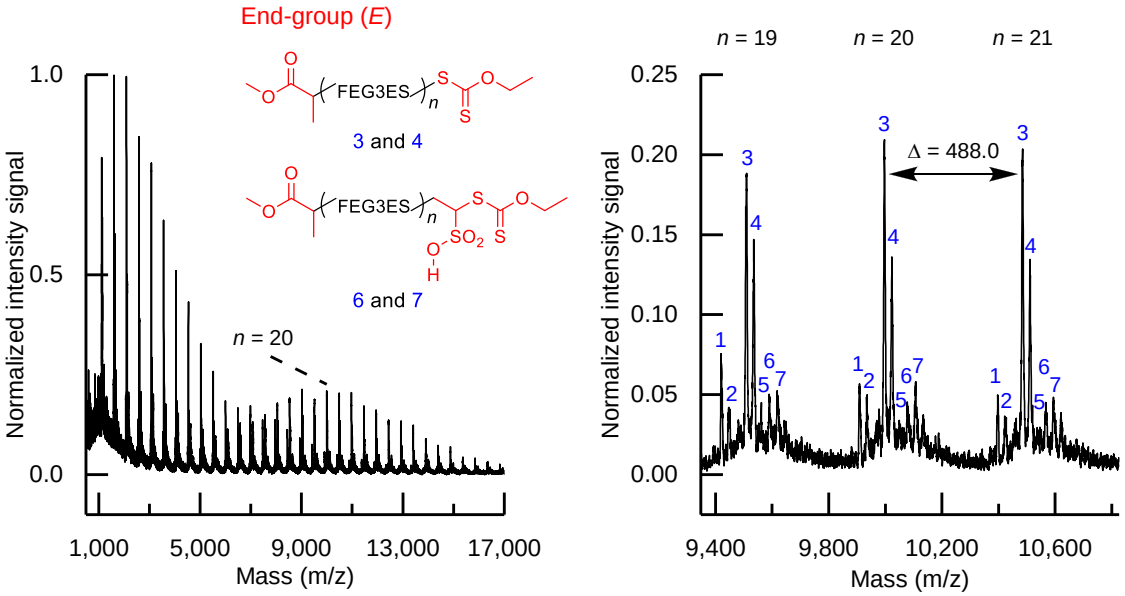

Fig. 46 MALDI-ToF MS spectrum of purified PFEG3ES-RAFT synthesized by RAFT polymerization in bulk at 60 °C using AIBN as a thermal initiator and OEMDTC as a CTA. The measurement was performed in reflectron positive mode with DHB as a matrix.

The peak numbers 1, 2 and 5 could not be assigned so far, but could be attributed to disproportionation or chain transfer reactions explaining the slight deviation of the molecular weight determined by MALDI-ToF MS from the theoretical one. Prolonged reaction times, as under RAFT, might also still promote chain transfer reactions from the methylene protons adjacent to the sulfonate ester group.

Table 14 End-group analysis of purified PFEG3ES-RAFT synthesized by RAFT polymerization in bulk at 60 °C using AIBN as a thermal initiator and OEMDTC as a CTA. The measurement was performed by MALDI-ToF MS in reflectron positive mode with DHB as a matrix.

Peak number	Observed mass[a] (m/z)	Mass of end group *E*[b] (m/z)	Calculated mass (m/z)
1	n.a.	n.a.	n.a.
2	n.a.	n.a.	n.a.
3	232.0	208.31	[*E* + Na^+] = 231.3
4	258.4	208.31	[*E* + Na^+ + HCN] = 258.3
5	n.a.	n.a.	n.a.
6	343.5	316.43	[*E* + H^+ + HCN] = 343.4
7	371.0	332.43	[*E* + K^+] = 371.5

[a]See Table 21 for raw data. Isotopic mean values of the end-groups averaged for each peak series shown in Fig. 46 (for *n* = 17-29). [b]M_{FEG3ES} = 488.18 g/mol. n.a. = not assigned.

Nevertheless, the high end-group functionalization of PFEG3ES-RAFT with the CTA, the unimodal molecular weight distributions and the lower dispersity in comparison to the one obtained from the FRP (*Đ* = 1.16 compared to *Đ* = 2.72 for PFEG2ES and *Đ* = 1.24 compared to *Đ* = 3.38 for PFEG3ES) show, that OEMDTC is a suitable CTA for the RAFT polymerization especially of the FEG3ES

monomer. The high end-group fidelity allows for the synthesis of more complex polymer architectures such as block copolymers.

As a possible solvent for the FRP and RAFT polymerization of FEG3ES hexafluorobenzene was tested. It does not only dissolve PFEG3ES, but also cannot promote chain transfer reactions due to the high instability of fluorine and phenyl radicals. As expected for lower monomer concentrations in comparison to the bulk polymerization the monomer conversions were low (< 40% after 48 h, Table 15).

Table 15 Conventional free radical polymerization (FRP)[a] and RAFT[b] polymerization of FEG3ES in hexafluorobenzene (HFB) as a solvent at different monomer concentrations $[M]_0$ and at 60 °C using AIBN as a thermal initiator (I) and in the case of RAFT polymerization with OEMDTC as a CTA.[c]

Polymer	$[M]_0$ (mol/L)	*conv.*[d] (%)	$M_{n,\,theor}$[e] (g/mol)	$M_{n,\,SEC}$[f] (g/mol)	$Đ$[f]	$M_{p,\,SEC}$[f] (g/mol)
PFEG3ES-FRP-HFB1	16	24	-	6,300	1.65	9,500
PFEG3ES-FRP-HFB2	32	29	-	-[g]	-[g]	1,700[g]
PFEG3ES-RAFT-HFB1	16	24	6,100	-[g]	-[g]	1,500[g]
PFEG3ES-RAFT-HFB2	32	37	9,200	7,200	1.72	12,900
PFEG3ES-RAFT-HFB3	128	30	7,500	-[g]	-[g]	2,100[g]

[a] $[M]_0/[I]_0 = 100/1$. [b] $[M]_0/[CTA]_0/[I]_0 = 100/2/1$. [c] Data measured from the crude reaction mixture. [d] Determined by ^{1}H NMR spectroscopy and calculated according to equation (22) after a reaction time of 48 h. [e] Calculated according to equation (13). [f] Determined by SEC using HFIP containing 0.5 wt% KTFA as an eluent and calibrated with PMMA standards. [g] Molecular weight peak was low and overlapped with the peak of the internal standard.

However, relatively high molecular weights with respect to the low monomer conversions for selected monomer concentrations were achieved (PFEG3ES-FRP-HFB1: 16 mol L^{-1} and PFEG3ES-RAFT-HFB2 32 mol L^{-1}, Fig. 47). So chain transfer to solvent reactions seemed to be absent.

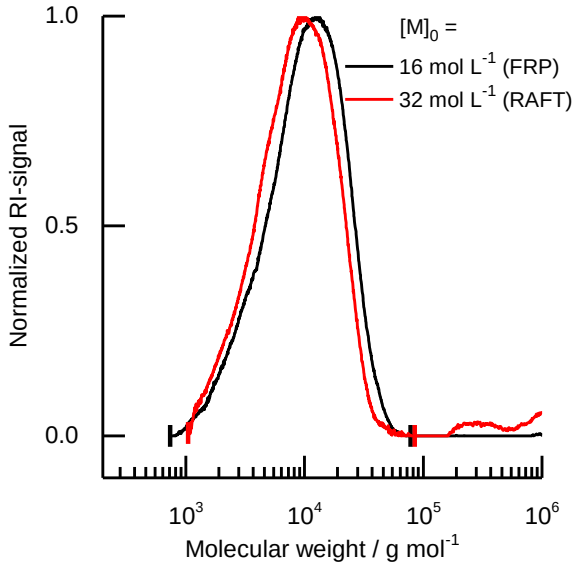

Fig. 47 SEC molecular weight distributions of crude PFEG3ES synthesized by FRP or RAFT polymerization at 60 °C using AIBN as a thermal initiator and hexafluorobenzene as a solvent at a monomer concentration $[M]_0$ of 16 mol L^{-1} (PFEG3ES-FRP-HFB1) and 32 mol L^{-1} (PFEG3ES-RAFT-HFB2). The measurements were performed with HFIP (with 0.5 wt% KTFA) as an eluent and PMMA standards for calibration.

3.2.4 Thermal properties

The thermal properties of PFEG2ES-RAFT, PFEG3ES-RAFT and PFEG3ES-RAFT-UP were determined by TGA, DMA and DSC. Those of PFEG3ES-FRP-UP will be presented in chapter 3.3.3 in connection with the thermal properties of its SPEs. TGA thermograms of PEES-RAFT2, PFEG2ES-RAFT, PFEG3ES-RAFT and PFEG3ES-RAFT-UP are shown in Fig. 48. All polymers start to degrade significantly at about 200 °C revealing that the overall thermal stability of the fluorinated polymers is limited by the cleavage of the sulfonate ester and is not attributed to the decomposition of the fluorinated ethylene glycol groups. PFEG3ES-RAFT ($T_{d,\,1\%}$ = 187 °C) and PFEG3ES-RAFT-UP ($T_{d,\,1\%}$ = 200 °C) showed the highest thermal stability, followed by PEES-RAFT ($T_{d,\,1\%}$ = 171 °C) and PFEG2ES-RAFT ($T_{d,\,1\%}$ = 158 °C). PFEG2ES-RAFT, PFEG3ES-RAFT and PFEG3ES-RAFT-UP degraded nearly free of residues in one single step ending at about 400 °C. In contrast, PEES-RAFT2 degraded with an additional step starting at about 420 °C. As already shown by Shirai *et al.*, the structure of the pendant group determines the cleavage temperature of the sulfonate ester.[177] Even though sulfonate esters tend to hydrolyze easily at moderate temperature as shown in previous studies,[178] they can still be used at higher temperature for applications where water is completely absent.

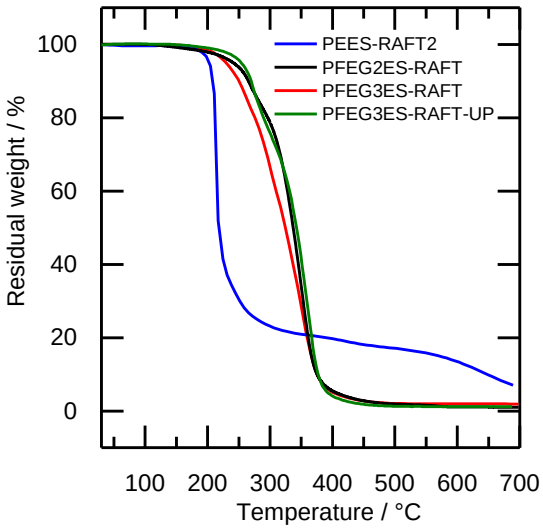

Fig. 48 TGA thermograms of PEES-RAFT2, PFEG2ES-RAFT, PFEG3ES-RAFT and PFEG3ES-RAFT-UP (under nitrogen, 10 K min^{-1}).

Whereas PFEG2ES-RAFT is still a hard solid at room temperature (20 °C), PFEG3ES-RAFT is already a gum-like solid which quickly liquefies at higher temperature. The analysis by DMA revealed three thermal transitions for PFEG2ES-RAFT ($T_{p,1}$ = -62 °C, $T_{p,2}$ = 34 °C and $T_{p,3}$ = 71 °C, Fig. 49). For PFEG3ES-RAFT only two thermal transitions by DMA were present. The peak temperature of the loss factor for the first thermal transition was $T_{p,1}$ = -75 °C. The second thermal transition was split into a double peak with $T_{p,2a}$ = 33 °C and $T_{p,2b}$ = 49 °C.

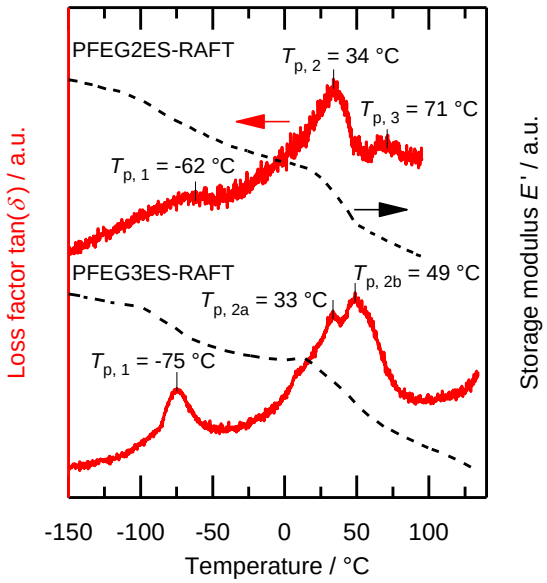

Fig. 49 Second heating DMA traces of PFEG2ES- and PFEG3ES-RAFT (under nitrogen, 2 K min^{-1}, 2 Hz).

Typically, the segmental motion of PFPE chains starts at about -100 °C which equals the process at a glass transition.[10] So the first thermal transitions might be attributed to the starting of segmental motion of the FEG2 and the FEG3 side-chains. The second thermal transitions could be attributed to glass transitions (T_g = 16 °C for PFEG2ES-RAFT and T_g = 17 °C for PFEG3ES-RAFT), as shown in the DSC thermograms in Fig. 50a. Probably caused by the shorter chain length of PFEG3ES-RAFT-UP compared to PFEG3ES-RAFT (Table 12), the T_g is only 6 °C for PFEG3ES-RAFT-UP (Fig. 50b). PFEG2ES-RAFT showed a melting peak T_m at 46 °C, whereas there was no additional melting peak of possible crystalline domains for PFEG3ES-RAFT.

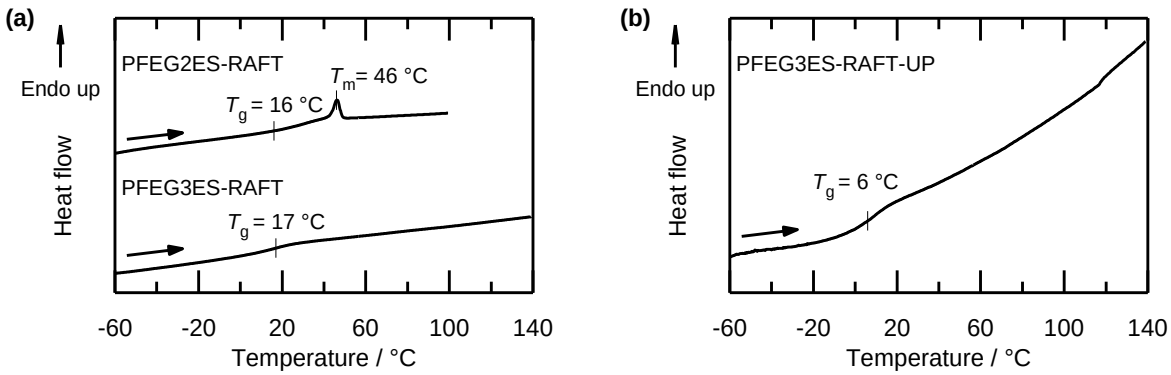

Fig. 50 Second heating DSC traces of (a) PFEG2ES-/PFEG3ES-RAFT and (b) PFEG3ES-RAFT-UP (under nitrogen, 10 K min^{-1}).

The amorphous character of PFEG3ES-RAFT was confirmed by WAXS measured at room temperature (Fig. 51). Only amorphous background scattering was detected with no reflexes as they would arise from crystalline domains. Obviously, the longer FEG3 side-chains prevent PFEG3ES-RAFT from crystallization in comparison to PFEG2ES-RAFT.

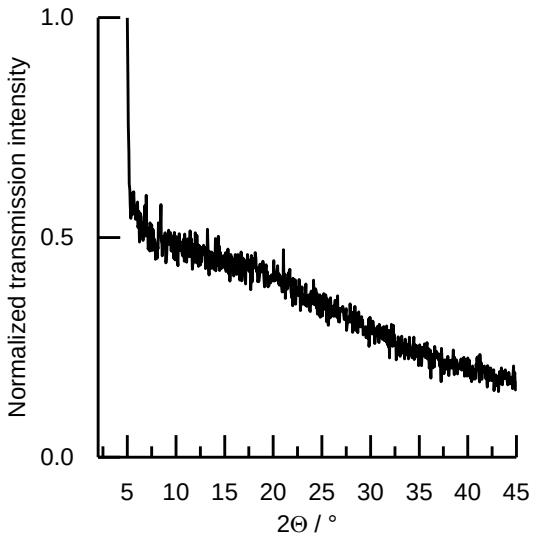

Fig. 51 WAXS diffractogram of PFEG3ES-RAFT measured at room temperature.

3.3 Enhancing the solubility of lithium salts in perfluoropolyether solid polymer electrolytes

3.3.1 Lithium salt synthesis and characterization

The lithium salt LiFEG3 was synthesized by the lithiation of an excess of the alcohol FEG3 with *n*-butyllithium (Scheme 11). Perfluorodecalin was used as a solvent for ^{1}H NMR spectroscopy to check possible residues of FEG3 after purification since the hydroxyl group proton can be detected in perfluorodecalin. The hydroxyl group proton cannot exchange with the deuterium of the solvent like in typical deuterated solvents. The disappearance of the hydroxyl group proton signal in the LiFEG3 spectrum indicated a successful lithiation of FEG3 and removement of excess FEG3 (Fig. 52a). The triplet signal and the hydrogen-fluorine coupling constant of the methylene protons shifted slightly from 3.64 ppm to 3.76 ppm and from 9.6 Hz to 12.5 Hz after the lithiation (additional overview spectra in Fig. 100 and Fig. 103).

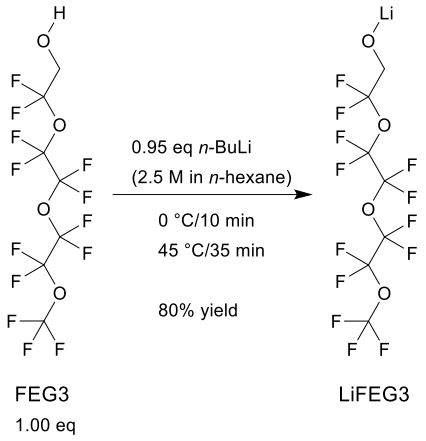

Scheme 11 Synthesis of the lithium salt LiFEG3 by the lithiation of the alcohol FEG3.

Due to their amphiphilic structure, FEG3 and LiFEG3 were only partly soluble in perfluorodecalin as could be deduced from the broadening of their methylene proton signals. In contrast, they were completely soluble in methanol as could be seen from their ^{1}H NMR spectra taken in deuterated methanol. The broadening of their methylene proton signals vanished (Fig. 52b). The triplet signal and the hydrogen-fluorine coupling constant of the methylene protons shifted slightly from 3.88 ppm to 3.93 ppm and from 10.3 Hz to 11.5 Hz after the lithiation (additional overview spectra in Fig. 99 and Fig. 102).

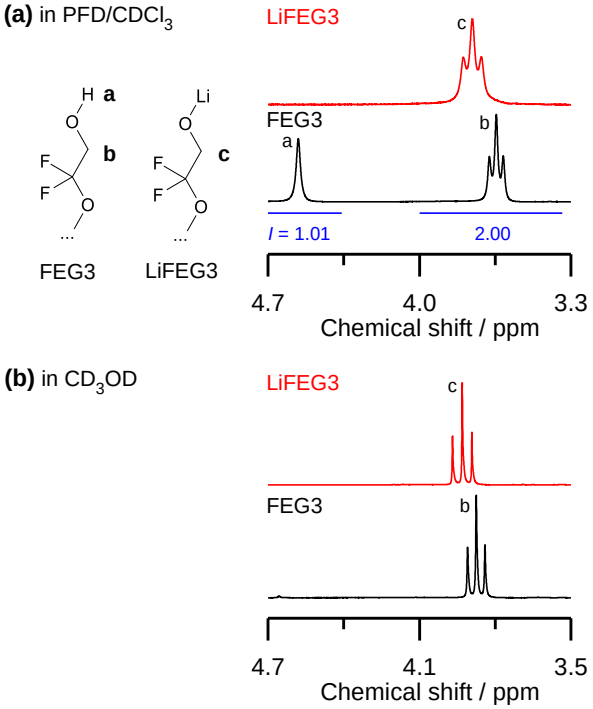

Fig. 52 ^{1}H NMR spectra of the alcohol FEG3 and the lithium salt LiFEG3 (a) in perfluorodecalin (PFD) with $CDCl_3$ in a coaxial insert and (b) in CD_3OD (see Fig. 99, Fig. 100, Fig. 102 and Fig. 103 for complete spectra).

3.3.2 Solid polymer electrolyte preparation

LiTFSI SPEs with PFEG3ES-FRP-UP as a host polymer with O/Li ratios of 69, 36, 27, 16 and 10 were tried to be prepared from polymer melt. However, regardless of the amount of salt, LiTFSI remained unsolved. The lower the O/Li ratio, the higher was the amount of unresolved LiTFSI.

LiFEG3 is thermally unstable above the melting temperature of PFEG3ES (see chapter 3.3.3). Therefore, the LiFEG3 SPEs with O/Li ratios of 69, 15, 10 and 5 (SPE-O/Li) were prepared from solution. The choice of solvent was restricted since PFEG3ES is only soluble in fluorinated solvents such as (trifluoromethoxy)benzene, hexafluorobenzene, perfluorodecalin and HFIP. Due to its low boiling point, toxicity and reactivity, hexafluorobenzene was used. LiFEG3 formed stable colorless turbid dispersions in hexafluorobenzene. After mixing PFEG3ES-FRP-UP with LiFEG3 in hexafluorobenzene, the solvent could be easily removed in vacuum (Scheme 12). Whereas SPE-69 can be regarded still as a salt-in-polymer electrolyte, SPE-5 resembles rather a polymer-in-salt electrolyte due to its high salt amount.

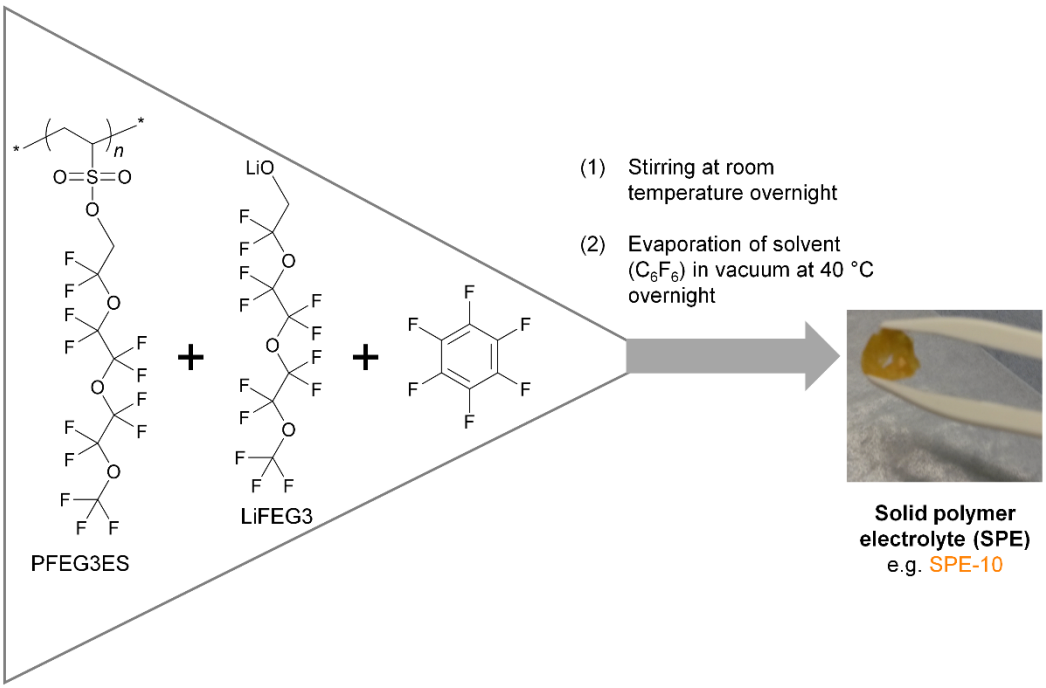

Scheme 12 SPE preparation from solution by mixing the polymer PFEG3ES with the lithium salt LiFEG3 in hexafluorobenzene as a solvent. The example is shown for the SPE with an O/Li ratio of 10 (SPE-10).

PFEG3ES-FRP-UP is chemically inert to the lithium salt LiFEG3 as proven by ^{1}H NMR spectroscopy using perfluorodecalin as a solvent. All the expected signals could be well assigned (Fig. 53a, complete

spectra in Fig. 105). For SPE-69, the LiFEG3 concentration was too low to detect the methylene proton signal of LiFEG3. Interestingly, the methylene proton signal of LiFEG3 broadened further with an increasing O/Li ratio (decreasing LiFEG3 concentration). This broadening might indicate an up to now unclear interaction of the FEG3 anion with PFEG3ES. The higher the salt concentration, the lower is the broadening effect of the signal since the interaction with the polymer decreases.

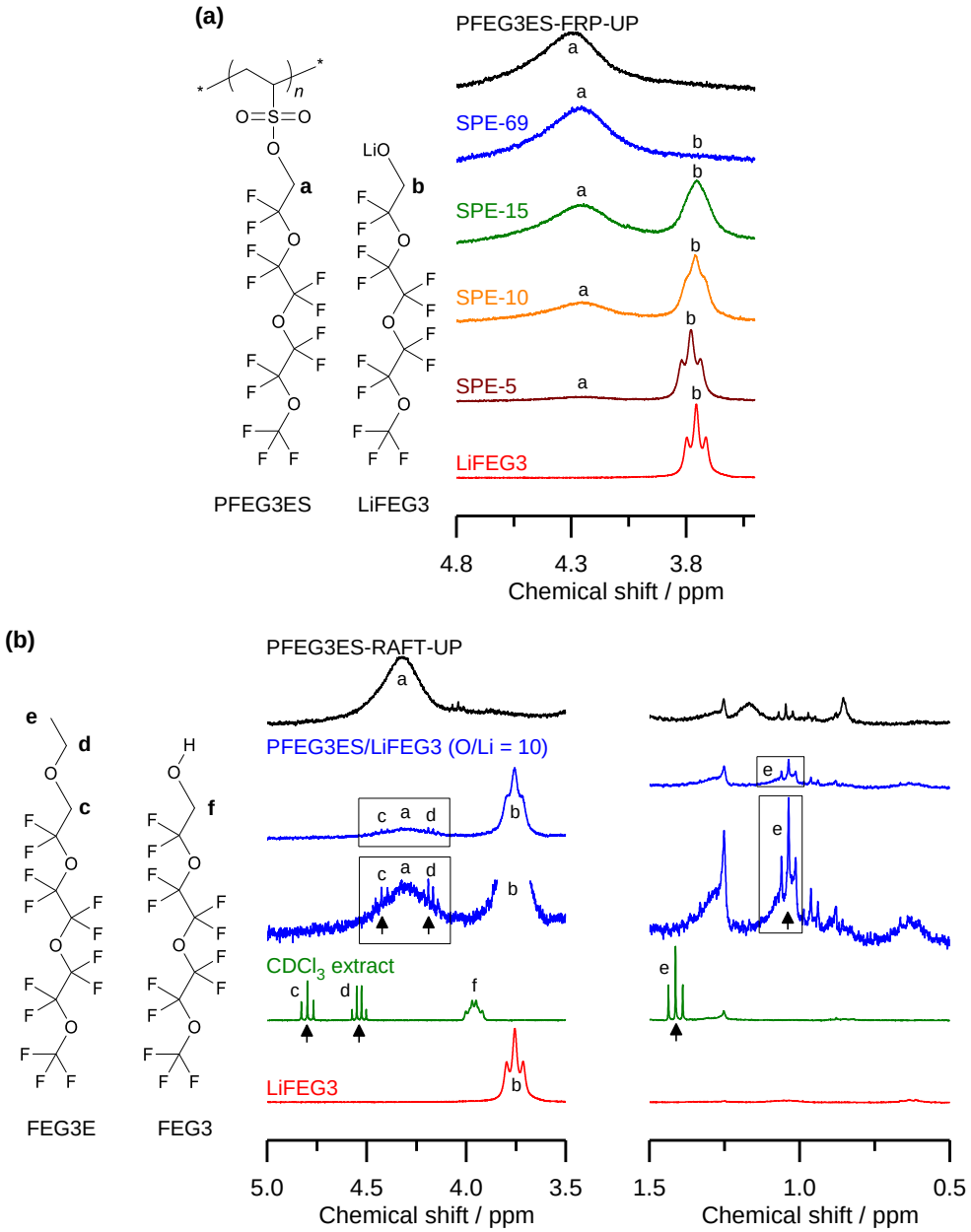

Fig. 53 ^{1}H NMR spectra of: (a) the polymer PFEG3ES-FRP-UP, the lithium salt LiFEG3 and SPE-69, -15, -10 and -5 (see Fig. 93, Fig. 100 and Fig. 105 for complete spectra); (b) the polymer PFEG3ES-RAFT-UP, the lithium salt LiFEG3, a PFEG3ES-RAFT-UP/LiFEG3 mixture (O/Li = 10) stirred for 16 h at room temperature and a $CDCl_3$ extract from that mixture (see Fig. 98, Fig. 100, Fig. 106 and Fig. 107 for complete spectra). The $CDCl_3$ extract spectrum was directly measured. The other spectra were recorded in perfluorodecalin with $CDCl_3$ in a coaxial insert.

In contrast to PFEG3ES-FRP-UP, PFEG3ES-RAFT-UP is reactive towards LiFEG3. New ^{1}H NMR signals appeared after a PFEG3ES-RAFT-UP/LiFEG3 mixture (O/Li = 10) had been stirred at room temperature for 16 h (Fig. 53b). The signals between 4.5 and 4.0 ppm (c and d), whose multiplicity indicate a low molecular weight structure, overlap with the broad polymer signal (a) of the methylene protons in PFEG3ES. Furthermore, a triplet (e) around 1.0 ppm is visible. The reaction product was extracted by $CDCl_3$ and directly measured by ^{1}H NMR spectroscopy. Unlike the measurement in perfluorodecalin in the presence of PFEG3ES, the three signals are downfield shifted. In addition, a new signal appeared at 3.96 ppm (f: triplet of a doublet, J = 9.7 Hz and 6.2 Hz). This can be attributed to the methylene protons in FEG3 which arose from the reaction of LiFEG3 with water being present as impurity in $CDCl_3$ (complete spectrum in Fig. 107).

The three signals (c: triplet, J = 9.1 Hz; d: quartet, J = 7.1 Hz; e: triplet, J = 7.1 Hz) can be assigned to an ethyl ether, 1,1,1,3,3,4,4,6,6,7,7,9,9-tridecafluoro-2,5,8,11-tetraoxatridecane (FEG3E, Scheme 13). A nucleophilic substitution of LiFEG3 at the xanthate end-group of PFEG3ES-RAFT-UP releases lithium ethoxide as a reactive intermediate. This can attact the positively polarized carbon atom of the methylene group adjacent to the sulfonate ester and CF_2 group of PFEG3ES. Next to a copolymer of lithium vinylsulfonate and FEG3ES, the ethyl ether FEG3E is formed.

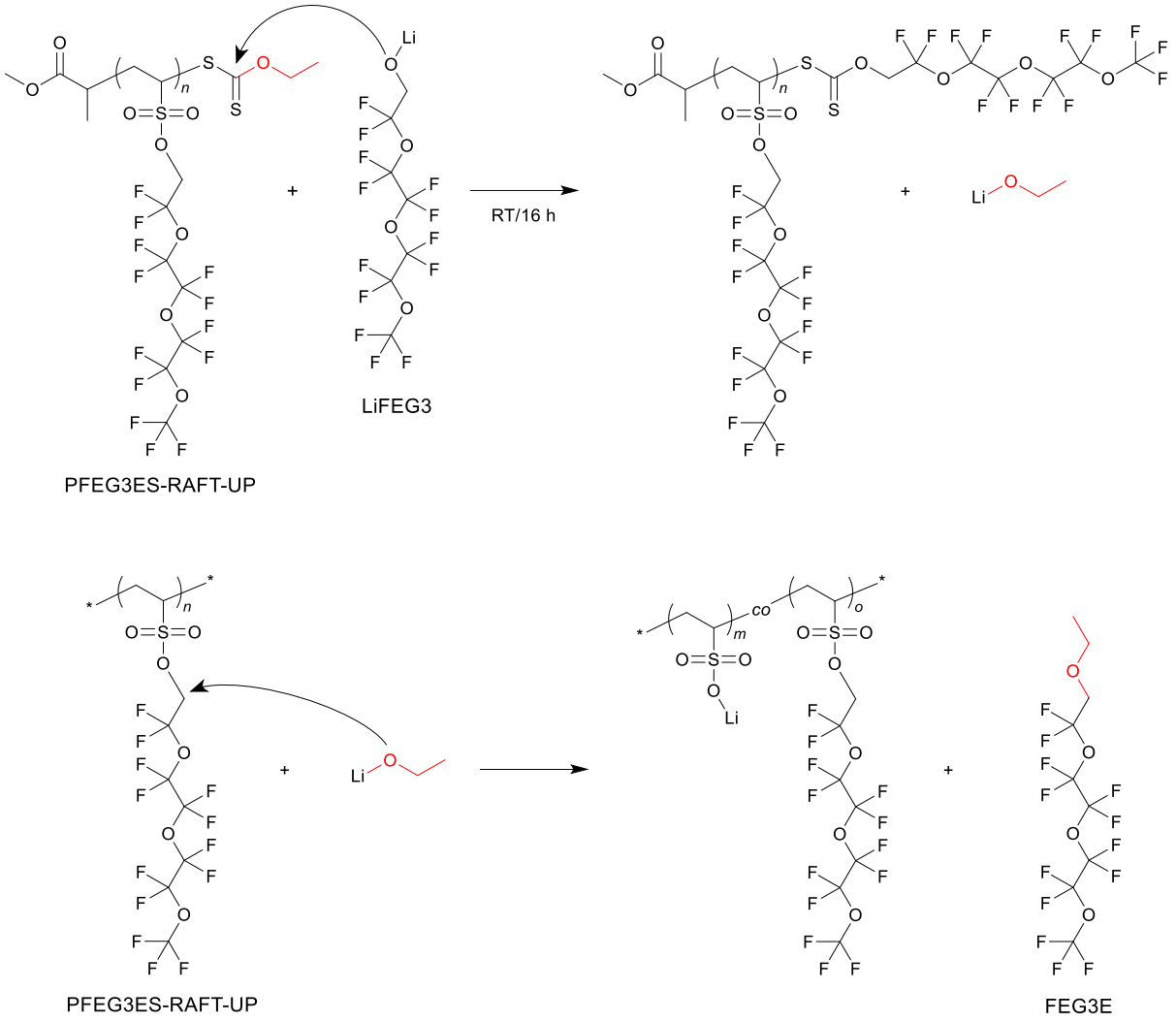

Scheme 13 Formation of the ethyl ether FEG3E via a nucleophilic substitution of LiFEG3 at the xanthate end-group of PFEG3ES-RAFT-UP with lithium ethoxide as a reactive intermediate arising during the mixing of PFEG3ES-RAFT-UP with LiFEG3 at room temperature.

Due to its undefined composition, the reaction mixture will not be further investigated for its electrochemical properties. PFEG3ES-RAFT requires the synthesis of novel lithium salts in future studies which do not react with the RAFT derived end-groups.

3.3.3 Thermal and morphological properties

3.3.3.1 Thermal stability

As can be seen from Fig. 54a and b, the thermal stability of PFEG3ES-FRP-UP was significantly higher than that of LiFEG3 ($T_{d,\,1\%}$ = 248 °C in comparison to $T_{d,\,1\%}$ = 83 °C). So the overall thermal stability of the SPEs was limited by LiFEG3. Nevertheless, the minimal thermal stability was not observed for

the highest salt concentration, SPE-5 ($T_{d,\,1\%}$ = 82 °C), but for SPE-10 ($T_{d,\,1\%}$ = 63 °C). As will be shown in the chapters 3.3.3.3 and 3.3.3.4, the lower crystallinity of SPE-10 in comparison to SPE-5 is supposed to result in a higher volatility of LiFEG3.

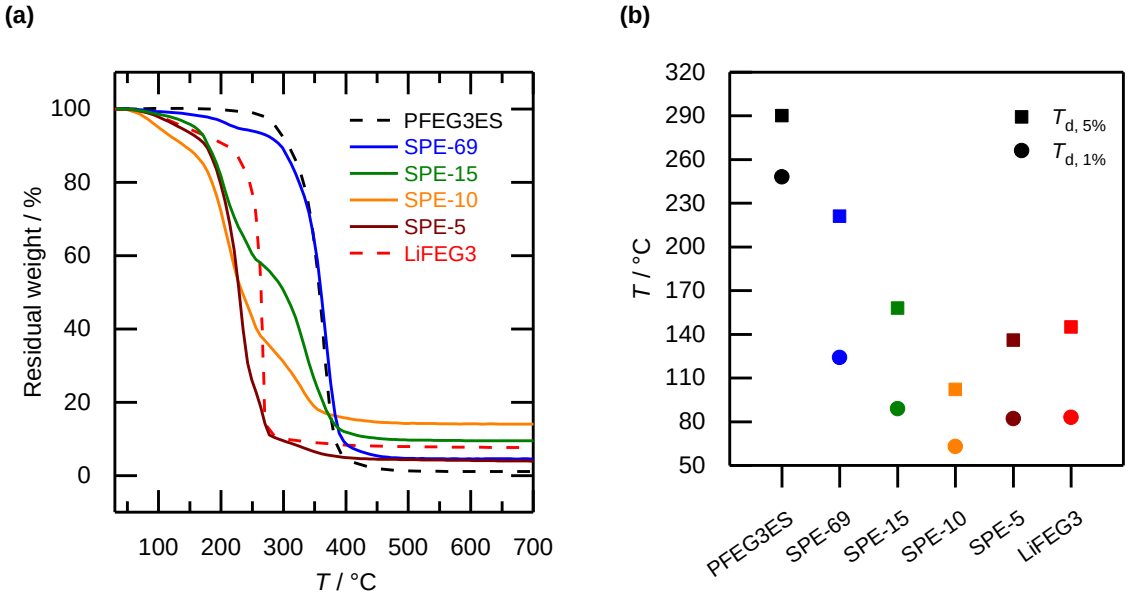

Fig. 54 (a) TGA thermograms (under nitrogen, 10 K min^{-1}) and (b) $T_{d,\,1\%}$ and $T_{d,\,5\%}$ values of the polymer PFEG3ES (PFEG3ES-FRP-UP), the lithium salt LiFEG3 and SPE-69, -15, -10 and -5.

3.3.3.2 Thermal and morphological properties of the polymer

PFEG3ES-FRP-UP is a yellowish and transparent soft solid at room temperature. By DMA two thermal transitions were observed (Fig. 55). The peak temperature of the loss factor was $T_{p,\,1b}$ = -76 °C for the first thermal transition and $T_{p,\,2}$ = 58 °C for the second thermal transition.

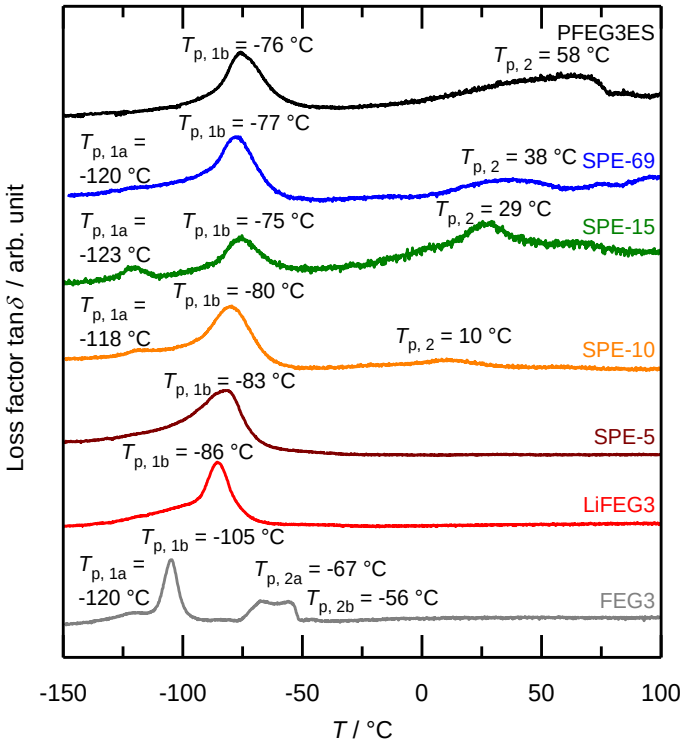

Fig. 55 Second heating DMA traces of PFEG3ES (PFEG3ES-FRP-UP), the lithium salt LiFEG3, the alcohol FEG3 and SPE-69, -15, -10 and -5 (under nitrogen, 2 K min^{-1}, 2 Hz, first heating trace in Fig. 62a).

The first thermal transition was comparable to the value measured in chapter 3.2.4 for PFEG3ES-RAFT despite a higher dispersity and molecular weight of PFEG3ES-FRP-UP ($M_{p,\,SEC}$ = 11,700 g mol^{-1} and $Đ$ = 1.87 in comparison to $M_{p,\,SEC}$ = 3,900 g mol^{-1} and $Đ$ = 1.24). As mentioned above, the first thermal transition can be attributed to the starting of segmental motion of the FEG3 side-chains of PFEG3ES. By the help of DSC the second thermal transition observed by DMA could be attributed to a glass transition (T_g = 34 °C, Fig. 56a). The higher molecular weight and dispersity of PFEG3ES-FRP-UP compared to PFEG3ES-RAFT increased the T_g from 17 °C to 34 °C.

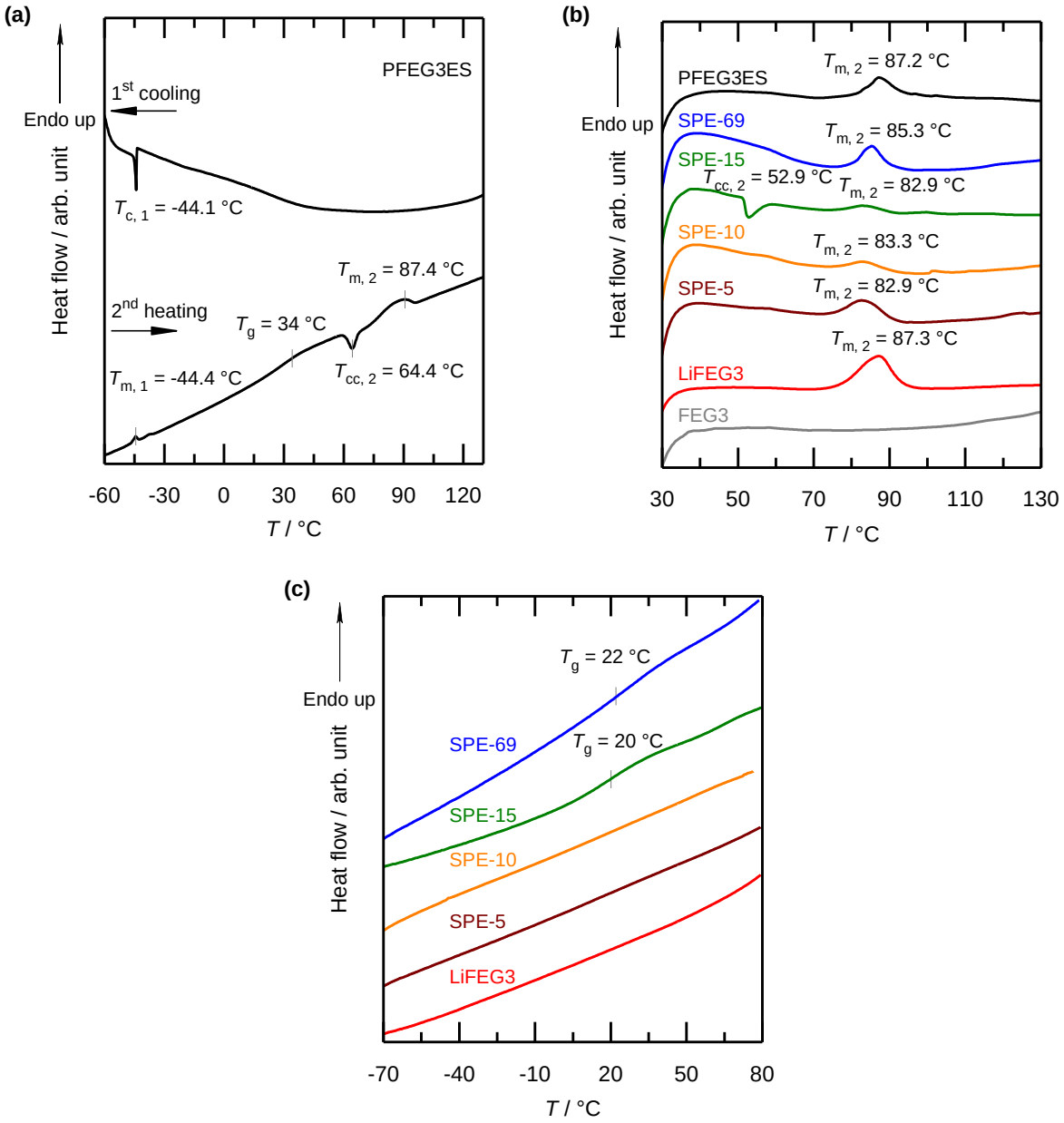

Fig. 56 DSC traces of PFEG3ES (PFEG3ES-FRP-UP), the lithium salt LiFEG3, the alcohol FEG3 and SPE-69, -15, -10 and -5 (under nitrogen, 10 K min^{-1}). (a) First cooling and second heating DSC traces, (b) first heating DSC traces measured comparably to the temperature program used for ionic conductivity measurements and (c) second heating DSC traces (first heating traces for (a) and (c) in Fig. 62b). For (a) and (c) needle-pierced aluminum crucibles and for (b) sealed high pressure stainless steel crucibles were used during the measurement.

In contrast to PFEG3ES-RAFT, two additional melting peaks by DSC, $T_{m,1}$ = -44.4 °C ($\Delta H_{m,1}$ = 0.13 J g^{-1}) and $T_{m,2}$ = 87.4 °C ($\Delta H_{m,2}$ = 0.71 J g^{-1}) were observed. The latter resulted from a preceding cold crystallization peak ($T_{cc,2}$ = 64.4 °C, $\Delta H_{cc,2}$ = -0.60 J g^{-1}). The melting peak $T_{m,1}$ was linked to a crystallization peak occurring in the preceding first cooling curve ($T_{c,1}$ = -44.1 °C,

$\Delta H_{c,\,1}$ = -0.16 J g^{-1}, Fig. 56a). The observations that $T_{m,\,1}$ was below T_g and the presence of the second melting temperature $T_{m,\,2}$ point to the presence of two phases.

3.3.3.3 Thermal and morphological properties of the lithium salt

The lithium salt LiFEG3 is a white, slightly turbid and viscous liquid at room temperature. As can be seen from the analysis by DMA and DSC, two thermal transitions were present (Fig. 55 and Fig. 56b). The first transition occurred at a peak temperature of $T_{p,\,1b}$ = -86 °C. As in the case of PFEG3ES, this transition can be assigned to the start of the segmental motion of the fluorinated ethylene glycol chains.[10] The second transition, a melting point as proven by DSC, occurred at T_m = 87.3 °C.
Polarization microscopy with crossed polarizers confirmed the observation from DSC. Birefringent crystallites melted between 80 °C and 100 °C resulting in a darkening of the microscopy image (Fig. 57). At room temperature, LiFEG3 is semi-crystalline containing a liquid amorphous phase and a crystalline phase explaining the turbid appearance of the salt. According to its thermal properties LiFEG3 can be classified as an ionic liquid.[179,180]

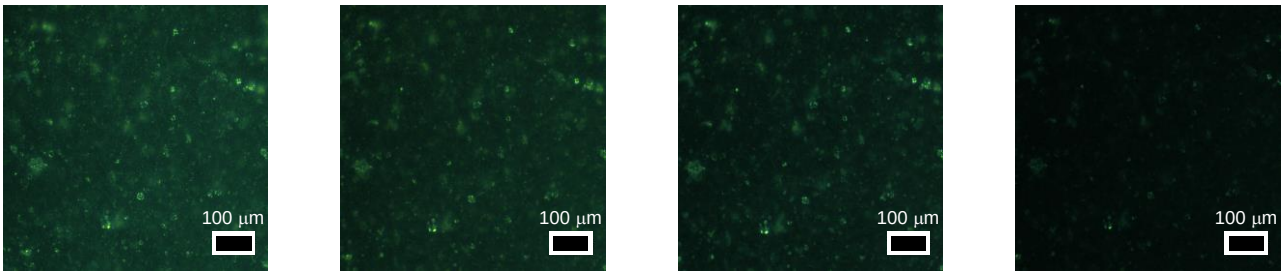

Fig. 57 Polarization microscope images of the lithium salt LiFEG3 heated from 25 to 100 °C at a rate of 10 K min^{-1}. Crossed polarizers were used. The bright regions are attributed to the birefringent crystalline domains of LiFEG3 which started melting around 80 °C resulting in a darkening of the images at higher temperatures.

The conclusion that T_m = 87.3 °C is a melting point and not an exothermal decomposition process of LiFEG3 was drawn from the following results. Possible decomposition products of LiFEG3 after the DSC measurement with high pressure crucibles were investigated by ^{1}H NMR spectroscopy (Fig. 56b and Fig. 58). Perfluorodecalin (PFD), $CDCl_3$, DMSO-d_6 and CD_3OD were used as solvents. Whereas the white, slightly turbid and viscous liquid was completely soluble in CD_3OD and PFD, it was insoluble in $CDCl_3$ and DMSO-d_6.

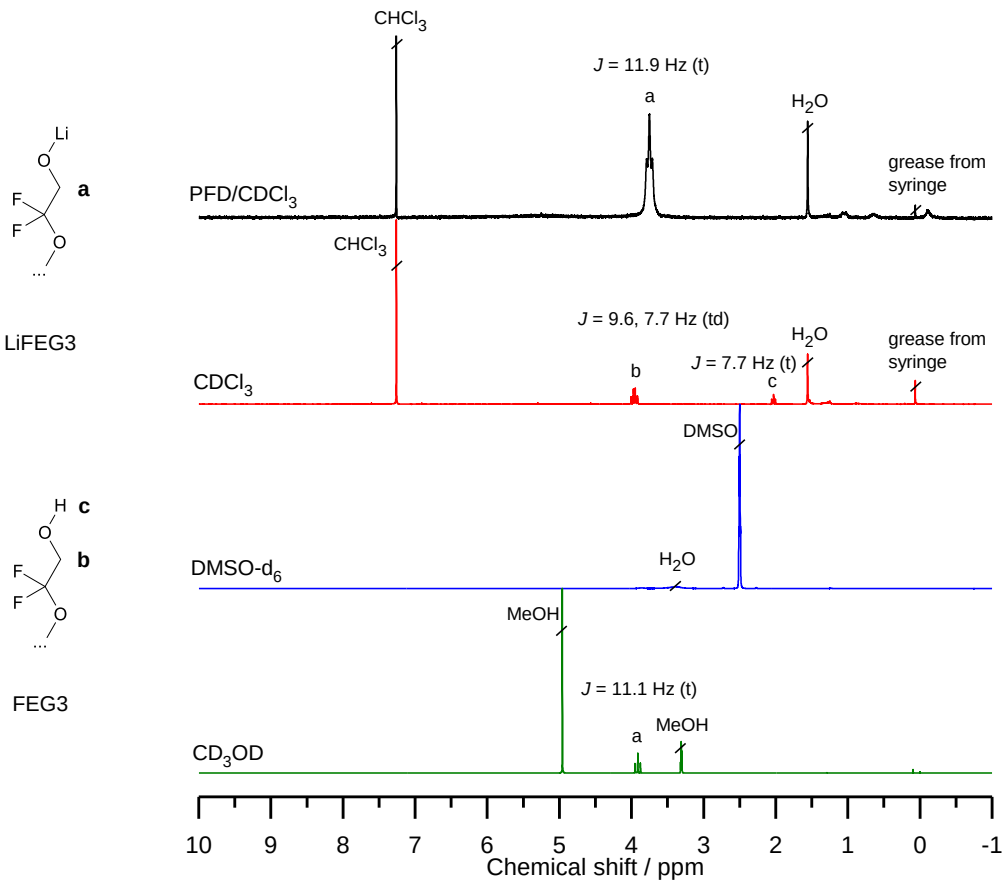

Fig. 58 ^{1}H NMR spectra of the salt LiFEG3 after the DSC measurement in high pressure crucibles in perfluorodecalin (PFD) with $CDCl_3$ in a coaxial insert, in $CDCl_3$, in DMSO-d_6 and in CD_3OD.

In the case of $CDCl_3$, signals of very low intensity of FEG3 were detected. These can result from a reaction of LiFEG3 with water which is present in low concentrations in $CDCl_3$. In all spectra there were no hints to possible decomposition products. LiFEG3 is probably highly volatile after the melting of its crystalline phase. Therefore, a weight loss above 80 °C started during the TGA measurement (chapter 3.3.3.1).

Unlike LiFEG3, the alcohol FEG3 used for the synthesis of LiFEG3 (Scheme 11) is a colorless transparent liquid at room temperature. It also showed two thermal transitions. However, both were significantly shifted to lower temperatures, quite below room temperature and spilt into double peaks, at $T_{p,\,1a}$ = -120 °C / $T_{p,\,1b}$ = -105 °C and at $T_{p,\,2a}$ = -67 °C / $T_{p,\,2b}$ = -56 °C (Fig. 55 and Fig. 56b). This comparison underpins the formation of LiFEG3 and the successful removal of excess FEG3 in LiFEG3. Moreover, this comparison suggests the formation of crystalline ionic clusters in the case of LiFEG3 below its T_m resulting from strong ionic interactions between the polar lithium/alkoxide head groups. In contrast, the interactions of the hydroxyl head groups in FEG3 must be significantly weaker since the second thermal transition is shifted to a much lower temperature.

3.3.3.4 Thermal and morphological properties of the solid polymer electrolytes

An increasing salt concentration in the SPEs resulted only in a slight decrease of the first thermal transition $T_{p,\,1b}$ determined by DMA. It decreased from -76 °C for the pure polymer to -77 °C for the SPE-69 and to -83 °C for the SPE-5 (Fig. 55). A decrease of the second thermal transition temperature $T_{p,\,2}$ determined by DMA and of the corresponding glass transition temperature T_g determined by DSC was more pronounced. In general, DMA was more sensitive to detect the glass transition temperatures. The thermal transitions determined by DMA occurred at higher temperatures than those measured by DSC. The $T_{p,\,2}$ decreased from 58 °C for the pure polymer to 38 °C for the SPE-69 and to 10 °C for the SPE-10 (Fig. 55 and Fig. 60a). The T_g decreased from 34 °C for the pure polymer to 22 °C for the SPE-69 and to 20 °C for the SPE-15 (Fig. 56a and c). For the SPE-69, -15 and -10 an additional thermal transition $T_{p,\,1a}$ occurred around -120 °C. Since $T_{p,\,1a}$ was not observed for the pure polymer and salt, it must result from interactions between PFEG3ES and LiFEG3.

The thermal transitions $T_{p,\,1a}$ and $T_{p,\,2}$ could not be detected for the SPE-5 due to the low concentration of polymer in the electrolyte. The same explanation can be the reason for the absence of the glass transition temperature T_g measured by DSC for the SPE-10 and -5 (Fig. 56c).

3.3.4 Electrochemical properties

3.3.4.1 Ionic conductivity

The ionic conductivity of all SPEs and LiFEG3 was determined by impedance spectroscopy. In general, there were two main tendencies for the dependency of the ionic conductivity on the salt concentration. Firstly, all SPEs with the exception of SPE-69 and -15 below 70 °C showed a higher ionic conductivity compared to the pure salt LiFEG3 (Fig. 59). Secondly, the ionic conductivity of the SPEs increased with increasing salt concentration reaching a maximum ionic conductivity of $(1.22 \pm 0.24) \times 10^{-6}$ S cm^{-1} at 80 °C for SPE-5.

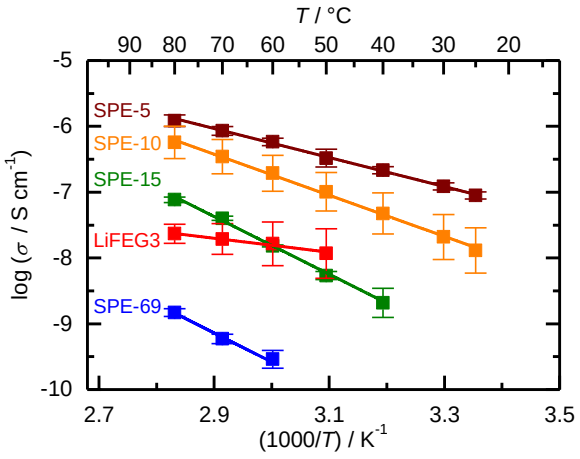

Fig. 59 Arrhenius plot for the ionic conductivity σ of the lithium salt LiFEG3 and the solid polymer electrolytes, SPE-69, -15, -10 and -5. The error bar for log σ was calculated according to the error propagation law from the standard deviation of at least three independently measured coin cells (equation (37)). Linear fitting curves are depicted as solid lines (see Table 23 for fitting data).

The T_g has a major influence on the ionic conductivity and is dependent on the salt concentration. The lower T_g, the higher is the chain mobility of the polymer above T_g. The ionic conductivity for a temperature of 70 °C, which is already above the glass transition temperatures of all SPEs, increases with increasing salt concentration. This behavior can be explained by the decrease of T_g as shown in Fig. 60a. Obviously, the FEG3 anion has a plasticizing effect on PFEG3ES which is comparable to the one of the TFSI anion in PEG-based polymer electrolytes.[32,76,162]

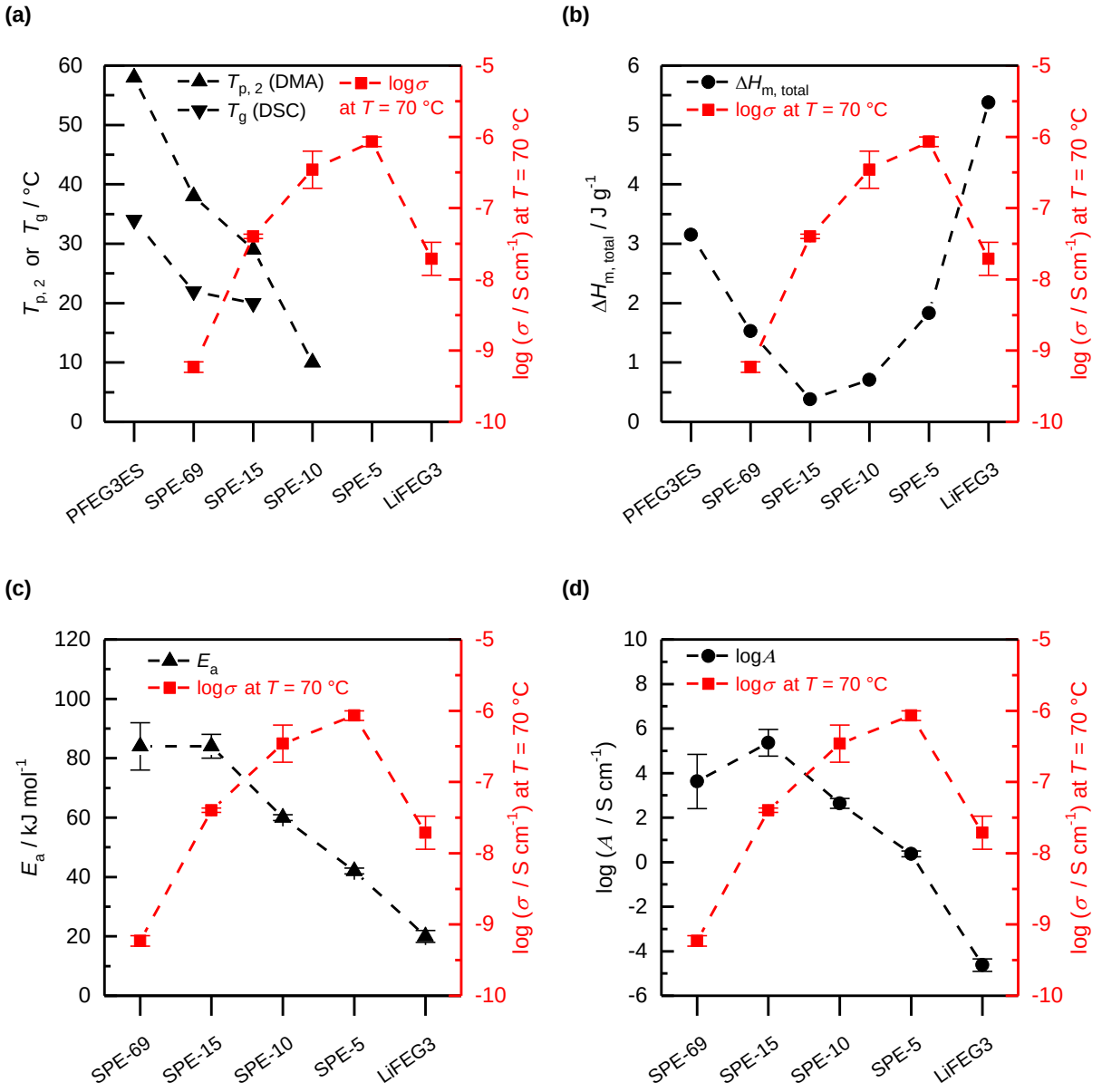

Fig. 60 Correlation of the logarithm of ionic conductivity log σ at 70 °C (a) with the second thermal transition $T_{p,2}$ determined by DMA (from Fig. 55) or the glass transition temperature T_g determined by DSC (from Fig. 56a and c), (b) with the total melting enthalpy of the SPEs $\Delta H_{m,\,total}$ (determined from the melting peaks in Fig. 56b), (c) with the activation energy for the ion movement E_a and (d) with the logarithm of the pre-exponential factor log A. The corresponding values for PFEG3ES (PFEG3ES-FRP-UP) and LiFEG3 were plotted as references. The error bars for log σ, E_a and log A were calculated according to the error propagation law (equations (37), (40) and (42)). The dashed lines are guides to the eyes.

The salt concentration dependent total melting enthalpy of the SPEs $\Delta H_{m,\,total}$ has another significant influence on the ionic conductivity. Only the total crystallinity could be considered since the melting temperature peaks of PFEG3ES and LiFEG3 appeared both around 85 °C (Fig. 56b). The addition of

LiFEG3 to PFEG3ES and *vice versa* resulted in a significant decrease of the total crystallinity and in an increase of the ionic conductivity at 70 °C (Fig. 60b). This temperature is still below the melting temperature of the crystalline domains.

As can be concluded from the linear dependency of the ionic conductivity on the inverse temperature T^{-1}, the temperature dependency of the ionic conductivity follows Arrhenius behavior (Fig. 59). The ion transport is dominated by thermal hopping processes in a mainly rigid environment without a contribution of the segmental motions of the polymer.[29,181] From the slope *m* and the intercept *b* of the linear fitting curves the activation energy for the ion movement E_a and the pre-exponential factor *A* were calculated (equations (36) and (38) to (41), Table 23).

The dependencies of E_a and *A* on the salt concentration and their correlation with the ionic conductivity at 70 °C are depicted in Fig. 60c and d. The course of the curve for E_a follows the development of T_g (Fig. 60a). The one of *A* is reciprocal to the course of $\Delta H_{m,\,total}$ (Fig. 60b). When the salt concentration decreased from an O/Li ratio of 69 to 15, E_a remained nearly constant within its error. *A* and the ionic conductivity at 70 °C increased by more than one order of magnitude. *A* is proportional to the concentration and charge of the ions which contribute to the ionic conductivity.[29,181] The maximum of *A* and the minimum of $\Delta H_{m,\,total}$ were observed for SPE-15. Therefore, a lower $\Delta H_{m,\,total}$ can be the reason for a higher concentration of conducting ions. The maximum ionic conductivity did not correlate with the minimum of $\Delta H_{m,\,total}$. In fact, it is shifted to a higher salt concentration, to an O/Li ratio of 5. For higher salt concentrations than O/Li = 15, E_a and *A* decreased. However, the decrease of E_a was crucial for the increase of the ionic conductivity. Even though the pure LiFEG3 showed the lowest E_a, it also exhibited the lowest *A*. Thus, the ionic conductivity decreased significantly in comparison to SPE-15. The E_a of LiFEG3 (20 kJ mol^{-1}) is already in the range of typical gel polymer electrolytes.[181,182]

All in all, to escape the dilemma of increasing crystallinity of the SPE with increasing salt amount, the salt concentration should be kept constant at an O/Li ratio of 15. At the same time, T_g should be decreased independently from *A* by the addition of plasticizing additives different from LiFEG3.

3.3.4.2 Electrochemical stability

Cyclic voltammetry (CV) was applied to evaluate the electrochemical stability window of SPE-10 as a representative for all SPEs. Copper was used as a working and lithium as a reference/counter electrode. At first, CV of the pure polymer PFEG3ES and the lithium salt LiFEG3 was measured to check their purity. They were electrochemically stable up to at least 10 V vs. Li/Li$^+$ at 60 °C (Fig. 61a and b). Only

weak capacitive current occurred in the case of LiFEG3 as it was expected due to the internal polarization of the electrolyte.

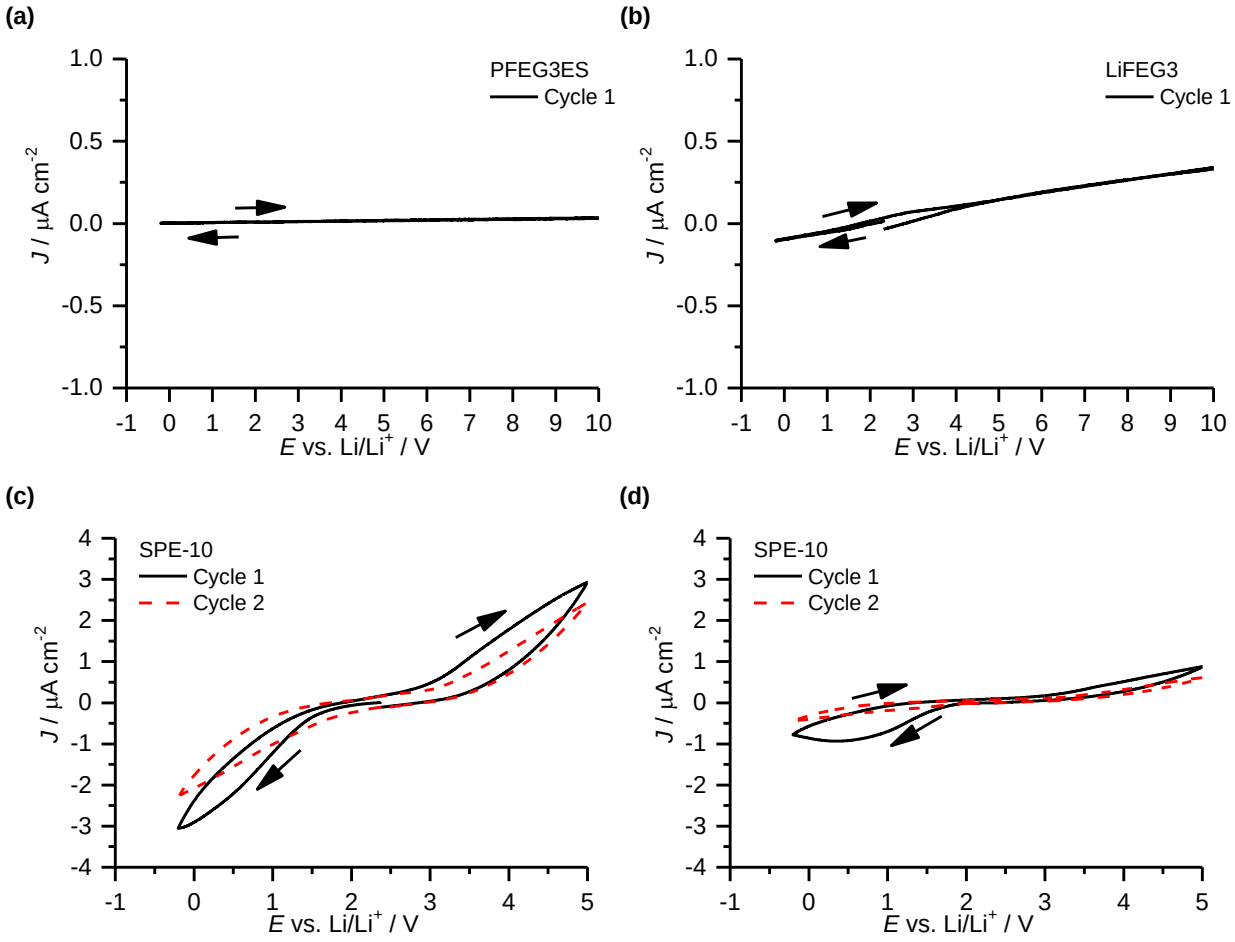

Fig. 61 Cyclic voltammograms vs. Li/Li^+ of (a) the polymer PFEG3ES (PFEG3ES-FRP-UP) measured at 80 °C, (b) the lithium salt LiFEG3 and (c, d) the SPE-10 measured each at 60 °C. (a-c) were measured at a scan rate of 1 mV s^{-1}; (d) was measured at 0.2 mV s^{-1}.

For LiFEG3 and SPE-10 neither lithium plating nor stripping on the copper electrode were observed (Fig. 61c). They typically occur as a sharp anodic and cathodic peak at a potential being just smaller and higher than 0 V vs. Li/Li^+, respectively. As reported in the literature, the use of electrode materials different from copper or new additives might enable the lithium plating/stripping process by lowering the electrode/electrolyte interface resistance.[183,184]

SPE-10 showed a more distinct hysteresis character than LiFEG3 due to the more than tenfold higher ionic conductivity. No current peaks occurred as they typically arise from electrochemical reactions. The current density *J* was lower than 4.0 µA cm^{-2} within the given potential range between -0.2 V and 5 V vs. Li/Li^+. *J* was even lower when the scan rate was decreased from 1 mV s^{-1} to 0.2 mV s^{-1} (Fig. 61d). These observations revealed that the SPE-10 and thus the perfluoropolyether, alkoxy and

sulfonate ester groups were electrochemically stable up to at least 5 V vs. Li/Li^+ at 60 °C. So the SPEs are of great importance for the application in lithium polymer batteries in combination with high-potential cathode materials.

4 Experimental Section

4.1 Materials

Most chemicals were purchased from Sigma-Aldrich, TCI Germany, Merck Schuchardt or abcr and used as received. The following compounds were treated as follows before use. All solvents and 2-difluoro-2-(1,1,2,2-tetrafluoro-2-(1,1,2,2-tetrafluoro-2-(trifluoromethoxy)ethoxy)ethoxy)ethanol (FEG3, 98%) were distilled. The solvents were also dried over molecular sieves. 2-Methoxyethanol was purchased in anhydrous form. 2,2'-Azobis(isobutyronitrile) (AIBN, 98%) was purified by recrystallization from methanol. PEG750-OH with a molecular weight of 750 g mol^{-1} (Sigma-Aldrich) and PEG2000-OH with a molecular weight of 2000 g mol^{-1} (Fluka), as noted by the suppliers, were used. PEG750-OH, PEG2000-OH and LiTFSI (Sigma-Aldrich, battery grade, ≥ 99.99%) were dried in high vacuum at 80 °C for one day and stored in an argon-filled glovebox before the SPE preparation. The Kapton® (DuPont, HN grade) ring spacers, the stainless steel electrodes (MTI Corporation, 304 stainless), the copper foil (ChemPUR, ≥ 99.99%) and all parts of the CR2032 coin cell set-up (MTI Corporation) were washed with ethanol and dried in high vacuum overnight. The surfaces of the copper and lithium (Sigma-Aldrich, ≥ 99.9%) foils were slightly scraped in the glovebox before the use as electrodes.

4.2 General sample handling

All SPE and LiFEG3 containing samples were prepared in an argon-filled glovebox with an oxygen content < 1 ppm and a water content < 0.1 ppm. For the thermal gravimetric analysis (TGA), dynamic mechanical analysis (DMA) and analysis by polarization microscopy, hermetical sealing of the samples in the glovebox was not possible, but the samples were transferred under argon to the instrument just before starting the measurement. The samples for differential scanning calorimetry (DSC) were prepared and hermetically sealed in crucibles in the glovebox. All cell assemblies and disassemblies for the electrochemical characterization were performed in the glovebox.

4.3 Methods

4.3.1 Infrared spectroscopy

Infrared (IR) spectra were recorded with a PerkinElmer Spectrum 100 FT (Fourier transform)-IR spectrometer using the attenuated total reflection (ATR) method. Structure elements written in bold indicate the vibrating group at the noted wavenumber given in cm^{-1}.

4.3.2 NMR spectroscopy

^{1}H (300 MHz), ^{13}C (75 MHz) and ^{19}F (282 MHz) NMR spectra were recorded on a Bruker Avance 250 spectrometer at room temperature. Chemical shifts δ were noted in ppm and coupling constants J in Hz. Multiplicities were reported as singlet (s), doublet (d), triplet (t), quartet (q), doublet of doublets (dd), multiplet (m) and broadened (br). The signal was caused by the structure elements written in italics. For ^{1}H and ^{13}C NMR spectroscopy chemical shifts were noted relative to the known value of residual non-deuterated solvent: $CDCl_3$ (^{1}H: 7.26 ppm and ^{13}C: 77.0 ppm), CD_3OD (^{1}H: 3.31 ppm) and DMSO-d_6 (^{1}H: 2.50 ppm). When perfluorodecalin (PFD) was used as a solvent, a $CDCl_3$ filled coaxial insert for locking the NMR signal was added. For ^{19}F NMR spectroscopy, $CDCl_3$ or CD_3OD were used as solvents, but chemical shifts were noted relative to the known value of hexafluorobenzene (HFB) added as an internal standard: C_6F_6 (^{19}F: -164.9 ppm).

4.3.3 Elemental analysis

Weight contents (in wt%) of carbon, hydrogen, nitrogen and sulfur were determined by a HEKAtech EA 3000 element analyzer.

4.3.4 THF-Size exclusion chromatography

SEC was performed to determine the number-average molecular weight $M_{n,\,SEC}$, the peak molecular weight $M_{p,\,SEC}$ and the dispersity $Đ$ of the molecular weight distribution. For all other compounds than PPOS-*g*-PEG750 and PPOS-*g*-PEG2000, only THF was used as an eluent. For PTMSPOS, PPOS, PEG750-N3 and PEG2000-N3, the set-up was equipped with two separation columns (Agilent, PL Resipore, particle size 3 µm). For PPOS-*g*-PEG750 and PPOS-*g*-PEG2000, THF with 0.25 wt% tetrabutylammonium bromide (TBAB) was used as an eluent. The system was composed of a guard

column (Polymer Standards Service GmbH (PSS), gel on styrene divinylbenzene-basis, particle size 5 µm) and two separation columns (Varian, mixed-C gel, particle size 5 µm). For both SEC systems a Waters 510 HPLC pump, a refractive index (RI) detector (Waters 410) and a UV detector (Waters 2489) were used. For all other samples, the system was equipped with a Waters 515 HPLC pump, a guard column (ResiPore Guard, 5 x 0.75 cm, particle size 3 µm), two separation columns (ResiPore, 30 x 0.75 cm, particle size 3 µm) and an RI detector (Waters 414). For all samples, a flow rate of 0.5 mL min^{-1}, linear poly(styrene) (PS) standards for calibration and 1,2-dichlorobenzene as an internal reference were used. Samples were filtered through a syringe filter (PTFE, pore size 0.2 µm) previous to injection. Integration thresholds were noted as small markers in the SEC traces if the whole shown curve was not integrated.

4.3.5 HFIP-Size exclusion chromatography

$M_{n,\,SEC}$, $M_{p,\,SEC}$ and $Đ$ of the molecular weight distribution were obtained by size exclusion chromatography (SEC) with hexafluoroisopropanol (HFIP) containing 0.5 wt% potassium trifluoroacetate (KTFA) as an eluent. Small peaks in the SEC traces were observed appearing at higher molecular weights next to the main peak (Fig. 41 and Fig. 42b). Since these peaks were not detected by MALDI-ToF MS (Fig. 44), they must be measurement artifacts of the sample on the SEC column. Therefore, HFIP-SEC served only for a qualitative and fast analysis tool to estimate and compare the molecular weight distributions of the fluorinated polymers. For PFEG2ES-FRP, only one separation column (PSS PFG 300, particle size 7 µm) was used, whereas for the other samples the SEC was equipped with an additional column (PSS PFG 100, particle size 7 µm). A flow rate of 0.5 mL/min was provided by an Agilent 1200 isocratic pump. Molecular weight distributions were recorded with an RI detector (Gynkotek) at 23 °C. Poly(methyl methacrylate) (PMMA) standards for calibration were used and toluene as an internal reference. Integration thresholds were noted as small markers in the SEC trace.

4.3.6 Matrix-assisted laser desorption/ionization time-of-flight mass spectrometry

MALDI-ToF MS spectra were recorded on a Bruker Reflex III time-of-flight mass spectrometer equipped with a nitrogen laser (337 nm) and a HIMAS detector. Protein standards served for mass calibration. For PEG750-N3, PEG2000-N3, PPOS-*g*-PEG750 and PPOS-*g*-PEG2000, *trans*-3-indoleacrylic acid (IAA) was used as a matrix. Solutions of IAA (0.01 mg $µL^{-1}$) and of polymer

(0.01 mg μL^{-1}) in THF were mixed in a 20/5 (v/v) ratio. For PEGES-FRP, *trans*-2-[3-(4-*tert*-butyl-phenyl)-2-methyl-2-propenylidene]malononitrile (DCTB) was used as a matrix. Solutions of DCTB (0.02 mg/µL) and of polymer (0.01 mg/µL) in THF were mixed in a 30/2 (v/v) ratio. For PEES-RAFT1, solutions of IAA (0.02 mg/µL) and of polymer (0.01 mg/µL) in THF were mixed in a 30/1 (v/v) ratio. For PEES-RAFT2, the resolution of the spectrum was best when the solutions were mixed in a 4/1 (v/v) ratio. For PFEGES-RAFT, 2,5-dihydroxybenzoic acid (DHB) was used as a matrix. Solutions of DHB (0.02 mg/µL) in HFB/THF (4/1 (v/v)) and of polymer (0.01 mg/µL) in HFB were mixed in a 30/1 (v/v) ratio. The solutions were dotted onto a MALDI target plate and dried at room temperature before the measurement. In all cases MALDI spectra showed a better resolution and higher intensity without the use of a salt. The peak molecular weight $M_{p,\,MALDI}$ was determined from the peak with the highest intensity of the spectra. The isotopic mean values of the end-groups averaged over all noted peak series were calculated from the isotopic mean values for each peak series.

4.3.7 Thermal gravimetric analysis

For PFEG2ES-RAFT, PFEG3ES-RAFT and PEES-RAFT2, TGA thermograms were obtained with a Mettler Toledo TGA/SDTA851. For all other samples, a Mettler Toledo TGA/DSC 3^+ system was used. Samples (5-20 mg) were heated from 30 to 700 °C at a rate of 10 K min^{-1} under nitrogen flow. The temperature at which the samples lost 1 wt% and 5 wt% were denoted as $T_{d,\,1\%}$ and $T_{d,\,5\%}$, respectively (listed in Table 16 for PFEG3ES-FRP-UP, its SPEs and LiFEG3).

Table 16 Thermal properties of the polymer PFEG3ES-FRP-UP, the alcohol FEG3, the lithium salt LiFEG3 and SPE-69, -15, -10 and -5.

Sample	$T_{d,\,1\%}$[a] (°C)	$T_{d,\,5\%}$[a] (°C)	$T_{p,\,1a}$[b] (°C)	$T_{p,\,1b}$[b] (°C)	$T_{p,\,2}$[b] (°C)	T_g[c] (°C)
PFEG3ES-FRP-UP	248	290	n.o.	-76	58	34
SPE-69	124	221	-120	-77	38	22
SPE-15	89	158	-123	-75	29	20
SPE-10	63	102	-118	-80	10	n.o.
SPE-5	82	136	n.o.	-83	n.o.	n.o.
LiFEG3	83	145	n.o.	-86	n.o.	n.o.
FEG3	-	-	-120	-105	-67[e]	-

$T_{m,\,1}$[c] (°C)	$T_{cc,\,2}$[c] (°C)	$T_{m,\,2}$[c] (°C)	$T_{cc,\,2}$[d] (°C)	$\Delta H_{cc,\,2}$[d] (J g^{-1})	$T_{m,\,2}$[d] (°C)	ΔH_m[d] (J g^{-1})
-44.4	64.4	87.4	n.o.	n.o.	87.2	3.15
n.o.	n.o.	-	n.o.	n.o.	85.3	1.53
n.o.	n.o.	-	52.9	0.51	82.9	0.38
n.o.	n.o.	-	n.o.	n.o.	83.3	0.71
n.o.	n.o.	-	n.o.	n.o.	82.9	1.83
n.o.	n.o.	-	n.o.	n.o.	87.3	5.38
-	-	-	n.o.	n.o.	n.o.	n.o.

[a]Determined by TGA (under nitrogen, 10 K min^{-1}). [b]Obtained from the second heating DMA trace (under nitrogen, 2 K min^{-1}, 2 Hz). [c]Obtained from the second heating DSC trace (pin holed aluminum crucibles, under nitrogen, 10 K min^{-1}). [d]Obtained from the first heating DSC trace (closed high pressure crucibles, under nitrogen, 10 K min^{-1}). [e]Multiple peak. n.o.: not observed. '-': not measured.

4.3.8 Dynamic mechanical analysis

Dynamic mechanical analysis (DMA) traces were obtained from a Mettler Toledo DMA 1 Star^e system measuring in single cantilever bending geometry. Samples were measured at a bending frequency of 2 Hz and a heating/cooling rate of 2 K min^{-1} under nitrogen flow. After each temperature ramp, the sample was kept for 10 min at the respective temperature. For the loss factor tan δ, which is the ratio of the loss modulus E'' to the storage modulus E', the peak temperature T_p was reported from the second heating (Fig. 49, Fig. 55 and Table 16). For PFEG3ES-FRP-UP, PFEG2ES-RAFT and PFEG3ES-RAFT, the sample was molten at 100 °C in the sample holder on a hot plate and cooled down to room temperature again to achieve a homogeneous polymer film. It was heated from 25 °C to 100 °C (PFEG2ES-RAFT) and to 140 °C (PFEG3ES-FRP-UP and PFEG3ES-RAFT), respectively, cooled down to -150 °C and then heated again (second heating). The PFEG3ES-FRP-UP/LiFEG3 SPEs and LiFEG3 were treated similar to the temperature program which was used for the measurement of the ionic conductivity. The samples were tempered at 40 °C for 5 h, cooled to 25 °C, heated to 110 °C,

cooled to -150 °C and heated to 110 °C (second heating). FEG3 was directly cooled from 20 to -150 °C and heated to 110 °C (pseudo second heating), since it has already been liquid at room temperature (first heating DMA traces are shown in Fig. 62a).

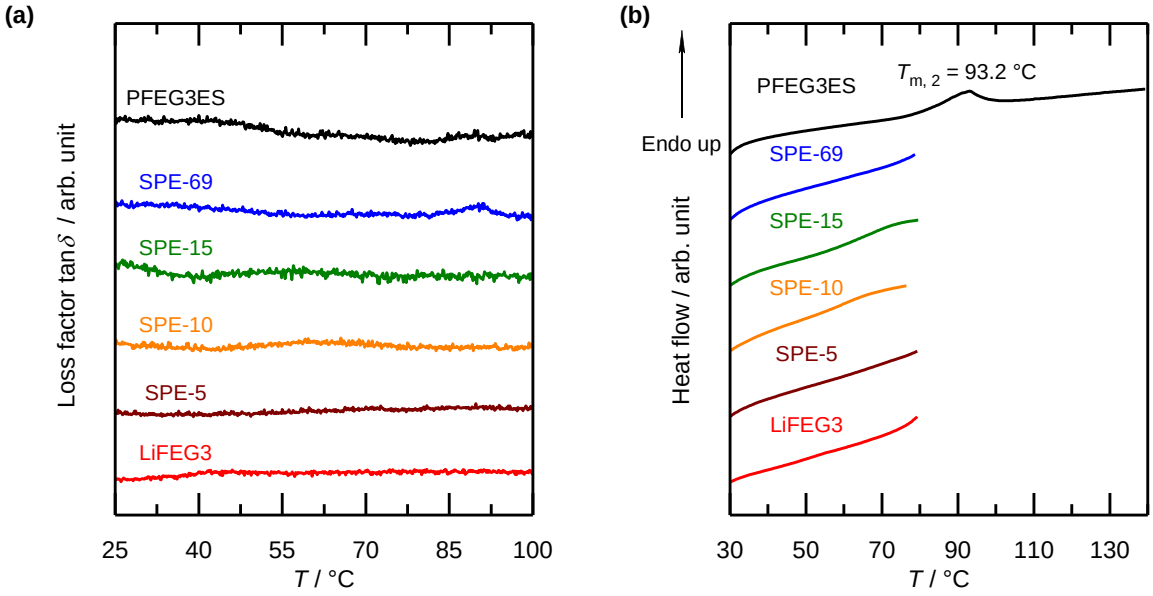

Fig. 62 Thermal properties of the polymer PFEG3ES (PFEG3ES-FRP-UP), the lithium salt LiFEG3 and SPE-69, -15, -10 and -5 determined by DMA (under nitrogen, 2 K min^{-1}, 2 Hz) and DSC (under nitrogen, 10 K min^{-1}). (a) First heating DMA traces and (b) first heating DSC traces (during the measurement needle-pierced aluminum crucibles).

4.3.9 Differential scanning calorimetry

DSC thermograms were obtained using a Mettler Toledo DSC 3$^+$ or DSC 2 system. All samples were measured at a heating/cooling rate of 10 K min^{-1} under nitrogen flow. After each temperature ramp, an isothermal step of 10 min was performed at the end temperature. Calibration was performed with an indium standard. All DSC traces were plotted with the endothermic heat flow shown up on the ordinate axis. The glass transition temperature T_g was defined as the inflection point of the heating trace. The melt-crystallization temperature T_c, cold-crystallization temperature T_{cc} and melting temperature T_m were defined as the minimum and maximum peak values of the cooling/heating traces, respectively. Some of the shown differential scanning calorimetry (DSC) curves were enlarged for an easier identification of the thermal transitions. The normalized melt-crystallization enthalpy ΔH_c, cold-crystallization enthalpy ΔH_{cc} and melting enthalpy ΔH_m were determined from the raw data curves by the integration of the peaks (Table 2, Table 3, Fig. 50 and Table 16).

For the Mettler Toledo DSC 3$^+$ system, aluminum crucibles were used which were pierced with a needle during the measurement. PEG750-OH, PEG2000-OH, L750-25, L750-16 and L750-12 were

heated from -80 °C to 200 °C, cooled to -80 °C (first cooling) and then heated again (second heating). The other polymers which served for the synthesis of the PPOS-*g*-PEG750 and PPOS-*g*-PEG2000 SPEs as well as these SPEs themselves were heated to an upper end temperature of 150 °C instead of 200 °C (Fig. 30-32). PFEG2ES-RAFT and PFEG3ES-RAFT/PFEG3ES-RAFT-UP were heated from 25 °C to 100 °C and to 140 °C, respectively, cooled to -80 °C (first cooling) and then heated again (second heating, Fig. 50). PFEG3ES-FRP-UP was heated from 25 to 140 °C (first heating, Fig. 62b), cooled to -80 °C (first cooling) and heated to 140 °C (second heating, Fig. 56a). The PFEG3ES-FRP-UP/LiFEG3 SPEs and LiFEG3 were treated comparably to the temperature program which was used for the measurement of the ionic conductivity. The samples were tempered at 40 °C for 5 h, cooled to 25 °C, heated to 80 °C (first heating, Fig. 62b), cooled to -80 °C and heated to 80 °C (second heating, Fig. 56c).

DSC thermograms, for which sealed high pressure stainless steel crucibles were necessary to prevent a possible material release of LiFEG3 or FEG3 at temperatures > 80 °C into the instrument, were obtained using a Mettler Toledo DSC 2 system (Fig. 56b). PFEG3ES-FRP-UP and FEG3 were heated from 25 to 140 °C (first heating). The PFEG3ES-FRP-UP/LiFEG3 SPEs and LiFEG3 were tempered at 40 °C for 5 h, cooled to 25 °C and heated to 140 °C (first heating). To detect possible decomposition products of LiFEG3 after the DSC measurement, the high pressure crucible of LiFEG3 was opened and the content was investigated by ^{1}H NMR spectroscopy using PFD, $CDCl_3$, DMSO-d_6 and CD_3OD as solvents (Fig. 58).

4.3.10 Wide-angle x-ray scattering

WAXS data were collected by a Bruker D8 advance X-ray diffractometer. The sample was fixed between two glass slides and measured in transmission geometry using Cu-Kα radiation (λ = 1.54 Å) in an angular range (2θ) from 5° to 45°. A step size of 0.05° and an acquisition time of 30 s per step was applied.

4.3.11 Polarization microscopy

Polarization microscope images were obtained using an Inverse Nikon Diaphot system with crossed polarizers. The sample was sealed between two glass slides and fixed by a 50 µm thick Kapton® ring spacer. Images were taken at the noted temperatures during heating from 25 to 100 °C at a rate of 10 K min^{-1}.

4.4 Syntheses and characterization

4.4.1 Monomers

4.4.1.1 4-(3'-Trimethylsilylpropargyloxy)styrene (TMSPOS)

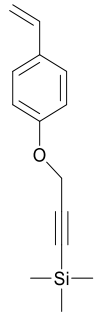

TMSPOS

The monomer 4-(propargyloxy)styrene (POS) and its protected form 4-(3'-trimethylsilylpropargyloxy)styrene (TMSPOS) were synthesized analogous to the literature with slight modifications.[151,154] Deviating from the literature, the reaction temperatures were kept as low as possible to prevent a possible themal initiated polymerization of the styrene derivatives. The separation performance of the column chromatography for the purification of TMSPOS was best when a volume ratio of *n*-hexane/ethyl acetate = 20/1 instead of 100/1 was used as an eluent.

A mixture of 4-acetoxystyrene (23.58 mL, 154.1 mmol, 1.0 eq) and water (125 mL) was cooled down to near 0 °C. Under stirring, potassium hydroxide (25.95 g, 462.2 mmol, 3.0 eq) was added in portions within 1 h. The mixture was stirred at room temperature for another 20 h resulting in a yellowish solution. Under argon, acetone (300 mL) and afterwards propargyl bromide (80 wt% in toluene, 24.91 mL, 231.2 mmol, 1.5 eq,) were added. The turbid mixture was stirred at room temperature for 69 h. The organic solvents were removed under reduced pressure at 40 °C. The aqueous residue was extracted by chloroform (25 mL thrice). The addition of sodium chloride and centrifugation facilitated phase separation. The organic phase was dried over $MgSO_4$ and the solvent was removed under reduced pressure yielding crude POS as a slightly yellow and transperent oil (19.2 g, 79%). ^{1}H NMR ($CDCl_3$) δ 7.46-7.29 (m, 2H, Ar*H*), 7.03-6.85 (m, 2H, Ar*H*), 6.67 (dd, *J* = 17.6, 10.9, 1H, H_2C=C*H*–), 5.63 (dd, *J* = 17.6, 0.9, 1H, H_2C=CH–), 5.15 (dd, *J* = 10.9, 0.9, 1H, H_2C=CH–), 4.70 (d, *J* = 2.4, 2H, -O-CH_2-), 2.53 (t, *J* = 2.4, 1H, ≡C*H*), Fig. 63.

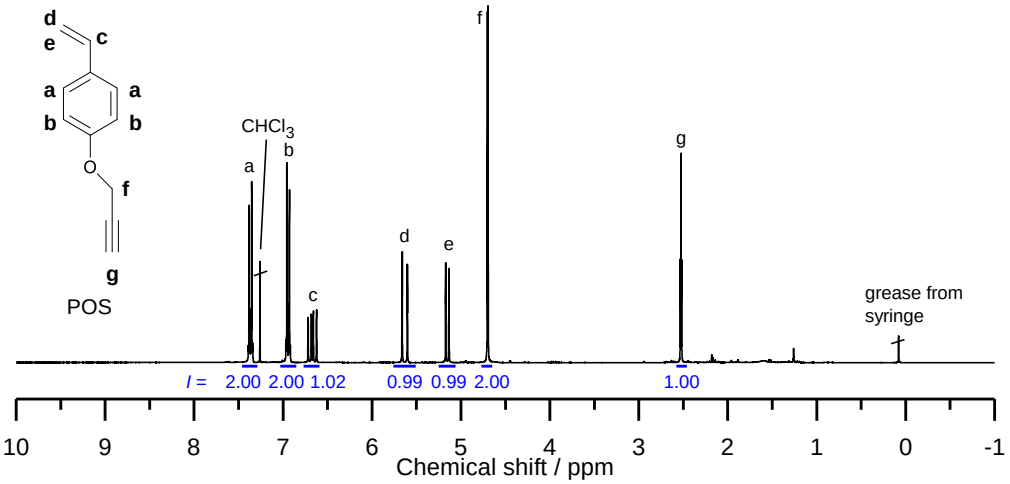

Fig. 63 ^{1}H NMR spectrum of crude POS in $CDCl_3$.

A mixture of 1,8-diazabicyclo[5.4.0]undec-7-en (19.91 mL, 133.4 mmol, 1.1 eq), silver chloride (1.74 g, 12.1 mmol, 0.1 eq) and crude POS (19.18 g, 121.2 mmol, 1.0 eq) in dry DCM (100 mL) was heated under reflux and nitrogen atmosphere at 55 °C. Chlorotrimethylsilane (24.68 mL, 194.0 mmol, 1.6 eq) was added dropwise within 30 min. Since the reaction did not progress further after 20.5 h as proven by the constant intensity of the alkyne proton NMR signal at 2.53 ppm, the mixture was cooled down to toom temperature. DCM was removed under reduced pressure and the mixture was diluted with *n*-hexane (250 mL). The mixture was washed with hydrochloric acid (1 N, 150 mL), an aqueous saturated solution of sodium hydrogen carbonate (350 mL) and water (100 mL twice) until neutrality. The organic phase was dried over $MgSO_4$ and the solvent was removed under reduced pressure. Further purification was carried out by column chromatography on silica with a mixture of *n*-hexane/ethyl acetate (20/1 by volume) as an eluent and drying in high vacuum at room temperature overnight yielding TMSPOS as a colorless and transparent oil (15.3 g, 55%). ^{1}H NMR ($CDCl_3$) δ 7.46-7.29 (m, 2H, Ar*H*), 7.03-6.85 (m, 2H, Ar*H*), 6.68 (dd, J = 17.6, 10.9, 1H, H_2C=C*H*–), 5.64 (dd, J = 17.6, 0.9, 1H, *H*$_2$C=CH–), 5.15 (dd, J = 10.9, 0.9, 1H, *H*$_2$C=CH–), 4.68 (s, 2H, -O-C*H*$_2$-), 0.19 (s, 9H, -Si(-C*H*$_3$)$_3$), Fig. 64.

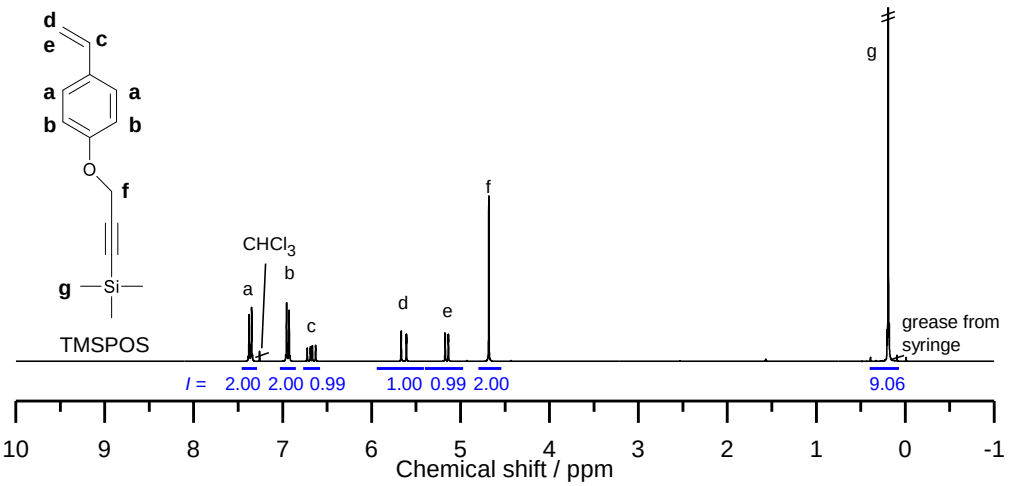

Fig. 64 ^{1}H NMR spectrum of TMSPOS in $CDCl_3$.

4.4.1.2 Ethenesulfonate monomers

General synthetic procedure

All ethenesulfonate (ES) monomer syntheses were performed in a dried closed apparatus under argon, since 2-chloroethanesulfonyl chloride is sensitive to moisture and toxic. After adding all reactants, the reaction mixtures were stirred at room temperature for 19 h yielding a yellowish suspension containing a white solid. The suspension was filtered and the filter cake was washed with DCM (30 mL) to get the crude product in the filtrate. The latter was purified as described below. Finally, all monomers were dried in high vacuum at room temperature for two days and stored under argon.

Synthesis of ethyl ethenesulfonate (EES)

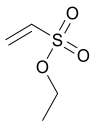

EES

EES was prepared as described previously with slight modifications.[140–142] A solution of 2-chloroethanesulfonyl chloride (15.00 mL, 142.8 mmol, 1.0 eq) in DCM (180 mL) was cooled down to 0 °C. Under stirring, a solution of dry ethanol (9.99 mL, 171.4 mmol, 1.2 eq) and triethylamine (43.79 mL, 314.2 mmol, 2.2 eq) in DCM (20 mL) was added dropwise within 1 h. The mixture was stirred at room temperature for another 19 h resulting in a yellowish suspension containing a white solid. After filtration and washing the filter cake with DCM (30 mL), the alkaline filtrate was washed with hydrochloric acid (1 N, 50 mL) and water (60 mL twice) until neutrality. The organic phase was dried over $MgSO_4$ and the solvent was removed under reduced pressure. Further purification was

carried out by vacuum distillation (bp 32 °C/1.24 Pa), yielding EES as a colorless and transparent oil (12.0 g, 69%). Anal. Calcd for $C_4H_8O_3S$: C, 35.3; H, 5.9; N, 0.0; S, 23.5. Found: C, 34.9; H, 5.9; N, 0.0; S, 23.2%. ^{1}H NMR ($CDCl_3$) δ 6.52 (dd, J = 16.6, 9.7, 1H, H_2C = C*H*-), 6.38 (d, J = 16.6, 1H, *H*$_2$C = CH-), 6.12 (d, J = 9.7, 1H, *H*$_2$C = CH-), 4.17 (q, J = 7.1, 2H, -SO_2-O-C*H*$_2$-), 1.37 (t, J = 7.1, 3H, *H*$_3$C-), Fig. 65.

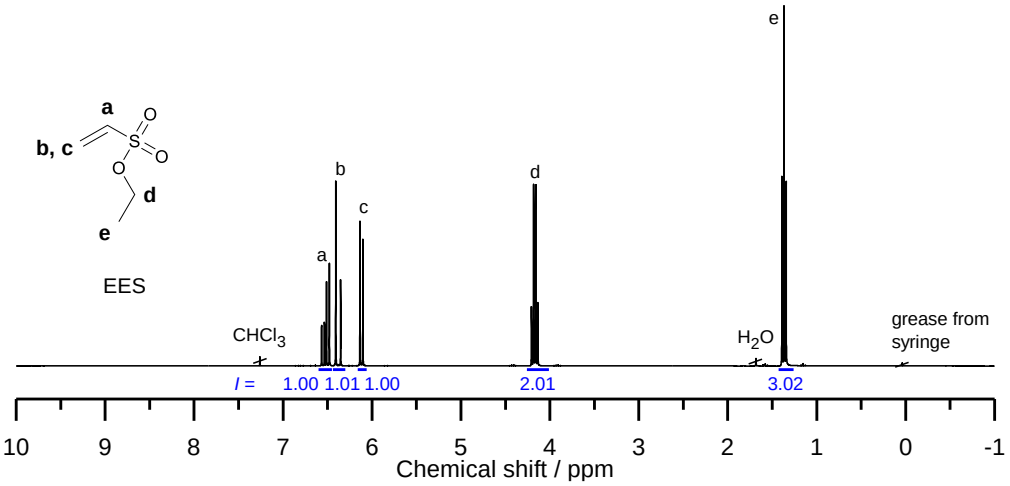

Fig. 65 ^{1}H NMR spectrum of EES in $CDCl_3$.

^{13}C NMR ($CDCl_3$) δ 132.4 (H_2C = *C*H-), 130.1 (H_2C = CH-), 67.1 (-SO_2-O-*C*H_2-), 14.8 (H_3C-), Fig. 66.

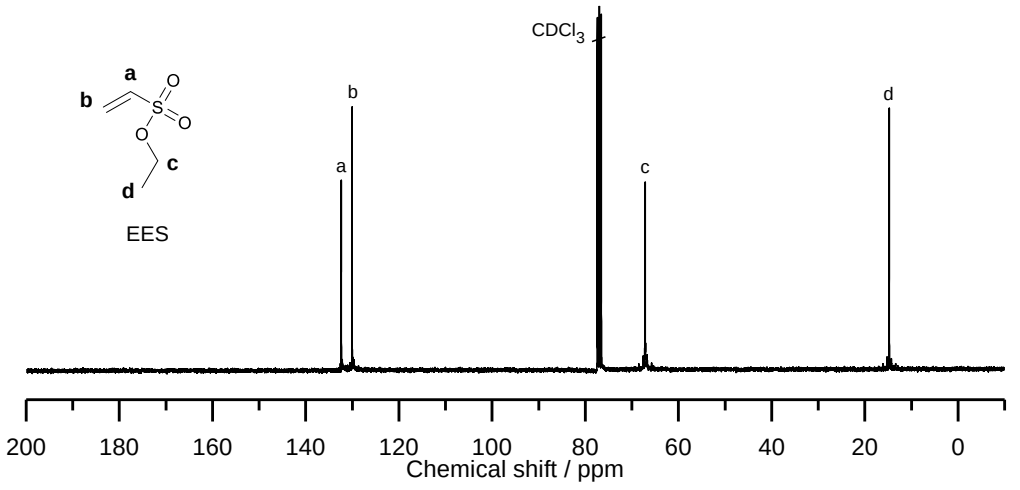

Fig. 66 ^{13}C NMR spectrum of EES in $CDCl_3$.

Synthesis of 2-methoxyethyl ethenesulfonate (EG1ES)

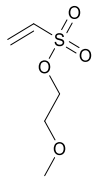

EG1ES

A solution of 2-chloroethanesulfonyl chloride (10.00 mL, 95.2 mmol, 1.0 eq) in DCM (160 mL) was cooled down to 0 °C. Under stirring, a solution of 2-methoxyethanol (9.01 mL, 114.2 mmol, 1.2 eq) and triethylamine (33.17 mL, 238.0 mmol, 2.5 eq) in DCM (20 mL) was added dropwise within 1 h. After the filtration the alkaline filtrate was washed with water (three times 100 mL) until neutrality. The organic phase was dried over $MgSO_4$ and the solvent was removed under reduced pressure. Further purification was carried out by vacuum distillation (bp 46 °C/0.26 Pa), yielding EG1ES as a colorless and transparent oil (13.0 g, 82%). Anal. Calcd for $C_5H_{10}O_4S$: C, 36.1; H, 6.1; N, 0.0; S, 19.3. Found: C, 35.8; H, 6.2; N, 0.0; S, 19.0%. ^{1}H NMR ($CDCl_3$) δ 6.56 (dd, J = 16.6, 9.8, 1H, H_2C = C*H*-), 6.39 (d, J = 16.6, 1H, *H_2*C = CH-), 6.12 (d, J = 9.8, 1H, *H_2*C = CH-), 4.28 – 4.16 (m, 2H, -SO_2-O-C*H_2*-), 3.66 – 3.59 (m, 2H, -SO_2-O-CH_2-C*H_2*-), 3.36 (s, 3H, *H_3*C-), Fig. 67.

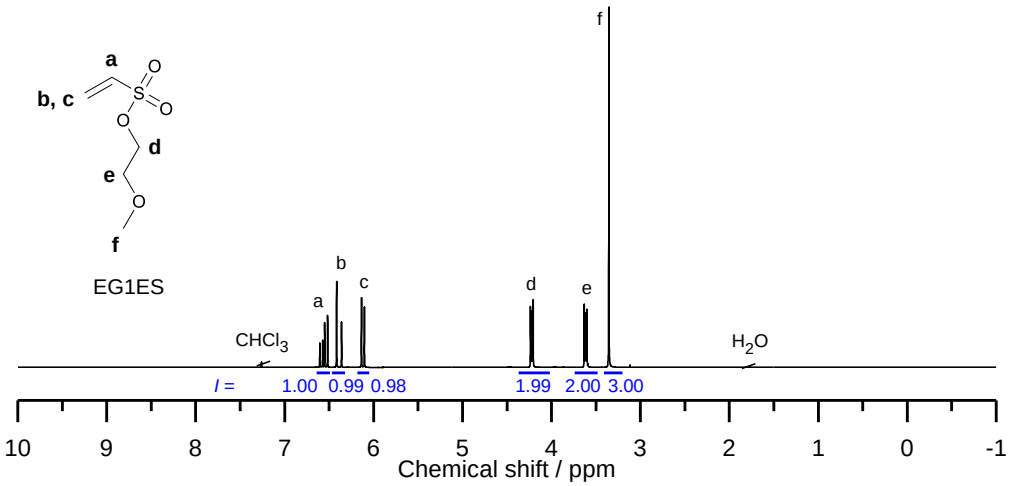

Fig. 67 ^{1}H NMR spectrum of EG1ES in $CDCl_3$.

^{13}C NMR ($CDCl_3$) δ 132.2 (H_2C = *C*H-), 130.2 (*H_2*C = CH-), 69.8 and 69.5 (2C, -SO_2-O-*C*H_2-*C*H_2-), 58.9 (q, J = 4.2, H_3*C*-), Fig. 68.

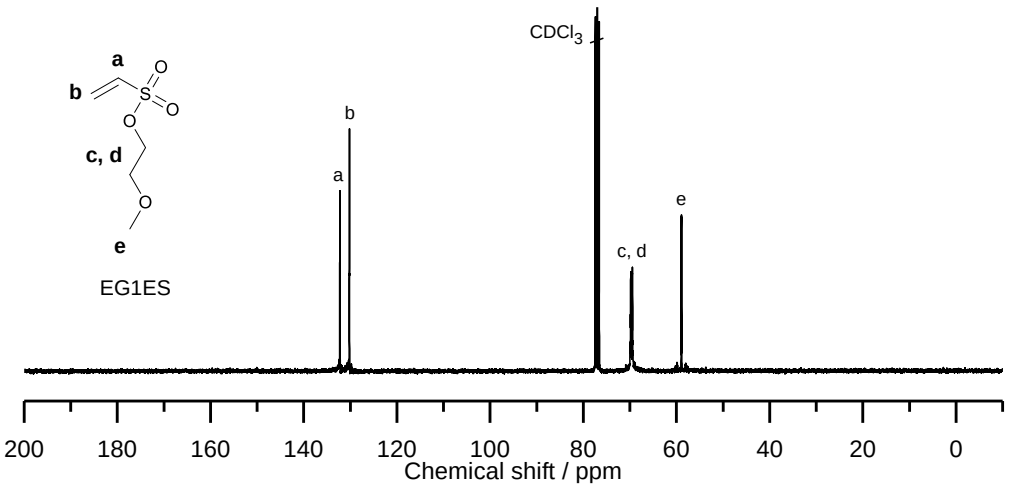

Fig. 68 ^{13}C NMR spectrum of EG1ES in $CDCl_3$.

Synthesis of 2-(2-(2-methoxyethoxy)ethoxy)ethyl ethenesulfonate (EG3ES)

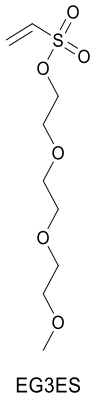

A solution of 2-chloroethanesulfonyl chloride (14.00 mL, 133.3 mmol, 1.0 eq) in DCM (150 mL) was cooled down to 0 °C. Under stirring, a solution of triethylene glycol monomethyl ether (25.25 mL, 159.9 mmol, 1.2 eq) and triethylamine (46.44 mL, 333.2 mmol, 2.5 eq) in DCM (30 mL) was added dropwise within 40 min. After the filtration the alkaline filtrate was washed with an aqueous solution of sodium carbonate (10 wt%, 100 mL), hydrochloric acid (0.1 N, 100 mL) and water until neutrality. The organic phase was dried over $MgSO_4$ and the solvent was removed under reduced pressure. Further purification was carried out by column chromatography on silica with ethyl acetate as an eluent yielding EG3ES as a yellow oil (29.9 g, 88%). Anal. Calcd for $C_9H_{18}O_6S$: C, 42.5; H, 7.1; N, 0.0; S, 12.6. Found: C, 42.0; H, 7.1; N, 0.0; S, 13.0%. ^1H NMR ($CDCl_3$) δ 6.57 (dd, J = 16.6, 9.9, 1H, H_2C = C*H*-), 6.34 (d, J = 16.6, 1H, *H*$_2$C = CH-), 6.08 (d, J = 9.9, 1H, *H*$_2$C = CH-), 4.25 – 4.14 (m, 2H, -SO_2-O-C*H*$_2$-), 3.74 – 3.65 (m, 2H, -SO_2-O-CH_2-C*H*$_2$-), 3.63 – 3.53 (m, 6H, H_3C-O-CH_2-C*H*$_2$-O-C*H*$_2$-C*H*$_2$-), 3.52 – 3.44 (m, 2H, H_3C-O-C*H*$_2$-), 3.31 (s, 3H, *H*$_3$C-), Fig. 69.

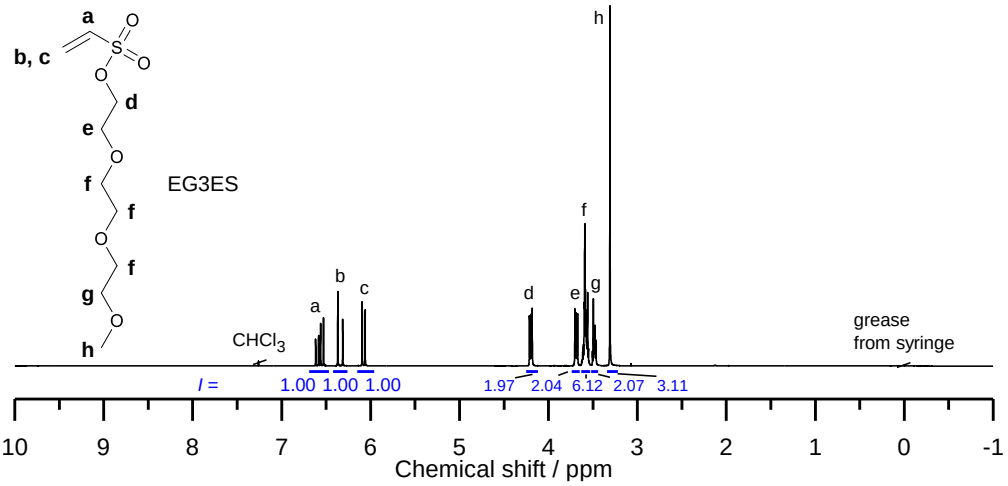

Fig. 69 ^{1}H NMR spectrum of EG3ES.

^{13}C NMR ($CDCl_3$) δ 132.3 (H_2C = *C*H-), 130.0 (H_2*C* = CH-), 71.6 (H_3C-O-*C*H_2-), 70.8 – 70.05 (3C, H_3C-O-CH_2-*C*H_2-O-*C*H_2-*C*H_2-), 69.6 and 68.5 (2C, -SO_2-O-*C*H_2-*C*H_2-), 58.8 (q, J = 3.2, H_3*C*-), Fig. 70.

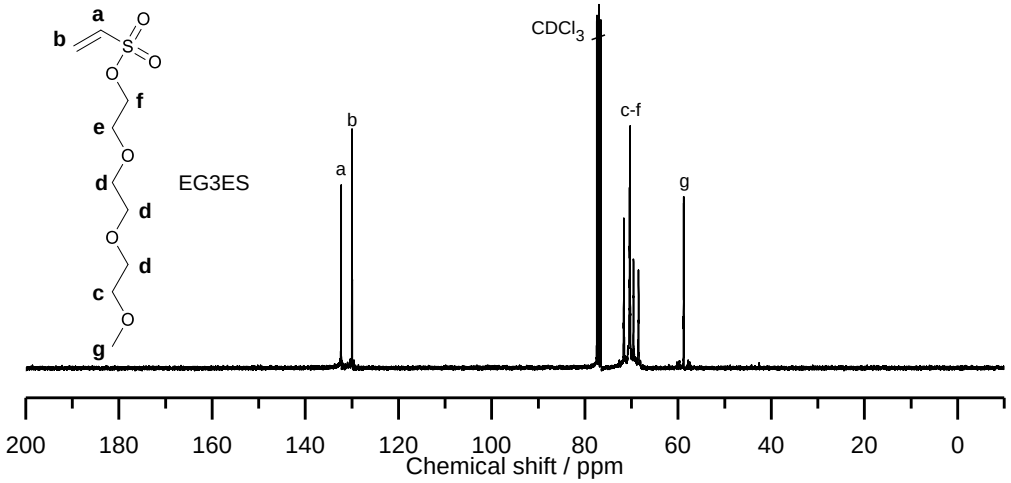

Fig. 70 ^{13}C NMR spectrum of EG3ES in $CDCl_3$.

Synthesis of 2,2-difluoro-2-(1,1,2,2-tetrafluoro-2-(trifluoromethoxy)ethoxy)ethyl ethenesulfonate (FEG2ES)

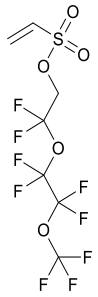

FEG2ES

A solution of 2-chloroethanesulfonyl chloride (4.00 mL, 38.1 mmol, 1.0 eq) in DCM (50 mL) was cooled down to 0 °C. Under stirring, a solution of 2,2-difluoro-2-(1,1,2,2-tetrafluoro-2-(trifluoromethoxy)ethoxy)ethanol (FEG2, 7.39 mL, 41.9 mmol, 1.1 eq) and triethylamine (13.27 mL, 95.2 mmol, 2.5 eq) in DCM (10 mL) was added dropwise within 1.5 h. After the filtration the alkaline filtrate was washed with water (five times 50 mL) until neutrality. The organic phase was dried over $MgSO_4$ and the solvent was removed under reduced pressure. Further purification was carried out by vacuum distillation (bp 36 °C/0.52 Pa), yielding FEG2ES as a colorless and transparent oil (9.0 g, 64%). Anal. Calcd for $C_7H_5F_9O_5S$: C, 22.6; H, 1.35; N, 0.0; S, 8.6. Found: C, 22.2; H, 1.4; N, 0.0; S, 8.95%. ^{1}H NMR ($CDCl_3$) δ 6.60 (dd, J = 16.5, 9.0, 1H, H_2C = C*H*-), 6.50 (d, J = 16.5, 1H, *H*$_2$C = CH-), 6.24 (d, J = 9.0, 1H, *H*$_2$C = CH-), 4.44 (t, J = 8.8, 2H, -O-C*H*$_2$-CF$_2$-), Fig. 71.

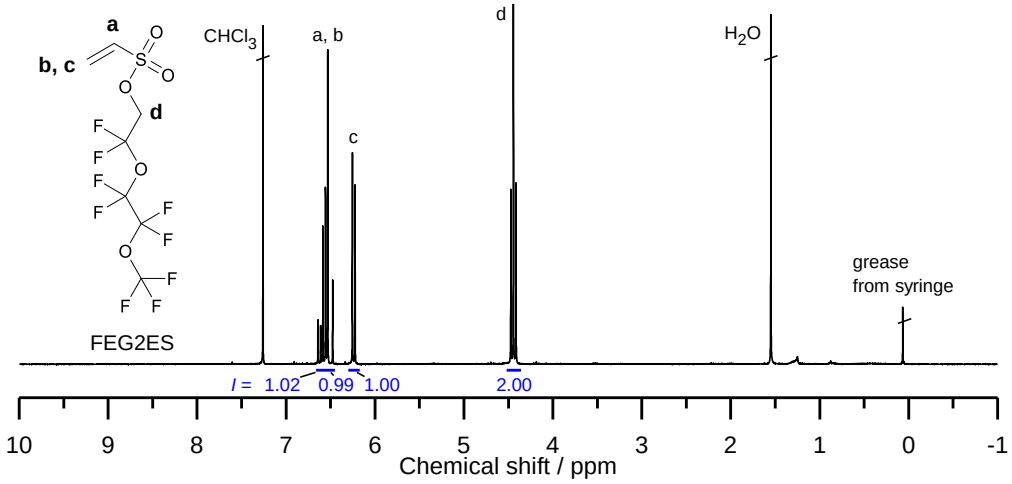

Fig. 71 ^{1}H NMR spectrum of FEG2ES in $CDCl_3$.

^{19}F NMR ($CDCl_3$ with C_6F_6 as an internal reference) δ -58.4 (t, J = 8.8, 3F, *F*$_3$C-), -80.2 – -80.5 (m, 2F, F$_3$C-O-C*F*$_2$-), -91.5 – -91.8 (m, 2F, F$_3$C-O-CF$_2$-C*F*$_2$-), -93.6 – -93.9 (m, 2F, -C*F*$_2$-CH$_2$-), Fig. 72.

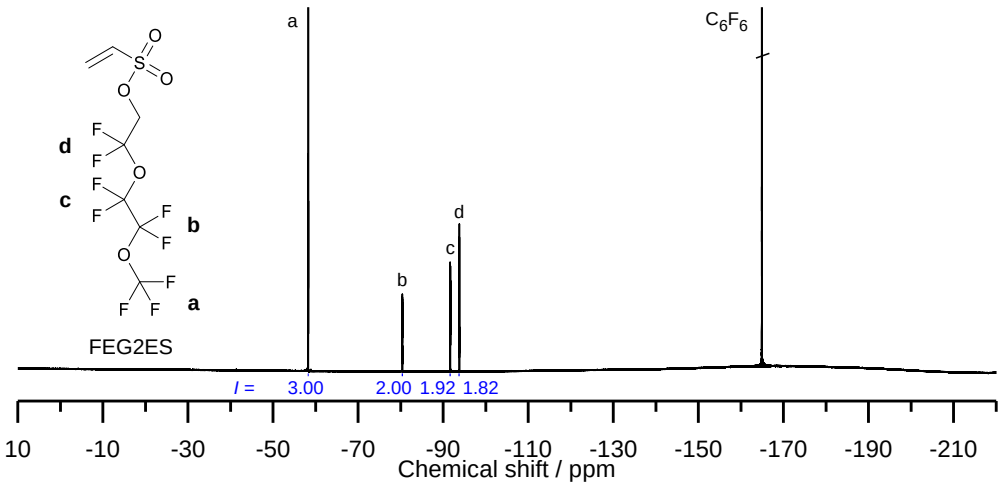

Fig. 72 ^{19}F NMR spectrum of FEG2ES in $CDCl_3$ with C_6F_6 as an internal reference.

A sample for ^{1}H NMR spectroscopy was taken from the residue after distillation. 2,2-Difluoro-2-(1,1-,2,2-tetrafluoro-2-(trifluoromethoxy)ethoxy)ethyl 2-(2,2-difluoro-2-(1,1,2,2-tetrafluoro-2-(trifluoromethoxy)ethoxy)ethoxy)ethanesulfonate (2FEG2ES) was identified as a by-product. ^{1}H NMR ($CDCl_3$) δ 4.50 (t, J = 9.0, 2H, -SO_2-O-CH_2-), 4.06 (t, J = 5.7, 2H, -SO_2-CH_2-CH_2-), 3.90 (t, J = 9.6, 2H, -SO_2-CH_2-CH_2-O-CH_2-), 3.52 (t, J = 5.7, 2H, -SO_2-CH_2-), Fig. 73.

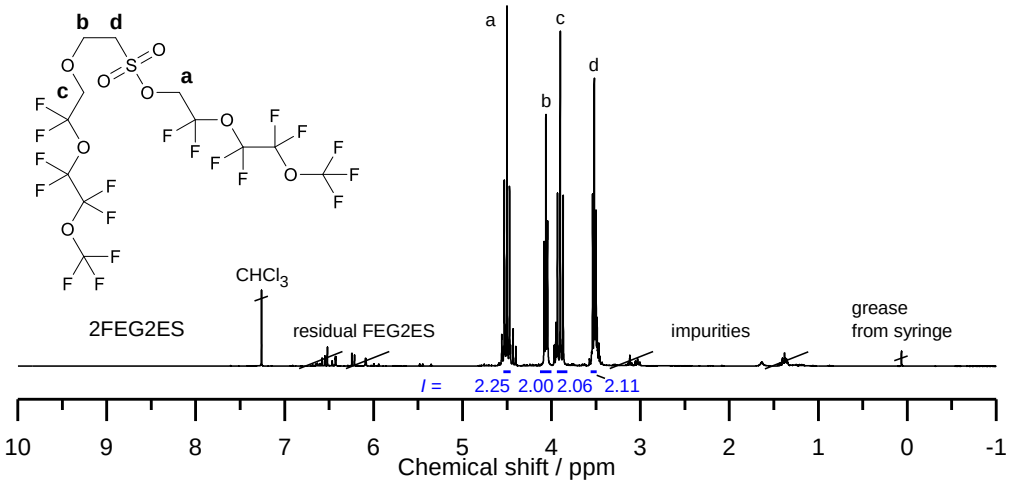

Fig. 73 ^{1}H NMR spectrum of the by-product 2FEG2ES from the synthesis of FEG2ES in $CDCl_3$. The sample was taken from the residue after distillation of the product FEG2ES.

For the test reaction of the by-product formation, a solution of FEG2ES (0.324 g, 0.87 mmol, 1.0 eq) and FEG2 (0.17 mL, 0.96 mmol, 1.1 eq) in DCM (2 mL) was stirred at room temperature for 20 h. Since no reaction was observed, as proved by ^{1}H NMR spectroscopy, triethylamine (0.13 mL, 0.96 mmol, 1.1 eq) was added and the solution was stirred for another 26 h. Nearly quantitative conversion of FEG2ES occurred. The same ^{1}H NMR signals were found as shown above for 2FEG2ES.

Synthesis of 2,2-difluoro-2-(1,1,2,2-tetrafluoro-2-(1,1,2,2-tetrafluoro-2-(trifluoromethoxy)-ethoxy)ethoxy)ethyl ethenesulfonate (FEG3ES)

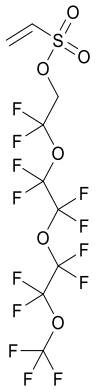

FEG3ES

A solution of 2-chloroethanesulfonyl chloride (12.00 mL, 114.2 mmol, 1.0 eq) in DCM (170 mL) was cooled down to 0 °C. Under stirring, a solution of 2,2-difluoro-2-(1,1,2,2-tetrafluoro-2-(1,1,2,2-tetrafluoro- 2 -(trifluoromethoxy)ethoxy)ethoxy)ethanol (FEG3, 30.20 mL, 125.7 mmol, 1.1 eq) and triethylamine (39.8 mL, 285.6 mmol, 2.5 eq) in DCM (30 mL) was added dropwise within 2.5 h. After the filtration the alkaline filtrate was washed with water (six times 150 mL) until neutrality. The organic phase was dried over $MgSO_4$ and the solvent was removed under reduced pressure. Further purification was carried out by vacuum distillation (bp 43 °C/0.32 Pa), yielding FEG3ES as a colorless and transparent oil (33.4 g, 60%). Anal. Calcd for $C_9H_5F_{13}O_6S$: C, 22.1; H, 1.0; N, 0.0; S, 6.6. Found: C, 21.7; H, 1.0; N, 0.3; S, 6.5%. ^{1}H NMR ($CDCl_3$) δ 6.58 (dd, J = 16.5, 9.0, 1H, H_2C = C*H*-), 6.48 (d, J = 16.5, 1H, *H*$_2$C = CH-), 6.22 (d, J = 9.0, 1H, *H*$_2$C = CH-), 4.42 (t, J = 8.8, 2H, -O-C*H*$_2$-CF$_2$-), Fig. 74.

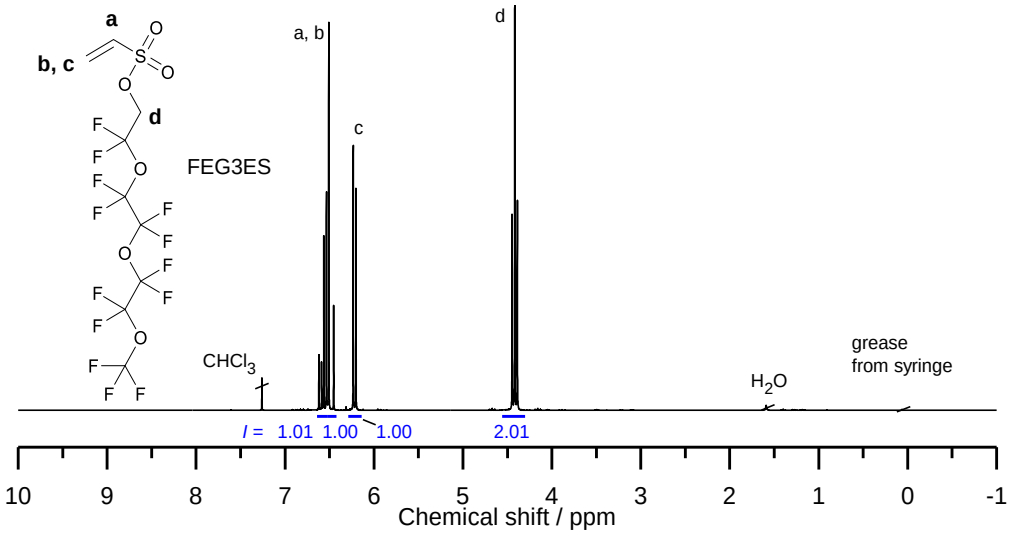

Fig. 74 ^{1}H NMR spectrum of FEG3ES in $CDCl_3$.

^{19}F NMR ($CDCl_3$ with C_6F_6 as an internal reference) δ -58.3 (t, J = 8.8, 3F, F_3C-), -80.3 – -80.7 (m, 2F, F_3C-O-CF_2-), -91.2 – -92.4 (m, 6F, F_3C-O-CF_2-CF_2-O-CF_2-CF_2-), -93.6 – -93.9 (m, 2F, -CF_2-CH_2-), Fig. 75.

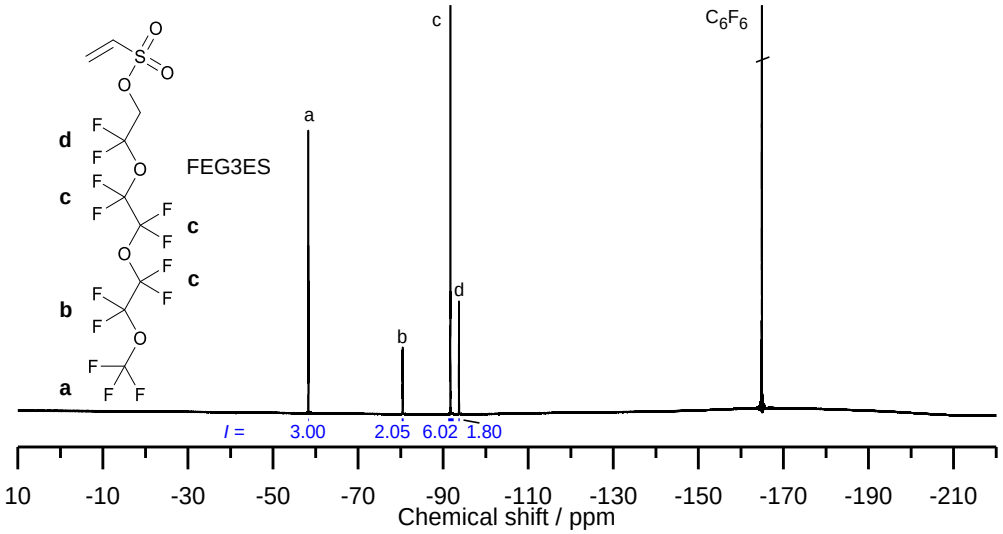

Fig. 75 ^{19}F NMR spectrum of FEG3ES in $CDCl_3$ with C_6F_6 as an internal reference.

A sample for ^{1}H NMR spectroscopy was taken from the residue after distillation. 2,2-Difluoro-2-(1,1-,2,2-tetrafluoro-2-(1,1,2,2-tetrafluoro-2-(trifluoromethoxy)ethoxy)ethoxy)ethyl 1,1,1,3,3,4,4,6,6,7,7,-9,9-tridecafluoro - 2,5,8,11-tetraoxatridecane-13–sulfonate (2FEG3ES) was identified as a by-product. ^{1}H NMR ($CDCl_3$) δ 4.48 (t, J = 9.0, 2H, -SO_2-O-CH_2-), 4.04 (t, J = 5.7, 2H, -SO_2-CH_2-CH_2-), 3.88 (t, J = 9.6, 2H, -SO_2-CH_2-CH_2-O-CH_2-), 3.49 (t, J = 5.7, 2H, -SO_2-CH_2-), Fig. 76.

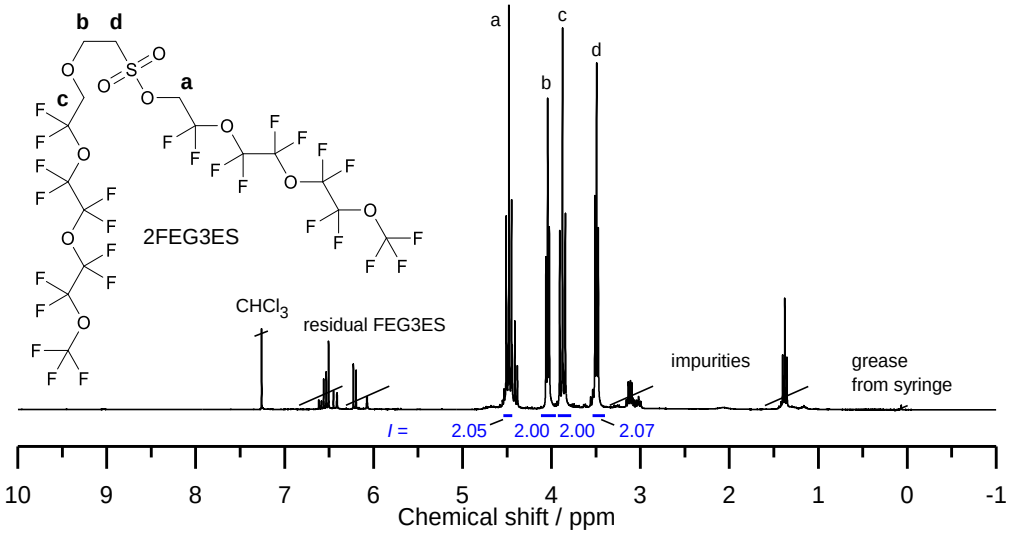

Fig. 76 ^{1}H NMR spectrum of the by-product 2FEG3ES from the synthesis of FEG3ES in $CDCl_3$. The sample was taken from the residue after distillation of the product FEG3ES.

4.4.2 Chain transfer agent

4.4.2.1 *O*-ethyl-*S*-(1-methoxycarbonyl) ethyldithiocarbonate (OEMDTC)

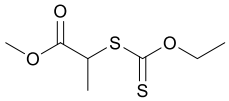

OEMDTC

The synthesis of OEMDTC was performed similarly to the literature,[185] but with an excess of methyl 2-bromopropionate instead of potassium ethyl xanthogenate to prevent a second nucleophilic substitution by the ethyl xanthogenate. The latter reaction was expected to yield the double substituted by-product 2-(ethoxycarbonothioylthio)propanoic (*O*-ethyl carbonothioic) thioanhydride (EPETA) which could also act as a CTA. It turned out, that the removal of excess methyl 2-bromopropionate was easier in comparison to the removal of EPETA.

A solution of methyl 2-bromopropionate (9.96 g, 59.6 mmol, 1.05 eq) in ethanol (300 mL) was cooled down to 0 °C. Under stirring, potassium ethyl xanthogenate (9.08 g, 56.6 mmol, 1.00 eq) was added in portions within 1 h. The mixture was stirred at room temperature overnight yielding in a yellowish suspension containing a white solid. The suspension was diluted by a mixture of diethyl ether/pentane (2/1 by volume, 400 mL) and washed with water (twice 150 mL). The aqueous phase was extracted with a mixture of diethyl ether/pentane (2/1 by volume, 100 mL). The combined organic phases were washed with water (twice 150 mL) and dried over $MgSO_4$. After filtration, the solvent was removed under reduced pressure. The product was purified by column chromatography on silica with a mixture of *n*-hexane/ethyl acetate (10/1 by volume) as an eluent and drying in high vacuum at room temperature for two days yielding OEMDTC as a yellow oil (9.3 g, 79%). The product was stored under argon. The density of the product was determined by weighing thrice a volume of 1 mL and calculating the arithmetic mean (1.183 g/mL at 22 °C). Two different ^{1}H NMR quartet signals of the methylene protons in OEMDTC were observed which had not been noted in previous studies. This splitting must arise from the presence of (*R*)- and (*S*)-OEMDTC. ^{1}H NMR ($CDCl_3$) δ 4.60 and 4.59 (q, J = 7.1, 2H, (*R*)- and (*S*)-OEMDTC, H_3C-CH_2-), 4.35 (q, J = 7.4, 1H, *H*-C(CH_3)($COOCH_3$)-), 3.71 (s, 3H, H_3C-O-), 1.53 (d, J = 7.4, 3H, H_3C-CH($COOCH_3$)-), 1.38 (t, J = 7.1, 3H, H_3C-CH_2-), Fig. 77.

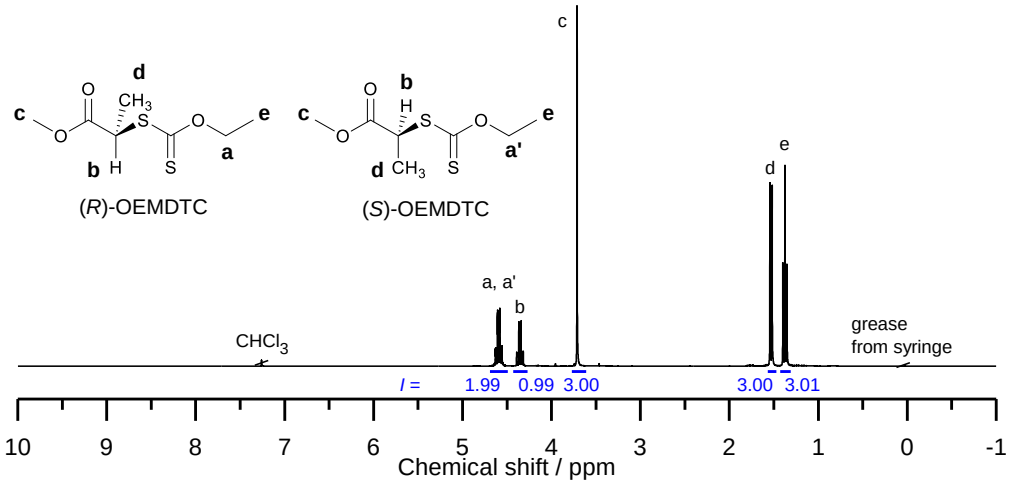

Fig. 77 ^{1}H NMR spectrum of OEMDTC in $CDCl_3$.

^{13}C NMR ($CDCl_3$) δ 211.76 (=*C*(OC_2H_5)-), 171.72 (=*C*(OCH_3)-), 70.35 – 69.94 (m, H_3C-*C*H_2-), 52.62 (q, J = 6.1, H_3*C*-O-), 46.81 (d, J = 7.6, -*C*H(CH_3)-), 16.69 (H_3*C*-CH(CH_3)($COOCH_3$)-), 13.51 (H_3*C*-CH_2-), Fig. 78.

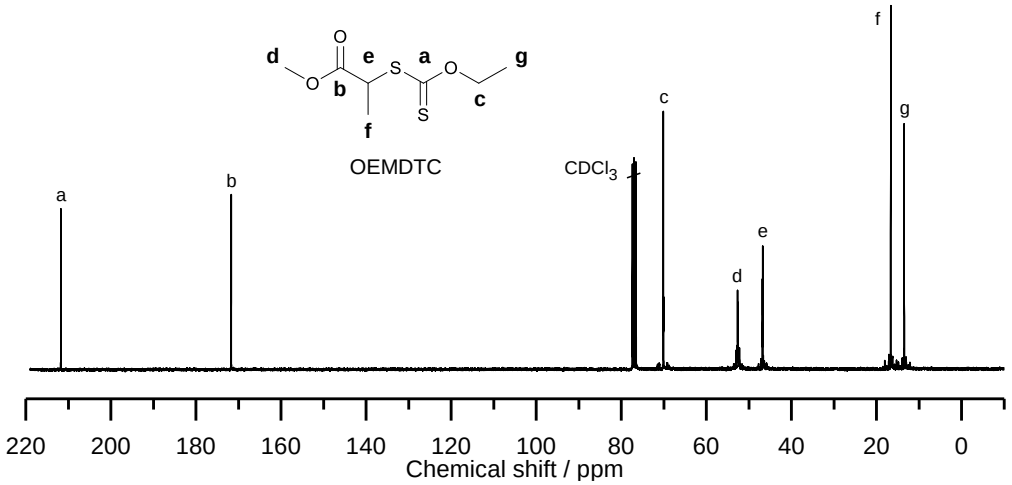

Fig. 78 ^{13}C NMR spectrum of OEMDTC in $CDCl_3$.

4.4.3 Polymers

4.4.3.1 Poly(4-(propargyloxy)styrene)-*grafted*-poly(ethylene glycol) (PPOS-*g*-PEG)

Synthesis of poly(4-(3'-trimethylsilylpropargyloxy)styrene) (PTMSPOS)

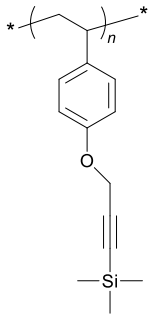

PTMSPOS

The polymer poly(4-(3'-trimethylsilylpropargyloxy)styrene) (PTMSPOS) was synthesized by the nitroxide-mediated radical polymerization (NMRP) similar to the literature.[102,151,154] The polymerization was performed in a dried Schlenk round-bottom flask under argon equipped with a magnetic stir bar and sealed by a septum. TMSPOS (5.28 g, 22.94 mmol, 35 eq.), *N*-*tert*-butyl-*O*-[1-[4-(chloromethyl)phenyl]ethyl]-*N*-(2-methyl-1-phenylpropyl)hydroxylamine (NMRP initiator, 245.1 mg, 655 µmol, 1 eq.) and TIPNO (14.4 mg, 65 µmol, 0.1 eq.) were dissolved in anisole (2.61 mL) and degassed by purging with argon through a cannula for 20 min at room temperature. The solution was stirred at 125 °C for 11 h. The polymerization was stopped by quenching the flask in an ice bath. The monomer conversion *conv.* was determined by ^{1}H NMR spectroscopy. The integral of the monomer's vinyl proton I_a (5.26 – 5.10 ppm) was compared with the integral of the methylene protons which are adjacent to the alkyne group in both the monomer I_b and the polymer I_c (4.86 – 4.42 ppm, Fig. 79):

$$conv. = \frac{1 - 2I_a}{I_b + I_c} \cdot 100\% \quad (15)$$

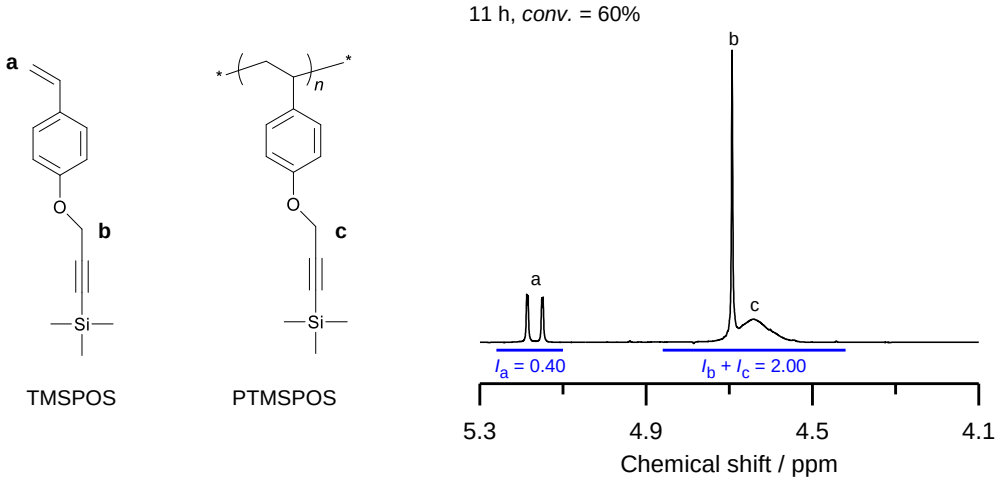

Fig. 79 ^{1}H NMR spectrum in $CDCl_3$ taken during the polymerization of TMSPOS after a reaction time of 11 h. The monomer conversion *conv.* was calculated by equation (15) with the integration of the monomer's vinyl proton I_a (5.26 – 5.10 ppm) and the integration of the methylene protons adjacent to the alkyne group in both the monomer I_b and the polymer I_c (4.86 – 4.42 ppm).

The degree of polymerization DP_n for PTMSPOS was determined by:

$$DP_n = \frac{[M]_0}{[I]_0} \cdot \frac{conv.}{100\%} \tag{16}$$

where $[M]_0$ and $[I]_0$ are the initial molar concentrations of the monomer and the NMRP initiator, respectively. The theoretical number-average molecular weight of PTMSPOS under consideration of equation (14) and an ideal NMRP process $M_{n,\,theor}$(PTMSPOS) was calculated according to:

$$M_{n,\,theor}(\text{PTMSPOS}) = DP_n\, M(\text{TMSPOS}) + M(\text{I}) \tag{17}$$

where M(TMSPOS) and M(I) are the molecular weights of TMSPOS (230.38 g mol^{-1}) and the NMRP initiator (373.96 g mol^{-1}), respectively.[149]

The crude reaction mixture was purified by diluting with chloroform (5 mL) and precipitating twice in ice-cooled ethanol (25 mL each). The product was dried under high vacuum at room temperature yielding PTMSPOS as a yellowish solid (yield: 2.00 g; 60% at 60% monomer conversion). ^{1}H NMR ($CDCl_3$) δ 7.18-6.13 (br, 4H, Ar*H*), 4.91-4.44 (br, 2H, -O-C*H*$_2$-), 2.45-0.48 (br, 3H, polymer backbone signals C*H* and C*H*$_2$, overlapping with proton end-group signals), 0.41-0.08 (br, 9H, -Si(-C*H*$_3$)$_3$), Fig. 80.

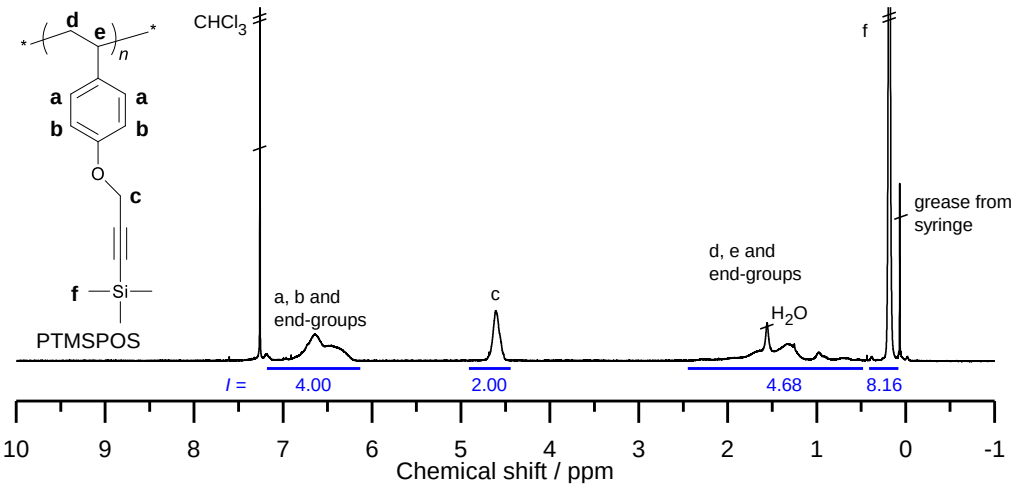

Fig. 80 ^{1}H NMR spectrum of TMSPOS in $CDCl_3$.

IR 3031 (**C_{ar}-H**), 2959, 2920 (**C_{ali}-H**), 2854, 2178 (**-C≡C-**), 1609 (**C_{ar}=C_{ar}**), 1584 (**C_{ar}=C_{ar}**), 1508 (**C_{ar}=C_{ar}**), 1450 (**C_{ar}=C_{ar})**, 1365, 1303, 1249 (**-Si-(CH)$_3$**), 1215, 1176, 1112, 1038, 1015, 987, 839 (**-Si-(CH)$_3$**), 827 (**C_{ar}-H**), 759 (**-Si-(CH)$_3$**), 700, Fig. 26.

PTMSPOS was desilylated to the unprotected form PPOS by an excess of tetrabutylammonium fluoride (TBAF) similar to the literature.[151,154] PTMSPOS (1.60 g, 6.45 mmol monomer units, calculated for a degree of polymerization of 21, 1 eq.) was dissolved in THF (10.47 mL) and degassed by purging with argon through a cannula for 20 min at room temperature. Under cooling at 0 °C, a solution of TBAF in THF (1 M, 19.34 mL, 19.34 mmol calculated for TBAF as trihydrate, 3 eq.) and acetic acid (1.11 mL, 19.34 mmol, 3 eq.) were added dropwise under argon. The solution was stirred at 0 °C for 30 min and at room temperature for 1 h. Volatile components were removed under reduced pressure. The residue was dissolved in DCM (40 mL) and washed with water (three times, 15 mL). The aqueous phase was washed with DCM (20 mL). The united organic phases were dried over $MgSO_4$ and the solvent was removed under reduced pressure. The product was dried under high vacuum at room temperature yielding PPOS as a yellowish solid (yield: 0.82 g; 72% calculated for a degree of polymerization of 21). ^{1}H NMR ($CDCl_3$) δ 7.06-6.13 (br, 4H, Ar*H*), 4.82-4.35 (br, 2H, -O-CH_2-), 2.69-2.31 (br, 1H, -C≡C*H*), 2.31-0.29 (br, 3H, polymer backbone signals C*H* and CH_2), Fig. 27.

IR 3287 (≡**C-H**), 3031 (**C_{ar}-H**), 2920 (**C_{ali}-H**), 2862, 2121 (**-C≡C-**), 1883, 1731, 1608 (**C_{ar}=C_{ar}**), 1584 (**C_{ar}=C_{ar}**), 1507 (**C_{ar}=C_{ar}**), 1450 (**C_{ar}=C_{ar})**, 1423, 1370, 1303, 1263, 1214, 1176, 1112, 1026, 923, 826 (**C_{ar}-H**), 733, 675, Fig. 26.

The theoretical number-average molecular weight of PPOS $M_{n,\,theor}$(PPOS) was calculated according to:

$$M_{\mathrm{n,\,theor}}(\mathrm{PPOS}) = DP_{\mathrm{n}}\, M(\mathrm{POS}) + M(\mathrm{I}) \quad (18)$$

where M(POS) is the molecular weight of POS (158.20 g mol^{-1}).

Synthesis of poly(ethylene glycol) monomethyl ether azides (PEG750-N3 and PEG2000-N3)

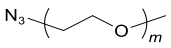

PEG750-N3 and PEG2000-N3

The poly(ethylene glycol) monomethyl ether azides, PEG750-N3 and PEG2000-N3, were synthesized by a double nucleophilic substitution of PEG750-OH or PEG2000-OH via the poly(ethylene glycol) monomethyl ether tosylates, PEG750-Ts or PEG2000-Ts, similar to the literature.[156] The syntheses were performed in dried Schlenk round-bottom flasks under argon equipped with a magnetic stir bar and sealed by a septum.

For the synthesis of PEG750-Ts, PEG750-OH (10.03 g, 13.37 mmol, 1 eq.), triethylamine (11.12 mL, 80.24 mmol, 6 eq.) and 4-toluenesulfonyl chloride (25.49 g, 133.73 mmol, 10 eq.) were dissolved in DCM (100 mL) and stirred at room temperature for 96 h. The crude reaction mixture was diluted with DCM (150 mL) and purified by washing with an aqueous saturated ammonium chloride solution (two times 200 mL). The aqueous phase was washed with DCM (50 mL). The united organic phases were washed until neutrality with water (two times 200 mL) and dried over $MgSO_4$. The solvent was removed under reduced pressure. Final purification was carried out by column chromatography. Thereby the excess of 4-toluenesulfonyl chloride was removed by flushing with DCM. The polymer was retrieved by a 10/1 mixture of DCM and ethyl acetate. The solvent was removed under reduced pressure yielding PEG750-Ts as a yellowish highly viscous oil (yield: 9.81 g; 81% calculated by a molecular weight of 904.19 g/mol for PEG750-Ts). ^{1}H NMR ($CDCl_3$) δ 7.88-7.71 (br, 2H, Ar*H* meta position to –CH_3), 7.40-7.30 (br, 2H, Ar*H* ortho position to –CH_3), 4.23-4.02 (br, 2H, -C*H*$_2$-OSO_2-), 3.96-3.39 (br, 63H, all other methylene protons), 3.39-3.32 (br, 3H, -O-C*H*$_3$), 2.50-2.38 (br, 3H, -Ar-C*H*$_3$), Fig. 81.

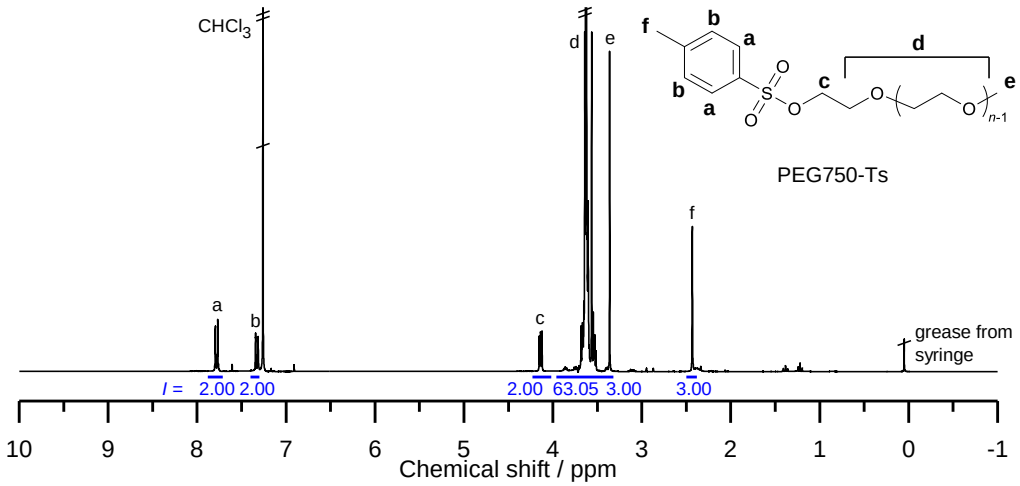

Fig. 81 ^{1}H NMR spectrum of PEG750-Ts in $CDCl_3$.

For the synthesis of PEG2000-Ts, PEG2000-OH (10.03 g, 5.02 mmol, 1 eq.), triethylamine (4.17 mL, 30.09 mmol, 6 eq.) and 4-toluenesulfonyl chloride (19.12 g, 100.30 mmol, 20 eq.) were dissolved in DCM (80 mL) and stirred at room temperature for 96 h. The crude reaction mixture was diluted with DCM (150 mL) and purified by washing with an aqueous saturated ammonium chloride solution (100 mL). The aqueous phase was washed with DCM (50 mL). The united organic phases were washed until neutrality with water (two times 100 mL) and dried over $MgSO_4$. The solvent was removed under reduced pressure. Final purification was carried out by precipitating the product from DCM in cold diethyl ether (400 mL). The product was dried under high vacuum at room temperature yielding PEG2000-Ts as a white solid (yield: 9.96 g; 92% calculated by a molecular weight of 2154.19 g/mol for PEG2000-Ts). ^{1}H NMR ($CDCl_3$) δ 7.84-7.76 (br, 2H, Ar*H* meta position to $-CH_3$), 7.37-7.32 (br, 2H, Ar*H* ortho position to $-CH_3$), 4.19-4.09 (br, 2H, -C*H*$_2$-OSO$_2$-), 3.92-3.40 (br, 134H, all other methylene protons), 3.40-3.34 (br, 3H, -O-C*H*$_3$), 2.50-2.39 (br, 3H, -Ar-C*H*$_3$), Fig. 82.

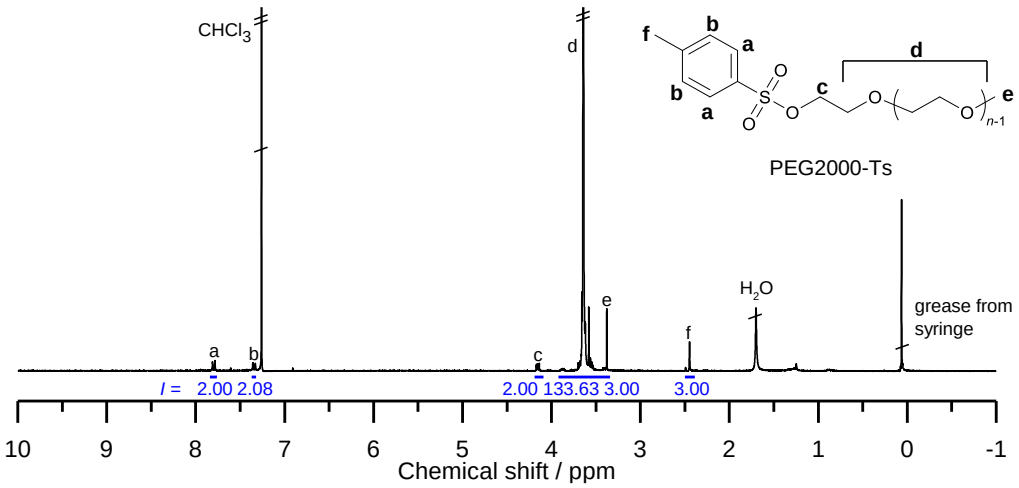

Fig. 82 ^{1}H NMR spectrum of PEG2000-Ts in $CDCl_3$.

For the synthesis of PEG750-N3, PEG750-Ts (9.81 g, 10.85 mmol calculated by a molecular weight of 904.19 g/mol for PEG750-Ts, 1 eq.) and sodium azide (3.53 g, 54.25 mmol, 5 eq.) were dissolved in dimethylformamide (50 mL) and stirred at 100 °C for 68 h. The crude reaction mixture was diluted with DCM (150 mL) and purified by washing with an aqueous saturated sodium chloride solution and water (each two times 200 mL). The organic phase was dried over $MgSO_4$ and the solvent was removed under reduced pressure. Final purification was carried out by column chromatography on silica with a mixture of DCM/methanol (5/1 by volume) as an eluent. The product was dried under high vacuum at room temperature yielding PEG750-N3 as a yellowish highly viscous oil (yield: 8.20 g; 98% calculated by a molecular weight of 775.01 g/mol for PEG750-N3). ^{1}H NMR ($CDCl_3$) δ 3.92-3.35 (br, 57H, all methylene protons), 3.35-3.31 (br, 3H, -O-CH_3), Fig. 83.

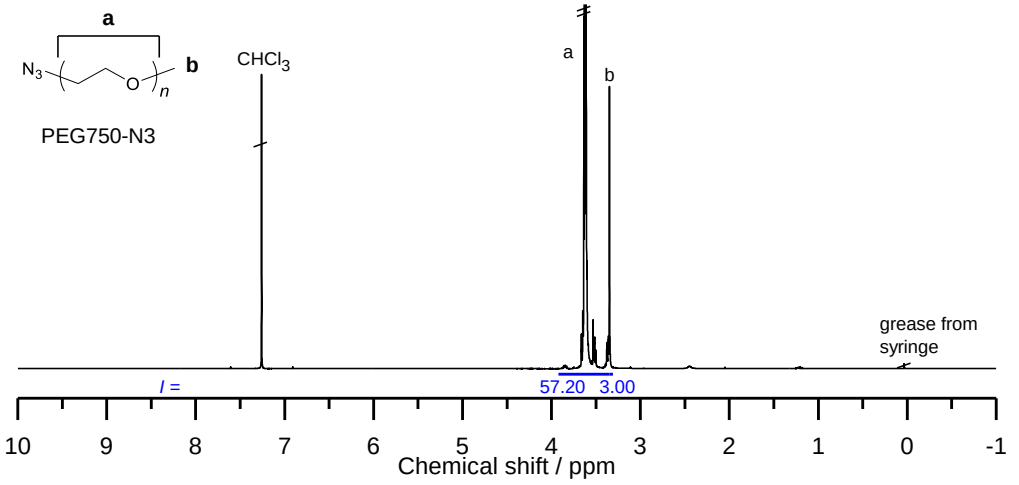

Fig. 83 ^{1}H NMR spectrum of PEG750-N3 in $CDCl_3$.

IR 3581, 2865 (**C_{ali}-H**), 2102 (**-N_3**), 1738, 1643, 1455, 1349, 1324, 1296, 1248, 1199, 1095 (asymmetric –H_2**C-O-C**H_2- stretch), 1038, 993, 946, 849 (symmetric –H_2**C-O-C**H_2- stretch), Fig. 84.

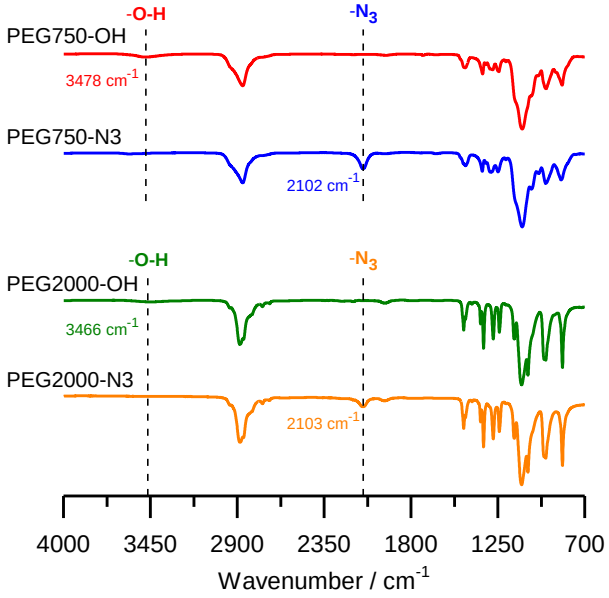

Fig. 84 Transmission IR spectra of PEG750-OH, PEG750-N3, PEG2000-OH and PEG2000-N3.

The theoretical number-average molecular weight of PEG750-N3 $M_{n,\,theor}$(PEG750-N3) was calculated according to:

$$M_{\mathrm{n,\,theor}}(\mathrm{PEG750-N3}) = DP_{\mathrm{m}}\, M(\mathrm{EO}) + M(\mathrm{CH_3}) + M(\mathrm{N_3}) \qquad (19)$$

where DP_m is the degree of polymerization of PEG750-N3 determined by MALDI-ToF MS (Fig. 85a). M(EO), M(CH_3) and M(N_3) are the molecular weights of an ethylene oxide repeating unit (44.05 g mol^{-1}), a methyl group (15.04 g mol^{-1}) and an azide group (42.03 g mol^{-1}), respectively.

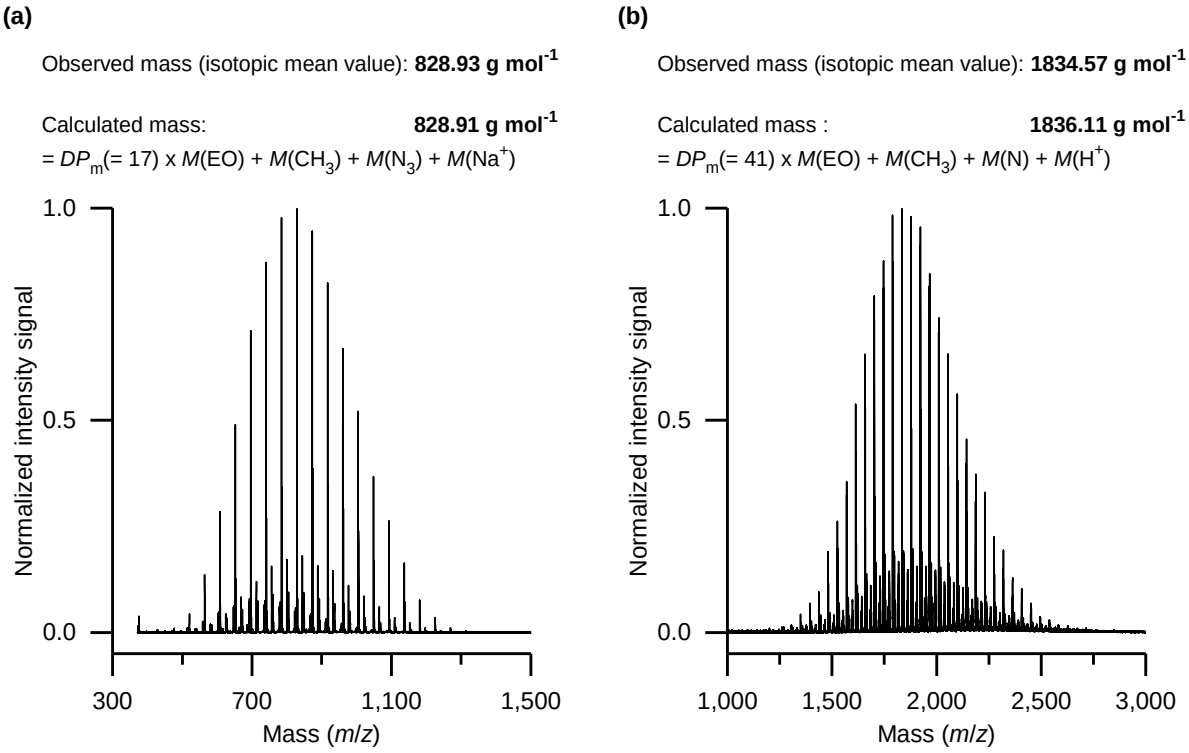

Fig. 85 MALDI-ToF MS spectra of (a) PEG750-N3 and (b) PEG2000-N3. Measurements were performed in reflectron positive mode. The observed mass was averaged over all isotopic peaks for the series with the highest intensity.

For the synthesis of PEG2000-N3, PEG2000-Ts (9.96 g, 4.62 mmol calculated by a molecular weight of 2154.19 g/mol for PEG2000-Ts, 1 eq.) and sodium azide (1.50 g, 23.11 mmol, 5 eq.) were dissolved in dimethylformamide (50 mL) and stirred at 100 °C for 68 h. The crude reaction mixture was diluted with DCM (200 mL) and purified by washing with an aqueous saturated sodium chloride solution and water (each two times 200 mL). The organic phase was dried over $MgSO_4$ and the solvent was removed under reduced pressure. Final purification was carried out by precipitating the product from DCM in cold diethyl ether (500 mL). The product was dried under high vacuum at room temperature yielding PEG2000-N3 as a white solid (yield: 8.55 g; 91% calculated by a molecular weight of 2025.01 g/mol for PEG2000-N3). ^{1}H NMR ($CDCl_3$) δ 3.93-3.39 (br, 145H, all methylene protons), 3.39-3.34 (br, 3H, -O-CH_3), Fig. 86.

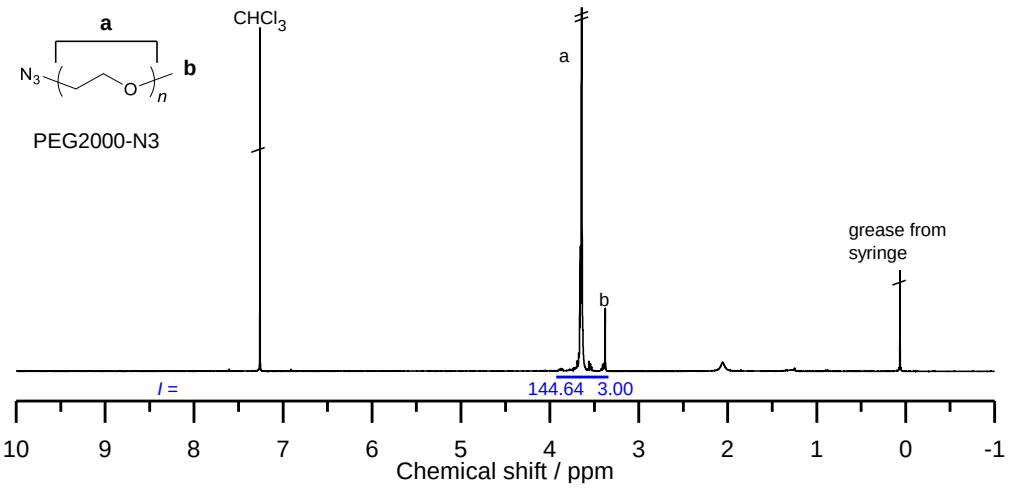

Fig. 86 ^{1}H NMR spectrum of PEG2000-N3 in $CDCl_3$.

IR 2946, 2883 (**C_{ali}-H**), 2860 (**C_{ali}-H**), 2741, 2695, 2162, 2103 (-**N_3**), 1966, 1467, 1455, 1413, 1360, 1341, 1279, 1240, 1198, 1147, 1099 (asymmetric –H_2**C-O-C**H_2- stretch), 1060, 957, 947, 841 (symmetric –H_2**C-O-C**H_2- stretch), Fig. 84.

The theoretical number-average molecular weight of PEG2000-N3 $M_{\mathrm{n,\,theor}}$(PEG2000-N3) was calculated according to:

$$M_{\mathrm{n,\,theor}}(\mathrm{PEG2000-N3}) = DP_{\mathrm{m}}\, M(\mathrm{EO}) + M(\mathrm{CH_3}) + M(\mathrm{N_3}) \tag{20}$$

where DP_{m} is the degree of polymerization of PEG2000-N3 determined by MALDI-ToF MS (Fig. 85b).

Synthesis of poly(4-(propargyloxy)styrene)-*grafted*-poly(ethylene glycol)s (PPOS-*g*-PEG750 and PPOS-*g*-PEG2000)

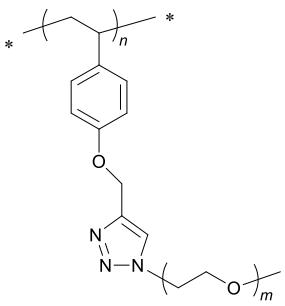

PPOS-*g*-PEG750 and
PPOS-*g*-PEG2000

The graft copolymers, PPOS-*g*-PEG750 and PPOS-*g*-PEG2000, were synthesized similar to the literature.[102,103,158] The syntheses were performed in dried Schlenk tubes under argon equipped with a magnetic stir bar and sealed by a glass cap.

For the synthesis of PPOS-*g*-PEG750, PPOS (395 mg, 2.24 mmol monomer units, calculated for a degree of polymerization of 21, 1 eq.) and PEG750-N3 (2.09 g, 2.69 mmol calculated by a molecular weight of 775.01 g/mol for PEG750-N3, 1.2 eq.) were dissolved in dried THF (33 mL) and degassed by purging with argon through a cannula for 20 min at room temperature. A 20 min argon-purged stock solution of CuI and PMDETA (molar ratio = 1/1) in THF (c = 0.07 mol L^{-1}, 6.41 mL, 0.45 mmol, 0.2 eq.) was added at 40 °C to start the reaction which was monitored by ^{1}H NMR spectroscopy (not shown). Samples were taken before adding the CuI/PMDETA stock solution and after stirring at 40 °C for 72 h. The sample solutions were filtered through a syringe filter (PTFE, 0.45 µm) before the measurement. Since full conversion was achieved after 72 h, the reaction was stopped by cooling and flushing the solution with air through a cannula till the solution became black. The copper catalyst could not be removed by filtration over silica or aluminum oxide since the graft copolymer stuck too strong to these materials. Therefore, the solvent was removed under reduced pressure, the black residue was suspended in DCM (30 mL) and the solution was separated from the black catalyst residue by centrifugation. Finally, last remains of catalyst were removed by washing the DCM solution (40 mL) with an aqueous tetrasodium ethylenediaminetetraacetate hydrate (Na_4EDTA) solution (two times 5 mL each containing 0.2 g Na_4EDTA). The removal of copper residues was confirmed by washing with aqueous ammonium hydroxide solution (25 wt%, 2 mL) which stayed colorless after the washing. The organic phase was washed with water until neutrality (two times 5 mL) and the solvent was removed under reduced pressure. Unreacted PEG was removed by dialysis (molecular weight cut-off: 2.0 kDa) in Millipore water. Water was removed under reduced pressure at 40 °C until constant weight yielding PPOS-*g*-PEG750 as a yellowish highly viscous oil (yield: 1.48 g; 69%).

^{1}H NMR ($CDCl_3$) δ 8.16-7.85 (br, 1H, triazole ring proton), 7.07-6.02 (br, 4H, Ar*H*), 5.54-4.85 (br, 2H, Ar-O-C*H*$_2$-), 4.84-4.26 (br, 2H, triazole ring-C*H*$_2$-CH$_2$-O-), 4.07-3.78 (br, 2H, triazole ring-CH$_2$-C*H*$_2$-O-), 3.74-3.39 (br, 54H, all other methylene protons in PEG side-chain), 3.39-3.30 (br, 3H, -O-C*H*$_3$), 2.36-0.47 (br, 3H, polymer backbone signals C*H* and C*H*$_2$ overlapping with proton end-group signals), Fig. 87.

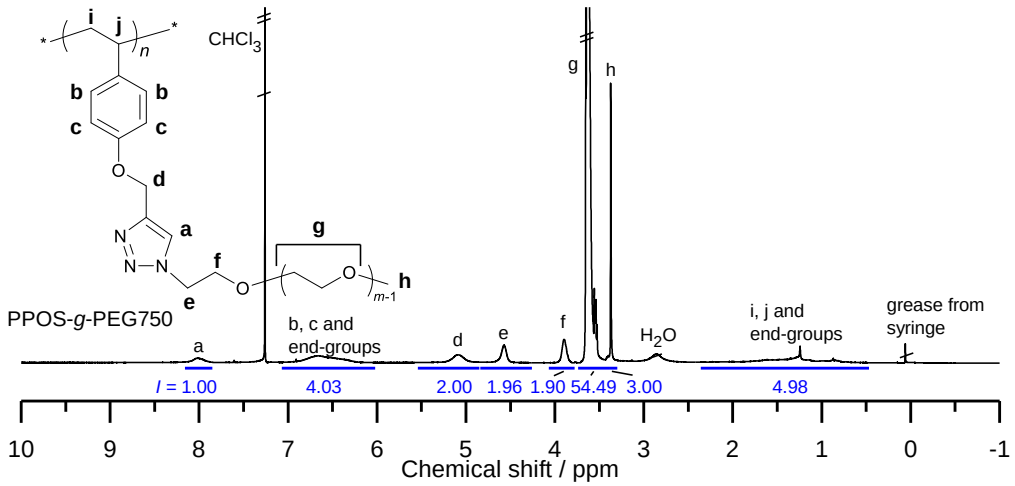

Fig. 87 ^{1}H NMR spectrum of PPOS-*g*-PEG750 in $CDCl_3$.

IR 3581, 2866 (**C$_{ali}$-H**), 1609 (**C$_{ar}$=C$_{ar}$**), 1583 (**C$_{ar}$=C$_{ar}$**), 1509 (**C$_{ar}$=C$_{ar}$**), 1456, 1349, 1325, 1298, 1241, 1177, 1095 (asymmetric –H$_2$**C-O-C**H$_2$- stretch), 1048, 1034, 946, 830 (symmetric –H$_2$**C-O-C**H$_2$- stretch), 735, 706, 666, Fig. 88.

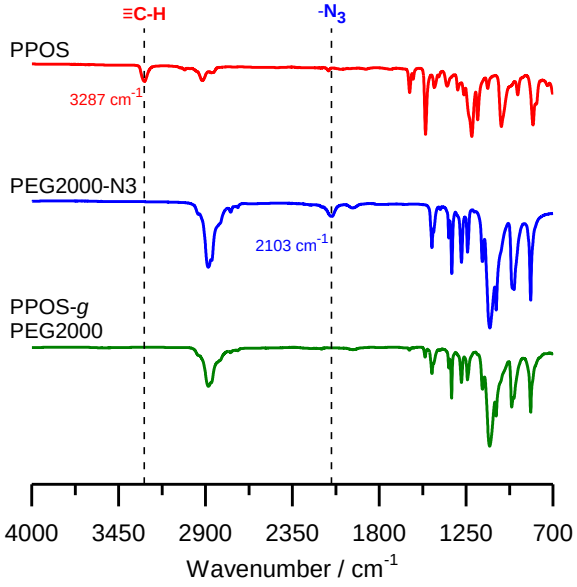

Fig. 88 Transmission IR spectra of PPOS, PEG750-N3 and PPOS-*g*-PEG750.

For the synthesis of PPOS-*g*-PEG2000, PPOS (179 mg, 1.02 mmol monomer units, calculated for a degree of polymerization of 21, 1 eq.) and PEG2000-N3 (2.27 g, 1.12 mmol calculated by a molecular weight of 2025.01 g/mol for PEG2000-N3, 1.1 eq.) were dissolved in dried THF (30 mL) and degassed by purging with argon through a cannula for 20 min at room temperature. A 20 min argon-purged stock solution of CuI/PMDETA (molar ratio = 1/1) in THF (c = 0.07 mol L^{-1}, 2.91 mL, 0.20 mmol, 0.2 eq.) was added at 40 °C to start the reaction which was monitored by ^{1}H NMR spectroscopy (not shown).

Samples were taken before adding the CuI/PMDETA stock solution and after stirring at 40 °C for 72 h and 96 h. The sample solutions were filtered through a syringe filter (PTFE, 0.45 µm) before the measurement. Since the grafting density was higher than 95% after 96 h, the reaction was stopped by cooling and flushing the solution with air through a cannula till the solution became black. The copper catalyst could not be removed by filtration over silica or aluminum oxide since the graft copolymer stuck too strong to these materials. Therefore, the solvent was removed under reduced pressure, the black residue was suspended in DCM (30 mL) and the solution was separated from the black catalyst residue by centrifugation. Finally, last remains of catalyst were removed by washing the DCM solution (40 mL) with an aqueous Na_4EDTA solution (10 mL containing 0.4 g Na_4EDTA). The removal of copper residues was confirmed by washing with aqueous ammonium hydroxide solution (25 wt%, 2 mL) which stayed colorless after the washing. The organic phase was washed with water until neutrality (two times 5 mL) and the solvent was removed under reduced pressure. Unreacted PEG was removed by dialysis (molecular weight cut-off: 15.0 kDa) in methanol. The solvent was removed under reduced pressure and the product was dried under high vacuum at room temperature yielding PPOS-*g*-PEG2000 as a white solid (yield: 1.45 g; 65%).

^{1}H NMR ($CDCl_3$) δ 8.57-7.92 (br, 1H, triazole ring proton), 7.07-6.02 (br, 4H, Ar*H*), 5.41-4.50 (br, 4H, Ar-O-C*H*$_2$- and triazole ring-C*H*$_2$-CH$_2$-O-), 4.07-3.38 (br, 225H, triazole ring-CH$_2$-C*H*$_2$-O- and all other methylene protons in PEG side-chain), 3.38-3.37 (br, 3H, -O-C*H*$_3$), 1.95-0.65 (br, 3H, polymer backbone signals C*H* and C*H*$_2$ overlapping with proton end-group signals), Fig. 89.

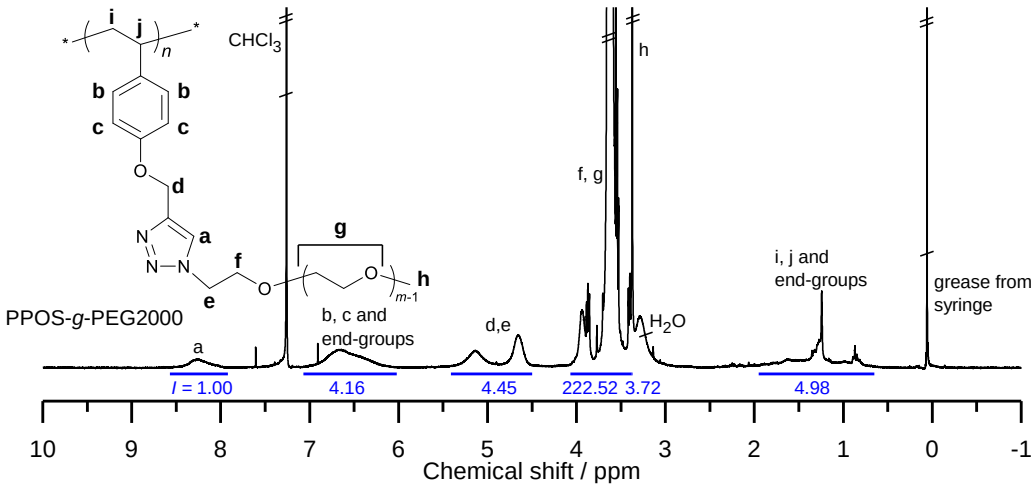

Fig. 89 ^{1}H NMR spectrum of PPOS-*g*-PEG2000 in $CDCl_3$.

IR 2946, 2881 (**C$_{ali}$-H**), 2741, 2695, 1609 (**C$_{ar}$=C$_{ar}$**), 1583 (**C$_{ar}$=C$_{ar}$**), 1509 (**C$_{ar}$=C$_{ar}$**), 1466, 1455, 1413, 1360, 1342, 1279, 1241, 1177, 1146, 1100 (asymmetric –H$_2$**C-O-C**H$_2$- stretch), 1060, 961, 947, 841 (symmetric –H$_2$**C-O-C**H$_2$- stretch), 706, Fig. 90.

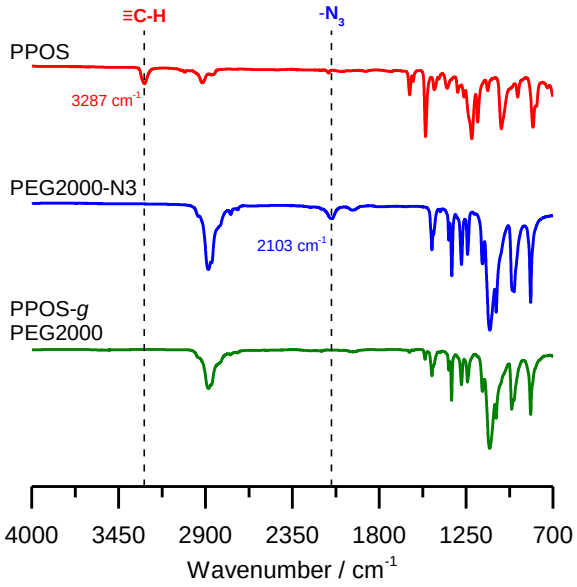

Fig. 90 Transmission IR spectra of PPOS, PEG2000-N3 and PPOS-*g*-PEG2000.

The theoretical number-average molecular weights of PPOS-*g*-PEG for the two different PEG side-chains $M_{\mathrm{n,\,theor}}$(PPOS-*g*-PEG) was calculated according to:

$$M_{\mathrm{n,\,theor}}(\mathrm{PPOS}-g-\mathrm{PEG}) = DP_{\mathrm{n}}\, M_{\mathrm{n,\,theor}}(\mathrm{PEG}-\mathrm{N3}) + M_{\mathrm{n,\,theor}}(\mathrm{PPOS}) \tag{21}$$

4.4.3.2 Poly(ethenesulfonate)s (PRES)

General polymerization procedure

The polymerizations were performed under argon in a dried Schlenk tube (round-bottom flask for PEES-RAFT1) equipped with a magnetic stir bar and sealed by a septum. For PFEG3ES-FRP-UP and PFEG3ES-RAFT-UP, a Schlenk tube with a home-made PTFE magnetic stirring bar extension paddle was used to guarantee sufficient mixing (Fig. 91).

Fig. 91 Schlenk tube with a home-made PTFE magnetic stirring bar extension paddle used for the syntheses of PFEG3ES-FRP-UP and PFEG3ES-RAFT-UP.

For FRP conditions the monomer (M) was used in combination with AIBN as a thermal initiator (I). For RAFT polymerizations OEMDTC as a CTA was also added according to the initial molar concentration ratio $[M]_0/[CTA]_0/[I]_0$. The components were mixed and degassed by purging with argon through a cannula for 20 min at room temperature. The polymerizations were started at 60 °C and stirred for different times as noted. The color of all reaction mixtures changed from colorless to light yellow. To stop the polymerizations, the reaction vessels were quenched in an ice bath and were exposed to the air. After different reaction times samples were taken, where stated, without further purification for analysis by ^{1}H NMR spectroscopy, SEC and MALDI-ToF MS. Purified PFEG2ES and PFEG3ES were only soluble in fluorinated solvents such as (trifluoromethoxy)benzene, hexafluoro-benzene, perfluorodecalin, HFIP and α,α,α,-trifluorotoluene. In contrast, their monomers, FEG2ES and FEG3ES, were also still soluble in DCM, DMSO, THF, chloroform and diethyl ether.

^{1}H NMR spectroscopy was used to calculate the monomer conversion *conv.*. The integral of the monomer's vinyl proton I_a (at about 6.1 ppm for the polymerization of EES, EG1ES and EG3ES and at about 5.7 ppm for FEG2ES and FEG3ES) was compared to the integral of the methylene protons adjacent to the sulfonate group in both the polymer I_b and the monomer I_c (at about 4.5-4.1 ppm for the polymerization of EES, 4.6-4.2 ppm for EG1ES, 4.5-4.2 ppm for EG3ES and at about 4.9-3.9 ppm for FEG2ES and FEG3ES), exemplarily shown for PFEG2ES- and PFEG3ES-RAFT in Fig. 92:

$$conv. = \frac{1 - 2I_a}{I_b + I_c} \cdot 100\% \quad (22)$$

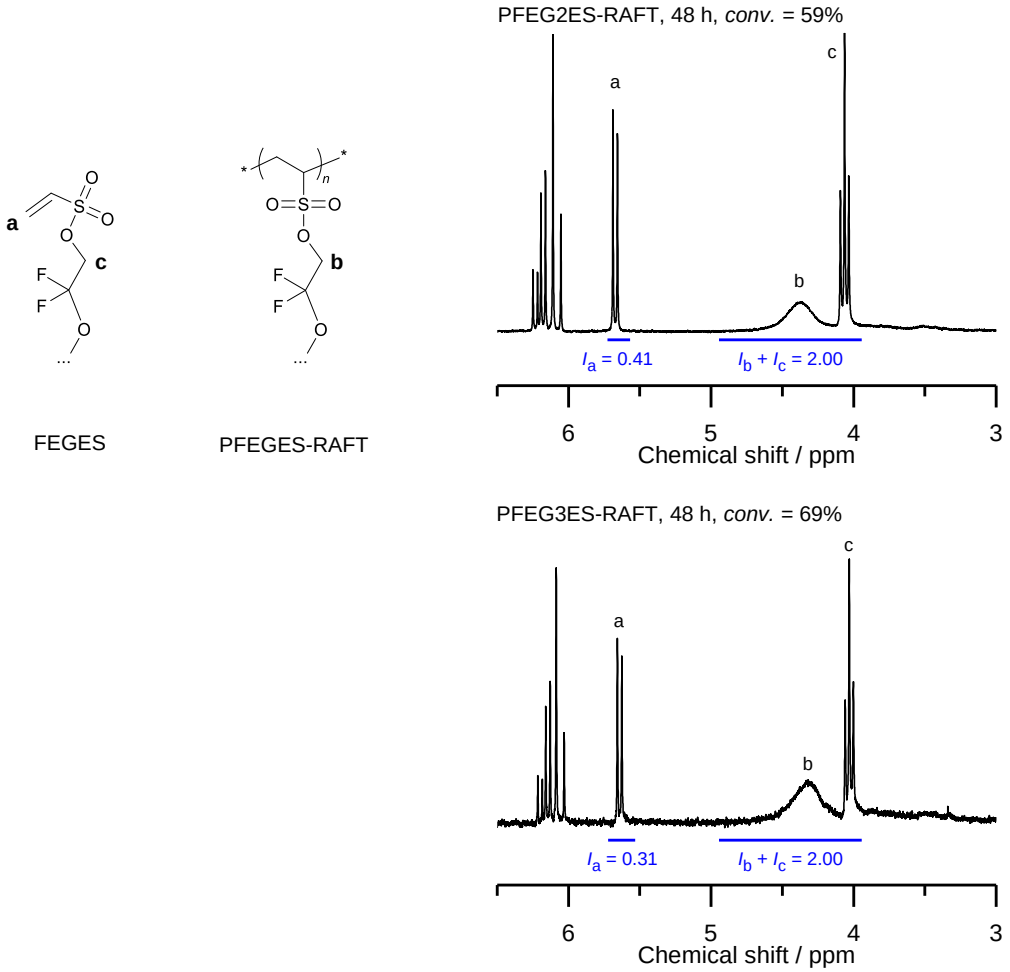

Fig. 92 ^{1}H NMR spectrum taken during the synthesis of (above) PFEG2ES-RAFT and (below) PFEG3ES-RAFT after a reaction time of 48 h. The monomer conversion *conv.* was calculated by equation (22) with the integration of the vinyl proton of the monomer I_a (5.73-5.57 ppm for PFEG2ES-RAFT and 5.72-5.53 ppm for PFEG3ES-RAFT) and the integration of the methylene protons adjacent to the sulfonate group of both the polymer I_b and the monomer I_c (4.95-3.94 ppm for PFEG2ES- and PFEG3ES-RAFT).

The ^{1}H NMR signals of PFEG2ES and PFEG3ES were shifted in the presence of the monomers (Fig. 92) in comparison to the pure state (Fig. 96 and Fig. 97). So the signal of the polymer methylene protons adjacent to the sulfonate group did not overlap with the corresponding polymer backbone signals when monomer was still present.

In the case of RAFT conditions, the theoretical number-average molecular weight $M_{n,\,theor}$ was calculated according to equation (13).

Synthesis of poly(ethyl ethenesulfonate) by FRP (PEES-FRP)

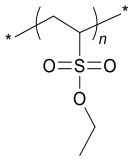

PEES-FRP

EES (1.22 g, 8.95 mmol, 500 eq) and AIBN (2.94 mg, 0.02 mmol, 1 eq) were used for the polymerization. The reaction mixture changed from lowly viscous to highly viscous. The polymerization was stopped after 24 h without further purification.

Synthesis of poly(2-methoxyethyl ethenesulfonate) by FRP (PEG1ES-FRP)

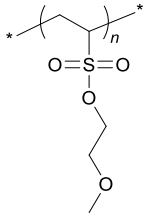

PEG1ES-FRP

EG1ES (1.21 g, 7.31 mmol, 100 eq) and AIBN (12.00 mg, 0.07 mmol, 1 eq) were used for the polymerization. The viscosity of the reaction mixture increased only slightly. The polymerization was stopped after 48 h without further purification.

The isotopic mean values received by MALDI-ToF MS from Fig. 40a are listed in Table 17.

Table 17 Isotopic mean values for crude PEG1ES-FRP. The measurement was performed in reflectron negative mode with DCTB as a matrix.

Peak number	$n = x$	$n = x + 1$	$n = x + 2$	$n = x + 3$
1 (x = 5)	1007.1	1173.4	1339.6	1505.8
2 (x = n.a.)	1027.9	1194.1	1360.2	1526.4
3 (x = 4)	1077.8	1244.0	1410.2	1576.3
4 (x = 5)	1103.8	1270.0	1436.2	1602.4
5 (x = n.a.)	1136.0	1302.3	1468.5	1634.6
6 (x = n.a.)	1147.9	1314.1	1480.3	1646.5

Synthesis of poly(2-(2-(2-methoxyethoxy)ethoxy)ethyl ethenesulfonate) by FRP (PEG3ES-FRP)

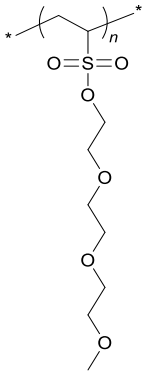

PEG3ES-FRP

EG3ES (1.18 g, 4.66 mmol, 100 eq) and AIBN (7.65 mg, 0.05 mmol, 1 eq) were used for the polymerization. The viscosity of the reaction mixture increased only slightly. The polymerization was stopped after 48 h without further purification.

The isotopic mean values received by MALDI-ToF MS from Fig. 40b are listed in Table 18.

Table 18 Isotopic mean values for crude PEG3ES-FRP. The measurement was performed in reflectron negative mode with DCTB as a matrix.

Peak number	$n = x$	$n = x + 1$	$n = x + 2$	$n = x + 3$	$n = x + 4$	$n = x + 5$	$n = x + 6$	$n = x + 7$
1 ($x = 0$)	843.6	1098.0	1352.4	-	-	-	-	-
2 ($x = 2$)	869.8	1124.2	1378.5	1632.8	1887.1	2141.6	2395.7	2649.9
3 ($x = 0$)	913.8	1168.2	1422.7	1677.0	1931.2	-	-	-
4 ($x = 3$)	939.2	1193.7	1448.0	-	-	-	-	-
5 ($x = 0$)	990.1	1244.2	1498.5	-	-	-	-	-
6 ($x = 1$)	1035.8	1290.1	1544.3	-	-	-	-	-

Synthesis of poly(2,2-difluoro-2-(1,1,2,2-tetrafluoro-2-(trifluoromethoxy)ethoxy)ethyl ethene-sulfonate) by FRP (PFEG2ES-FRP)

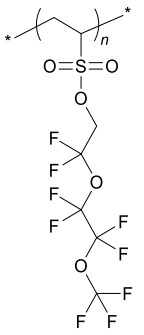

PFEG2ES-FRP

FEG2ES (1.08 g, 2.89 mmol, 100 eq) and AIBN (4.75 mg, 0.03 mmol, 1 eq) were used for the polymerization. The reaction mixture changed from lowly viscous to highly viscous. The polymerization was stopped after 19 h without further purification.

Synthesis of poly(2,2-difluoro-2-(1,1,2,2-tetrafluoro-2-(1,1,2,2-tetrafluoro-2-(trifluoromethoxy)-ethoxy)ethoxy)ethyl ethenesulfonate) (PFEG3ES) by FRP

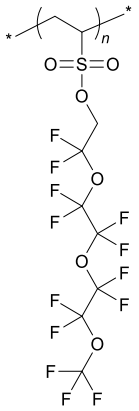

PFEG3ES-FRP

Synthesis of PFEG3ES-FRP

FEG3ES (1.42 g, 2.91 mmol, 100 eq) and AIBN (4.78 mg, 0.03 mmol, 1 eq) were used for the polymerization. The reaction mixture changed from lowly viscous to highly viscous. The polymerization was stopped after 21 h without further purification.

Synthesis of PFEG3ES-FRP-UP

FEG3ES (46.60 g, 95.46 mmol, 100 eq) and AIBN (156.75 mg, 0.95 mmol, 1 eq) were used for the polymerization. The reaction mixture changed from lowly viscous to moderately viscous. The polymerization was stopped after 29 h. The crude reaction mixture was purified by diluting with hexafluorobenzene (10 mL) and precipitating in dichloromethane (three times 200 mL). The product was dried under high vacuum at room temperature overnight yielding the polymer as a yellowish and transparent soft solid (yield 17.50 g; 75% at 50% monomer conversion). Residual FEG3ES could be recycled from the supernatant solution by vacuum distillation. ^{1}H NMR (perfluorodecalin as a solvent with a $CDCl_3$-filled coaxial insert) δ 5.51-0.27 (br, all polymer signals), Fig. 93.

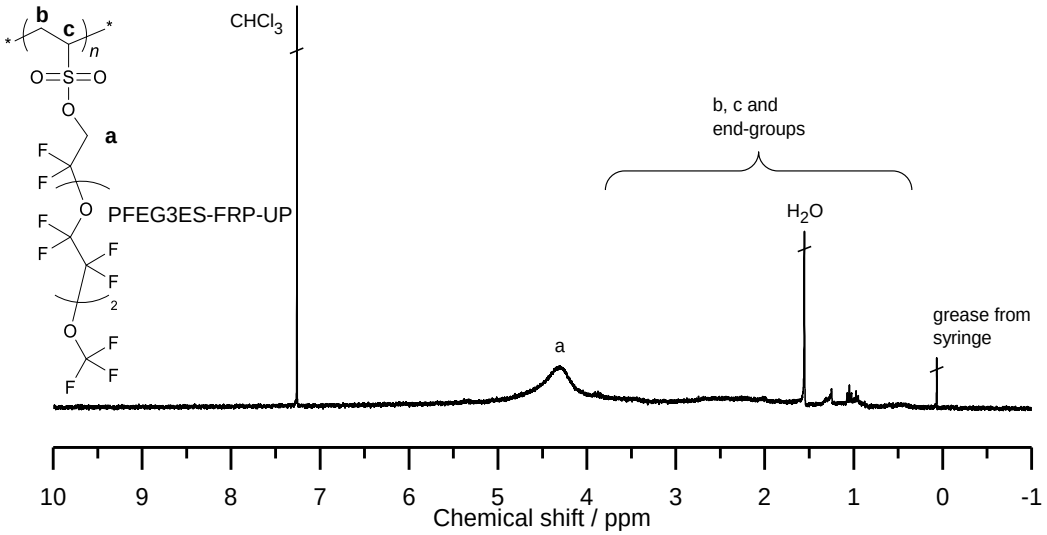

Fig. 93 ^{1}H NMR spectrum of purified PFEG3ES-FRP-UP synthesized by FRP in bulk at 60 °C using AIBN as a thermal initiator. The measurement was performed in perfluorodecalin with $CDCl_3$ in a coaxial insert.

Synthesis of PFEG3ES-FRP-HFB1

FEG3ES (2.33 g, 4.77 mmol, 100 eq) and AIBN (7.83 mg, 0.05 mmol, 1 eq) in hexafluorobenzene (0.30 mL) were used for the polymerization. The viscosity of the reaction mixture increased only slightly. The polymerization was stopped after 48 h without further purification.

Synthesis of PFEG3ES-FRP-HFB2

FEG3ES (2.35 g, 4.82 mmol, 100 eq) and AIBN (7.91 mg, 0.05 mmol, 1 eq) in hexafluorobenzene (0.15 mL) were used for the polymerization. The viscosity of the reaction mixture increased only slightly. The polymerization was stopped after 48 h without further purification.

Synthesis of poly(ethyl ethenesulfonate) (PEES) by RAFT

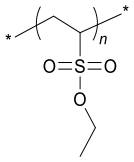

PEES-RAFT

Synthesis of PEES-RAFT1

EES (10.72 g, 78.72 mmol, 500 eq), OEMDTC (138.64 µL, 0.79 mmol, 5 eq) and AIBN (25.85 mg, 0.16 mmol, 1 eq) were used for the polymerization. The reaction mixture changed from lowly viscous to highly viscous. The polymerization was stopped after 20.5 h. The crude reaction mixture was

purified by diluting with chloroform (15 mL) and precipitating in hexane (four times 400 mL). Further purification was carried out by soxhlet extraction with hexane at 85 °C for 7 h. The product was dissolved in chloroform (100 mL) and dried under vacuum at 50 °C yielding the polymer as a white solid (yield: 4.03 g; 61% at 60% monomer conversion). ^{1}H NMR ($CDCl_3$) δ 4.54-4.25 (br, 2H, -O-C*H*$_2$-), 4.15-1.58 (br, 3H, polymer backbone signals C*H* and C*H*$_2$, overlapping with proton end-group signals), 1.55-1.34 (br, 3H, -O-CH$_2$-C*H*$_3$), 1.31-0.79 (br, 3H, polymer backbone signals C*H* and C*H*$_2$, overlapping with proton end-group signals), Fig. 94.

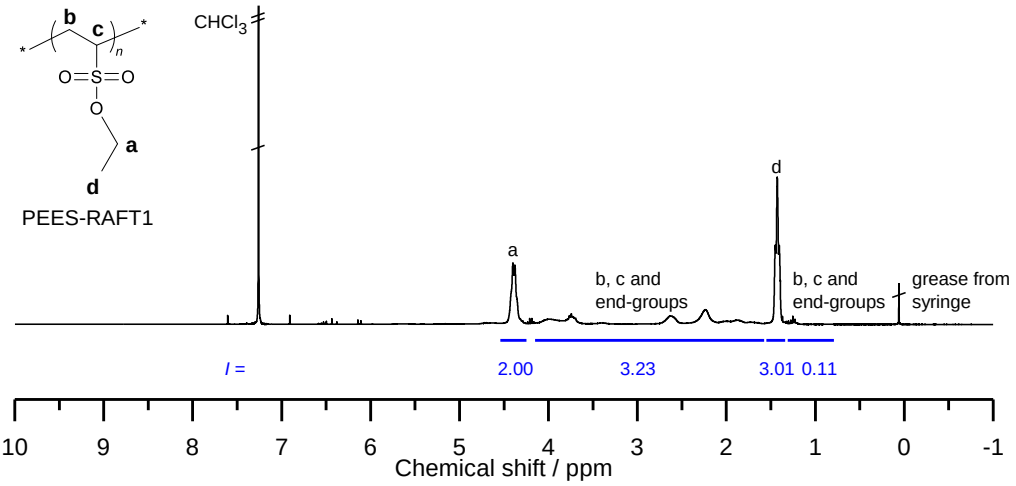

Fig. 94 ^{1}H NMR spectrum of PEES-RAFT1 in $CDCl_3$.

The isotopic mean values received by MALDI-ToF MS from Fig. 43a are listed in Table 19.

Table 19 Isotopic mean values (Gaussian fit) for purified PEES-RAFT1. The measurement was performed in reflectron positive mode with IAA as a matrix.

Peak number	*n* = 32	*n* = 33	*n* = 34
1	4558.6	4695.0	4832.3
2	4582.9	4719.6	4854.9
3	4602.5	4738.8	4874.9
4	4626.5	4762.1	4899.2

Synthesis of PEES-RAFT2

EES (1.16 g, 8.49 mmol, 500 eq), OEMDTC (14.95 µL, 0.08 mmol, 5 eq) and AIBN (2.79 mg, 0.02 mmol, 1 eq) were used for the polymerization. The reaction mixture changed from lowly viscous to highly viscous. The polymerization was stopped after 17.5 h. The crude reaction mixture was purified by diluting with chloroform (0.5 mL) and precipitating in hexane (four times 30 mL). The product was dissolved in chloroform (5 mL) and dried under high vacuum at room temperature yielding the polymer as a white solid (yield: 0.80 g; 98% at 69% monomer conversion). ^{1}H NMR ($CDCl_3$) δ 4.58-4.23 (br, 2H, -O-C*H*$_2$-), 4.22-1.58 (br, 3H, polymer backbone signals C*H* and C*H*$_2$, overlapping

with proton end-group signals), 1.55-1.33 (br, 3H, -O-CH_2-CH_3), 1.31-0.79 (br, 3H, polymer backbone signals C*H* and CH_2, overlapping with proton end-group signals), Fig. 95.

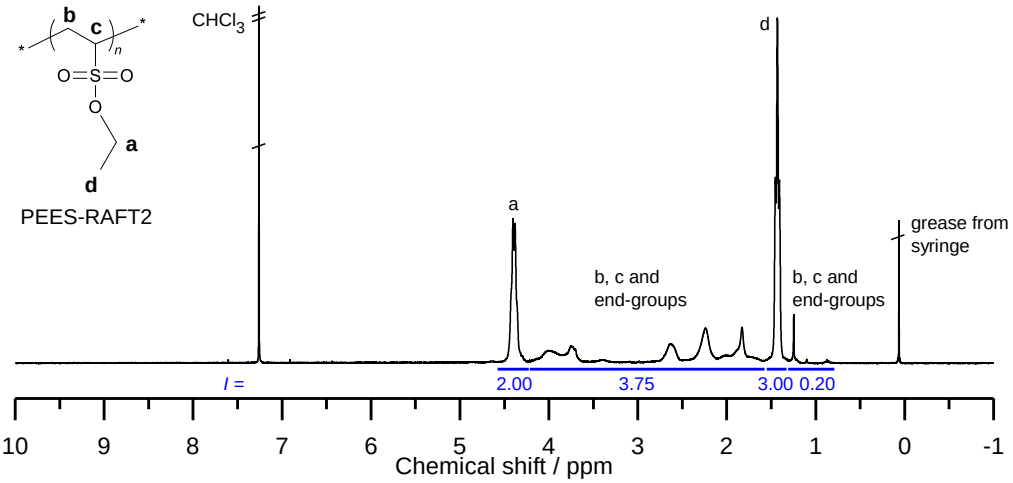

Fig. 95 ^{1}H NMR spectrum of PEES-RAFT2 in $CDCl_3$.

Synthesis of poly(2,2-difluoro-2-(1,1,2,2-tetrafluoro-2-(trifluoromethoxy)ethoxy)ethyl ethene-sulfonate) by RAFT (PFEG2ES-RAFT)

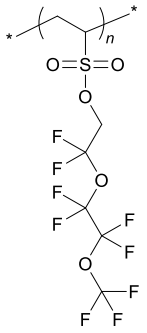

PFEG2ES-RAFT

FEG2ES (3.10 g, 8.32 mmol, 100 eq), OEMDTC (29.31 µL, 0.17 mmol, 2 eq) and AIBN (13.66 mg, 0.08 mmol, 1 eq) were used for the polymerization. The reaction mixture changed from lowly viscous to moderately viscous. The polymerization was stopped after 48 h. The crude reaction mixture was purified by diluting with hexafluorobenzene (2 mL) and precipitating in DCM (two times 20 mL). The product was dried under high vacuum at room temperature yielding the polymer as a yellowish and transparent solid (yield: 1.34 g; 72% at 59% monomer conversion). ^{1}H NMR (perfluorodecalin as a solvent with a $CDCl_3$-filled coaxial insert) δ 5.33-0.15 (br, all polymer signals), Fig. 96.

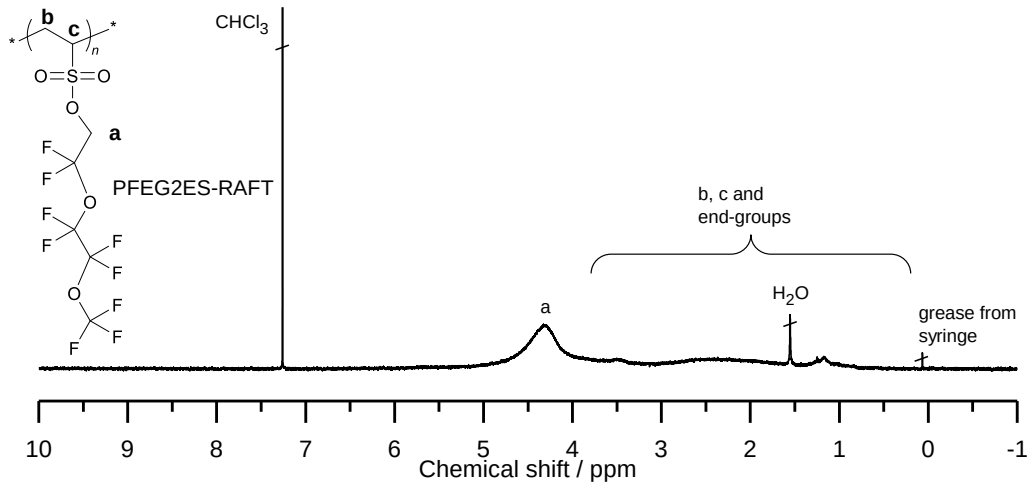

Fig. 96 ^{1}H NMR spectrum of purified PFEG2ES-RAFT synthesized by RAFT polymerization in bulk at 60 °C using AIBN as a thermal initiator and OEMDTC as a CTA. The measurement was performed in perfluorodecalin with $CDCl_3$ in a coaxial insert.

The isotopic mean values received by MALDI-ToF MS from Fig. 45 are listed in Table 20.

Table 20 Isotopic mean values for purified PFEG2ES-RAFT. The measurement was performed in reflectron positive mode with DHB as a matrix.

Peak number	*n* = 12	*n* = 13	*n* = 14	*n* = 15	*n* = 16	*n* = 17	*n* = 18	*n* = 19	*n* = 20	*n* = 21
1	4617.1	4989.1	5361.4	5732.4	6104.3	6477.4	6849.9	7223.6	7595.0	7966.2
2	4642.2	5014.2	5386.4	5759.4	6130.5	6503.7	6875.9	7248.8	7619.8	7993.4
3	4669.1	5040.3	5412.3	5785.3	6158.5	6529.5	6903.5	7277.6	7646.5	8019.1
4	4712.1	5084.2	5457.1	5827.5	6200.6	6573.4	6944.6	7318.0	7689.5	8063.9
5	4730.2	5102.3	5475.3	5847.4	6219.4	6591.8	6963.8	7336.5	7708.6	8080.9
6	4756.2	5128.2	5500.5	5873.5	6246.6	6617.8	6990.8	7362.9	7734.2	8107.3

n = 22	*n* = 23	*n* = 24
8339.3	8711.8	-
8365.8	8737.8	9108.4
8391.0	-	-
-	-	-
8453.4	8825.8	9198.3
8480.4	8851.7	9224.1

Synthesis of poly(2,2-difluoro-2-(1,1,2,2-tetrafluoro-2-(1,1,2,2-tetrafluoro-2-(trifluoromethoxy)-ethoxy)ethoxy)ethyl ethenesulfonate) (PFEG3ES) by RAFT

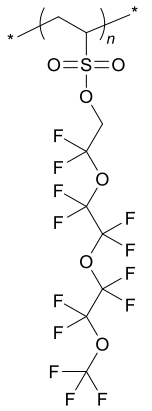

PFEG3ES-RAFT

Synthesis of PFEG3ES-RAFT

FEG3ES (3.09 g, 6.33 mmol, 100 eq), OEMDTC (22.31 µL, 0.13 mmol, 2 eq) and AIBN (10.40 mg, 0.06 mmol, 1 eq) were used for the polymerization. The reaction mixture changed from lowly viscous to moderately viscous. The polymerization was stopped after 48 h. The crude reaction mixture was purified by diluting with hexafluorobenzene (2 mL) and precipitating in chloroform (three times 25 mL). The product was dried under high vacuum at room temperature yielding the polymer as a yellowish and transparent solid (yield 1.62 g; 75% at 69% monomer conversion). ^{1}H NMR (perfluorodecalin as a solvent with a $CDCl_3$-filled coaxial insert) δ 5.33-0.15 (br, all polymer signals), Fig. 97.

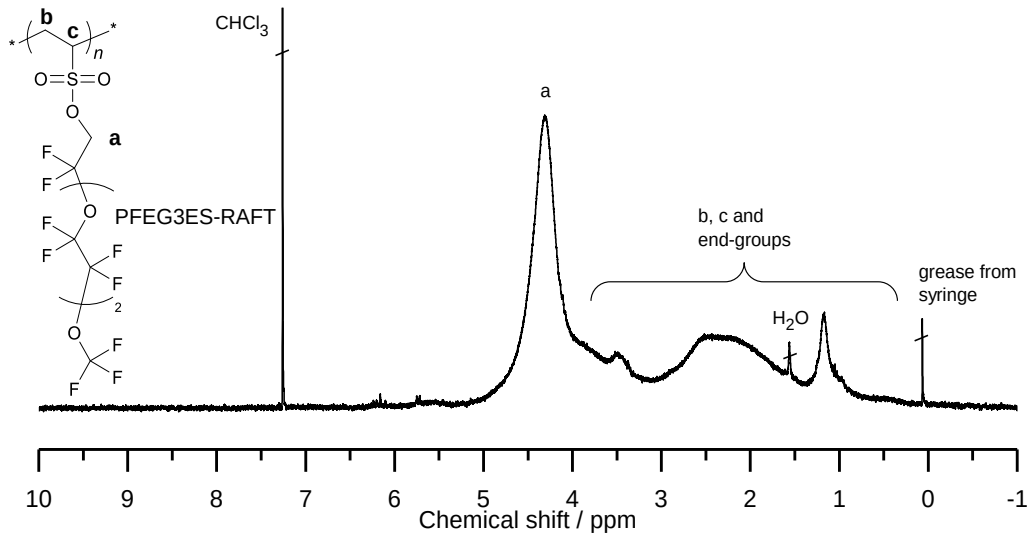

Fig. 97 ^{1}H NMR spectrum of purified PFEG3ES-RAFT synthesized by RAFT polymerization in bulk at 60 °C using AIBN as a thermal initiator and OEMDTC as a CTA. The measurement was performed in perfluorodecalin with $CDCl_3$ in a coaxial insert.

The isotopic mean values received by MALDI-ToF MS from Fig. 46 are listed in Table 21.

Table 21 Isotopic mean values for purified PFEG3ES-RAFT. The measurement was performed in reflectron positive mode with DHB as a matrix.

Peak number	*n* = 17	*n* = 18	*n* = 19	*n* = 20	*n* = 21	*n* = 22	*n* = 23	*n* = 24	*n* = 25
1	8445.1	8932.8	9419.6	9909.0	10397.3	10884.5	11371.4	11861.7	12347.1
2	8472.6	8960.2	9447.2	9935.8	10421.7	10910.1	11400.1	11885.5	12373.4
3	8533.3	9020.9	9509.6	9996.7	10484.7	10971.7	11460.2	11948.2	12436.4
4	8559.3	9047.9	9535.3	10023.0	10510.7	10999.3	11486.8	11975.0	12462.4
5	8615.8	9104.1	9590.0	10077.3	10566.6	11056.5	11542.0	12031.7	12518.6
6	8644.2	9130.9	9618.1	10108.0	10594.0	11082.0	11571.6	12061.0	12547.4
7	8671.8	9158.7	9646.0	10134.2	10621.1	11110.3	11599.6	12089.6	12573.9

n = 26	*n* = 27	*n* = 28	*n* = 29
-	-	-	-
-	-	-	-
12923.1	13411.1	13898.0	14387.8
12949.3	13437.1	13925.5	14413.3
-	-	-	-
-	-	-	-
-	-	-	-

Synthesis of PFEG3ES-RAFT-UP

FEG3ES (48.38 g, 99.10 mmol, 100 eq), OEMDTC (349.07 µL, 1.98 mmol, 2 eq) and AIBN (162.74 mg, 0.99 mmol, 1 eq) were used for the polymerization. The reaction mixture changed from lowly viscous to moderately viscous. The polymerization was stopped after 72 h. The crude reaction mixture was purified by diluting with hexafluorobenzene (10 mL) and precipitating in dichloromethane (two times 200 mL). The product was dried under high vacuum at room temperature overnight yielding the polymer as a yellowish and transparent highly viscous liquid (yield 20.50 g; 76% at 56% monomer conversion). Residual FEG3ES could be recycled from the supernatant solution by vacuum distillation. ^{1}H NMR (perfluorodecalin as a solvent with a $CDCl_3$-filled coaxial insert) δ 5.33-0.15 (br, all polymer signals), Fig. 98.

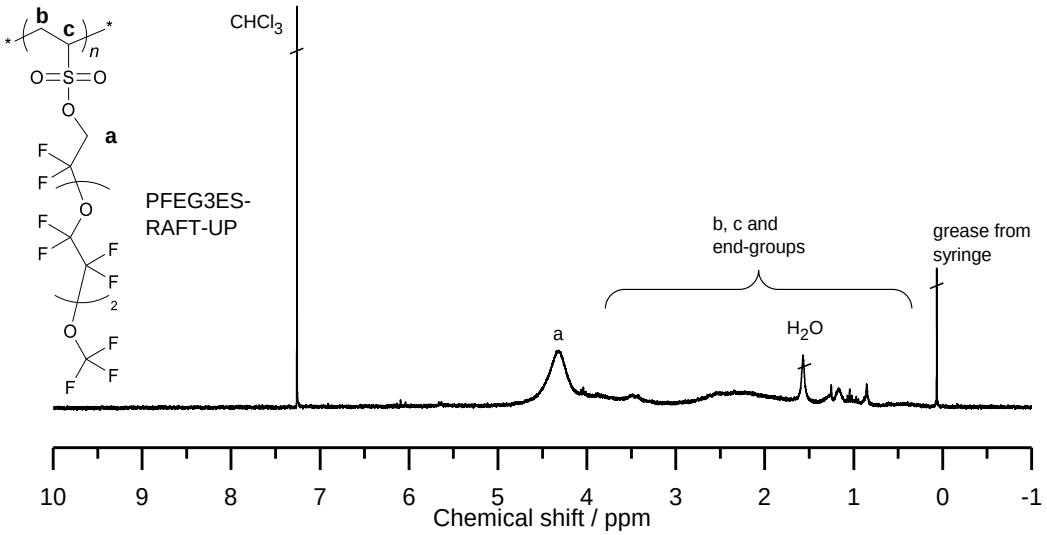

Fig. 98 ^{1}H NMR spectrum of purified PFEG3ES-RAFT-UP synthesized by RAFT polymerization in bulk at 60 °C using AIBN as a thermal initiator and OEMDTC as a CTA. The measurement was performed in perfluorodecalin with $CDCl_3$ in a coaxial insert.

Synthesis of PFEG3ES-RAFT-HFB1

FEG3ES (3.19 g, 6.53 mmol, 100 eq), OEMDTC (23.00 µL, 0.13 mmol, 2 eq) and AIBN (10.72 mg, 0.07 mmol, 1 eq) in hexafluorobenzene (0.41 mL) were used for the polymerization. The viscosity of the reaction mixture increased only slightly. The polymerization was stopped after 48 h without further purification.

Synthesis of PFEG3ES-RAFT-HFB2

FEG3ES (2.41 g, 4.93 mmol, 100 eq), OEMDTC (17.36 µL, 0.10 mmol, 2 eq) and AIBN (8.09 mg, 0.05 mmol, 1 eq) in hexafluorobenzene (0.15 mL) were used for the polymerization. The viscosity of

the reaction mixture increased only slightly. The polymerization was stopped after 48 h without further purification.

Synthesis of PFEG3ES-RAFT-HFB3

FEG3ES (2.31 g, 4.74 mmol, 100 eq), OEMDTC (16.68 µL, 0.09 mmol, 2 eq) and AIBN (7.78 mg, 0.05 mmol, 1 eq) in hexafluorobenzene (0.04 mL) were used for the polymerization. The viscosity of the reaction mixture increased only slightly. The polymerization was stopped after 48 h without further purification.

4.4.4 Lithium salt synthesis

4.4.4.1 Lithium 2,2-difluoro-2-(1,1,2,2-tetrafluoro-2-(1,1,2,2-tetrafluoro-2-(trifluoromethoxy)-ethoxy)ethoxy)ethan-1-olate (LiFEG3)

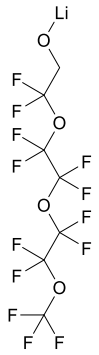

LiFEG3

For the synthesis of LiFEG3, *n*-butyllithium (2.5 M in *n*-hexane, 8.00 mL, 20.0 mmol, 0.95 eq) was added dropwise to ice-cooled FEG3 (5.05 mL, 21.0 mmol, 1.0 eq) under stirring and gas evolution within 10 min resulting in a colorless turbid two-phase system. The viscous reaction mixture was stirred for another 35 min at 45 °C and became slowly clear. Excess of FEG3 was removed at 60 °C for 1 h and at room temperature overnight under high vacuum yielding LiFEG3 as a white turbid, slightly transparent and viscous liquid (6.50 g, 80%). Anal. Calcd for $C_7H_2F_{13}LiO_4$: C, 20.8; H, 0.5; N, 0.0. Found: C, 21.2; H, 0.5; N, 0.3%. ^{1}H NMR (CD_3OD) δ 3.93 (t, J = 11.5, 2H, -O-CH_2-), Fig. 99.

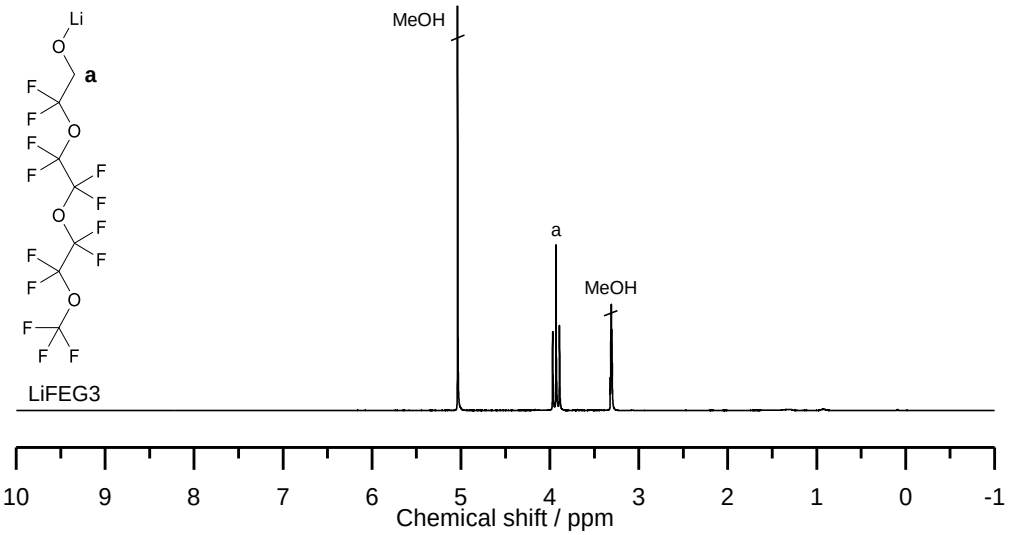

Fig. 99 ^{1}H NMR spectrum of LiFEG3 in CD_3OD.

(Perfluorodecalin as a solvent with a $CDCl_3$ filled coaxial insert) δ 3.76 (t, J = 12.5, 2H, -O-CH_2-), Fig. 100.

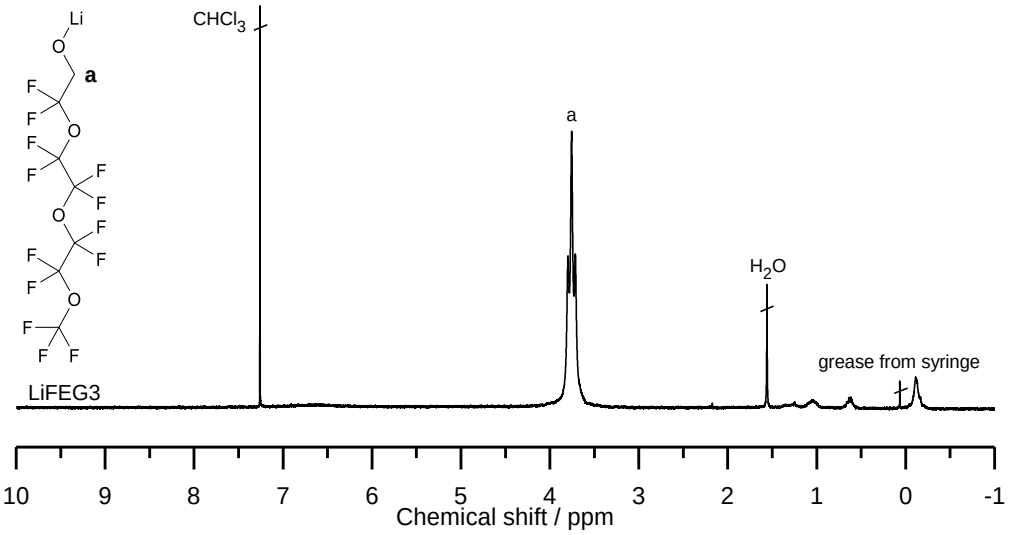

Fig. 100 ^{1}H NMR spectrum of LiFEG3 in perfluorodecalin with $CDCl_3$ in a coaxial insert.

^{19}F NMR (CD_3OD with C_6F_6 as an internal reference) δ -56.5 (t, J = 9.0, 3F, F_3C-), -80.7 – -81.9 (m, 2F, F_3C-O-CF_2-), -88.6 – -90.5 (m, 6F, F_3C-O-CF_2-CF_2-O-CF_2-CF_2-), -91.1 – -92.3 (m, 2F, -CF_2-CH_2-), Fig. 101.

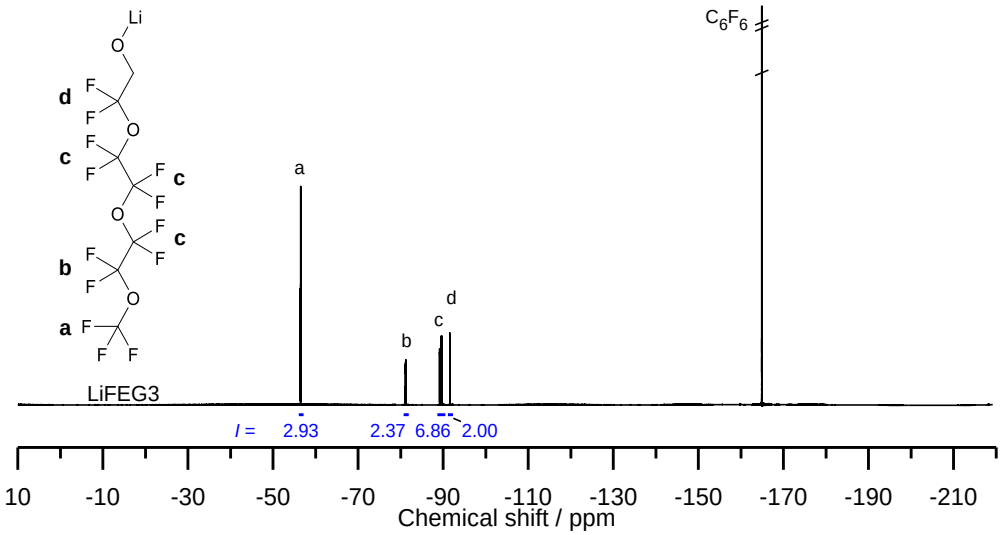

Fig. 101 ^{19}F NMR spectrum of LiFEG3 in CD_3OD with C_6F_6 as an internal reference.

For a comparison with distilled FEG3: ^{1}H NMR (CD_3OD) δ 3.88 (t, J = 10.3, 2H, -O-CH_2-), Fig. 102.

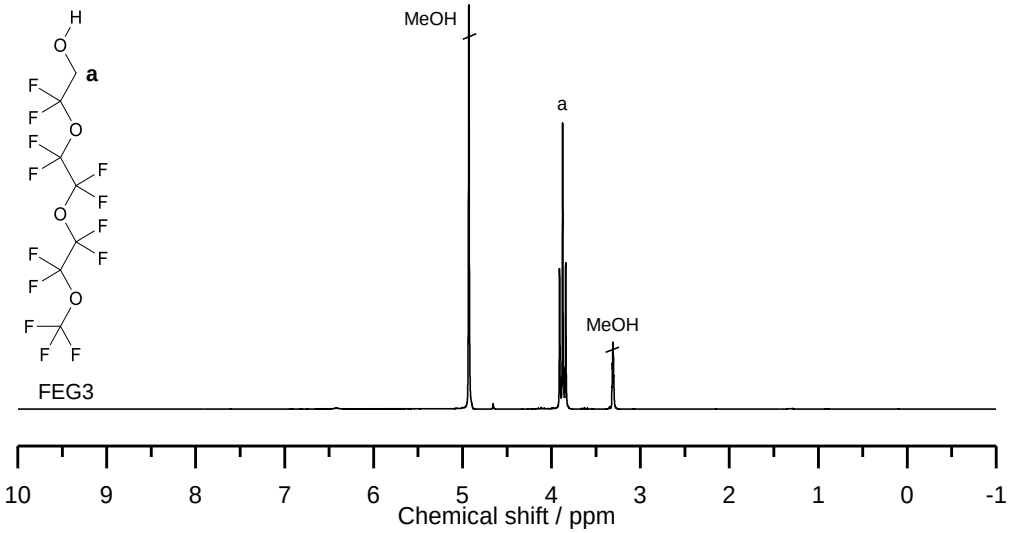

Fig. 102 ^{1}H NMR spectrum of FEG3 in CD_3OD.

For a comparison with distilled FEG3: (Perfluorodecalin as a solvent with a $CDCl_3$ filled coaxial insert) δ 4.56 (s, 1H, *H*O-), 3.64 (t, J = 9.6, 2H, -O-CH_2-), Fig. 103.

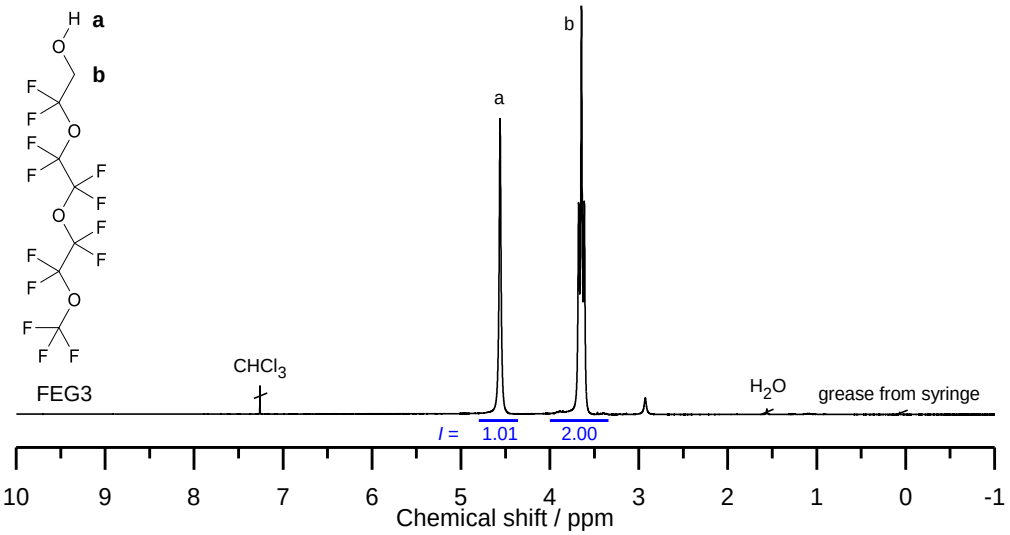

Fig. 103 ^{1}H NMR spectrum of FEG3 in perfluorodecalin with $CDCl_3$ in a coaxial insert.

For a comparison with distilled FEG3: ^{19}F NMR (CD_3OD with C_6F_6 as an internal reference) δ -56.5 (t, J = 9.0, 3F, F_3C-), -80.4 – -82.4 (m, 2F, F_3C-O-CF_2-), -88.6 – -90.6 (m, 6F, F_3C-O-CF_2-CF_2-O-CF_2-CF_2-), -91.1 – -92.3 (m, 2F, -CF_2-CH_2-), Fig. 104.

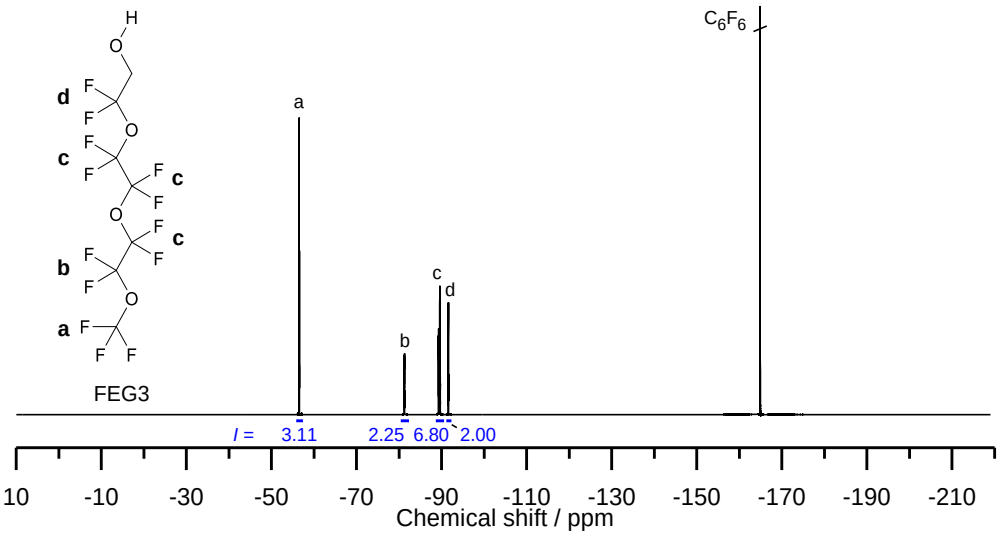

Fig. 104 ^{19}F NMR spectrum of FEG3 in CD_3OD with C_6F_6 as an internal reference.

4.5 Solid polymer electrolyte preparation

The molar ratio of oxygen to lithium O/Li is given by the molar amount of oxygen atoms n_O in both the polymer monomer units and the salt, and by the molar amount of lithium ions in the salt n_{Li+}. The number of oxygen atoms in the polymer monomer unit $N_{O,\,polymer}$ was 1 for PEG750 and PEG2000, 17 for PPOS-*g*-PEG750, 41 for PPOS-*g*-PEG2000 and 6 for PFEG3ES. The number of oxygen atoms in the lithium salt $N_{O,\,salt}$ was 0 for LiTFSI and 3 for LiFEG3. The oxygen atom carrying the negative

charge in LiFEG3 was not considered. The number of lithium atoms in the lithium salt $N_{Li+,\,salt}$ was 1 for LiTFSI and LiFEG3. The O/Li ratio was calculated according to:

$$O/Li = \frac{n_O}{n_{Li+}} = \frac{N_{O,\,polymer}\, n_{polymer} + N_{O,\,salt}\, n_{salt}}{N_{Li+,\,salt}\, n_{salt}} \tag{23}$$

where $n_{polymer}$ and n_{salt} are the molar amounts of the polymer monomer units and of the lithium salt. By inserting $n = m/M$ with m being the mass and M the molar mass follows:

$$O/Li = \frac{N_{O,\,polymer}\, m_{polymer}/M_{polymer} + N_{O,\,salt}\, m_{salt}/M_{salt}}{N_{Li+,\,salt}\, m_{salt}/M_{salt}} \tag{24}$$

For a given mass of polymer $m_{polymer}$ the mass of lithium salt m_{salt} was calculated by:

$$m_{salt} = \frac{N_{O,\,polymer}\, m_{polymer}\, M_{salt}}{M_{polymer}\left(N_{Li+,\,salt}\, O/Li - N_{O,\,salt}\right)} \tag{25}$$

where $M_{polymer}$ is the molar mass of one monomer unit, so that the end-groups of the polymer were neglected in the above derivation. $M_{polymer}$ was 44.05 g mol^{-1} for PEG750 and PEG2000, 964.07 g mol^{-1} for PPOS-*g*-PEG750 (calculated from $M_{n,\,theor}$ after subtraction of end-group molecular weight, equation (21)), 2021.27 g mol^{-1} for PPOS-*g*-PEG2000 (calculated from $M_{n,\,theor}$ after subtraction of end-group molecular weight, equation (21)) and 488.17 g mol^{-1} for PFEG3ES.

PEG or PPOS-*g*-PEG/LiTFSI SPEs (with O/Li ratios of 25, 16 and 10 for the L750, G750 and G2000 SPEs and of 16, 12 and 8 for the L2000 SPEs) were were prepared from polymer melt. For a typical preparation, such as for L750-16, LiTFSI (948.1 mg, equation (25), 3.30 mmol) was dissolved in a melt of PEG750-OH (2328 mg) under stirring at 60 °C for one hour.

PFEG3ES-FRP-UP/LiTFSI SPEs with O/Li ratios of 69, 36, 27, 16 and 10 were prepared from polymer melt. For instance, for an O/Li ratio of 69, PFEG3ES-FRP-UP (700.0 mg) was molten at 110 °C and mixed with LiTFSI (35.8 mg, equation (25), 0.12 mmol). Still after 20 hours of stirring at 110 °C, the LiTFSI remained unresolved. The same observation was made for the other O/Li ratios.

PFEG3ES-FRP-UP/LiFEG3 SPEs with O/Li ratios of 69, 15, 10 and 5 were prepared from solution. For a typical preparation, such as for SPE-10, LiFEG3 (108.5 mg, equation (25), 0.27 mmol) and hexafluorobenzene (0.52 mL) were added to PFEG3ES-FRP-UP (153.0 mg), so that the total mass

concentration was 0.5 g mL^{-1}. After being stirred for 2 h at room temperature, the mixture was dried at 40 °C under reduced pressure overnight yielding the SPE-10 as an amber-colored, slightly turbid and highly viscous transparent liquid. Regarding all SPEs, the viscosity increased significantly with decreasing salt content. Whereas the SPE-5 was still liquid, the SPE-15 and -69 were highly viscous and nearly solid at room temperature. All SPEs were of a transparent and amber/yellow-colored appearance. The SPE-5 and -10 were still slightly turbid, while the SPE-15 and -69 were clear. SPE-69, -15, -10 and -5: ^{1}H NMR (perfluorodecalin as a solvent with a $CDCl_3$ filled coaxial insert), Fig. 53 and Fig. 105.

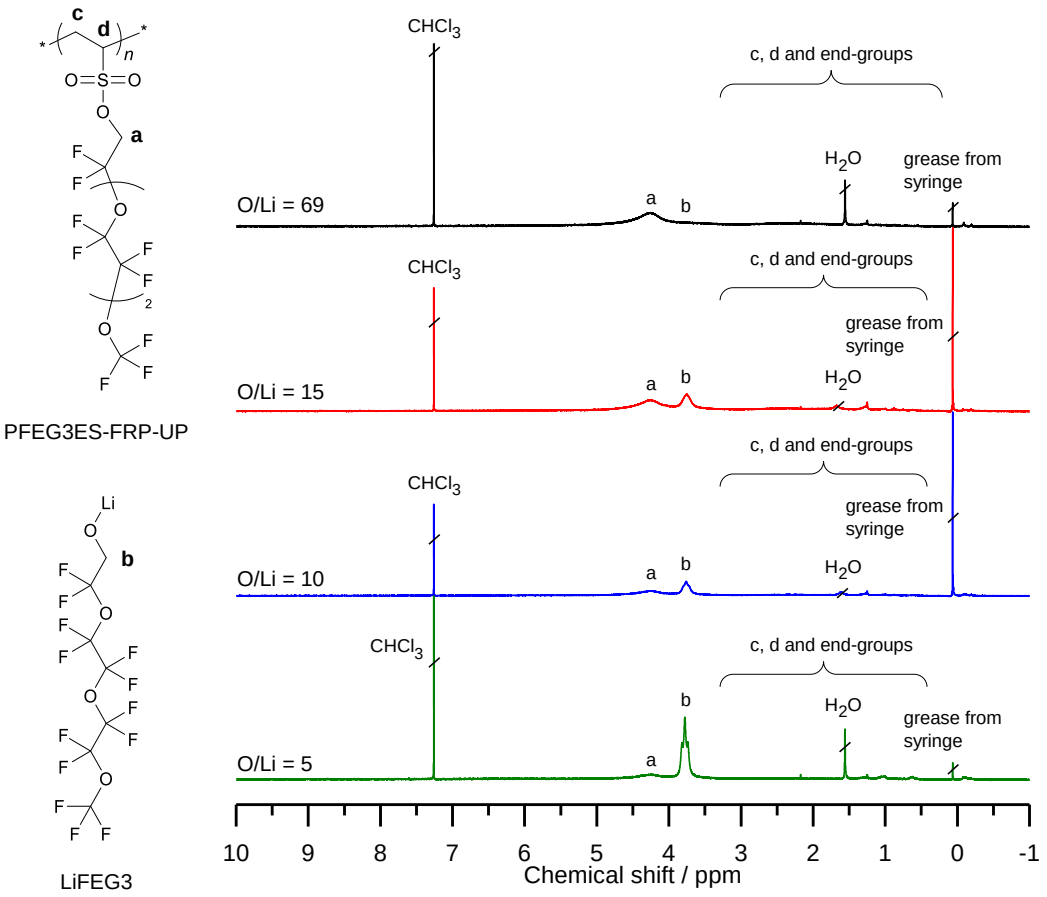

Fig. 105 ^{1}H NMR spectra of PFEG3ES-FRP-UP/LiFEG3 SPEs in perfluorodecalin with $CDCl_3$ in a coaxial insert.

To test the chemical stability of the end-groups of PFEG3ES-RAFT-UP towards LiFEG3, PFEG3ES-RAFT-UP (335.5 mg) and LiFEG3 (238.0 mg, equation (25), 0.59 mmol) were stiredd for 16 h at room temperature. The slightly turbid and viscous PFEG3ES-RAFT-UP/LiFEG3 mixture (O/Li = 10) changed from yellow to intense orange. ^{1}H NMR (perfluorodecalin as a solvent with a $CDCl_3$ filled coaxial insert), Fig. 53 and Fig. 106.

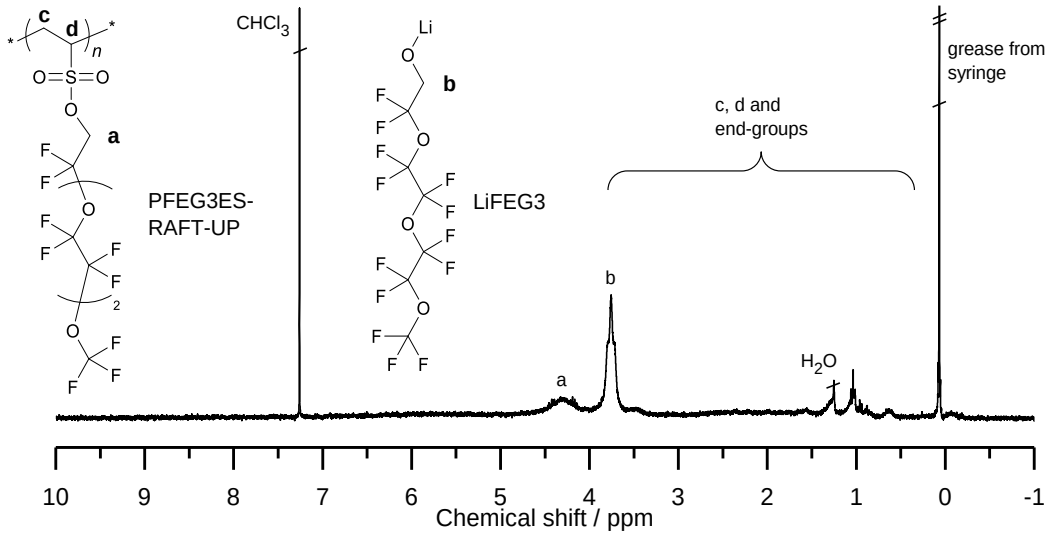

Fig. 106 ^{1}H NMR spectrum of a PFEG3ES-RAFT-UP/LiFEG3 mixture (O/Li = 10) in perfluorodecalin with $CDCl_3$ in a coaxial insert. The mixture was stirred for 16 h at room temperature.

$CDCl_3$ (0.6 mL) was added to the PFEG3ES-RAFT-UP/LiFEG3 mixture (O/Li = 10) and stirred for 1 h at room temperature. After allowing the emulsion to rest for 1 h, the supernatant solution was pipetted off from the vicous polymer phase and directly ivestigated by ^{1}H NMR spectroscopy. FEG3E: ^{1}H NMR ($CDCl_3$) δ 4.80 (t, J = 9.1, 2H, -CH_2-CF_2-), 4.54 (q, J = 7.1, 2H, -O-CH_2-CH_3), 1.41 (t, J = 7.1, 3H, H_3C-). FEG3: δ 3.96 (td, J = 9.7, 6.2, 2H, -O-CH_2-), 2.00 (t, J = 6.2, 1H, HO-), Fig. 107.

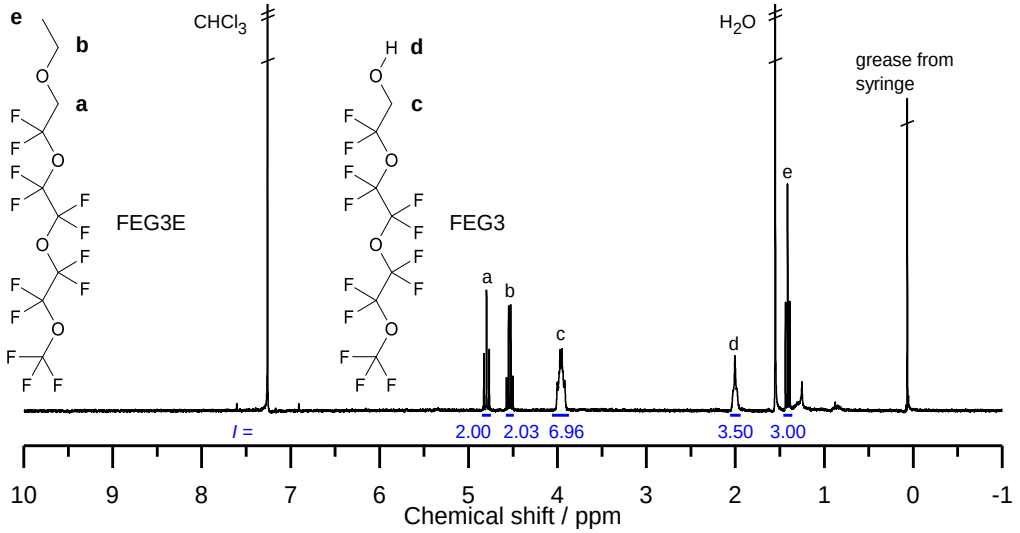

Fig. 107 ^{1}H NMR spectrum of the $CDCl_3$ extract from a PFEG3ES-RAFT-UP/LiFEG3 mixture (O/Li = 10) stirred for 16 h at room temperature. FEG3E could be identified as a product of the reaction of LiFEG3 with the xanthate end-group of PFEG3-RAFT-UP (Scheme 13).

4.6 Electrochemical characterization

The electrochemical characterization was performed with a BioLogic VMP3 potentiostat. The temperature was controlled by a Vötsch VT 4002 oven.

4.6.1 Ionic conductivity

4.6.1.1 PEG or PPOS-*g*-PEG/LiTFSI SPEs

For ionic conductivity measurements the prepared PEG or PPOS-*g*-PEG/LiTFSI SPE melts were pressed and hermetically sealed in the inner circle (area a = 28.3 mm^2 for L750, G750 and G2000; a = 12.6 mm^2 for L2000) of a Kapton® ring spacer (500 µm-thick for L750, G750 and G2000; 130 µm-thick for L2000) between two 500 µm-thick blocking stainless steel electrodes in a CR2032 coin cell set-up. Before all measurements the cells were annealed at 60 °C for 3 h and before each measurement at the respective temperature for 1.5 h. This guarantees an equilibration of the open circuit voltage and a good contact between the electrolyte and the electrodes. Measurements were done from 80 to 30 °C in increments of 10 °C and at 25 °C. The temperature between the thermal annealing steps was changed within 15 min. PEIS in a frequency range from 1 MHz to 1 Hz was performed at each temperature. The voltage amplitude of the sinusoidal signal was 20 mV. According to the literature and chapter 1.3, the bulk resistance R_b is equal to the minimum of the low frequency side of the first semi-circle in the Nyquist plot exemplarily shown for L750-16 and G750-16 (Fig. 108).[164,186] The electrical resistance and inductance of the apparatus were neglected.

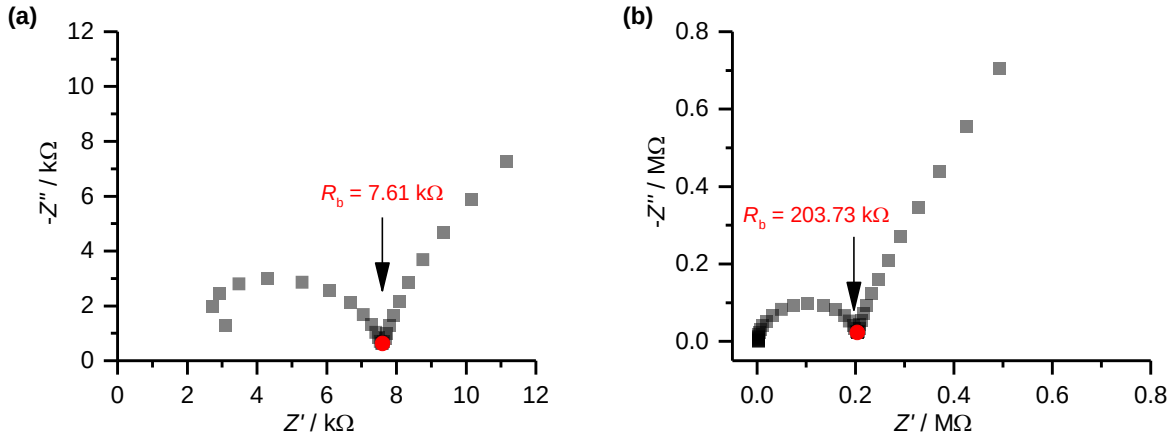

Fig. 108 Nyquist-plots using (a) L750-16 and (b) G750-16 as examples and measured by PEIS in a frequency f range from 1 MHz to 1 Hz at 25 °C (enlargements: (a) 0.52 MHz > f > 100 Hz; (b) 1 MHz > f > 1.9 Hz). The bulk resistance R_b was taken as the minimum of the low frequency side of the first semi-circle to calculate the ionic conductivity σ.

The area of the inner circle of the spacer defined the active cell area a. The electrolyte thickness t was determined by a micrometer table as the difference of the disassembled cell after the measurement and the empty cell assembly without the electrolyte and without the Kapton® ring spacer. The ionic conductivity σ at a given temperature T was calculated using equation (9) under consideration of the cell deminsions:

$$\sigma = \frac{t}{R_b\, a} \tag{26}$$

The mean value of at least three independently measured coin cells was used. The ionic conductivity data were evaluated by the Vogel-Tammann-Fulcher (VTF) relation, which can be expressed by the following expression:

$$\sigma = A_{VTF}\, T^{-1/2} \exp\left(\frac{-B}{T - T_0}\right) \tag{27}$$

where A_{VTF} is a material-dependent pre-exponential factor, B is a material-dependent constant, and T_0 is the thermodynamic Kauzmann temperature.[165,187] T_0 and its error ΔT_0 were determined by fitting σ in dependence on T with the exponential VTF equation form (equation (27), Table 22).

Table 22 Comparison of T_0, T_g, (T_g - 30 K) and (T_g - 50 K).

SPE-O/Li	$T_0 \pm \Delta T_0$[a] (K)	T_g[b] (K)	T_g - 30 K (K)	T_g - 50 K (K)
L750-16	186.57 ± 5.18	214.14	184.14	164.14
L2000-12	201.04 ± 3.47	223.94	193.94	173.94
G2000-16	192.40 ± 2.18	228.56	198.56	178.56
G750-16	190.62 ± 1.69	235.49	205.49	185.49

[a]Determined by fitting σ in dependence on T with the exponential VTF equation form (equation (27)). [b]Obtained from the second heating DSC trace (under nitrogen, 10 K min^{-1}).

The translational movement of the whole polymer with the coordinated salt might occur to a considerable extent at higher temperatures and is not considered by the VTF relation. Therefore, the temperature range for fitting was limited up to 70 °C for the SPEs L750-16, L2000-12 and G750-16. For G2000-16, the whole temperature range was fitted since PPOS-*g*-PEG2000 is much bulkier than PPOS-*g*-PEG750 or the linear PEGs.

To determine B and A_{VTF}, the VTF relation was fitted in a linear equation form with the slope m and the intercept b in which log ($\sigma T^{1/2}$) was plotted against 1000 $(T - T_0)^{-1}$:

$$\log\left(\sigma T^{1/2}\right) = \underbrace{\frac{-B}{1000 \ln 10}}_{m} \frac{1000}{T - T_0} + \underbrace{\log A_{VTF}}_{b} \tag{28}$$

The error bars for log σ and for log ($\sigma\, T^{1/2}$) were calculated from the standard deviation $\Delta\sigma$ of at least three independently measured coin cells according to the error propagation law:

$$\Delta \log\, \sigma = \sqrt{\left(\frac{\delta \log\, \sigma}{\delta \sigma}\right)^2 (\Delta\, \sigma)^2} = \frac{1}{\sigma \ln\, 10} \Delta\, \sigma \tag{29}$$

$$\Delta \log\left(\sigma T^{1/2}\right) = \sqrt{\left(\frac{\delta \log\left(\sigma T^{1/2}\right)}{\delta \sigma}\right)^2 (\Delta\, \sigma)^2} = \frac{1}{\sigma \ln\, 10} \Delta\, \sigma \tag{30}$$

B and A_{VTF} were obtained from the linear equation form (28) as:

$$B = -1000\, m \ln 10 \tag{31}$$

$$A_{VTF} = 10^b \tag{32}$$

Their errors were gained from the standard error of the slope Δm and of the intercept Δb according to the error propagation law as:

$$\Delta B = \sqrt{\left(\frac{\delta B}{\delta m}\right)^2 (\Delta\, m)^2} = 1000\ \Delta m \ln 10 \tag{33}$$

$$\Delta A_{\mathrm{VTF}} = \sqrt{\left(\frac{\delta A}{\delta b}\right)^2 (\Delta b)^2} = 10^{\mathrm{b}}\ \Delta b \ln\ 10 \tag{34}$$

4.6.1.2 PFEG3ES-FRP-UP/LiFEG3 SPEs or LiFEG3

For ionic conductivity measurements about 40 mg of the PFEG3ES-FRP-UP/LiFEG3 SPEs or of pure LiFEG3 were pressed in the inner circle of a 75 µm-thick Kapton® ring spacer between two 500 µm-thick blocking stainless steel electrodes in a CR2032 coin cell setup at room temperature. The inner circle of the spacer was taken to be the active cell area *a* (12.6 mm^2). Before all measurements the cells were annealed at 40 °C for 5 h and before each measurement at the respective temperature for 1.5 h to guarantee a good contact between the electrolyte and the electrodes as well as an equilibration of the open circuit voltage. After the cells were cooled to 25 °C at which temperature the first measurement was performed, further measurements were done from 30 to 80 °C in increments of 10 °C. PEIS in a frequency range from 1 MHz to 1 Hz was performed. Similar to the literature and as explained in chapter 1.3, the bulk resistance R_b of the electrolyte was determined by fitting the first semi-circle in the high frequency regime of the Nyquist plot with the EEC R_b/CPE_b (exemplarily shown for SPE-10 in Fig. 109).[126]

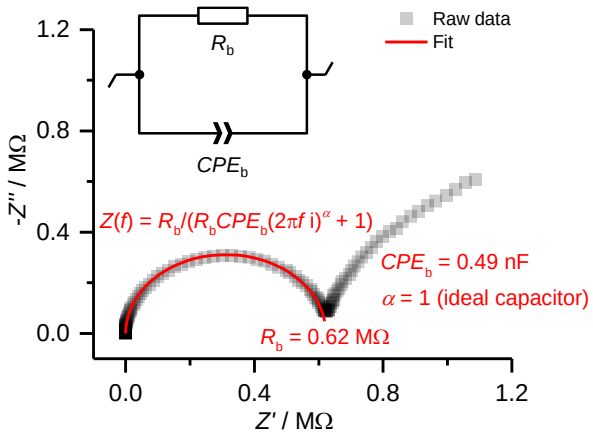

Fig. 109 Nyquist-plot using SPE-10 as an example and measured by PEIS in a frequency *f* range from 1 MHz to 1 Hz at 60 °C. The first semi-circle in the high frequency regime was fitted by the shown EEC, including R_b and CPE_b of the electrolyte to calculate the ionic conductivity σ.

The electrical resistance and inductance of the apparatus were neglected since R_b was much higher. To investigate a potential influence of the applied voltage amplitude of the sinusoidal signal on the ionic conductivity, the latter was measured at different amplitudes (10, 50, 100 and 500 mV) exemplarily for SPE-10 at 40, 60 and 80 °C. Within its error, the ionic conductivity showed the same value for all voltage amplitudes (Fig. 110).

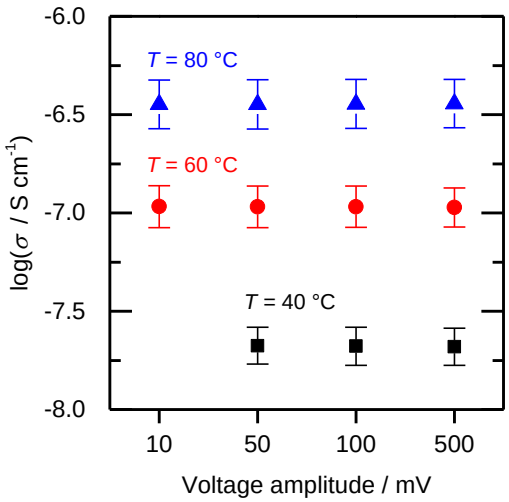

Fig. 110 The ionic conductivity σ for SPE-10 in dependence on the applied voltage amplitude of the sinusoidal signal during the PEIS measurement at different temperatures. No accurate measurement could be performed for a voltage amplitude of 10 mV at a temperature of 40 °C. The measured current was too low. The error bar for log σ was calculated according to the error propagation law (equation (37)).

In the case of small ionic conductivities (high R_b, for example at 40 °C) only a relatively high voltage amplitude guaranteed a low signal-to-noise ratio. Therefore, a voltage amplitude of 500 mV was used for the ionic conductivity measurements of all SPEs. The ionic conductivity σ at a given temperature T was calculated analogue above according to equation (26).

The ionic conductivity data were evaluated by the Arrhenius law, which is given by the following expression:

$$\sigma = A \exp\left(\frac{-E_a}{RT}\right) \tag{35}$$

where A is the pre-exponential factor, E_a is the activation energy for the ion movement and R is the molar gas constant (8.314472 J mol^{-1} K^{-1}).[29,181] The Arrhenius relationship was expressed in a linear equation form with the slope m and the intercept b in which log σ was plotted against 1000 T^{-1}:

$$\log \sigma = \underbrace{\frac{-E_a}{1000\, R \ln 10}}_{m} \frac{1000}{T} + \underbrace{\log A}_{b} \tag{36}$$

The error bar for log σ (Fig. 59, Fig. 60 and Fig. 110) was calculated from the standard deviation $\Delta\sigma$ of at least three independently measured coin cells according to the error propagation law:

$$\Delta \log\, \sigma = \sqrt{\left(\frac{\delta \log\, \sigma}{\delta \sigma}\right)^2 (\Delta\, \sigma)^2} = \frac{1}{\sigma \ln\, 10} \Delta\, \sigma \tag{37}$$

E_a and A were obtained from the linear equation form (36) as:

$$E_a = -1000\, R\, m \ln 10 \tag{38}$$

$$A = 10^b \tag{39}$$

Their errors, ΔE_a and ΔA, (Fig. 60c and Table 23) were gained from the standard error of the slope Δm and of the intercept Δb according to the error propagation law as:

$$\Delta E_a = \sqrt{\left(\frac{\delta E_a}{\delta m}\right)^2 (\Delta m)^2} = 1000\, R\, \Delta m \ln 10 \quad (40)$$

$$\Delta A = \sqrt{\left(\frac{\delta A}{\delta b}\right)^2 (\Delta b)^2} = 10^b \Delta b \ln 10 \quad (41)$$

Table 23 Linear fitting data of the Arrhenius plot shown in Fig. 59. The activation energy for the ion movement E_a and the pre-exponential factor A were calculated according to equations (38) to (41).

Electrolyte	Adjusted R^2	$m \pm \Delta m$ (K)	$b \pm \Delta b$ (log of S cm^{-1})	$E_a \pm \Delta E_a$ (kJ mol^{-1})	$A \pm \Delta A$ (S cm^{-1})
SPE-69	0.9817	-4.40 ± 0.42	3.62 ± 1.22	84 ± 8	(4.19 ± 11.75) x 10^3
SPE-15	0.9915	-4.39 ± 0.20	5.36 ± 0.60	84 ± 4	(2.29 ± 3.18) x 10^5
SPE-10	0.9969	-3.13 ± 0.07	2.64 ± 0.22	60 ± 1	(4.36 ± 2.19) x 10^2
SPE-5	0.9980	-2.21 ± 0.04	0.37 ± 0.13	42 ± 1	2.34 ± 0.69
LiFEG3	0.9759	-1.06 ± 0.10	-4.62 ± 0.28	20 ± 2	(2.39 ± 1.53) x 10^{-5}

The error bar for log A (Fig. 60d) was calculated from the error ΔA according to the error propagation law:

$$\Delta \log A = \sqrt{\left(\frac{\delta \log A}{\delta A}\right)^2 (\Delta A)^2} = \frac{1}{A \ln 10} \Delta A \quad (42)$$

4.6.2 Cyclic voltammetry

The electrochemical stability window of the electrolytes was determined by cyclic voltammetry (CV). The electrolyte was pressed and hermetically sealed in the inner circle (area a = 12.6 mm^2 for PEG or PPOS-*g*-PEG/LiTFSI SPE melts; a = 7.1 mm^2 for PFEG3ES-FRP-UP, LiFEG3 or SPE-10) of a Kapton® ring spacer (thickness: 130 µm for PEG or PPOS-*g*-PEG/LiTFSI SPE melts; 75 µm for PFEG3ES-FRP-UP, LiFEG3 or SPE-10) between one 250 µm-thick copper working and a 380 µm-thick lithium reference/counter electrode at room temperature. A CR2032 coin cell set-up was used. Before the measurements, the cells were annealed in order to obtain a good contact between the electrolyte and the electrodes (PEG or PPOS-*g*-PEG/LiTFSI SPEs: at 70 °C for 12 h; PFEG3ES-FRP-UP: at 80 °C for 5 h; LiFEG3 or SPE-10: at 60 °C for 5 h). The open circuit voltage after annealing was around 2.6 V vs. Li/Li$^+$ for all SPEs. For the PEG or PPOS-*g*-PEG/LiTFSI SPEs, a potential range between -0.2 V and 3.7 V vs. Li/Li$^+$ was scanned twice at a scan rate of 1 mV s^{-1} at 70 °C. The scan rate was 2 mV s^{-1} for L750-16. For PFEG3ES-FRP-UP and LiFEG3, a potential range between -0.2 V

and 10 V vs. Li/Li$^+$ was scanned at a scan rate of 1 mV s^{-1}. SPE-10 was scanned between -0.2 V and 5 V vs. Li/Li$^+$ at a scan rate of 0.2 mV s^{-1} and 1 mV s^{-1}, respectively. The measurement temperature was 80 °C for PFEG3ES-FRP-UP and 60 °C for LiFEG3 or SPE-10. The scans started in direction of -0.2 V vs. Li/Li$^+$. The current density J was calculated by dividing the measured current by a.

4.6.3 Lithium ion transference number

The lithium ion transference number t^+ was determined by the Bruce-Vincent method (t^+_{BV}) and according to Watanabe *et al.* (t^+_W) at 70 °C as described in chapter 1.3. t^+_{BV} and t^+_W were calculated by equations (11) and (12), respectively. All resistance values were got from the respective minima in the Nyquist plots as exemplarily shown in Fig. 38a (Table 6). EECs for mathematical fitting were not used. The prepared SPE melt was pressed and hermetically sealed in the inner circle (a = 12.6 mm^2) of a 130 µm-thick Kapton® ring spacer between two 380 µm-thick non-blocking lithium electrodes in a CR2032 coin cell set-up at room temperature. A 500 µm-thick stainless steel spacer was placed on top of one lithium electrode to ensure an equal distribution of the coin cell spring pressure. Before the measurement, the cells were short-circuited and annealed at 70 °C for 12 h. A PEIS measurement in a frequency range from maximal 0.2 MHz to 1 Hz with a voltage amplitude of 20 mV and a subsequent CA measurement were performed. For the CA measurement, the cells were subjected to a DC voltage ΔV (10 mV for L750-16 and L2000-12; 50 mV for G750-16 and G2000-16 due to the higher bulk resistance of the electrolytes) until I_s was reached. One hour was sufficient to ensure an I_s in each case. Then, a second PEIS measurement was performed with the same settings as the first PEIS measurement.

5 Summary and Outlook

In summary, the first chapter of this thesis exposed how the thermal, morphological and electrochemical properties of linear and graft copolymer PEG SPEs differ depending on the graft copolymer side-chain length. The graft copolymer poly(4-(propargyloxy)styrene)-*grafted*-poly(ethylene glycol) (PPOS-*g*-PEG) contains a poly(4-(propargyloxy)styrene) (PPOS) backbone. This provides a poly(styrene) (PS) derivative for mechanical strength and 1,4-disubstituted 1,2,3-triazole (TR)-linking groups for grafting PEG side-chains. T_g, T_m, T_c and ΔH_m were significantly lower for the pure PPOS-*g*-PEG with the shorter side-chain length (PPOS-*g*-PEG750 in contrast to PPOS-*g*-PEG2000). The same relation was obtained for the graft copolymers compared to their linear counterparts (PPOS-*g*-PEG compared to PEG-OH). Due to the plasticizing effect of LiTFSI, all PPOS-*g*-PEG750 SPEs (G750 SPEs) and the PPOS-*g*-PEG2000 SPE with the highest LiTFSI concentration (G2000-12) were amorphous. At a given O/Li ratio, T_m and ΔH_m were lower for the graft copolymer SPEs compared to their linear counterparts. However, above T_m in the amorphous melt state, T_g was the decisive parameter which influenced the ion mobility. A shorter PEG side-chain (G750-16 compared to G2000-16) increased T_g and the derived pseudo-activation energy parameter B for ion movement. As also expected from the higher T_g values, B was significantly higher for the graft copolymer SPEs compared to their linear counterparts. The temperature dependency of σ in the amorphous melt state followed Vogel-Tammann-Fulcher behavior, with a maximum value for σ of 1.4×10^{-4} S cm^{-1} for G750-16 and 4.0×10^{-4} S cm^{-1} for G2000-16 at 60 °C. A positive contribution to the ionic conductivity was achieved by a higher charge carrier concentration for the graft copolymer SPEs compared to their linear counterparts and for a shorter PEG side-chain. A higher amount of TR groups supports the LiTFSI dissociation. All SPEs showed for PEG/LiTFSI electrolytes typical lithium ion transference numbers with values below 0.2 at 70 °C.

The results suggest that graft copolymer SPEs should be synthesized with a well-defined structure using controlled or living polymerization techniques. The side-chain length in graft copolymer SPEs is decisive for the electrochemical properties. Especially below T_m, graft copolymer electrolytes can lead to higher ionic conductivities than their linear counterparts due to their lower crystallinity. The functional TR-linking group enables a defined polymer structure and can improve the ionic conductivity. Their good thermal and electrochemical stability plus their ability for lithium plating/stripping at an electrode make the new graft copolymer SPEs to suitable materials for lithium-ion batteries (LIB).

The second chapter of this study revealed how the fluorination of oligo ethylene glycol ethenesulfonate (EGES) monomers influences their polymerization behavior. When polymerized by conventional free radical polymerization EGES monomers formed only oligomers, while the fluorinated EGES (FEGES) monomers showed high conversions and high molecular weights. Deduced from end-group analysis by MALDI-ToF MS, chain transfer reactions from methylene ether and methoxy groups are the main reason for this observation. The results imply that chain transfer reactions seem to be a big issue for the polymerization of non-fluorinated ethenesulfonate (ES) monomers in general. However, fluorinated monomers do not suffer from this problem to a larger extent. MADLI-ToF MS was used to determine the molecular weight and end-group structure of poly(ethenesulfonate)s. High end-group fidelity was achieved when FEG3ES was polymerized by RAFT allowing for the synthesis of more complex polymer architectures such as block copolymers in future studies. For the first time, the synthesis of PFEG2ES and PFEG3ES as new graft copolymers comprising a PES backbone and oligomeric per-fluoropolyether (PFPE) side-chains was presented. Their adequate thermal stability and especially the fully amorphous character of PFEG3ES-RAFT make them suitable materials for potential applications as solid state and nonflammable electrolytes in LIBs.

The third chapter of this thesis showed how the incorporation of fluorophilic tails into lithium salts can increase the solubility and thus the ionic conductivity in PEG-free PFPE SPEs. The new fluorosurfactant lithium salt LiFEG3 was synthesized. It contains a PFPE tail to increase the solubility in the SPE host polymer PFEG3ES. Despite its slightly fluorophilic character LiTFSI was insoluble in PFEG3ES. In contrast, LiFEG3 SPEs with different O/Li ratios could be prepared from solution with hexafluorobenzene. The SPEs were thermally stable up to 80 °C, where LiFEG3 began to melt and evaporate. PFEG3ES, LiFEG3 and their SPEs are semi-crystalline. The segmental motion of the FEG3 chains in PFEG3ES and LiFEG3 starts below -70 °C. PFEG3ES showed one glass transition temperature at 34 °C and two melting temperatures at -44 °C and 87 °C. LiFEG3 consists of an amorphous and a crystalline phase at room temperature explaining the white turbid appearance of the viscous liquid.

The glass transition temperature of the SPEs decreased with increasing salt concentration. Simultaneously, the ionic conductivity of the SPEs increased. It was maximal for SPE-5 reaching a value of $(1.22 \pm 0.24) \times 10^{-6}$ S cm^{-1} at 80 °C. The FEG3 anion had a plasticizing effect on PFEG3ES which reduced T_g. The activation energy for ion movement E_a decreased with a lower T_g. In contrast to the PEG SPEs presented in the first chapter, the ion transport was mainly dominated by thermal hopping processes (Arrhenius behavior).

The addition of LiFEG3 to PFEG3ES and *vice versa* resulted in a significant decrease of the total melting enthalpy $\Delta H_{m,\,total}$ and in an increase of σ. The ion concentration A contributing to σ increased with a decreasing $\Delta H_{m,\,total}$. The maximum A was observed for SPE-15. However, the maximum of σ was shifted to SPE-5 since it showed the lowest E_a of all SPEs. In future studies T_g should be decreased independently from A by the addition of plasticizing additives different from LiFEG3. Anions with a higher delocalization of the charge than alkoxides might also further increase σ. Cyclic voltammetry revealed the absence of lithium plating/stripping on a copper electrode. The use of electrode materials different from copper or new additives might enable the process by lowering the electrode/electrolyte interface resistance. The SPEs are electrochemically stable up to at least 5 V vs. Li/Li^+ at 60 °C. Resulting from the presented findings the incorporation of PFPE moieties into lithium salts in electrolytes for LIBs can achieve a higher solubility in highly fluorophilic host polymers.

Comparing PEG and PEG-free PFPE SPEs investigated in this thesis, PEG SPEs might provide a higher ionic conductivity in LIBs, but PFPE SPEs stand out by their excellent electrochemical stability. This makes them of great interest for the use in lithium polymer batteries in combination with high-potential cathode materials while ensuring high safety.

6 Zusammenfassung und Ausblick

Im ersten Kapitel dieser Arbeit wurde gezeigt, wie sich die thermischen, morphologischen und elektrochemischen Eigenschaften von linearen und Pfropfcopolymer-PEG-SPEs in Abhängigkeit von der Seitenkettenlänge des Pfropfcopolymers unterscheiden. Das Pfropfcopolymer Poly(4-(propargyloxy)styrol)-*gepfropftes*-Poly(ethylenglykol) (PPOS-*g*-PEG) enthält ein Poly(4-(propargyloxy)styrol)-Rückgrat (PPOS). Dieses stellt ein Poly(styrol) (PS)-Derivat für die mechanische Festigkeit und 1,4-disubstituierte 1,2,3-Triazol (TR)-Verknüpfungsgruppen zum Pfropfen von PEG-Seitenketten bereit. T_g, T_m, T_c und ΔH_m waren für das reine PPOS-*g*-PEG mit der kürzeren Seitenkettenlänge deutlich niedriger (PPOS-*g*-PEG750 im Gegensatz zu PPOS-*g*-PEG2000). Dieselbe Relation wurde für die Pfropfcopolymere im Vergleich zu ihren linearen Gegenstücken festgestellt (PPOS-*g*-PEG verglichen mit PEG-OH). Aufgrund des Weichmachereffekts von LiTFSI waren alle PPOS-*g*-PEG750 SPEs (G750 SPEs) und das PPOS-*g*-PEG2000 SPE mit der höchsten LiTFSI-Konzentration (G2000-12) amorph. Bei einem gegebenen O/Li-Verhältnis waren T_m und ΔH_m für die Pfropfcopolymer-SPEs verglichen mit ihren linearen Gegenstücken niedriger. Oberhalb von T_m im amorphen Schmelzzustand war jedoch T_g der entscheidende Parameter, der die Ionenmobilität beeinflusste. Eine kürzere PEG-Seitenkette (G750-16 verglichen mit G2000-16) erhöhte T_g und den abgeleiteten Pseudo-Aktivierungsenergieparameter *B* für die Ionenbewegung. Wie aufgrund der höheren T_g-Werte zu erwarten, war *B* bei den Pfropfcopolymer-SPEs im Vergleich zu ihren linearen Gegenstücken deutlich höher. Die Temperaturabhängigkeit von σ im amorphen Schmelzzustand folgt dem Verhalten gemäß Vogel-Tammann-Fulcher, mit einem maximalen Wert für σ von $1{,}4 \times 10^{-4}$ S cm^{-1} für G750-16 und $4{,}0 \times 10^{-4}$ S cm^{-1} für G2000-16 bei 60 °C. Ein positiver Einfluss auf die Ionenleitfähigkeit wurde durch eine höhere Ladungsträgerkonzentration für die Pfropfcopolymer-SPEs im Vergleich zu ihren linearen Gegenstücken und für eine kürzere PEG-Seitenkette erreicht. Ein höherer Anteil an TR-Gruppen unterstützt die Dissoziation von LiTFSI. Alle SPEs zeigten für PEG/LiTFSI-Elektrolyte typische Lithiumionenübertragungszahlen mit Werten unter 0,2 bei 70 °C.

Die Ergebnisse legen nahe, dass Pfropfcopolymer-SPEs mit einer wohl definierten Struktur durch kontrollierte oder lebende Polymerisationstechniken synthetisiert werden sollten. Die Seitenkettenlänge in Pfropfcopolymer-SPEs ist für die elektrochemischen Eigenschaften entscheidend. Insbesondere unterhalb von T_m können Pfropfcopolymerelektrolyte aufgrund ihrer geringeren Kristallinität zu höheren Ionenleitfähigkeiten führen als ihre linearen Gegenstücke. Die funktionelle TR-Verknüpfungsgruppe ermöglicht eine definierte Polymerstruktur und kann die Ionenleitfähigkeit

verbessern. Ihre gute thermische und elektrochemische Stabilität, sowie ihre Fähigkeit Lithium an einer Elektrode abzuscheiden und wieder abzulösen, machen die neuen Pfropfcopolymer-SPEs zu geeigneten Materialien für Lithium-Ionen-Batterien.

Das zweite Kapitel dieser Arbeit offenbarte, wie die Fluorierung von Oligoethylenglykol-Ethensulfonat (EGES)-Monomeren deren Polymerisationsverhalten beeinflusst. Bei der konventionellen radikalischen Polymerisation bildeten die EGES-Monomere nur Oligomere, während die fluorierten EGES (FEGES)-Monomere hohe Umsätze und hohe Molekulargewichte aufwiesen. Aus einer Endgruppenanalyse mittels MALDI-ToF MS wurde abgeleitet, dass Kettenübertragungsreaktionen von Methylenether- und Methoxygruppen der Hauptgrund für diese Beobachtung sind. Die Ergebnisse implizieren, dass Kettenübertragungsreaktionen bei der Polymerisation von nicht-fluorierten Ethensulfonat (ES)-Monomeren im Allgemeinen ein großes Problem darstellen. Fluorierte Monomere leiden hingegen nicht in hohem Ausmaß unter diesem Problem. MADLI-ToF MS wurde verwendet, um das Molekulargewicht und die Endgruppenstruktur von Poly(ethensulfonat)en zu bestimmen. Bei der RAFT-Polymerisation von FEG3ES wurde eine hohe Endgruppenqualität erreicht, was in zukünftigen Studien die Synthese komplexerer Polymerarchitekturen wie zum Beispiel Blockcopolymere ermöglicht. Zum ersten Mal wurde die Synthese von PFEG2ES und PFEG3ES als neue Pfropfcopolymere vorgestellt, die ein PES-Rückgrat und oligomere Perfluorpolyether (PFPE)-Seitenketten enthalten. Aufgrund ihrer ausreichenden thermischen Stabilität und insbesondere aufgrund des vollständig amorphen Charakters von PFEG3ES-RAFT eignen sich diese Materialien für potenzielle Anwendungen als feste und nicht brennbare Elektrolyte in Lithium-Ionen-Batterien.

Das dritte Kapitel dieser Arbeit zeigte auf, wie der Einbau von fluorophilen Schwänzen in Lithiumsalze die Löslichkeit und damit die ionische Leitfähigkeit in PEG-freien PFPE-SPEs erhöhen kann. Das neue Fluortensid-Lithiumsalz LiFEG3 wurde synthetisiert. Es enthält einen PFPE-Schwanz, um die Löslichkeit in dem SPE-Hostpolymer PFEG3ES zu erhöhen. Trotz seines leicht fluorophilen Charakters war LiTFSI in PFEG3ES unlöslich. Im Gegensatz dazu konnten LiFEG3-SPEs mit unterschiedlichen O/Li-Verhältnissen aus Lösung mit Hexafluorbenzol hergestellt werden. Die SPEs waren bis zu 80 °C thermisch stabil, danach begann LiFEG3 zu schmelzen und zu verdampfen. PFEG3ES, LiFEG3 und ihre SPEs sind teilkristallin. Die Segmentbewegung der FEG3-Ketten in PFEG3ES und LiFEG3 beginnt unterhalb von -70 °C. PFEG3ES zeigte eine Glasübergangstemperatur bei 34 °C und zwei Schmelztemperaturen bei -44 °C und 87 °C. LiFEG3 besteht bei Raumtemperatur aus einer amorphen und einer kristallinen Phase, was die weiß-trübe Erscheinung der viskosen Flüssigkeit erklärt.

Die Glasübergangstemperatur der SPEs nahm mit steigender Salzkonzentration ab. Gleichzeitig stieg die Ionenleitfähigkeit der SPEs an. Sie war bei SPE-5 am höchsten und erreichte einen Wert von $(1{,}22 \pm 0{,}24) \times 10^{-6}$ S cm^{-1} bei 80 °C. Das FEG3-Anion hatte eine weichmachende Wirkung auf PFEG3ES, wodurch sich T_g verringerte. Die Aktivierungsenergie für die Ionenbewegung E_a nahm mit niedrigerem T_g. ab. Im Gegensatz zu den PEG-SPEs, welche in dem ersten Kapitel vorgestellt wurden, wurde der Ionentransport hauptsächlich durch thermische Sprungprozesse (Arrhenius-Verhalten) dominiert.

Die Zugabe von LiFEG3 zu PFEG3ES und umgekehrt führte zu einer deutlichen Verringerung der Gesamtschmelzenthalpie $\Delta H_{m,\,total}$ und zu einem Anstieg von σ. Die Ionenkonzentration A, die zu σ beiträgt, stieg mit abnehmendem $\Delta H_{m,\,total}$ an. Die höchste A wurde für SPE-15 beobachtet. Das Maximum von σ wurde jedoch zu SPE-5 verlagert, da es von allen SPEs die niedrigste E_a aufwies. In zukünftigen Untersuchungen sollte T_g unabhängig von A durch die Zugabe von anderen Weichmacheradditiven als LiFEG3 gesenkt werden. Anionen mit einer stärkeren Delokalisierung der Ladung als Alkoxide könnten σ ebenfalls weiter erhöhen. Cyclovoltammetrie zeigte, dass keine Lithiumabscheidung/-ablösung an einer Kupferelektrode möglich ist. Die Verwendung von Elektrodenmaterialien abweichend von Kupfer, oder von neuen Additiven könnte den Prozess durch eine Verringerung des Grenzflächenwiderstands zwischen der Elektrode und dem Elektrolyten ermöglichen. Die SPEs sind elektrochemisch bis zu mindestens 5 V vs. Li/Li$^+$ bei 60 °C stabil. Aus den vorgestellten Ergebnissen geht hervor, dass der Einbau von PFPE-Anteilen in Lithiumsalze in Elektrolyten für Lithium-Ionen-Batterien eine höhere Löslichkeit in stark fluorophilen Hostpolymeren erreichen kann.

Vergleicht man die in dieser Arbeit untersuchten PEG- und PEG-freien PFPE-SPEs, so könnten die PEG-SPEs vielleicht eine höhere Ionenleitfähigkeit in Lithium-Ionen-Batterien aufweisen, aber die PFPE-SPEs zeichnen sich durch ihre hervorragende elektrochemische Stabilität aus. Dies macht sie für den Einsatz in Lithium-Polymer-Batterien in Kombination mit Hochpotential-Kathodenmaterialien bei gleichzeitiger Gewährleistung einer hohen Sicherheit besonders interessant.

References

[1] B. Scrosati, J. Hassoun, Y.-K. Sun, *Energy Environ. Sci.* **2011**, *4*, 3287.

[2] B. Scrosati, J. Garche, *J. Power Sources* **2010**, *195*, 2419.

[3] M. Li, J. Lu, Z. Chen, K. Amine, *Adv. Mater. (Weinheim, Ger.)* **2018**, *30*, 1800561.

[4] T. Chen, Y. Jin, H. Lv, A. Yang, M. Liu, B. Chen, Y. Xie, Q. Chen, *Trans. Tianjin Univ.* **2020**, *26*, 208.

[5] X. He, Z. Hu, F. Restuccia, J. Fang, G. Rein, *Appl. Therm. Eng.* **2022**, *212*, 118621.

[6] L. Bravo Diaz, X. He, Z. Hu, F. Restuccia, M. Marinescu, J. V. Barreras, Y. Patel, G. Offer, G. Rein, *J. Electrochem. Soc.* **2020**, *167*, 90559.

[7] Mayser GmbH & Co. KG **2023**: *INDUCON® Komprischaum: Komprimierte PUR-Spezialschaumstoffe für technische Anwendungen. Compression Pad für Batteriezellen*, [https://www.mayser.com/de/schaumstofftechnik-und-formteile/inducon-komprischaum-1], accessed on 12.09.2023.

[8] Compagnie de Saint Gobain SA **2023**: *Compression Pads for EV Batteries*, [https://www.tapesolutions.saint-gobain.com/na/markets/automotive/ev/compression-pads#], accessed on 12.09.2023.

[9] A. Hammami, N. Raymond, M. Armand, *Nature (London, U. K.)* **2003**, *424*, 635.

[10] D. H. C. Wong, J. L. Thelen, Y. Fu, D. Devaux, A. A. Pandya, V. S. Battaglia, N. P. Balsara, J. M. DeSimone, *Proc. Natl. Acad. Sci. U. S. A.* **2014**, *111*, 3327.

[11] E-Lyte Innovations GmbH **2023**. *Electrolytes for innovative battery systems in E-Lyte quality*, [https://e-lyte-innovations.de/products/electrolytes-for-batteries/], accessed on 17.04.2023.

[12] G. Li, *Adv. Energy Mater.* **2021**, *11*, 2002891.

[13] P. Zhu, D. Gastol, J. Marshall, R. Sommerville, V. Goodship, E. Kendrick, *J. Power Sources* **2021**, *485*, 229321.

[14] W. A. v. Schalkwijk, *Advances in lithium-ion batteries*, Kluwer Acad./Plenum Publ., New York, **2002**.

[15] M. Park, X. Zhang, M. Chung, G. B. Less, A. M. Sastry, *J. Power Sources* **2010**, *195*, 7904.

[16] Z. Xue, D. He, X. Xie, *J. Mater. Chem. A* **2015**, *3*, 19218.

[17] J. W. Fergus, *J. Power Sources* **2010**, *195*, 939.

[18] A. Eftekhari, *ACS Sustainable Chem. Eng.* **2019**, *7*, 3684.

[19] C. M. Hayner, X. Zhao, H. H. Kung, *Annu. Rev. Chem. Biomol. Eng.* **2012**, *3*, 445.

[20] H. Xia, Z. Luo, J. Xie, *Prog. Nat. Sci.* **2012**, *22*, 572.

[21] M. S. Whittingham, *Chem. Rev. (Washington, DC, U. S.)* **2004**, *104*, 4271.

[22] C. Tian, F. Lin, M. M. Doeff, *Acc. Chem. Res.* **2018**, *51*, 89.

[23] A. Zülke, Y. Li, P. Keil, R. Burrell, S. Belaisch, M. Nagarathinam, M. P. Mercer, H. E. Hoster, *Batteries Supercaps* **2021**, *4*, 934.

[24] A. Purwanto, C. S. Yudha, U. Ubaidillah, H. Widiyandari, T. Ogi, H. Haerudin, *Mater. Res. Express* **2018**, *5*, 122001.

[25] K.-J. Park, J.-Y. Hwang, H.-H. Ryu, F. Maglia, S.-J. Kim, P. Lamp, C. S. Yoon, Y.-K. Sun, *ACS Energy Lett.* **2019**, *4*, 1394.

[26] X. Ji, K. T. Lee, L. F. Nazar, *Nat. Mater.* **2009**, *8*, 500.

[27] T. Liu, J. P. Vivek, E. W. Zhao, J. Lei, N. Garcia-Araez, C. P. Grey, *Chem. Rev. (Washington, DC, U. S.)* **2020**, *120*, 6558.

[28] P. Chen, F. Bai, J. W. Deng, B. Liu, T. Zhang, *Front. Chem. (Lausanne, Switz.)* **2022**, *10*, 1035691.

[29] D. W. Bruce, D. O'Hare, R. I. Walton (Eds.) *Energy Materials*. *Polymer Electrolytes*, John Wiley & Sons, Chichester, **2011**.

[30] H. Stöcker, *Taschenbuch der Physik*. *Formeln, Tabellen, Übersichten*, Harri Deutsch, Frankfurt am Main, **2007**.

[31] B. K. Wheatle, J. R. Keith, S. Mogurampelly, N. A. Lynd, V. Ganesan, *ACS Macro Lett.* **2017**, *6*, 1362.

[32] S. Sylla, J.-Y. Sanchez, M. Armand, *Electrochim. Acta* **1992**, *37*, 1699.

[33] L. Li, S. Zhou, H. Han, H. Li, J. Nie, M. Armand, Z. Zhou, X. Huang, *J. Electrochem. Soc.* **2011**, *158*, A74.

[34] Gamry Instruments Inc **2007**: *Basics of Electrochemical Impedance Spectroscopy*. *Application Note*, [https://web.archive.org/web/20090201184606/http://gamry.com/App_Notes/EIS_Primer/EIS_Primer.htm#About_The_EIS_Primer], accessed on 13.04.2023.

[35] X. Qian, N. Gu, Z. Cheng, X. Yang, E. Wang, S. Dong, *Electrochim. Acta* **2001**, *46*, 1829.

[36] B.-Y. Chang, *J. Electrochem. Sci. Technol.* **2020**, *11*, 318.

[37] F. Groce, F. Gerace, G. Dautzemberg, S. Passerini, G. B. Appetecchi, B. Scrosati, *Electrochim. Acta* **1994**, *39*, 2187.

[38] G. B. Appetecchi, S. Scaccia, S. Passerini, *J. Electrochem. Soc.* **2000**, *147*, 4448.

[39] T. Zhang, N. Imanishi, S. Hasegawa, A. Hirano, J. Xie, Y. Takeda, O. Yamamoto, N. Sammes, *J. Electrochem. Soc.* **2008**, *155*, A965.

[40] T. Zhang, N. Imanishi, S. Hasegawa, A. Hirano, J. Xie, Y. Takeda, O. Yamamoto, N. Sammes, *Electrochem. Solid-State Lett.* **2009**, *12*, A132.

[41] I. Olsen, R. Koksbang, E. Skou, *Electrochim. Acta* **1995**, *40*, 1701.

[42] D. M. Pesko, K. Timachova, R. Bhattacharya, M. C. Smith, I. Villaluenga, J. Newman, N. P. Balsara, *J. Electrochem. Soc.* **2017**, *164*, E3569.

[43] G. Cameron, J. Harvie, M. Ingram, *Solid State Ionics* **1989**, *34*, 65.

[44] P. G. Bruce, C. A. Vincent, *J. Electroanal. Chem.* **1987**, *225*, 1.

[45] J. Evans, C. A. Vincent, P. G. Bruce, *Polymer* **1987**, *28*, 2324.

[46] M. Watanabe, S. Nagano, K. Sanui, N. Ogata, *Solid State Ionics* **1988**, *28–30, Part 2*, 911.

[47] Y. Kato, M. Watanabe, K. Sanui, N. Ogata, *Solid State Ionics* **1990**, *40-41*, 632.

[48] A. Nishimoto, M. Watanabe, Y. Ikeda, S. Kohjiya, *Electrochim. Acta* **1998**, *43*, 1177.

[49] K. Pożyczka, M. Marzantowicz, J. R. Dygas, F. Krok, *Electrochim. Acta* **2017**, *227*, 127.

[50] K. M. Abraham, *Electrochim. Acta* **1993**, *38*, 1233.

[51] M. C. Smart, *J. Electrochem. Soc.* **1999**, *146*, 486.

[52] M. S. Ding, K. Xu, S. Zhang, T. R. Jow, *J. Electrochem. Soc.* **2001**, *148*, A299.

[53] J. M. Tarascon, D. Guyomard, *Solid State Ionics* **1994**, *69*, 293.

[54] R. J. Brodd, W. Huang, J. R. Akridge, *Macromol. Symp.* **2000**, *159*, 229.

[55] P. Tundo, M. Selva, *Acc. Chem. Res.* **2002**, *35*, 706.

[56] A. W. Golubkov, D. Fuchs, J. Wagner, H. Wiltsche, C. Stangl, G. Fauler, G. Voitic, A. Thaler, V. Hacker, *RSC Adv.* **2014**, *4*, 3633.

[57] X. Du, B. Yang, Y. Lu, X. Guo, G. Zu, J. Huang, *J. Mater. Chem. C* **2021**, *9*, 6760.

[58] C. Monroe, J. Newman, *J. Electrochem. Soc.* **2005**, *152*, A396.

[59] N. S. Schauser, K. J. Harry, D. Y. Parkinson, H. Watanabe, N. P. Balsara, *J. Electrochem. Soc.* **2015**, *162*, A398.

[60] T. Tatsuma, M. Taguchi, N. Oyama, *Electrochim. Acta* **2001**, *46*, 1201.

[61] M. Dollé, L. Sannier, B. Beaudoin, M. Trentin, J.-M. Tarascon, *Electrochem. Solid-State Lett.* **2002**, *5*, A286.

[62] K. Xu, *Chem. Rev. (Washington, DC, U. S.)* **2004**, *104*, 4303.

[63] R. Bouchet, S. Maria, R. Meziane, A. Aboulaich, L. Lienafa, J.-P. Bonnet, T. N. T. Phan, D. Bertin, D. Gigmes, D. Devaux *et al.*, *Nat. Mater.* **2013**, *12*, 452.

[64] I. L. Johansson, D. Brandell, J. Mindemark, *Batteries Supercaps* **2020**, *3*, 527.

[65] L. Liu, J. Lyu, J. Mo, H. Yan, L. Xu, P. Peng, J. Li, B. Jiang, L. Chu, M. Li, *Nano Energy* **2020**, *69*, 104398.

[66] S. A. Mullin, G. M. Stone, A. Panday, N. P. Balsara, *J. Electrochem. Soc.* **2011**, *158*, A619.

[67] Q. Zhang, K. Liu, F. Ding, X. Liu, *Nano Res.* **2017**, *10*, 4139.

[68] D.E. Fenton, J.M. Parker, P.V. Wright, *Polymer* **1973**, *14*, 589.

[69] S. D. Druger, A. Nitzan, M. A. Ratner, *J. Chem. Phys.* **1983**, *79*, 3133.

[70] A. Nitzan, M. A. Ratner, *J. Phys. Chem.* **1994**, *98*, 1765.

[71] B. L. Papke, M. A. Ratner, D. F. Shriver, *J. Electrochem. Soc.* **1982**, *129*, 1694.

[72] G. Zardalidis, E. Ioannou, S. Pispas, G. Floudas, *Macromolecules (Washington, DC, U. S.)* **2013**, *46*, 2705.

[73] C. Berthier, W. Gorecki, M. Minier, M. B. Armand, J. M. Chabagno, P. Rigaud, *Solid State Ionics* **1983**, *11*, 91.

[74] W. Gorecki, M. Jeannin, E. Belorizky, C. Roux, M. Armand, *J. Phys.: Condens. Matter* **1995**, *7*, 6823.

[75] S. Lascaud, M. Perrier, A. Vallée, S. Besner, J. Prud'homme, M. Armand, *Macromolecules (Washington, DC, U. S.)* **1994**, *27*, 7469.

[76] A. Vallée, S. Besner, J. Prud'homme, *Electrochim. Acta* **1992**, *37*, 1579.

[77] J. Shi, C. A. Vincent, *Solid State Ionics* **1993**, *60*, 11.

[78] G. R. Strobl, *The physics of polymers*. *Concepts for understanding their structures and behavior*, Springer, Berlin, **2011**.

[79] A. A. Teran, M. H. Tang, S. A. Mullin, N. P. Balsara, *Solid State Ionics* **2011**, *203*, 18.

[80] K. P. Barteau, M. Wolffs, N. A. Lynd, G. H. Fredrickson, E. J. Kramer, C. J. Hawker, *Macromolecules (Washington, DC, U. S.)* **2013**, *46*, 8988.

[81] F. S. Bates, *MRS Bull.* **2005**, *30*, 525.

[82] A. Panday, S. Mullin, E. D. Gomez, N. Wanakule, V. L. Chen, A. Hexemer, J. Pople, N. P. Balsara, *Macromolecules (Washington, DC, U. S.)* **2009**, *42*, 4632.

[83] M. Singh, O. Odusanya, G. M. Wilmes, H. B. Eitouni, E. D. Gomez, A. J. Patel, V. L. Chen, M. J. Park, P. Fragouli, H. Iatrou *et al.*, *Macromolecules (Washington, DC, U. S.)* **2007**, *40*, 4578.

[84] N. S. Wanakule, A. Panday, S. A. Mullin, E. Gann, A. Hexemer, N. P. Balsara, *Macromolecules (Washington, DC, U. S.)* **2009**, *42*, 5642.

[85] P. Jannasch, *Chem. Mater.* **2002**, *14*, 2718.

[86] S. Feng, D. Shi, F. Liu, L. Zheng, J. Nie, W. Feng, X. Huang, M. Armand, Z. Zhou, *Electrochim. Acta* **2013**, *93*, 254.

[87] Y. Ikeda, Y. Wada, Y. Matoba, S. Murakami, S. Kohjiya, *Electrochim. Acta* **2000**, *45*, 1167.

[88] N. Kobayashi, M. Uchiyama, E. Tsuchida, *Solid State Ionics* **1985**, *17*, 307.

[89] A. Krimalowski, M. Thelakkat, *Macromolecules (Washington, DC, U. S.)* **2019**, *52*, 4042.

[90] S. Li, A. I. Mohamed, V. Pande, H. Wang, J. Cuthbert, X. Pan, H. He, Z. Wang, V. Viswanathan, J. F. Whitacre *et al.*, *ACS Energy Lett.* **2018**, *3*, 20.

[91] T. Niitani, M. Shimada, K. Kawamura, K. Dokko, Y.-H. Rho, K. Kanamura, *Electrochem. Solid-State Lett.* **2005**, *8*, A385.

[92] D. Rosenbach, N. Mödl, M. Hahn, J. Petry, M. A. Danzer, M. Thelakkat, *ACS Appl. Energy Mater.* **2019**, *2*, 3373.

[93] H. Kosonen, S. Valkama, J. Hartikainen, H. Eerikäinen, M. Torkkeli, K. Jokela, R. Serimaa, F. Sundholm, G. ten Brinke, O. Ikkala, *Macromolecules (Washington, DC, U. S.)* **2002**, *35*, 10149.

[94] C. Kirsch, M. Pulst, M. H. Samiullah, P. Ruda, N. Hasan, J. Kressler, *Solid State Ionics* **2017**, *309*, 163.

[95] M. Pulst, M. H. Samiullah, U. Baumeister, M. Prehm, J. Balko, T. Thurn-Albrecht, K. Busse, Y. Golitsyn, D. Reichert, J. Kressler, *Macromolecules (Washington, DC, U. S.)* **2016**, *49*, 6609.

[96] M. H. Samiullah, M. Pulst, Y. Golitsyn, K. Busse, S. Poppe, H. Hussain, D. Reichert, J. Kressler, *Macromolecules (Washington, DC, U. S.)* **2018**, *51*, 4407.

[97] M. Meldal, C. W. Tornøe, *Chem. Rev. (Washington, DC, U. S.)* **2008**, *108*, 2952.

[98] M. Pulst, J. Balko, Y. Golitsyn, D. Reichert, K. Busse, J. Kressler, *Phys. Chem. Chem. Phys.* **2016**, *18*, 6153.

[99] J. E. Hein, V. V. Fokin, *Chem. Soc. Rev.* **2010**, *39*, 1302.

[100] V. V. Rostovtsev, L. G. Green, V. V. Fokin, K. B. Sharpless, *Angew. Chem.* **2002**, *114*, 2708.

[101] C. W. Tornøe, C. Christensen, M. Meldal, *J. Org. Chem.* **2002**, *67*, 3057.

[102] A. S. Lang, A. Neubig, M. Sommer, M. Thelakkat, *Macromolecules (Washington, DC, U. S.)* **2010**, *43*, 7001.

[103] P. M. Reichstein, S. Gödrich, G. Papastavrou, M. Thelakkat, *Macromolecules (Washington, DC, U. S.)* **2016**, *49*, 5484.

[104] R. Meziane, J.-P. Bonnet, M. Courty, K. Djellab, M. Armand, *Electrochim. Acta* **2011**, *57*, 14.

[105] Q. Ma, H. Zhang, C. Zhou, L. Zheng, P. Cheng, J. Nie, W. Feng, Y.-S. Hu, H. Li, X. Huang *et al.*, *Angew. Chem., Int. Ed.* **2016**, *55*, 2521.

[106] Y. Tominaga, K. Yamazaki, *Chem. Commun. (Cambridge, U. K.)* **2014**, *50*, 4448.

[107] Y. Tominaga, *Polym. J. (Tokyo, Jpn.)* **2017**, *49*, 291.

[108] J. Zhang, J. Zhao, L. Yue, Q. Wang, J. Chai, Z. Liu, X. Zhou, H. Li, Y. Guo, G. Cui *et al.*, *Adv. Energy Mater.* **2015**, *5*, 1501082.

[109] J.-C. Lee, M. H. Litt, *Macromolecules (Washington, DC, U. S.)* **2000**, *33*, 1618.

[110] S.-J. Kwon, D.-G. Kim, J. Shim, J. H. Lee, J.-H. Baik, J.-C. Lee, *Polymer* **2014**, *55*, 2799.

[111] P. C. Barbosa, L. C. Rodrigues, M. M. Silva, M. J. Smith, *Solid State Ionics* **2011**, *193*, 39.

[112] M. Smith, *Solid State Ionics* **2001**, *140*, 345.

[113] B. Sun, J. Mindemark, K. Edström, D. Brandell, *Solid State Ionics* **2014**, *262*, 738.

[114] J. Mindemark, E. Törmä, B. Sun, D. Brandell, *Polymer* **2015**, *63*, 91.

[115] J. Mindemark, B. Sun, E. Törmä, D. Brandell, *J. Power Sources* **2015**, *298*, 166.

[116] C. P. Fonseca, D. S. Rosa, F. Gaboardi, S. Neves, *J. Power Sources* **2006**, *155*, 381.

[117] C. Polo Fonseca, S. Neves, *J. Power Sources* **2006**, *159*, 712.

[118] C. M. Friesen, B. Améduri, *Prog. Polym. Sci.* **2018**, *81*, 238.

[119] G. Marchionni, G. Ajroldi, G. Pezzin, *Eur. Polym. J.* **1988**, *24*, 1211.

[120] M. Chintapalli, K. Timachova, K. R. Olson, S. J. Mecham, D. Devaux, J. M. DeSimone, N. P. Balsara, *Macromolecules (Washington, DC, U. S.)* **2016**, *49*, 3508.

[121] D. H. C. Wong, A. Vitale, D. Devaux, A. Taylor, A. A. Pandya, D. T. Hallinan, J. L. Thelen, S. J. Mecham, S. F. Lux, A. M. Lapides *et al.*, *Chem. Mater.* **2015**, *27*, 597.

[122] K. Timachova, M. Chintapalli, K. R. Olson, S. J. Mecham, J. M. DeSimone, N. P. Balsara, *Soft Matter* **2017**, *13*, 5389.

[123] M. Skalický, V. Skalická, J. Paterová, M. Rybáčková, M. Kvíčalová, J. Cvačka, A. Březinová, J. Kvíčala, *Organometallics* **2012**, *31*, 1524.

[124] D. Devaux, Y. H. Chang, I. Villaluenga, X. C. Chen, M. Chintapalli, J. M. DeSimone, N. P. Balsara, *J. Power Sources* **2016**, *323*, 158.

[125] K. R. Olson, D. H. C. Wong, M. Chintapalli, K. Timachova, R. Janusziewicz, W. F. M. Daniel, S. Mecham, S. Sheiko, N. P. Balsara, J. M. DeSimone, *Polymer* **2016**, *100*, 126.

[126] D. Devaux, I. Villaluenga, M. Bhatt, D. Shah, X. C. Chen, J. L. Thelen, J. M. DeSimone, N. P. Balsara, *Solid State Ionics* **2017**, *310*, 71.

[127] J.-H. Baik, D.-G. Kim, J. H. Lee, S. Kim, D. G. Hong, J.-C. Lee, *Ind. Eng. Chem.* **2018**, *64*, 453.

[128] G. Lopez, M. Guerre, J. Schmidt, Y. Talmon, V. Ladmiral, J.-P. Habas, B. Améduri, *Polym. Chem.* **2016**, *7*, 402.

[129] R. Berger, G. Resnati, P. Metrangolo, E. Weber, J. Hulliger, *Chem. Soc. Rev.* **2011**, *40*, 3496.

[130] M. Yano, T. Taketsugu, K. Hori, H. Okamoto, S. Takenaka, *Chem. - Eur. J.* **2004**, *10*, 3991.

[131] M. Chintapalli, K. Timachova, K. R. Olson, M. Banaszak, J. L. Thelen, S. J. Mecham, J. M. DeSimone, N. P. Balsara, *Soft Matter* **2017**, *13*, 4047.

[132] Y. Ren, T. P. Lodge, M. A. Hillmyer, *Macromolecules (Washington, DC, U. S.)* **2000**, *33*, 866.

[133] a) Y. Ren, T. P. Lodge, M. A. Hillmyer, *Macromolecules (Washington, DC, U. S.)* **2001**, *34*, 4780; b) Y. Ren, T. P. Lodge, M. A. Hillmyer, *Macromolecules (Washington, DC, U. S.)* **2002**, *35*, 3889.

[134] E. Cznotka, S. Jeschke, M. Grünebaum, H.-D. Wiemhöfer, *Solid State Ionics* **2016**, *292*, 45.

[135] A. Abouimrane, I. Belharouak, K. Amine, *Electrochem. Commun.* **2009**, *11*, 1073.

[136] Q. Cheng, Z. Cui, J. Li, S. Qin, F. Yan, J. Li, *J. Power Sources* **2014**, *266*, 401.

[137] J. M. Sarapas, G. N. Tew, *Macromolecules (Washington, DC, U. S.)* **2016**, *49*, 1154.

[138] F. Wu, H. Zhou, Y. Bai, H. Wang, C. Wu, *ACS Appl. Mater. Interfaces* **2015**, *7*, 15098.

[139] C. Marestin, X. Thiry, S. Rojo, E. Chauveau, R. Mercier, *Polymer* **2017**, *108*, 179.

[140] H. Mori, E. Kudo, Y. Saito, A. Onuma, M. Morishima, *Macromolecules (Washington, DC, U. S.)* **2010**, *43*, 7021.

[141] H. Mori, Y. Saito, E. Takahashi, K. Nakabayashi, A. Onuma, M. Morishima, *Polymer* **2012**, *53*, 3861.

[142] H. Mori, Y. Saito, E. Takahashi, K. Nakabayashi, A. Onuma, M. Morishima, *React. Funct. Polym.* **2013**, *73*, 658.

[143] H.-G. Elias, *Makromoleküle. Chemische Struktur und Synthesen*, Wiley-VCH, Weinheim, **1999**.

[144] J. Chiefari, Y. K. Chong, F. Ercole, J. Krstina, J. Jeffery, T. P. T. Le, R. T. A. Mayadunne, G. F. Meijs, C. L. Moad, G. Moad *et al.*, *Macromolecules (Washington, DC, U. S.)* **1998**, *31*, 5559.

[145] C. J. Hawker, A. W. Bosman, E. Harth, *Chem. Rev. (Washington, DC, U. S.)* **2001**, *101*, 3661.

[146] C. Barner-Kowollik, *Handbook of RAFT Polymerization*, Wiley, **2008**.

[147] C. Barner-Kowollik, M. Buback, B. Charleux, M. L. Coote, M. Drache, T. Fukuda, A. Goto, B. Klumperman, A. B. Lowe, J. B. Mcleary *et al.*, *J. Polym. Sci., Part A: Polym. Chem.* **2006**, *44*, 5809.

[148] G. Moad, E. Rizzardo, S. H. Thang, *Aust. J. Chem.* **2005**, *58*, 379.

[149] J. Nicolas, Y. Guillaneuf, C. Lefay, D. Bertin, D. Gigmes, B. Charleux, *Prog. Polym. Sci.* **2013**, *38*, 63.

[150] D. Benoit, V. Chaplinski, R. Braslau, C. J. Hawker, *J. Am. Chem. Soc.* **1999**, *121*, 3904.

[151] S. Fleischmann, H. Komber, B. Voit, *Macromolecules (Washington, DC, U. S.)* **2008**, *41*, 5255.

[152] H. Burchardt-Tofaute, M. Thelakkat, *Polym. Chem.* **2018**, *9*, 4172.

[153] M. Hummel, M. Markiewicz, S. Stolte, M. Noisternig, D. E. Braun, T. Gelbrich, U. J. Griesser, G. Partl, B. Naier, K. Wurst *et al.*, *Green Chem.* **2017**, *19*, 3225.

[154] A. S. Lang, M. Thelakkat, *Polym. Chem.* **2011**, *2*, 2213.

[155] P. Leophairatana, S. Samanta, C. C. de Silva, J. T. Koberstein, *J. Am. Chem. Soc.* **2017**, *139*, 3756.

[156] Y.-W. Chung, J.-K. Lee, W.-C. Zin, B.-K. Cho, *J. Am. Chem. Soc.* **2008**, *130*, 7139.

[157] Y. Li, J. N. Hoskins, S. G. Sreerama, S. M. Grayson, *Macromolecules (Washington, DC, U. S.)* **2010**, *43*, 6225.

[158] A. J. T. Dirks, S. S. van Berkel, N. S. Hatzakis, J. A. Opsteen, F. L. van Delft, J. J. L. M. Cornelissen, A. E. Rowan, J. C. M. van Hest, F. P. J. T. Rutjes, R. J. M. Nolte, *Chem. Commun. (Cambridge, U. K.)* **2005**, 4172.

[159] D. C. Schriemer, L. Li, *Anal. Chem. (Washington, DC, U. S.)* **1997**, *69*, 4169.

[160] D. C. Schriemer, L. Li, *Anal. Chem. (Washington, DC, U. S.)* **1997**, *69*, 4176.

[161] H. Zhu, T. Yalcin, L. Li, *J. Am. Soc. Mass Spectrom.* **1998**, *9*, 275.

[162] P. Johansson, S. P. Gejji, J. Tegenfeldt, J. Lindgren, *Electrochim. Acta* **1998**, *43*, 1375.

[163] Y. Matsumiya, N. P. Balsara, J. B. Kerr, T. Inoue, H. Watanabe, *Macromolecules (Washington, DC, U. S.)* **2004**, *37*, 544.

[164] K. M. Diederichsen, H. G. Buss, B. D. McCloskey, *Macromolecules (Washington, DC, U. S.)* **2017**, *50*, 3831.

[165] C. A. Angell, R. D. Bressel, *J. Phys. Chem.* **1972**, *76*, 3244.

[166] D. Devaux, R. Bouchet, D. Glé, R. Denoyel, *Solid State Ionics* **2012**, *227*, 119.

[167] A. Ferry, M. Tian, *Macromolecules (Washington, DC, U. S.)* **1997**, *30*, 1214.

[168] K. M. Abraham, Z. Jiang, B. Carroll, *Chem. Mater.* **1997**, *9*, 1978.

[169] L. Edman, M. M. Doeff, A. Ferry, J. Kerr, L. C. de Jonghe, *J. Phys. Chem. B* **2000**, *104*, 3476.

[170] K. Timachova, H. Watanabe, N. P. Balsara, *Macromolecules (Washington, DC, U. S.)* **2015**, *48*, 7882.

[171] T. Fujigaya, S. Ando, Y. Shibasaki, S. Kishimura, M. Endo, M. Sasago, M. Ueda, *J. Photopolym. Sci. Technol.* **2002**, *15*, 643.

[172] J. F. King, J. H. Hillhouse, S. Skonieczny, *Can. J. Chem.* **1984**, *62*, 1977.

[173] G. Liu, G. L. Baker, *Soft Matter* **2008**, *4*, 1094.

[174] M. Shirai, J. Nakanishi, M. Tsunooka, T. Matsuo, M. Endo, *J. Photopolym. Sci. Technol.* **1998**, *11*, 641.

[175] R. B. Grossman, *The art of writing reasonable organic reaction mechanisms*, Springer, New York, **2010**.

[176] C. G. Overberger, D. E. Baldwin, H. P. Gregor, *J. Am. Chem. Soc.* **1950**, *72*, 4864.

[177] M. Shirai, A. Kawaue, H. Okamura, M. Tsunooka, *Chem. Mater.* **2003**, *15*, 4075.

[178] S. C. Miller, *J. Org. Chem.* **2010**, *75*, 4632.

[179] H. Ohno, *Bull. Chem. Soc. Jpn.* **2006**, *79*, 1665.

[180] N. V. Plechkova, K. R. Seddon, *Chem. Soc. Rev.* **2008**, *37*, 123.

[181] L. Zhao, Y. Huang, B. Liu, Y. Huang, A. Song, Y. Lin, M. Wang, X. Li, H. Cao, *Electrochim. Acta* **2018**, *278*, 1.

[182] S. Ferrari, E. Quartarone, P. Mustarelli, A. Magistris, M. Fagnoni, S. Protti, C. Gerbaldi, A. Spinella, *J. Power Sources* **2010**, *195*, 559.

[183] S.-T. Myung, Y. Hitoshi, Y.-K. Sun, *J. Mater. Chem.* **2011**, *21*, 9891.

[184] A. Lisowska-Oleksiak, H. D. Inerowicz, *J. Power Sources* **1999**, *81-82*, 813.

[185] M. Destarac, C. Brochon, J.-M. Catala, A. Wilczewska, S. Z. Zard, *Macromol. Chem. Phys.* **2002**, *203*, 2281.

[186] Z. Stoeva, I. Martin-Litas, E. Staunton, Y. G. Andreev, P. G. Bruce, *J. Am. Chem. Soc.* **2003**, *125*, 4619.

[187] N. Mohmeyer, P. Wang, H.-W. Schmidt, S. M. Zakeeruddin, M. Grätzel, *J. Mater. Chem.* **2004**, *14*, 1905.

Danksagung

An dieser Stelle möchte ich mich ganz herzlich bei allen bedanken, die mir bei der Anfertigung dieser Doktorarbeit mit Rat und Tat zur Seite gestanden haben.

Mein größter Dank gilt meinem Doktorvater *Prof. Mukundan Thelakkat*, der mir größtmögliche Freiheit bei der Gestaltung des Themas gwährt hat. Vielen Dank für die Schaffung des finanziellen und fachlichen Rahmens, deine motivierende und menschliche Art, die zielführenden Diskussionen sowie dein Vertrauen in meine wissenschaftliche Arbeit.

Für die Möglichkeit mein Wissen im Bereich der elektrochemischen Messverfahren zu vertiefen, möchte ich an dieser Stelle insbesondere *Lide Rodriguez-Martinez*, *Chunmei Li* und *Xabier Júdez* sowie allen weiteren Mitarbeiter/-innen des Forschungszentrums CIC energigune (Vitoria-Gasteiz, Spanien) danken, die mich dort während meines Aufenthalts unterstützt haben.

Meinen Laborkollegen in der B6, *Martin Hufnagel*, *Christian Müller*, *Tina Weller*, *Gert Krauss*, *Tanaji Gujar*, *Dominic Rosenbach* und *Alexander Krimalowski*, danke ich für das angenehme Arbeitsklima und den steten fachlichen Austausch. Darüber hinaus sei allen Kollegen vom Lehrstuhl MC I für die tolle Zusammenarbeit und die schöne Zeit gedankt! Bei *Petra Weiss* und *Christina Wunderlich* bedanke ich mich für die Hilfe bei den administrativen Hürden.

Ein gesonderter Dank gilt *Dominic Rosenbach* für die praktische Durchführung der thermischen und elektrochemischen Messungen der Polymerelektrolyte des ersten Kapitels dieser Arbeit.

Ebenfalls bedanke ich mich bei *Martina Fried* sowie meinen Praktikanten und HiWis, *Alexander Krimalowski*, *Moritz Salzmann*, *Michael Weiß*, *Timo Nachbar*, *Jannik Petry* und *Ferdinand Seibold*, die mich bei der Synthese der neuen Materialien in dieser Arbeit tatkräftig unterstützt haben. Meinen Mitstreitern bei dem Aufbau der elektrochemischen Messverfahren, *Jonas Mayer* und *Dominic Rosenbach*, gilt mein großer Dank. Für die Messung unzähliger GPC- und NMR-Proben bedanke ich mich insbesondere bei *Paul Reichstein*, *Katharina Neumann*, *Christina Saller*, *Tina Weller* und *Rika Schneider*.

Ein großer Dank gilt meinen Eltern sowie all meinen Verwandten und Freunden (Danke *Andy*!), die mich während der gesamten Zeit unterstützt und motiviert haben.

Ohne ihren Ansporn und unerlässlichen Rückhalt jedoch hätte ich es bis hierher nicht geschafft:

Mein herzlichster Dank gilt meiner Frau *Lena*!

Eidesstattliche Versicherung und Erklärungen

(§ 9 Satz 2 Nr. 3 PromO BayNAT)
Hiermit versichere ich eidesstattlich, dass ich die Arbeit selbstständig verfasst und keine anderen als die von mir angegebenen Quellen und Hilfsmittel benutzt habe (vgl. Art. 97 Abs. 1 Satz 8 BayHIG).

(§ 9 Satz 2 Nr. 3 PromO BayNAT)
Hiermit erkläre ich, dass ich die Dissertation nicht bereits zur Erlangung eines akademischen Grades eingereicht habe und dass ich nicht bereits diese oder eine gleichartige Doktorprüfung endgültig nicht bestanden habe.

(§ 9 Satz 2 Nr. 4 PromO BayNAT)
Hiermit erkläre ich, dass ich Hilfe von gewerblichen Promotionsberatern bzw. –vermittlern oder ähnlichen Dienstleistern weder bisher in Anspruch genommen habe noch künftig in Anspruch nehmen werde.

(§ 9 Satz 2 Nr. 7 PromO BayNAT)
Hiermit erkläre ich mein Einverständnis, dass die elektronische Fassung meiner Dissertation unter Wahrung meiner Urheberrechte und des Datenschutzes einer gesonderten Überprüfung unterzogen werden kann.

(§ 9 Satz 2 Nr. 8 PromO BayNAT)
Hiermit erkläre ich mein Einverständnis, dass bei Verdacht wissenschaftlichen Fehlverhaltens Ermittlungen durch universitätsinterne Organe der wissenschaftlichen Selbstkontrolle stattfinden können.

Lindenberg i. Allgäu, den

_____

Hubertus Burchardt-Tofaute